Water-Soluble Binders for Aqueously Processed Li-Ion Batteries

Chirag Patel

January 2025

A thesis submitted in partial fulfillment of the requirements for the degree of Doctor of Philosophy

University of Sheffield

Primary Supervisor: Dr Alisyn. J. Nedoma

Secondary Supervisors: Dr Alan Dunbar, Dr Abarasi Hart and Dr Gabriel. E. Perez

Acknowledgements

First and foremost, I thank my supervisor, Alisyn J. Nedoma, for the opportunity to undertake a PhD. I have never met someone so energetic and enthusiastic - your guidance has shaped me as a researcher. And thank you for many pints of craft beer - I'll keep my promise to supply you with a lifetime's worth of the stuff when I'm through with the viva! I thank my second supervisors: Alan Dunbar, Abarasi Hart, and Gabriel Perez, for their support and advice throughout the project. To everyone I've worked with in the lab: Josie, who taught me how to work with coin cells, and Sam. B, who taught me how to make a cathode slurry. To other folk heroes of the Kroto lab, namely Laura, Heather, Protein James, Jed, and Guo, who gets a thanks for supplying me with cathode active material when I ran low. I thank my MEng students: Sam. W, Will, and Ayo, for their invaluable efforts in sample preparation and testing. To Steve Ebbens, for training me on the DLS machine. To Igor, for teaching me how to use the QCMD, and for ensuring that it was available for me to use. A special mention to Laurie, the legendary muse of Kroto, renowned for in-lab singing and organizing social events - thank you for helping me both in the lab and with my electrochemical data, and for putting up with my shenanigans - both inside and outside the lab.

I would also like to thank the rest of my groupmates - the aptly named 'Nedoma Nutters': Georgia, Andy and Tom. You have all lifted me up and have been incredibly supportive. I give thanks to my friends outside my research group. Firstly Suruthi, for her encouragement and for supplying me with much-needed chai tea. To the D72 crew: George, Seb, Paul, Mollie, and Zoe. To Alex, who amongst other things helped me organize my leaving do. To Gareth, the coin cell connoisseur and prank co-conspirator - the wooden meter rule still has not yet arrived! You coined the phrase, "Not bad for a battery engineer", we know how badly you wanted to be one! To the C14/15 lot: Anna, Mahdi, Jack, and Lawson to name but a few. I have many fond memories with you guys, from lunches to attending ice hockey matches and more. To Kaan, the unofficial 'King of Kroto' - for many sessions both climbing and swing-dancing. A thank you to friends in Sheffield outside of academia, particularly Helen and Sheridan, for really being there for me and helping me make sense of things when I could not. You have all been an amazing bunch - I've had a lot of great times with you guys.

Finally, I would like to thank my parents Janita and Shailesh, and my brother, Nikhil, for their unconditional love and support towards me. I could not have accomplished this without you.

Publications

Chirag Patel, William Poizer, Ayo Omole, Laurence A Middlemiss, Heather Grievson, Abarasi Hart, Alan F. Dunbar, Igor Efimov, Kyra Sedransk-Campbell, Denis J. Cumming, Gabriel E. Pérez, and Alisyn J. Nedoma, "Optimizing the performance of water-processed NMC622 battery half cells by using pluronics to disperse carbon black", Manuscript in preparation.

Abarasi Hart, Xuesong Lu, Georgia Englezou, Laura Wheatcroft, **Chirag Patel**, Joe C. Stallard, Samuel G. Booth, Charles Stothard, Norman A. Fleck, Stephen J. Ebbens, Beverley J. Inkson, Serena A. Cussen, Denis J. Cumming and Alisyn J. Nedoma, "Effect of binder viscosity on the rheology of cathode slur ries and performance of lithium-ion battery half cells", Manuscript in preparation.

Conferences

C. Patel, W. Poizer, A. Omole, L. A. Middlemiss, I. Efimov, A. Dunbar, A. Hart, G. Pérez, and A. J. Nedoma, "Optimizing the performance of NMC622 battery half coin cells by using amphiphilic aqueous binders to modulate the percolation of carbon black", ECS PRiME 2024, Honolulu, October 2024.

C. Patel, A.Hart, G. Pérez, and A. J. Nedoma, "Optimizing the Slurry Microstructure for Aqueous Processed High Ni Cathodes with PEO as a Binder", poster, The Faraday Institution Conference, University of Birmingham, September 2023.

C. Patel, "Science Communication via Instagram & Public Engagement", conference talk, The Faraday Institution ECR Conference, University of Warwick, March 2023.

Abstract

As Li-ion battery technology is developed for the automotive sector, more environmentally friendly processing methods must be employed. The commonly used binder, PVDF, is being phased out due to legislation banning PFAS substances, providing an opportunity to re-evaluate the solvent. Aqueous processing with hydrophilic polymer binders is an emerging alternative to the conventional NMP/PVDF solvent/binder system for Li-ion batteries, offering advantages; namely nontoxic, unrestricted use, and cost-effectiveness. Aqueous binders can offer improvements in performance over typically processed cathodes with NMP, providing an opportunity to explore novel solvent/binder systems.

To screen for potential aqueous cathode binders, the chemical affinity of polymers to carbon black was quantified via adsorption measurements. Polyethylene oxide (PEO) was the most adsorbing homopolymer, and is cheap, commercially available and biodegradable. Early work with PEO resulted in low-capacity battery cells, likely because the molecular weight of the binder was not taken into consideration, resulting in low-viscosity slurries outside of the optimal range for cathode formation. To test this hypothesis, two high molecular weights of PEO were selected in order to evaluate the impact of viscosity on slurry structure. Various concentrations of each PEO were chosen to match the viscosity of two polymer solutions with different molecular weights, thereby determining whether slurry structure is strictly affected by viscosity or whether the molecular weight of the polymer has a role, presumably through the thickness of the adsorbed layer. Slurries are optically opaque and cannot be characterized by light-scattering methods, so rheology and conductivity were employed to study the microstructure. Varying the polymer concentration in the slurry enabled control over the percolation of carbon black. To assess PEO as a potential binder for high-nickel cathodes, coin cells were assembled. Despite PEO-containing slurries appearing smooth and homogeneous to the eye, the PEO cathodes performed worse than those made with NMP/PVDF.

The chemical affinity between the binder and carbon black was shown to correlate with the distribution of carbon black flocs, enabling tuning of 3D carbon black networks in the slurry. The distribution of carbon black was shown to affect both the cathode porosity and the contact resistance, which in turn affected the electrochemical performance of cathodes, likely due to more conductive pathways formed via better carbon black distribution in the slurry. Electrochemical charac-

terization revealed that the solid cathodes had varying microstructures, implying that cathode particles were not always uniformly dispersed within a matrix of CBD, again attributed to the distribution of carbon black in the dried cathode. The chemical affinity of the polymer binder to carbon black was therefore shown to predict the electrochemical performance of the cell.

Polymers with strong affinities for carbon black are hypothesised to result in better electrochemical performance, but adsorption is limited by the fact that hydrophobic polymers do not dissolve in water. To overcome this, an amphiphilic block copolymer (pluronic F68) was chosen to control the dispersion of carbon black in the slurry, yet its low viscosity renders it unsuitable for processing by itself. Therefore, to further study its effect on electrochemical performance, a series of blends were prepared with a high molecular weight PEO as a viscosity modifier. A series of formulations were developed that maximize the mass fraction of active material whilst ensuring enough binder was present to disperse the carbon black in water. By carefully controlling the viscosity, it was shown that electrochemical cell performance correlates strongly with the pluronic content.

It has been demonstrated that aqueous processed high-nickel cathodes can show comparable or better performance than cathodes processed conventionally with NMP, if the chosen binders have a strong chemical affinity to the conductive additive. Furthermore, amphiphilic block copolymers can be used for aqueous processing, as their hydrophobic block can adsorb onto the carbon surface, and their hydrophilic chains can disperse the flocs in water, resulting in improved carbon distribution compared to other aqueous binders. Both the solids loading and viscosity of the polymer blend can dictate carbon black distribution in the slurry and the dry electrode. This research demonstrates that aqueous-processed battery half-cells can achieve the same performance as those processed with the conventional organic solvent when the formulation is adapted to compensate for the hydrophobicity of the conductive additive.

Contents

List of Figures

List of Tables

1 Chapter 1: Introduction and Literature Review

1.1 Introduction

UK government legislation mandates that all new cars sold by 2030 be free of fossil fuels, driving vehicle electrification [1]. Battery cathodes are often the most expensive element of a battery cell and contribute heavily to pack costs [2, 3]. Increasing the specific capacity of cathode films is essential for achieving single charge ranges commensurate with internal combustion engine vehicles [4]. Most research is focused on the cathode chemistry [5–9]. Small gains in capacity from the mesostructure of cathode tape (as mediated by the binder) can have a large economic impact because cathode materials are expensive.

The role of the binder is generally underappreciated [10]. The binder modulates slurry interactions through adsorption (colloid stabilization). The type of binder and the amount used controls the viscosity of the electrode slurry [11, 12]. It significantly controls the kinetics of drying and structure formation. It also provides mechanical resilience in the dried cathode film and enables adhesion to the current collector. The benchmark polymer used in cathode formulations is poly(vinylidene fluoride) (PVDF) [10].

Water soluble binders will reduce environmental impact and may reduce battery cost for the following reasons. First, the cost of using water is 22 times less expensive than the solvent currently used in industry N-Methyl-2-pyrrolidone (NMP). Second, using water reduces drying energy due to reduced latent heat of evaporation for water. Third, aqueous polymers with backbone oxygen are often biodegradable and may aid battery recycling [13, 14].

Challenges remain for aqueous processing. High Ni cathodes are susceptible to water damage, through dissolution of costly transition metals and limited voltage stability window for certain aqueous polymers, e.g. polyethylene oxide (PEO), which is used in lithium-ion battery electrolytes [10].

The approach in this project is to translate physical understanding of similar systems to the conventional NMP/PVDF into aqueous systems. To start, a benchmark homopolymer will be chosen, then the stability of copolymers will be evaluated. From

this, semi-quantitative design rules will be developed to guide the formulation and processing of water-processed cathodes.

The aim of this PhD project is to understand and control the formulation and processing of aqueous cathode slurries towards optimizing battery performance.

This project has been split into three objectives:

1. To understand the structure and rheological properties of aqueous cathode slurries using a homopolymer binder.
2. To determine whether the chemical affinity between aqueous polymers and conductive carbon additive affects the distribution of conductive carbon additive in the electrode structure, thereby controlling electrochemical performance.
3. To optimize the formulation and processing of aqueous block copolymer cathode slurries using a surfactant to control the distribution of conductive carbon additive in the electrode structure.

The novelties in this project are determining if the chemical affinity of polymers to carbon black affect electrochemical performance, and using block copolymers as surfactants to disperse carbon black in water and bring it into closer contact with cathode active material particles.

1.2 Literature Review

Lithium-ion batteries (LIBs) are used for a wide range of applications, including modern electric vehicles (EVs), as they have the highest specific energy density of current rechargeable battery technologies, as lithium ions are comparatively small. Current $LiFePO_4$ (LFP) cathodes can be charged up to 5000 times [15] over their relatively long lifespans and lose comparatively little capacity compared to other battery technologies, e.g. NMC and lead-acid systems. LIBs are ideal for EVs due to their volumetric energy density (Wh L^{-1}), and their gravimetric energy density (Wh kg^{-1}) (see Fig. 1).

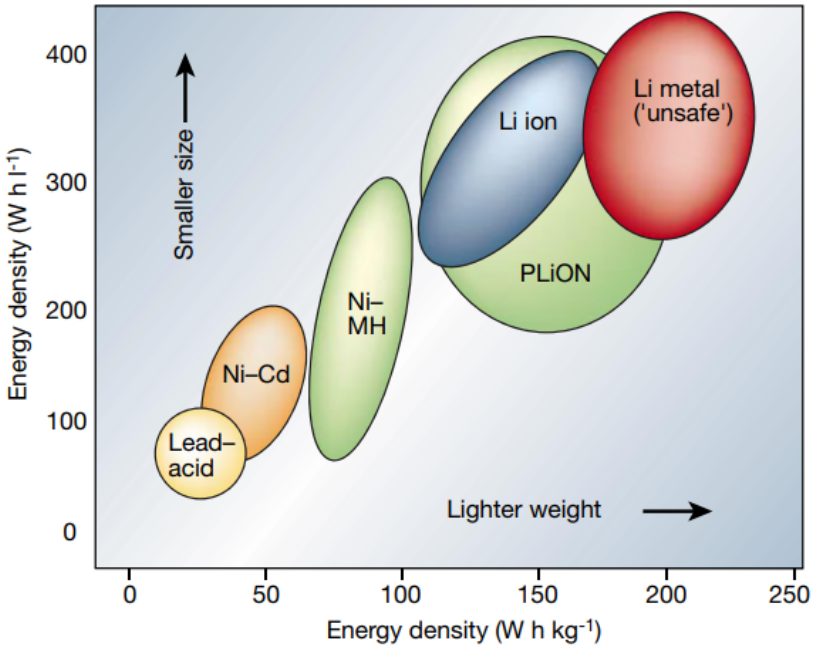

Figure 1: Ragone plot showing volumetric energy density versus gravimetric energy density for different battery chemistries [9].

The UK government aims to reduce greenhouse emissions to 'net zero' by 2050. In the UK, transport accounts for 27% of all greenhouse gas emissions, and cars account for 55% of those emissions, making them the largest polluting sector of the economy [16]. Electric vehicles reduce emissions because the national grid composition is 43.1% renewable as of 2020 [16]. The UK government aims to phase out the sale of internal combustion cars by 2030 and has stated that all new vehicles should be electrically propelled by 2035 if not sooner, driving a market for lithium-ion battery production [3]. Current EVs use batteries that do not provide high range due to energy densities

that are lower than the $\geq$ 800 Wh kg^{-1} at the cathode level, required to meet the higher energy densities demanded by electric vehicle applications [3, 17], so there is an emerging opportunity to develop a new ecosystem for battery manufacturing that emphasizes consumer needs, for instance, longer journey range. Developing a battery manufacturing ecosystem whilst internal combustion vehicles are phased out will save 100,000 jobs in the automotive sector [18]. The Business Research Company [18] states that the global lithium-ion batteries market was worth $31.4 billion in 2019, with the value of the market worth £5 billion ($6.8 billion) in the UK.

For the performance of an EV, the battery needs a long cycle life (10000 cycles [19]), has to have a high discharge capacity, be able to operate safely and have a high volumetric/gravimetric energy and power density [3]. These performance metrics are affected by the physical properties of the active materials during charge/discharge of the cell.

1.3 Cell charge and discharge

Batteries are devices consisting of electrochemical cells connected in series that store chemical energy and discharge electrical energy [20]. Electrochemical cells operate based on redox reactions, which refer to the electron transfer between reactants and products, resulting in their reduction and oxidation [20].

The components of a battery are: the anode (negative electrode), the cathode (positive electrode), the electrolyte and a separator. The cathode acts as a source of lithium for the lithium-ion batteries. The anode comprises a layered material; graphene or silicon are commonly used commercially. Currently, graphite is the most widely used material for commercially available anodes due to its hierarchical structure. The relatively large gaps between adjacent carbon layers serve as insertion sites for lithium ions as they intercalate in the anode material. Anode materials are chosen for their high surface area for lithium adsorption and storage when charged, which promotes electrode activity and reducing the length of lithium diffusion, which increases the charge transfer efficiency [21]. Both electrodes are porous, and each is attached to a current collector – typically a copper film is attached to the anode, and an aluminium film to the cathode as copper reacts with the cathode active material [22]. The electrodes are kept apart by a separator membrane, which is permeable to lithium ions [23]. A common

electrolyte in LIBs is $LiFP_6$ salt dissolved in carbonate and carbonate ester solvents, allowing lithium cation transport between the electrodes. Li^+ is a small cation, so it binds strongly to nucleophilic sites in the dissolved salt [24]. The separator prevents physical contact between the anode and the cathode so they should be mechanically robust, whilst enabling ion transport in the cell, so they must be porous and chemically inert.

Energy in electrochemical cells is stored via spatial separation of the oxidation and reduction processes, allowing them to occur on electrodes. During operation, the two electrodes are electrically connected via an external circuit. During discharge, lithium ions are spontaneously oxidised at the anode. Electrons flow from the anode to the cathode through the external circuit, performing useful work, whilst lithium ions diffuse across the liquid electrolyte to the cathode, where they intercalate within the cathode active material particles upon reaction with the electrons. When the battery is charged, a potential is applied (positive at the cathode) driving electrons into the anode and causing lithium to diffuse back into the anode to balance the charge. During both charge and discharge, the transport of charge is driven by differences in the electrochemical potential of the electrodes. A schematic of the operation of a LIB is shown in Fig. 2.

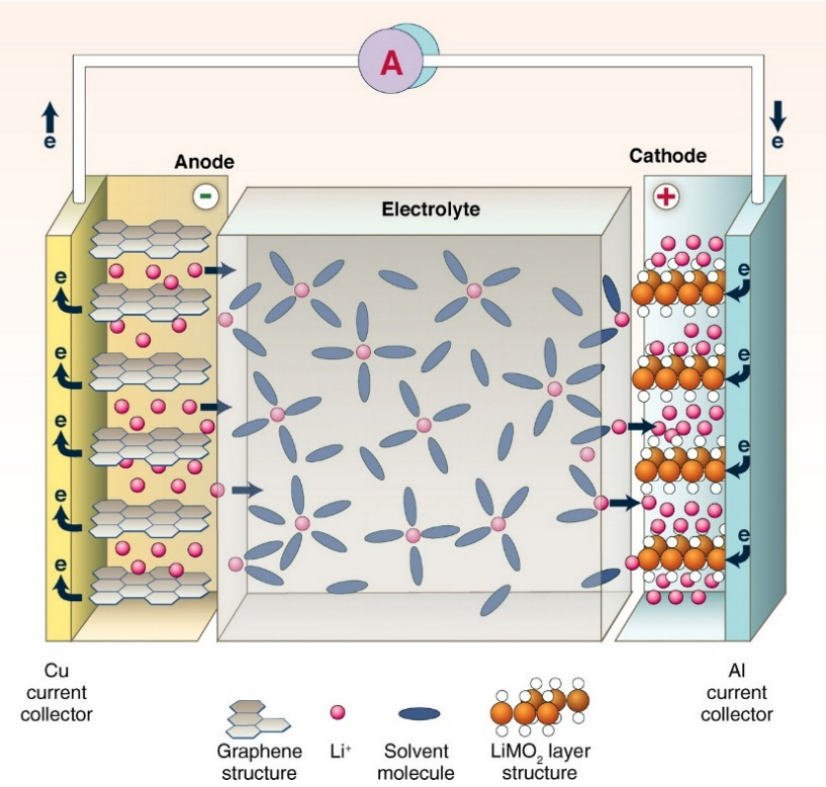

Figure 2: Schematic diagram of a LIB during discharge [25].

The voltage of the cell during discharge is produced by the difference in chemical potential between the anode and cathode (μ_A and μ_C respectively, see Fig. 1), [26]. The voltage is a measure of how much power a cell can produce [26,27] The cell voltage is given by Equation 2. where F is the Faraday constant (96485.3329 C/mol):

$$V_{cell} = \frac{\mu_c - \mu_A}{F} \tag{2}$$

For a high cell voltage, μ_c must be small and thus in a low energy state, and μ_A must be large, thus in a high energy state. However, the stability window of the electrolyte is also considered - see Fig. 3. When the voltage of the cell exceeds the stability window of the electrolyte, redox reactions form an SEI [26].

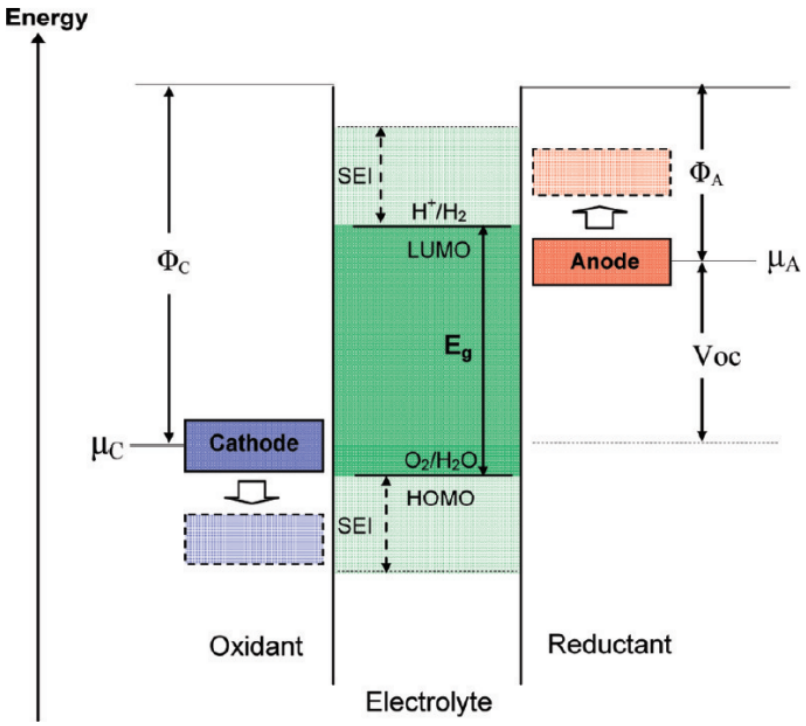

Figure 3: Schematic open-circuit energy diagram of an aqueous electrolyte. The anode and cathode work functions are ϕ_A and ϕ_C respectively. E_g is the thermodynamic stability window of the electrolyte. [26].

Charging is a non-spontaneous process; therefore an electrical potential must be applied to drive the intercalation reaction. This provides the activation energy to remove lithium ions and electrons from the cathode and transport them to the anode. The reverse process, or discharge, is a spontaneous reaction, wherein the electrons and Li-ions return to the cathode through the load and electrolyte respectively. In passing through the external circuit, electrons perform work such as powering a light or a motor [27].

The total energy stored in a lithium-ion cell is proportional to the amount of lithium that can be transported between the electrodes, as governed by

$$E_{Stored} = Q_{cell} \text{ x } V_{cell} \tag{3}$$

The stored energy can be increased by increasing the charge capacity of the cell, Q_{cell}, or the cell potential, V_{cell}. Standard carbonaceous anode potentials are 0 V vs. Li/Li^+ [26], so to increase the cell potential, cathode materials with low values of

cathode chemical potential (μ_C) are necessary, as to increase the energy-level separation between the cathode and the anode. For high Ni NMC cathodes as used in this project, the maximum voltage to avoid electrolyte degradation is 4.4V [28].

1.4 Cathodes

In battery development, the cathode contributes significantly to both the cost and mass of the battery. Cathode materials exhibit lower capacities and disproportionately higher costs relative to current commercial anode materials and are therefore a limiting factor for electrochemical performance in LIBs [3]. Typically, the cathode occupies a high proportion of the mass and volume of the battery, and up to half the cell cost. By contrast, the anode will occupy more of the cell volume but considerably lower mass, and lower cell cost. Cathode materials also often comprise low abundance, expensive transition metals like Co, and raise ethical concerns in the supply chain [3, 29–31].

1.5 Choice of cathode active material

There are several types of cathode-active materials in use or have been studied for LIBs. Energy density, safety and cost are the main factors contributing to the choice of cathode active material. An emerging cathode chemistry is $Li_xNi_xMn_{1-x-y}Co_yO_2$ (NMC). Ni contributes to improved capacity due to the Ni^{2+}/Ni^{4+} couple in deintercalation/intercalation of Li^+ ions. However, increasing Ni content will decrease thermal stability, as shown in Fig. 4. Mn contributes to thermal stability, and Co improves electronic conductivity [32]. In this project, NMC $Li_xNi_{0.6}Mn_{0.2}Co_{0.2}O_2$ (622) is chosen as it has a balance of high energy density provided by the Ni, yet is less prone to water degradation [32–34].

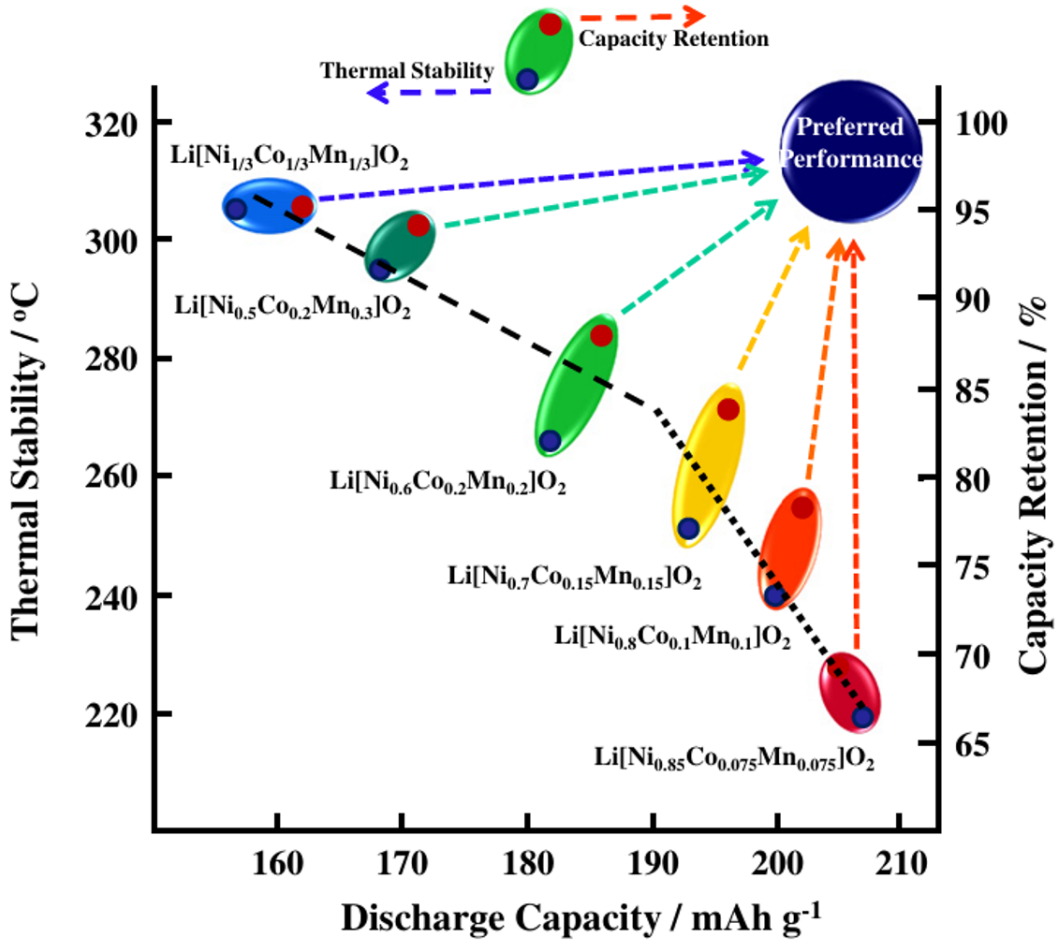

Figure 4: A map of relationship between discharge capacity, and thermal stability and capacity retention for NMC cathodes [35].

The cell reactions of NMC 622 during discharge are:

Anode: $\mathrm{Li} \rightarrow \mathrm{Li}^{+} + e^{-}$

Cathode: $\mathrm{Li}_{(1-x)}\ \mathrm{Ni}_{0.6}\mathrm{Mn}_{0.2}\mathrm{Co}_{0.2}\mathrm{O}_2 + \mathrm{xLi}^{+} + xe \rightarrow \mathrm{Li}_x\mathrm{Ni}_{0.6}\mathrm{Mn}_{0.2}\mathrm{Co}_{0.2}\mathrm{O}_2$

Overall cell reaction: $\mathrm{Li} + \mathrm{Li}_{(2-x)}\mathrm{Ni}_{0.6}\mathrm{Mn}_{0.2}\mathrm{Co}_{0.2}\mathrm{O}_2 \rightarrow \mathrm{xLiNi}_{0.6}\mathrm{Mn}_{0.2}\mathrm{Co}_{0.2}\mathrm{O}_2$

Increasing the nickel content of cathodes increases their energy density and specific capacity by allowing more interactions with lithium ions to occur in the cathode; however, the increase in nickel content results in reduced stability. The cathode surface reacts with the electrolyte to form a solid cathode-electrolyte interface (CEI) [29].

High-nickel cathode materials can degrade at the surface due to electrolyte degradation, to form a cathode electrolyte interphase (CEI) at the electrode-electrolyte interface, as well as structural degradation due to lattice distortion within the individual cathode particles [36].

Mechanical stress generated during cycling causes cathodes to become brittle, especially at a high charge rate when intercalation is rapid [37–39]. Mechanical stresses sufficient to form such cracks may arise from uneven distribution of strain within active material particles due to unequal charge distribution [37–39], changes in the phase of the active material lattice [21], [37] or anisotropy in the strain between neighbouring polycrystalline grains of active materials [40]. Such cracks expose a greater area of active material to the electrolyte, promoting CEI formation, leading to capacity fade [21].

1.6 Cathode processing

Whilst cathode performance has increased due to the shift from materials such as $LiFePO_4$ to Ni–rich materials e.g. NMCs, other factors limit their performance. In LIB cathodes, energy density presents a bottleneck. Doubling the energy density of the battery is very difficult without increasing the thickness of the electrode, which itself would result in problems resulting from excessive mass loading of electrodes [3, 41]. During the drying process, the cathode particles settle due to gravity, leading to an inhomogeneous binder distribution in the out-of-plane direction of the electrode [23]. As a result, electron transport and lithium-ion diffusion can be impeded, resulting in high polarization, reduced cycle life, and rate performance [42]. Once the binding strength no longer accommodates the volume expansion, pulverization of the cathode occurs and results in huge capacity loss e.g. 28% after 300 cycles for a $LiNi_{0.5}Mn_{1.5}O_4$ (LNMO) cell [29].

By studying capacity fade (long-term cycling), battery degradation is directly investigated. Loss of cyclable lithium has been linked to degradation mechanisms due to factors including structural changes, SEI formation, the increase of internal battery resistance, and mechanical degradation (active material pulverization or electrode crack formation) [43]. The integrity of the electrode is directly the responsibility of the binder. If the binder fails to do this, internal stress brought on by volume changes during lithiation may cause crack formation in the electrode. This would result in a loss

of interparticle interaction, electrical isolation of the active material, and a substantial reduction in capacity, especially during the initial cycles [43–45].

The differential capacity (dQ/dV) is calculated to determine the voltages at which redox reactions occur. The peaks on the dQ/dV curves typically represent material phase transitions [46]. The peak shift and changes in peak-to-peak capacity are used to calculate the contributions of various fatigue mechanisms, such as active cathode loss, anode loss, and loss of lithium inventory (LLI) [43].

1.7 Carbon black

The conductivity of cathode materials is poor as active materials are semi-conducting, therefore in all electrode formulations, a conductive additive is present to improve the electronic conduction. The conductive material's primary purpose is to improve the electrode's ability to conduct electricity [47].

Carbon black is a form of paracrystalline carbon. Carbon black is a common conductive additive for LIBs due to its small particle sizes and large surface area to volume ratio, enabling a good distribution of it throughout the cathode as well as being cheap and long-lasting [48, 49], and is also proven to increase cycle life and decrease polarisation of the electrode [49]. Despite having a relatively low weight percentage in commercial batteries, carbon black contributes significantly to the internal surface area of a cathode due to its small particle size (≈ 50 nm), low density, and high surface area, which allows for a large quantity of it to be dispersed within the cathode, meaning its conductive effects are evenly widespread [49, 50].

The primary particles that make up carbon black are typically between 30 and 40 nm in size, and they are fused together to form agglomerates, which are larger secondary particles of carbon black [51]. The main particles contain amorphous cores and turbostratic graphitic surface features, shown in Fig. 5. Fractals are formed by fusion of smaller nanoparticles [52].

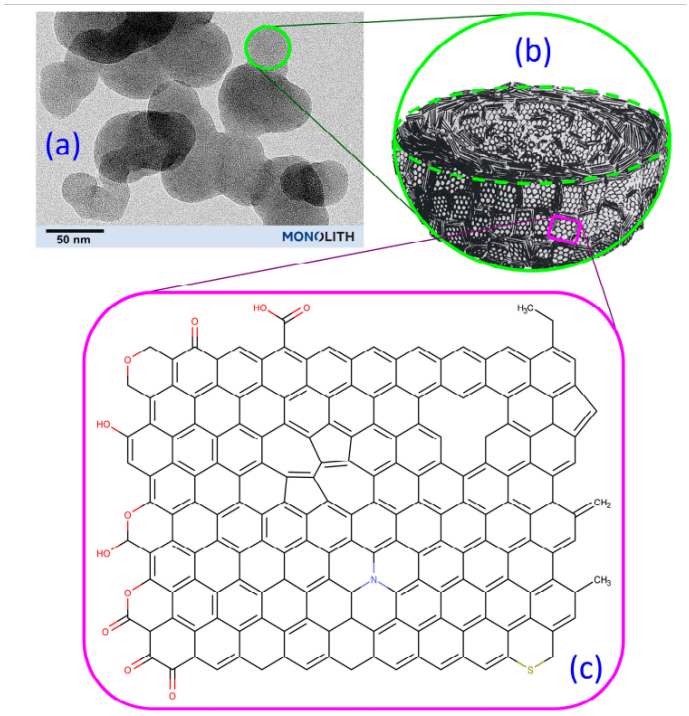

Figure 5: Schematic of carbon black showing the structure and chemistry present. (a) TEM image of N660 carbon black at the indicated magnification. (b) schematic of a primary particle (cut in half to show the internal structure); and (c) depiction of the different chemical groups on graphene sheets in carbon black [53].

Primary carbon black particles are two orders of magnitude smaller than the cathode active material particles ($\geq 10\mu m$). Consequently, due to size-ratio and structural factors, an electrode can display excellent electronic conductivity even with a small amount of carbon black [54–56]. Percolation theory provides an understanding of electronic conductivity in composites of conductive and insulating materials [54]. Here, the electronic conductivity of a composite containing conductive material above the percolation threshold is given as [51]:

$$\sigma = \sigma_0(\nu - \nu_c)^t \tag{4}$$

where σ_0 is the electronic conductivity of carbon black, ν is the volume fraction of the conductive carbon black, νc is the percolation threshold, and t is the critical exponent. So the volume fraction of the carbon black in the electrode affects the electronic conductivity.

When the electronically conducting additive reaches its percolation threshold (ν_c), the electrical percolation network forms [51]. When there is a critical amount of electronic conductive material, a sharp decrease in resistivity occurs, indicating the percolation threshold has been reached, as shown in Fig. 6. This threshold is reached when there is enough highly conductive material available to make a conducting channel through the entire electrode. When distances are possible, this channel could arise from direct contact between conductors allowing electron conduction, or by electron tunneling [51, 57]. Tunneling is important for battery electrodes because the surfaces of carbon black could have polymer binder (an insulator) adsorbed onto them (shown in Fig. 7).

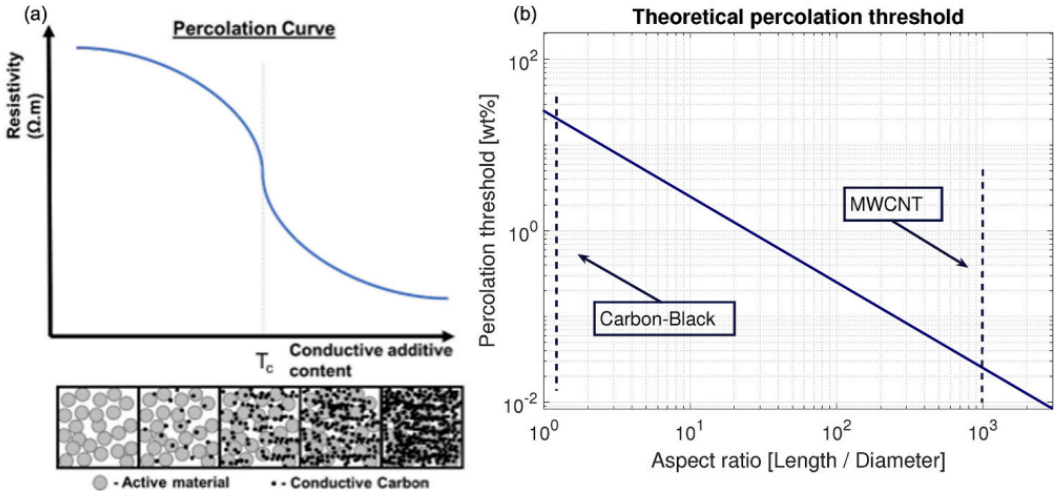

Figure 6: A percolation curve for a mixture of insulating active material particles and conducting carbon, and (b) Schematic showing reduction of the percolation threshold with increasing aspect ratio [58].

1.8 Electrode conductivity networks

Percolated conductive additives in the electrode *e.g* carbon black, result in electronic conductivity networks, which are necessary for battery function. Conduction occurs throughout the carbon-binder domain, or CBD, which is a network of conductive additives and polymer binder that the active material particles (shown in orange in Fig. 7) are placed within. It is porous with its holes filled with electrolyte [51]. In Fig. 7, the CBD is shown as black particles. There is evidence for both short-range and long-range conductivity networks in electrodes. Long-range electronic contacts refer

to a percolation network of conductive material. These networks are present between the active material particles. These typically have a length scale of 0.1–10 μm. Short-range contacts are the interactions arising from the direct contact between the CBD and active material, with a length scale of 1–100 nm [51]. A schematic for both types of contacts is shown in Fig. 7. The distribution of carbon black in the electrode has been shown to affect electrochemical performance of the cathode, with more uniform distribution resulting in greater performance [59].

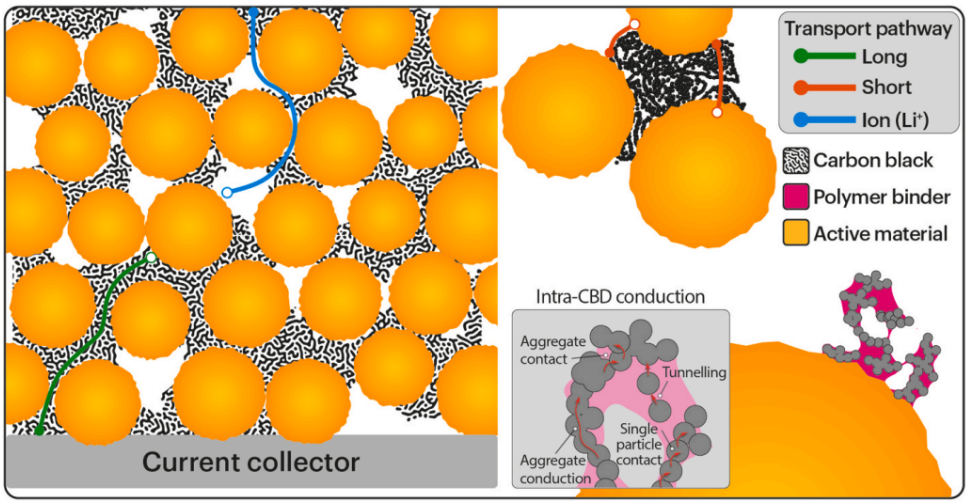

Figure 7: Schematic showing both short-range and long-range contacts and their resulting conductivity pathways. Here, the cathode-active material is connected by carbon black particles. Open pores are represented by white space [51].

1.9 Binders for cathodes

Connecting the active material and conductive additives, as well as ensuring the electrode materials adhere to the current collectors, are the primary roles of binders. This is done to prevent the disintegration of the active material as a result of the mechanical and chemical stress occurring during charge/discharge cycles. The binder used in current LIBs available on the market is polyvinylidene difluoride (PVDF), used for its thermal and electrochemical stability, its strong adhesion between electrode films and current collectors, and it does not react with the electrolyte. However, PVDF is electrochemically inert and insulating – so it adds electrochemically inactive mass and blocks conductive pathways in carbon black. This limits the maximum capacity achievable in cathodes, therefore limiting the performance of LIBs as a whole [29]. PVDF also exhibits poor binding affinity to the electrode components, as the primary binding

mechanism are weak van der Waals forces, and general interactions [44, 60]. Electrode processing utilises the organic solvent, N-methyl-2-pyrrolidone (NMP). This is problematic, as NMP is both toxic and expensive (1–3 $/kg, on top of the relatively high cost of PVDF of 8–10 $/kg [61]) and has a high boiling point of about 203°C, requiring more energy and higher temperatures for its evaporation during electrode fabrication. Additionally, When PVDF is exposed to the electrolyte solvent, it may swell or dissolve, which reduces the cell's capacity [62]. Furthermore, PVDF is a poly-fluoroalkyl substance (PFAS); the European Chemicals Agency (ECHA) has implemented regulations governing their use to mitigate environmental and health risks associated with the production and application of these substances. [63].

A list of common polymer binders and prices is shown in Table 1.

Polymer	Price	Source
PVDF	$0.05/g	Alibaba
PTFE	$0.02/g	Alibaba
CMC	$0.15/g	Sigma Aldrich
PEO	£0.67/g	Sigma Aldrich
Pluronics	£0.24/g	Sigma Aldrich
PVP	£0.2/g	Sigma Aldrich
Chitosan	£1.33/g	Sigma Aldrich
Sodium Alginate	£0.08/g	Sigma Aldrich
PPy	£26/g	Sigma Aldrich

Table 1: List of common binders and prices.

1.10 Aqueous binders

Many of the problems discussed above can be addressed by using binders that can be aqueously processed. Water is inexpensive; it has been calculated that it is 22 times more expensive to use NMP than water (per kg). Commonly used aqueous binders are inexpensive, with costs typically ranging from 2 to 5 kg. This means that aqueous processed batteries will be much less expensive to produce than ones conventionally using PVDF and NMP. Furthermore, using water will greatly reduce the environmental impact of electrode production by replacing NMP; this also reduces CO_2 emissions as well as production costs, as expensive solvent recovery is not needed [61,64]. The much

lower boiling point of water can quicken evaporation during electrode processing.

1.10.1 Desired properties of aqueous binders

For use in LIBs, aqueous binders need to be:

- Soluble in water.
- Cheap and readily avaliable.
- Electrochemically stable, to withstand the high voltage in the harsh operating environment [32, 65, 66]
- Thermally stable, as battery operating temperatures reach 60 °C [67]. Additionally, binders need to withstand the drying temperature for electrodes, so they should have thermal stabilities of at least 150 °C [65].
- Elastic and flexible to accommodate volume changes via deformation and relaxation to avoid crack formation [32, 68, 69].
- Suitably high viscosity, to establish repulsion forces within particles. This is to ensure slurries are homogeneous and well-dispersed, avoid self-agglomeration of electrode components, which will impede electrochemical performance. Slurries should also be shear-thinning to allow de-agglomeration of the carbon black [11, 32]. If the viscosity of the binder is high enough it can contribute to a yield stress of the cathode slurry, allowing weak 3D conductive networks of conductive carbon to form. If the viscosity of the binder is low, this can result in clusters of flocculated carbon additive, which consequently results in a low yield stress [70–73]. If the yield stress is too high, this can reduce the ability of the slurry to flow when coated [70–73].
- Suitable wetting properties with carbonate-based electrolyte solutions, enabling strong interaction with active materials and conductive carbon. The binder must swell in the electrolyte to allow fast lithium diffusion [32, 74, 75].

1.10.2 Challenges with aqueous processing

While aqueous processing is used extensively for graphite and silicon-based anodes, adopting this for cathodes is more challenging. Some cathode chemistries such as

$LiFePO_4$ are more suited for aqueous processing due to strong Fe-PO-O bonds which are not very sensitive to water [61]. High Ni NMC cathodes, conversely, can undergo degradation via Li^+ leaching to form LiOH and Li_2CO_3.

This process results in the loss of electrochemically available lithium, which results in lower capacities, and degradation of the interphase layer [32]. For NMCs, increasing Ni content exacerbates this degradation. Generally, the lower Ni content of NMC cathodes indicates better compatibility with water. This was studied by Wood et.al, who observed an increase in dissolved Li with increasing Ni content [34]. The NMC cathode used in this body of work is NMC 622 ($Li_xNi_{0.6}Mn_{0.2}Co_{0.2}$), with a specific capacity of 175.8 mAh g^{-1}.

The second issue is the degradation of the current collector, which is normally aluminum for cathodes. Aluminum oxidises to develop a thin protection layer, which is stable in the pH range 4.5 to 8.5 [32, 76]. The formation of LiOH and Li_2CO_3 increases the cathode slurry to a pH of 9, resulting in the dissolution of the protective aluminum oxide film and corroding the aluminum current collector [32,77]. This results in the release of H_2 gas, and creates large pores in the cathode structure which increase electronic resistance of the electrode/electrolyte interphase [32,76] To address this, the pH needs to be lowered. The addition of phosphoric acid to the slurry has been shown to achieve this, as transition metal oxides form instead of LiOH and Li_2CO_3, which helps stabilize the CEI. [76, 78]. For NMC 622 aqueous suspensions, between 2 - 4 % of Li can be lost for up to 4 hours [79]. The equations for NMC 622 leaching and Al degradation are shown below:

$$Li^+ + H_2O \rightarrow LiOH + H^+ (5)$$

$$Li_xNi_{0.6}Mn_{0.2}Co_{0.2}O_2 + xH_2O \rightarrow Li_{1-x}H_xNi_{0.6}Mn_{0.2}Co_{0.2}O_2 + xLiOH (6)$$

$$LiOH + CO_2 \rightarrow LiHCO_3 (7)$$

$$LiOH + LiHCO_3 \rightarrow H_2O + Li_2CO_3 (8)$$

$$Al + OH^{-} + 3\,H_2O \rightarrow Al(OH)_4^{-}(s) + \frac{3}{2}\,H_2(g) \quad (9)$$

The third issue with aqueous processing is that carbon black is very hydrophobic [80]. Even under high shear mixing, carbon black will re-agglomerate. Therefore, It is imperative to select water-soluble binders that have a chemical affinity to carbon black and can disperse it in water, thus lowering the interfacial energy between carbon black and water [81].

1.10.3 CMC

Carboxy-methyl cellulose (CMC) is an aqueous binder. It possesses strong noncovalent interactions and can form hydrogen bonds, which allows for its water solubility. CMC is a linear polymer that is derived from cellulose with up to 3 degrees of substitution (DS) of –OH groups by CH3COO carboxymethyl groups, as each monomeric unit has three —OH groups [82,83]. The anionic groups that result from the substituted groups' dissociation in water make CMC water soluble [84]. The cellulose chain is hydrophobic, which may aid adsorption to the conductive additive. CMC has a sodium salt form, sodium carboxymethyl cellulose (Na-CMC), which is widely utilized in many industries because it possesses effective mechanical, adhesive, and emulsifying qualities [82, 85].

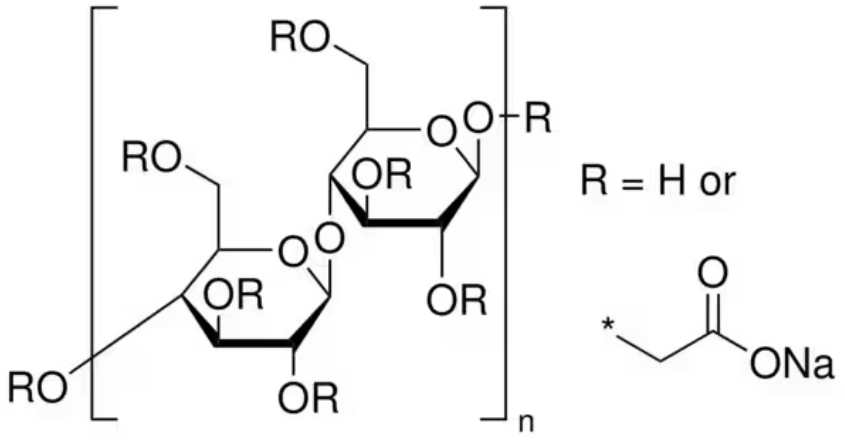

Figure 8: Chemical structure of CMC

Several studies have investigated CMC as a potential alternative aqueous binder to PVDF for different types of cathode material [32, 78, 85–89]. Despite its presence in the

literature, aqueous cathodes containing CMC underperform compared to conventional cathodes made with NMP/PVDF. The capacity fade data from Wood *et.al.* showed that NMC 811 cathodes made with H_2O/CMC had a lower capacity retention than those made with NMP/PVDF - 70 vs 76% respectively, despite the H_2O/CMC cathodes achieving a higher 1st discharge capacity. This is shown in Fig. 9. The rate capability data from the same authors show that their CMC cathodes performed worse at high C rates than the NMP/PVDF cathodes. The lesser performance of CMC cathodes is believed to be a result of formulation differences and a later of CMC on the active material, leading to slower Li^+ diffusion kinetics [89]. Studies have integrated other polymers with CMC as blends to improve physical and electrochemical properties of cathodes. Rolandi et.al. have employed acrylic latexes with CMC to improve the rheological properties of aqueous cathodes; the addition of latexes was found to improve the electrochemical performance of the cathodes [90]. A selection of studies where CMC was studied as an aqueous binder is shown in Table 2.

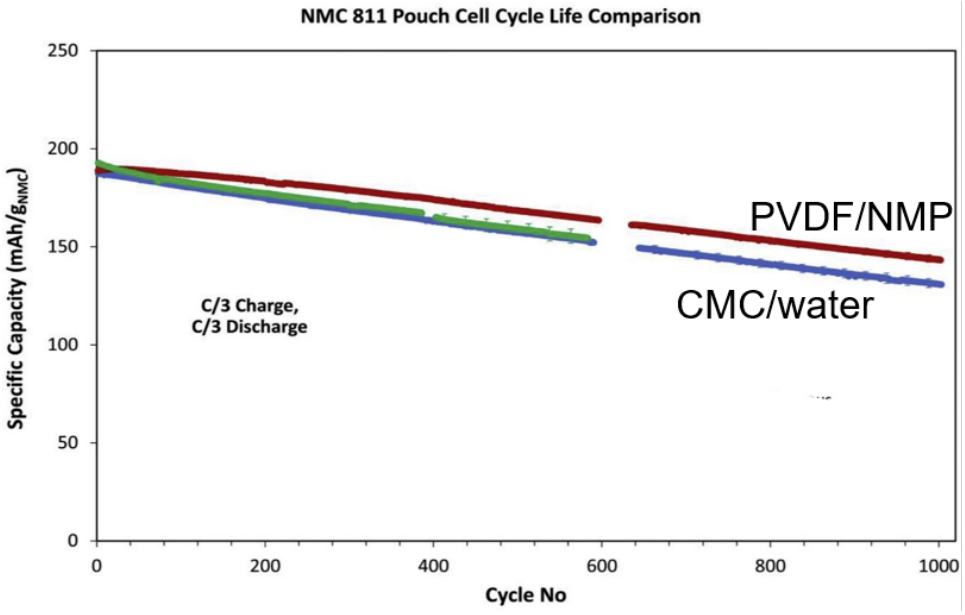

Figure 9: Capacity fade comparing the electrochemical performance of NMC 811 cathodes produced with CMC/DI H_2O vs NMP/PVDF [89].

Table 2: Summary of studies where CMC has been tested against PVDF.

AM	C Rate	CMC Capacity (mAh g^{-1})	PVDF Capacity (mAh g^{-1})	Ref
LFP	1C	146	120	Wang *et.al.* [87]
LFP	C	180	150	Qiu *et.al* [88]
NMC 111	0.5C	157.5	129.3	Xu *et.al.* [91]
NMC 811	C/3	205	200	Wood *et.al.* [89]

1.10.4 Sodium Alginate

Sodium alginate is a polysaccharide derived from brown algae and consists of blocks of (1→4)-linked -D-mannuronate (M) and -L-guluronate (G). The carboxylic groups on the polymer backbone enable strong adhesion to active material particles, therefore resulting in high adhesion strength [32,92]. Sodium alginate was investigated in LNMO cathodes by Bigoni *et.al.*, where it demonstrated comparable electrochemical properties to cathodes made with PVDF, explained by sodium alginates poor swelling ability and rigid structure, making electrolyte penetration less likely and therefore making the cathodes less susceptible to degradation and passivation processes [92].

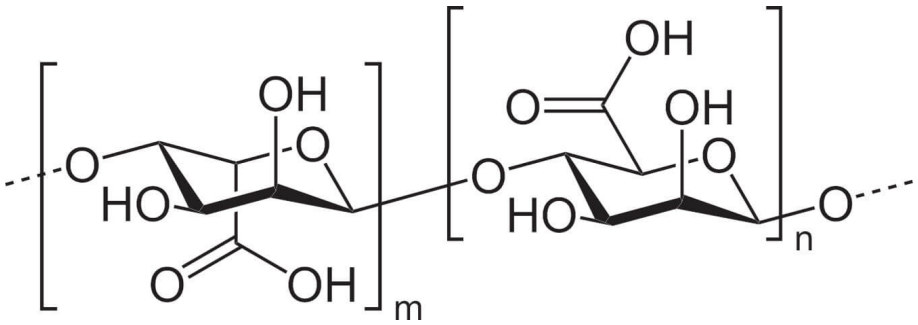

Figure 10: Chemical structure of Sodium Alginate

1.10.5 Chitosan

Chitosan is a linear polysaccharide consisting of of randomly distributed -(1→4)-linked D-glucosamine and N-acetyl-D-glucosamine. It is produced via de-acetylation of chitin, which is found in the exoskeletons of crustaceans such as crabs and shrimp. Studies have successfully utilized chitosan as a binder in $LiFePO_4$ cathodes [93, 94]. Work by Prasanna *et.al.* achieved higher discharge capacities at 0.1C than PVDF [94]. The presence of amino and hydroxyl groups enables chitosan to be cross-linkable, so can

effectively interconnect with active materials via hydrogen bonding [32]. Furthermore, the amine groups are electron-donating, which is said to enhance electronic conductivity [32, 94].

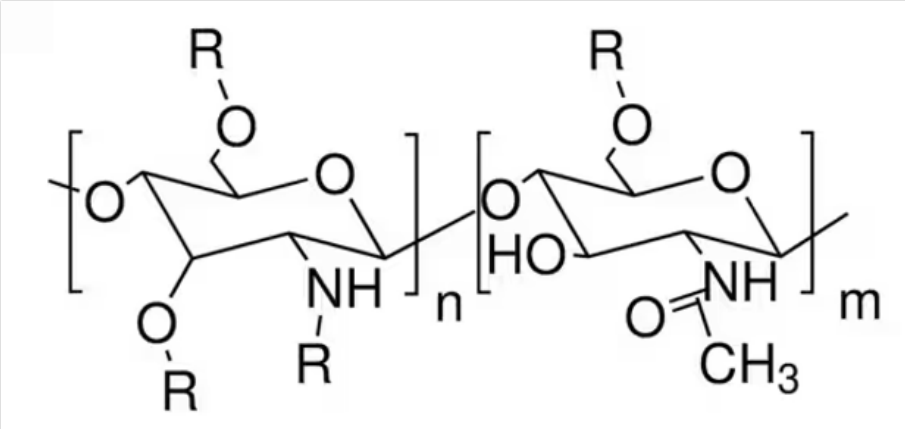

Figure 11: Chemical structure of Chitosan. R can be H, CH_2COOH or CH_2COONa.

1.10.6 PEO

Polyethylene oxides (PEO) are linear, non-ionic polymers that are soluble in water [95]. PEO is cheap and widely available. Fig. 12 shows the chemical structure of PEO. Mo *et.al.* investigated PEO independently and with PVDF as a binder for NMC 622 cathodes prepared with NMP as the solvent. They found that the electrode with a binder composition of 20% PEO and 80% PVDF had a higher specific capacity and showed better cycling stability than an electrode with only PVDF [96].

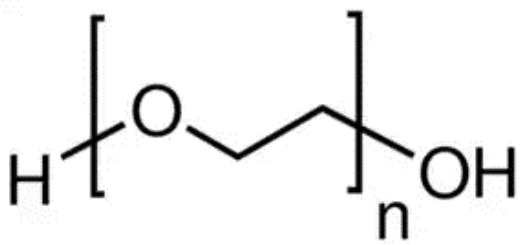

Figure 12: Chemical structure of PEO

PEO has demonstrated polymer-filler interactions with carbon black [97–99]. Guy *et.al.* studied NMP-based $Li_{1.2}V_3O_8$ cathodes with PVDF, PEO and blends of both polymers. Their cathodes using only PEO as the binder demonstrated the lowest performance, despite its apparent affinity with carbon black. They attribute the low per-

formance to PEO plasticizer forming insulating barriers between carbon black flocs. However, cathode blends of PEO and PVDF performed the best. The explanation provided suggests that PEO preferentially adsorbs onto the carbon black surface over PVDF. Electrode conductivity data from these authors supports the electrochemical performance data; they conclude that greater carbon black distribution results in a more efficient electronic carbon black conduction network [99].

1.10.7 PVP

Polyvinylpyrrolidine (PVP) is a synthetic water-soluble polymer. PVP has good wetting properties and can adsorb up to 40 % of its water by weight [100]. Liu et.al. used a partially carbonized PVP as a cathode binder for LIBs, where the performance was attributed to the nitrogen-containing groups, which facilitate ion transport [101]. The chemical affinity of PVP to carbon black could also explain its capailities of a binder. Sung et.al observed that PVP adsorbs better onto the surface of carbon black, stabilizing the carbon-binder matrix [102].

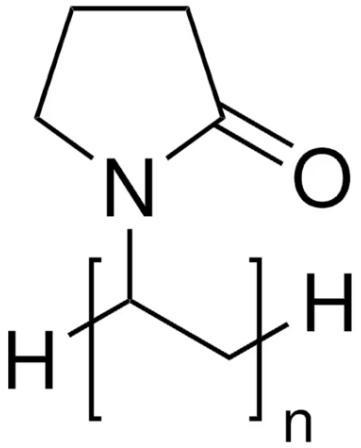

Figure 13: Chemical structure of PVP

1.11 Use of dispersants

One of the issues with aqueous processing is the need to disperse the hydrophobic carbon black in the cathode slurry. The aforementioned aqueous binders alone do not always result in well-dispersed conductive carbon [81, 103]. To make this easier, dispersants can be employed. Li et.al. studied the effect of dispersant content on aqueous $LiFePO_4$

suspensions, whereby the addition of poly4-styrene sulfonic acid (PSSA) was found to electrostatically stabilize both active material and conductive additive particles, and an optimum amount of dispersant was discovered [104]. Surfactants can also be employed to disperse active materials and conductive additives [81, 103]. The work of Porcher *et.al.* found that ideal surfactants for LIB cathodes are non-ionic, as ionic surfactants were found to cause corrosion of the current collector. Their non-ionic surfactant of choice was Triton X-100, which when used in conjunction with CMC, resulted in smaller agglomerates of carbon black, leading to improved rate capability performance [81]. The use of Triton X-100 was further investigated by Zhang *et.al*, who systematically varied the concentration of Triton X-100, and observed the greatest capacity retention using 1.5 wt% Triton X-100 in the dry cathode [103]. The authors' proposed carbon black dispersion mechanism using Triton-X 100 is shown in Fig.14, where it is suggested that the hydrophobic benzene ring adsorbs onto carbon black due to π-π stacking interactions, whilst the hydrophilic PEO provides steric stabilization to overcome the large van der Waals forces between carbon black particles [103].

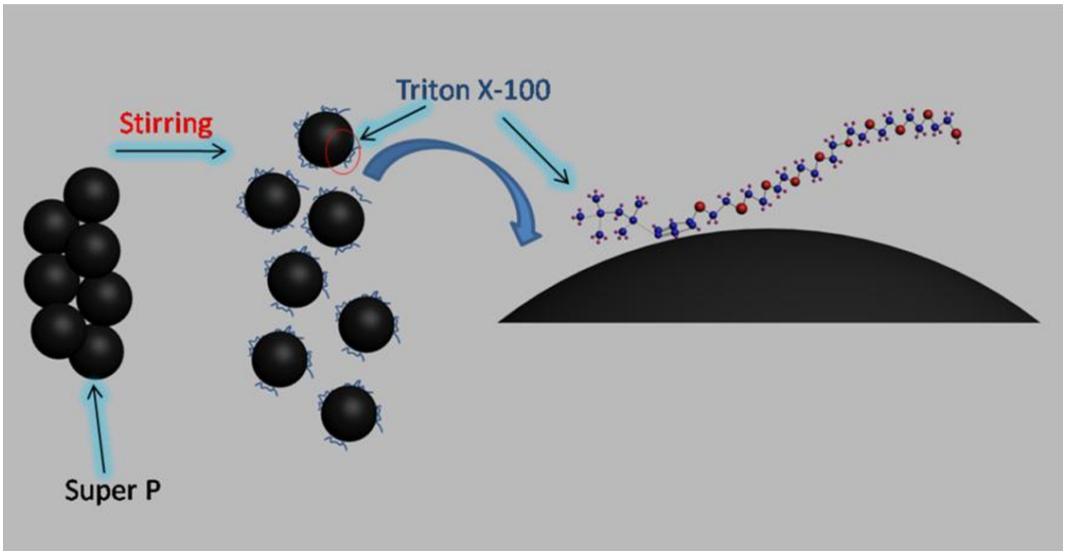

Figure 14: Schematic showing the dispersion of carbon black in the cathode slurry via adsorption of Triton-X 100 [103].

1.11.1 Pluronics

Pluronics are tri-block copolymers made up of poly(ethylene oxide) poly(propylene oxide)-poly(ethylene oxide) (PEO-PPO-PEO). Pluronics have an amphiphilic structure, meaning it has a polar, water-soluble group connected to a non-polar, water-insoluble

chain, owing to the hydrophilic ethylene oxide and the hydrophobic propylene oxide [105]. The chemical structure of Pluronic PF 127 is shown in Fig. 15. Their amphiphilic nature may be useful as a binder; their hydrophobic PPO component could bind to the carbon black, whereas their hydrophilic PEO component could aid dispersion in aqueous medium; studies have shown that pluronics do adsorb to the surface of carbon black in aqueous media [106, 107]. There is a gap in aqueous binder studies, pluronics are ideal because they are amphiphilic, cheap and commercially available.

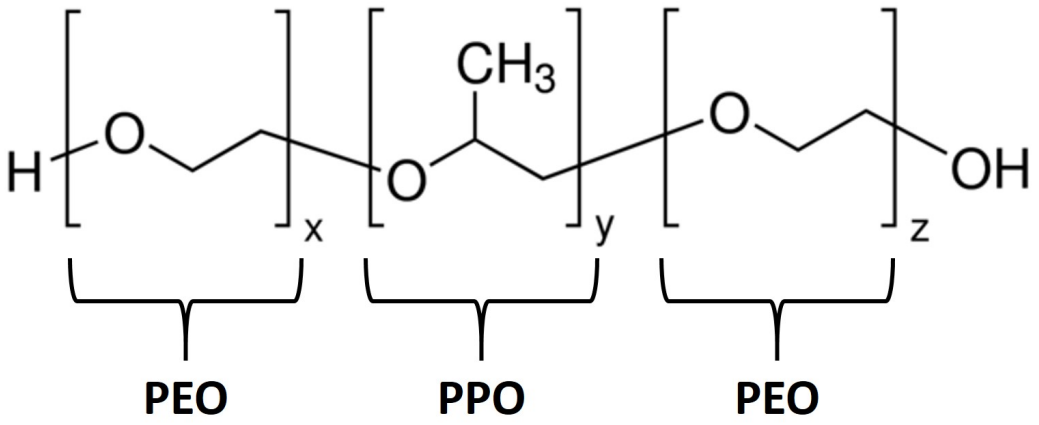

Figure 15: Chemical structure of pluronic PF127 showing PEO blocks (x and z) and PPO blocks (y) [108].

Airoldi *et.al.* [109] investigated pluronic P-123 as a binder for $LiMn_2O_4$ cathodes processed in aqueous media. They performed a rheological investigation against CMC as well as electrochemical cycling. They found that the P-123 cathode slurries exhibited higher yield stresses than that of CMC, implying a greater 3D network present in the pluronics slurries. This is attributed to the behaviour of PEO in water; as an amphiphilic polymer, the hydrophobic and hydrophilic components attract each other and form micelles, which when formed will aggregate and bind water, thus forming a gel. This gel results in the formation of a 3D network. They obtained a specific capacity of 113 mAh g^{-1} at 0.1 C (the theoretical specific capacity of $LiMn_2O_4$ is 148 mAh g^{-1} [110]).

1.11.2 Polymer adhesion to current collector

Adhesion between the electrode composite and current collector interface should be achieved to improve electron conduction [111]. Adhesion refers to the tendency of dissimilar materials to attract each other. It occurs as a result of attractive intermolecular forces between particles or substances.

Polymer adsorption onto a solid surface occurs when 'trains' of monomers adhere to a solid surface. Most long polymers will adsorb onto a solid surface due to the hydrophobic effect, whereby polymer adsorption frees up surface water to enter the solution. As free water has more entropy than free polymer, the Gibbs free energy of the system is reduced. DeGennes [112] came up with a mechanism of polymer adsorption on a flat surface. Here, the thickness of the polymer adsorbed is independent of its molecular weight, M_w - see Fig. 16. The soft nature of a polymer enables contact with a surface like a current collector via VDW forces. When a monomer in a chain makes contact with a surface, the next monomer in that chain is more likely to do so [112].

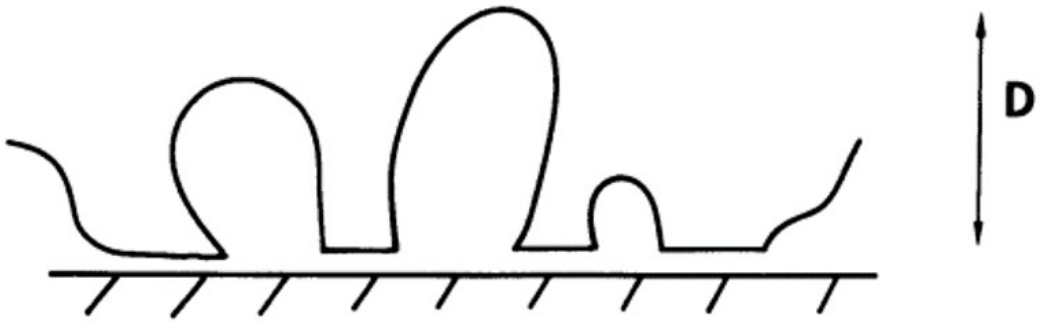

Figure 16: Polymer chains weakly adsorbed on a flat surface. For large molecular mass M_w, the thickness D is independent of M_w [112].

One of the most crucial properties that promotes Li^+ ion transport from the electrolyte solution to the active materials is the swelling behaviour of binders in an electrolyte solution. [85, 113, 114]. Upon contact with the electrolyte, the polymers form a gel. This gel is 'cross-linked' by physical chain entanglements with solvent electrolyte molecules swelling the polymer matrix. In such a system, there are no chemical crosslinks. The degree of swelling is dependent on polymer/electrolyte interactions. As the polymer binder coats the surface of the carbon conductive additive, binder swelling can reduce compactness of the carbon agglomerates [114]. Low swelling values impede

Li-ion transport because there is less access for Li-ions throughout the electrode composite, resulting in increased electrical resistance. Moderate swelling values between 10 and 20% are ideal, as lithium-ion transport is enabled within the carbon-binder domain (CBD) [51].

At higher temperatures (over 60 °C), the swelling rate of PVDF increases even further, which can reduce electrode electrochemical performance, as the electrolyte can easily migrate into the interface region between the binder, active material and conductive additive, reducing adhesion between the binder and these particles. [115]. As a result, the electrode particles tend to heavily agglomerate at this point, becoming inelastic and very viscous. The gel-like electrolyte seeps throughout the entire electrode, decreasing its mechanical characteristics and also thickening the electrode layer. Due to the electrode materials' separation from the current collectors, this reduces the cell capacity. Additionally, the fast swelling rate may cause active materials to lose electrical contact, increasing cell resistance and decreasing cell capacity as a result [85]. Li-ion diffusion through the CBD can be impacted by binder swelling, which may affect the porosity of the CBD [51, 116, 117]. This is due to the electrolyte and associated binder swelling reducing the electronic conductivity of the composite electrode. Overall electrode resistance has been found to be 3.5 times higher compared to a dry electrode [51, 118].

1.12 Polymer thermodynamics

The radius of gyration (R_g) is a physical distance that characterizes a polymer conformation, but unlike the end-to-end distance, it is readily measured using analytical techniques, e.g. light scattering. Specifically, the radius of gyration is the average distance (in a monodisperse polymer sample) between a chain's center-of-mass and each individual monomer. It is more meaningful than R_N because it captures the relationship between monomer locations via the center-of-mass.

Rg is given by Equation:

$$R_g = \sqrt{\frac{Nb^2}{6}} \tag{10}$$

Where N is the number of Kuhn monomer units and b is the Kuhn length.

The efficacy of the solvent can be approximated equation:

$$R_g \approx N^{\nu} \tag{11}$$

Where ν is the Flory exponent. For a good solvent, $\nu = 3/5$, the coil is a self–avoiding walk, so chains will swell. It is desirable to use a good solvent for a battery binder to ensure rapid and complete dissolution so that all of the binder is effectively used to enhance the viscosity of the slurry.

Fig.17 depicts a schematic representation of what is anticipated as the polymer solution concentration is raised from the dilute state to the "Semi-Dilute" regime. Coils reach a point where, on average, they just start to overlap as concentration is increased. This concentration, denoted by the symbol c*, is known as the "overlap concentration" and can be computed using Equation:

$$c^* \approx \frac{1.45}{[\eta]} \tag{12}$$

An example of a zero shear viscosity plot used to determine the overlap concentration of a polymer is shown in Fig. 17.

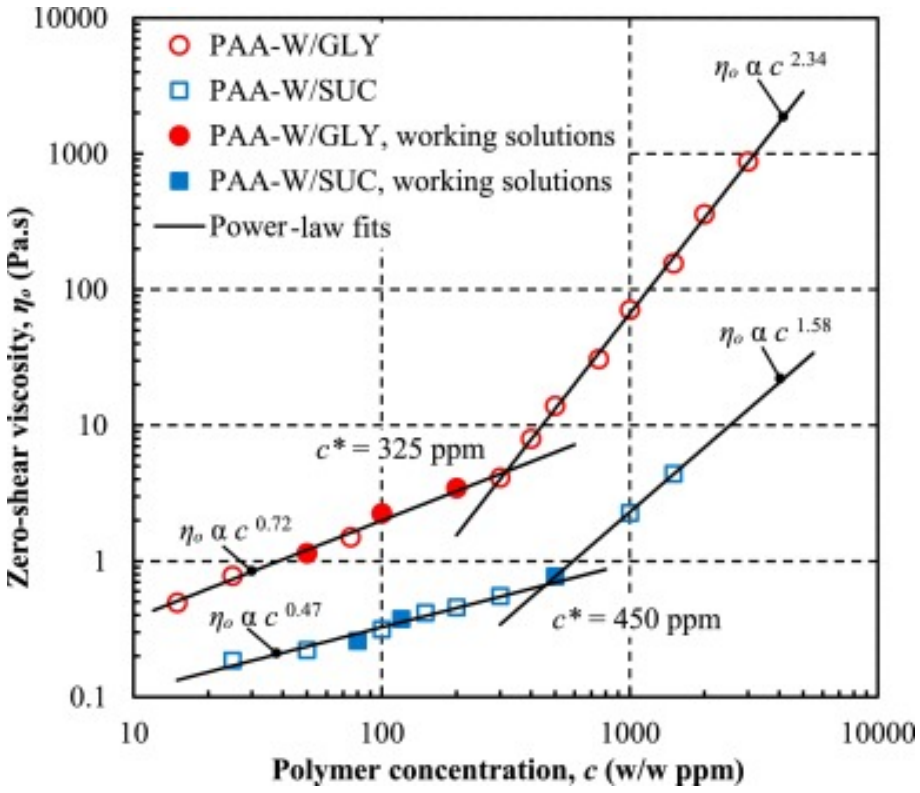

Figure 17: Zero-shear viscosity versus polymer concentration, showing overlap concentration [119].

The nature of the interaction between the polymer binder and the dispersed colloidal carbon black depends in part upon the radius of gyration of the solvated polymer coil, which relates to the polymer molecular weight. In this way, the binder can also modify the microstructure of the slurry by adsorbing onto the surface of solid particles and aggregates, modulating their interactions within the complex fluid [70, 102, 120]. As discussed earlier, carbon black is known to flocculate in cathode slurries, forming a weakly bonded network that can percolate. The polymer binder behaves as a flocculant, even in systems with negligible charge on the particles.

1.12.1 Colloidal Dispersions

Smaller particles (colloids) are buoyed up by the force that thermal energy applies to the surrounding medium, resulting in a mechanically stable dispersion. Nearly all particles charge in solution due to changes in the electronic structure at the solid/solution interface [121].

The polymer and carbon black can be thought of as behaving like a colloidal suspension [104, 106, 107, 122, 123]. Here, the polymer is dispersed in water. carbon black particles are coated with a layer of polymer (which is presumably adsorbed onto the surface of the carbon black). Attractive VDW forces and steric repulsion occur between carbon black particles coated with polymer, as when particles come close enough to one another, the polymer chains will not compress any further due to entropic constraints; as compressing the polymer chains will increase their free energy, which will decrease entropy and is therefore energetically unfavorable [104,122]. In a good solvent, the polymer chains will occupy more space than in a poor solvent. So in a good solvent, the chains will occupy a greater volume, therefore increasing the distance between carbon black particles and making agglomeration less energetically favorable [124].

Fig. 18 shows a schematic of polymer adsorption on carbon black particle. The length of the adsorbed polymer brush L, is a complex function of the solvent properties, particle surface morphologies, particle and polymer compositions, and polymer molecular weights [125]. The PVDF layer is absorbed, which leads to strong steric interaction between the particles [120].

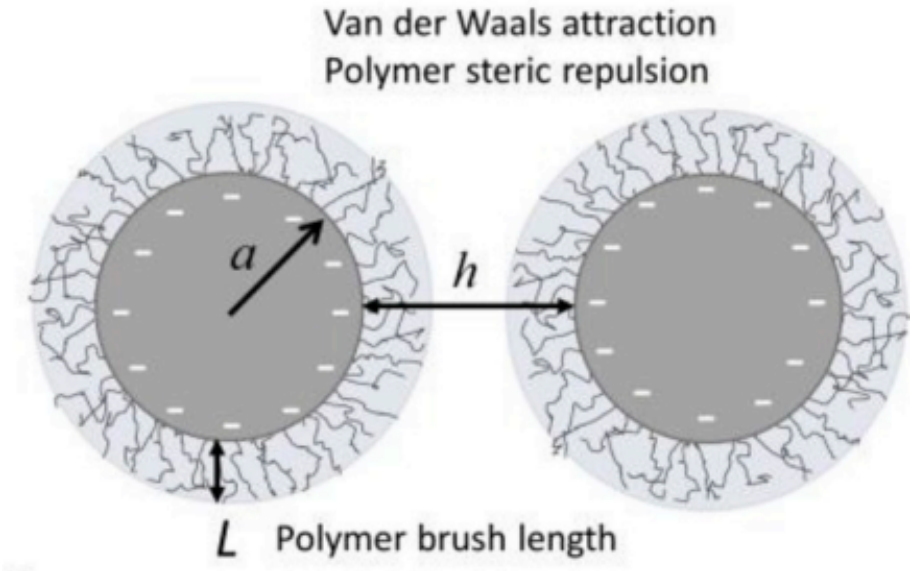

Figure 18: Schematic illustration of carbon black particles coated with adsorbed polymer, showing their interparticle colloidal interactions [120].

1.12.2 Battery slurry microstructure

The components present in an electrode (active material, conductive filler and binder) are dispersed in the solvent when mixed, forming a slurry. The electrode is created by coating this slurry onto a foil current collector, allowing it to dry, and calendaring (compressing) it. The electrode microstructure is important to its electronic properties [126] and has been demonstrated to be extremely reliant on the processing of each step, e.g., coating technique, [127] drying temperatures, [128], and calendaring.

Characterizing the microstructure can be difficult as electrode slurries are multi-component systems, and they are optically opaque, meaning techniques such as optical microscopy are not always ideal [71, 129, 130]. Studying the slurry rheology and conductivity provides insights into the microstructure. Steady-state rheology is used to assess factors such the zero shear viscosity [70], viscosity at shear rates corresponding to those used for coating the slurry [104, 131], and yield stress to assess the presence of 3D networks of conductive additive [11, 70, 86]. In addition, large amplitude oscillatory shear (LAOS) is used to assess the viscoelastic (liquid-like or solid-like) properties of the slurry. The presence of 3D networks is speculated if the storage modulus is consistently higher than the loss modulus across the frequency range - here, slurries are said to be gelled [70, 72, 102, 131, 132]. Measuring the conductivity of slurries can be used to determine whether percolation of the conductive additive is present [133]. Both steady-state rheology and LAOS are used in this investigation.

Viscosity directly affects the rate at which cathode particles settle in the slurry. In an electrode slurry, the active material increases the viscosity of the solution by drag forces on the particles. A low-viscosity slurry will stratify during drying because the particles settle. Low viscosities result in high flow of the slurry, which spreads and slumps after coating, reducing the energy density per area of the cathode. Whereas a high-viscosity slurry will not flow and coat well [70, 71, 129, 130, 134]. Compared to identical spherical particles, more irregularly shaped particles have a larger surface area and settle more slowly because of increased drag. At higher solids loading, hydrodynamic effects slow the settling of the particles. An ideal slurry will have a low enough viscosity to flow well, reduce inhomogeneity and minimize die swell [71, 129]. The main contributors to the viscosity of slurries are polymer entanglements and 3D structures of carbon black, although there are small contributions from cathode secondary particles [70, 71, 129, 130, 135, 136]. To understand the rheology of a battery slurry, the effects of all components

— active material, conductive filler, and polymer binder — need to be understood.

As discussed in Section 1.11.2, polymers can adsorb onto solid surfaces. When polymer chains adsorb onto carbon black, they can prevent particles of carbon black from coming into direct contact, therefore having a stabilising effect. However, free polymers in the suspension can interact with adsorbed polymers, as well as bridging of different carbon black particles by polymers adsorbed on either particle [41, 102, 137]. Thus 3D networks of carbon black are formed in the slurry [12, 130, 134]. The particle size affects the amount of polymer that is adsorbed; smaller particles have higher surface areas, meaning that more polymer chains can be adsorbed onto them. Stronger 3D network structures can be formed if the polymer has a greater affinity to carbon black by way of strength of adsorption [134]. Carbon black is deemed necessary to form a particulate gel with PVDF in NMP via bridging; gels are said to provide attraction between active material particles and contribute towards stabilising the slurry [134].

Due to the presence of several components, studies have varied the concentration of one component in slurries to determine its effect on the microstructure. Increasing the concentration of carbon black and PVDF binder in cathode slurries usually increases viscosity and yield stress, especially for conventional NMP/PVDF slurries, while increasing the concentration of cathode material has little effect on rheological properties [135]. Other studies working with binders that have a strong chemical affinity to carbon black find a non-monotonic relationship between polymer concentration and rheological properties; particularly in aqueous solutions [131, 138]. The chemical affinity of polymer to carbon black can be quantified by extracting parameters from adsorption isotherms, i.e. Langmuir or Freundlich [107, 131]. Under low polymer concentrations, the amount of polymer is enough to adsorb onto the carbon, forming a solid-like paste. Increasing the polymer concentration results in polymer entanglement, usually between hydrophobic groups, which can overcome VDW interactions between carbon black particles. This leads to more "liquid-like" properties of the slurry, so yield stress and viscosity is decreased. When the concentration of polymer is increased further, the slurry becomes more solid-like due to further entanglement of polymer chains, resulting in a gel-like structure [131, 138]. Further studies have discovered that weakly attractive interactions cause the carbon black particles to coalesce into highly branched flocs. At low concentrations of carbon black, discrete aggregates predominate the rheological characteristics of their carbon black solutions, while at high concentrations, the

continuous network of carbon black does [120].

Rheology can also be used to assess the effectiveness of the mixing stage because the interactions in the slurry are largely reliant on mixing. For instance, more intensive mixing will deagglomerate and disperse the components, resulting in smaller particle sizes, which can reduce the overall viscosity. The slurry can be affected by the order of mixing. For slurries made with NMP, if the carbon is mixed with NMP it can form a 3D network [70, 71, 129, 130], whereas if it is dry-mixed with the active material beforehand, the carbon black could adsorb onto the surface of the active material, reducing the amount of free carbon, therefore preventing network formation [130]. In aqueous systems, mixing the carbon black with a water-soluble polymer could enable a 3D network to form, providing that the polymer adsorbs to the carbon surface [71, 130, 139]. A schematic of possible structures is shown in Fig. 19. The 3D networks can form, due to the homogeneous distribution of carbon black (structure 1, Figure 2, left). Secondly, deagglomeration and dispersion of the conducting additive during mixing may occur simultaneously (structure 2), and adsorbed carbon is shown to cover the surface of the active material (structure 3) [130].

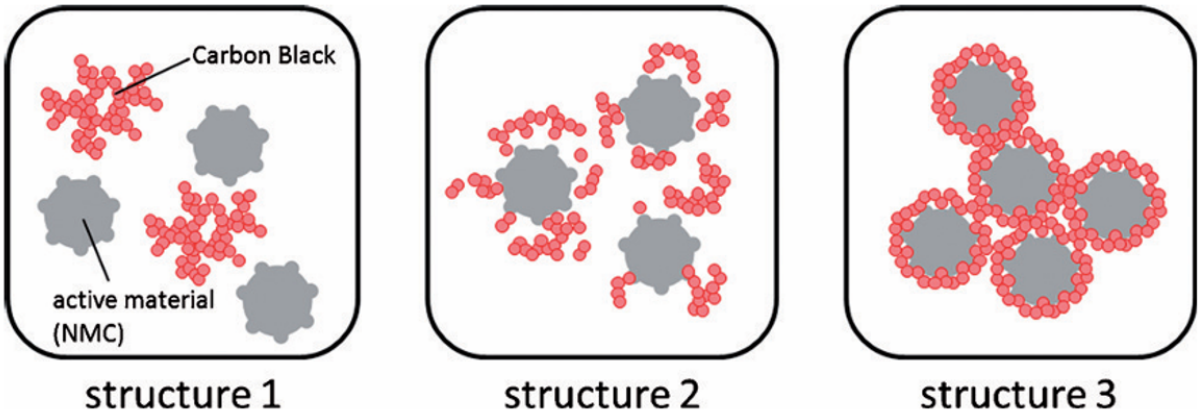

Figure 19: Schematic illustration of cathode slurry microstructures [130].

Studies have shown that the type of solvent and polymer affects the microstructures present in slurries. In carbon black/NMP/PVDF based systems, the slurry rheology is dictated mostly by carbon black, which can disperse in NMP, whereas in an aqueous system, the polymer (CMC) has a greater effect on the rheology [70]. The effect of slurry microstructure on electrochemical performance of cells across solvent and polymer type

was observed by Sahore *et.al*, who found that NMP/PVDF-based cathodes exhibited both a greater yield stress and storage modulus than aqueous CMC - based cathodes, which translated into better electrochemical performance [137].

As well as the type of polymer and solvent, controlling the solids content of the slurry has also been found to affect the electrode microstructure. By varying the solids loading (SL) of conventional carbon black/PVDF/NMP-based cathodes, increases in yield stress, storage modulus and slower active material sedimentation are observed, reasoning that PVDF adsorbs onto carbon black and forms bridging flocculation [72]. These reasons are suggested for higher viscosities and gel formation at high carbon loading [132, 133, 140]. The type of carbon black as well as its content in the slurry can also affect the percolation threshold, which contributes to the slurry microstructure.

The energy input in the slurry can affect the microstructure, and thereby the electrochemical performance of the dry cathode. The energy input is a result of the mixing shear and mixing time. If shear is too low, the resulting forces will not be enough to break up Van der Waals interactions among the conductive carbon flocs. If the mixing shear is optimal, then the conductive carbon flocs will be broken up and a 3D network structure will be able to form. If the shear is too high, then the network structures can be broken up [132, 141, 142]. The same trend can be observed when the mixing time is varied [141].

The microstructure of electrode slurries has been extensively studied. Table 3 summarizes selected relevant literature and material compositions used. The general picture is that the addition of either conductive carbon or polymer enhances the rheological and mechanical properties of the cathode slurry. Yield stresses arise from the percolation of the conductive additive to form a 3D network as well as polymer entanglement. In NMP-based slurries, the carbon additive disperses well without the polymer [43, 70, 72]. Whereas for aqueous processed cathodes, the polymer is needed to form 3D networks of carbon black [70, 131, 137, 138]. For binders that adsorb poorly or not at all onto the active material or conductive carbon, viscosity or yield stress increases monotonically with polymer concentration [43, 102]. For polymers that adsorb onto the active material or carbon e.g. CMC and PVP, a non-monotonic relationship between yield stress [138] and storage modulus [102] is seen, as adsorbed polymer can create steric repulsion between particles, whilst adding excess polymer increases the viscosity due

to entanglement [102, 138]. The active material is shown to have little effect on the rheological properties of the slurry, as active materials have little chemical affinity for polymer and conductive carbon, instead they are embedded in the 3D networks of carbon black [135, 143]. Some studies have linked the microstructure of the slurry to electrochemical performance. It is generally argued that slurries containing well-dispersed carbon black result in improved electrochemical performance of cathodes, as good dispersion means fewer large agglomerates of carbon in the dry electrode [11, 104, 133, 139]. However, Sahore et.al. did not observe this correlation; in their case they argue that corrosion of the current collector caused by aqueous processing reduced electrochemical performance [137].

Table 3: Summary of electrode slurry microstructure studies in literature.

Authors	AM	Conductive Additive	Polymer	Solvent	SL	Component Ratio	Varied	Key Findings
Ouyang [72]	LFP	Carbon Black	PVDF	NMP	57.2, 60.7, 63.2, 63.9, 66.3, 67.6, 68.4, 69.5	94:3:3 (AM:CB:Polymer)	SL	Viscosity and yield stress increase monotonically with SL. Higher SL decreases space between solid particles and polymer, meaning more bridging, allowing the formation of 3D networks.
Ligneel [73]	LFP	Carbon Black	PVDF	NMP	Solvent conc: 0.001 to 0.01 mL/mg	73:8:19 (AM:CB:Polymer)	SL	The electrochemical performance is low below and above the optimal solids loading due to poor electronic wiring of the active material. An optimal solvent concentration results in homogeneous electrodes and improved electrochemical performance. Here, the solid-liquid electrode dispersion is characterized by a low yield stress that is unlikely to inhibit flow during the mixing step.
Reynolds [70]	NMC 811 (Cathode), Graphite (Anode)	Carbon Black	PVDF (Cathode), CMC/SBR (Anode)	NMP (Cathode), DI H_2O (Anode)	60% (Cathode), 50% (Anode)	96:2:2 (Cathode), 95:1:4 (Anode) - (AM:CB:Polymer)	Slurry composition	Anode slurries (aq) demonstrate shear-thinning behaviour with zero shear. Cathode (NMP) slurries are weakly-gelled with a yield stress followed by shear thinning.
Sung [102]	NMC 111	Carbon Black	PVDF/PVP	NMP	3% (single solid)	-	Polymer concentration and type	PVP adsorbs strongly onto the CB surface, whilst PVDF adsorbs weakly, shown by non-monotonic relationship between polymer concentration and storage modulus.
Lu [140]	NMC 622	Carbon Black	PVDF	NMP	N/A	94:4:2, 95:3:2, 96:2:2, 97:1:2 (AM:CB:Polymer)	Carbon black content	Increased carbon loading increases viscosity at low shear and gel-like properties of the slurry.
Bin Zhao [135]	$LiFePO_4$	Carbon Black	PVDF	NMP	-	-	Carbon black content, PVDF content, active material content	Increased carbon and polymer loading increases yield stress, whilst increasing LFP had little effect on rheological properties. Carbon black forms a network structure in which LFP is embedded.

Gordon [138]	LFP	Carbon Black	CMC	DI H_2O	-	-	CMC content	Varying CMC results in a pronounced minimum in yield stress, attributed to polymer adsorption onto active material and carbon black. Further increase in yield stress is due to polymer entanglement.
Bauer [134]	LFP, NMC 111	Carbon Black	PVDF	NMP	-	-	Active material content	High Mw polymer can establish gel formation via bridging with carbon black. Gel formation also possible if active material particles are small and dense i.e. LFP.
Su [133]	LMFP	Carbon Black	PVDF	NMP	-	-	Carbon black content and type	Increasing the content of carbon additive increases the slurry conductivity and viscosity. Carbon black type and morphology can affect the percolation threshold. Low percolation threshold does not guarantee superior electrochemical performance of resulting electrode.
Park [131]	Graphite (Anode)	Carbon Black	CMC	DI H_2O	3-5% (CB), 45% (Graphite)	-	CMC content on carbon black and graphite	CMC acts as a dispersant to CB at low concentrations. At higher concentrations, CMC acts as a thickener. Slurry microstructure can be affected by the order of mixing as CMC adsorbs preferentially to whichever component it is mixed with first.
Cho [12]	$LiCoO_2$	Carbon Black	PVDF	NMP	70	95:2:3 (AM:CB:Polymer)	Characterization time	The polymer contributes to formation of carbon black network and electronic structures. Active materials also form a network structure. Structures degrade over time, as carbon black forms large agglomerates.
Kim [139]	$LiCoO_2$	Graphite	PVDF	NMP	66.7	89:6:5 (AM:CB:Polymer)	Mixing sequence	The mixing sequence can affect the slurry rheology and electrochemical performance. The best performance is obtained by pre-mixing dry particles, then adding binder and solvent solution. Rheological data

								indicates that this method results in greater dispersion of solid particles, contributing to high electrochemical performance.
Komoda [143]	$LiCoO_2$	Carbon Black	PVDF	NMP	59.6	90.5:3.6:5.9 (AM:CB:Polymer)	Mixing sequence and shear rate	If all slurry components are mixed together, then a carbon matrix forms, yet dispersing the active material is difficult. If the slurry is mixed in parts, then the active material is more easily dispersed within the carbon matrix. High shear mixing may prevent formation of conductive networks.
Hoffmann [142]	NMC 622	Carbon Black/Graphite	PVDF	NMP	-	93:2:1:4 (AM:CB:Polymer)	Mixing sequence and shear rate	Electrodes prepared by dispersing solid components at low shear outperformed those prepared by solids mixing, then adding solvent at high shear.
Wang [141]	$LiCoO_2$	Carbon Black/Graphite	PVDF	NMP	51.5	95:0.33:0.67:4 (AM:CB:Graphite PVDF)	Mixing shear rate and time	Optimum shear rates and mixing times were identified for a conductive network to form.
Tang [132]	NMC 622	Carbon Black	PVDF	NMP	-	97.5:1.5:1.5 (AM:CB:Polymer – Half-Cell), 90:5:5 (AM:CB:Polymer – Full-Cell)	SL, mixing shear rate and time	Low shear rate with high SL leads to homogeneous distribution of particles and improved electrochemical performance. Low SL leads to particle aggregation at both low and high mixing speeds. High SL and high mixing speeds results in degradation of slurry structure.
Sahore [137]	NMC 811	Carbon Black	PVDF, NMP, Latex, JSR, LiPAA	NMP, DI H_2O	-	90:5:5 (AM:CB:Polymer)	Binder type – NMP vs Aqueous processing	The binder type can control the microstructure of the cathode slurry. However, the microstructure did not correlate with electrochemical performance, likely due to corrosion of the Al current collector.

1.12.3 Film Drying

The properties of the electrode slurry, i.e. viscosity affect the behaviour of the dried electrode [70]. The physico-chemical performance of electrodes is strongly influenced by the drying process of the wet films. The porous electrode structure, and physical, mechanical and electrochemical properties of the electrode coatings are important in maintaining good consistency in LIBs, and are controlled by the drying process.

Figure 20 shows the drying process mechanism [144]. When the electrode is cast, it is in the liquid/slurry phase. During drying, the electrode undergoes a phase transition to form a semi–slurry upon removal of solvent. At this stage, the solvent evaporates at a constant rate from the film surface. As more solvent is transported upward toward

the surface and removed, the electrode becomes a semi-solid. The solvent is carried towards the surface by osmotic action, and the solvent evaporation rate from the film surface remains constant. A surface tension gradient is produced by solvent evaporation on the coating surface, which controls pore emptying. The film thickness reduces as a result of liquid outflow from the pores, which occurs when the solvent is removed from between the active material particles, causing them to come closer together. The pressure gradient causes suction from the pores due to capillary pressure [144–146]. This initial drying stage ends when the pore volume begins to empty. A change in the film surface indicates the occurrence of pore emptying. This change usually occurs at the end of film shrinkage; when the active material particles have formed a compact structure and the film thickness can no longer decrease. The constant drying rate extends beyond the beginning of pore emptying, indicating the occurrence of efficient internal mass transfer through the compact pore structure due to capillary forces [144–146]. When the electrode solidifies, the drying process is complete, and neither the density nor the thickness of the coating changes. At this stage, the arrangement of the solid phases (active material, conductive additive and binder) leads to the final porous microstructure, which determines the electronic and ionic conductivity of the electrode, and the electrochemically active area. Thus the drying temperature of the cathode indirectly contributes to electrochemical performance.

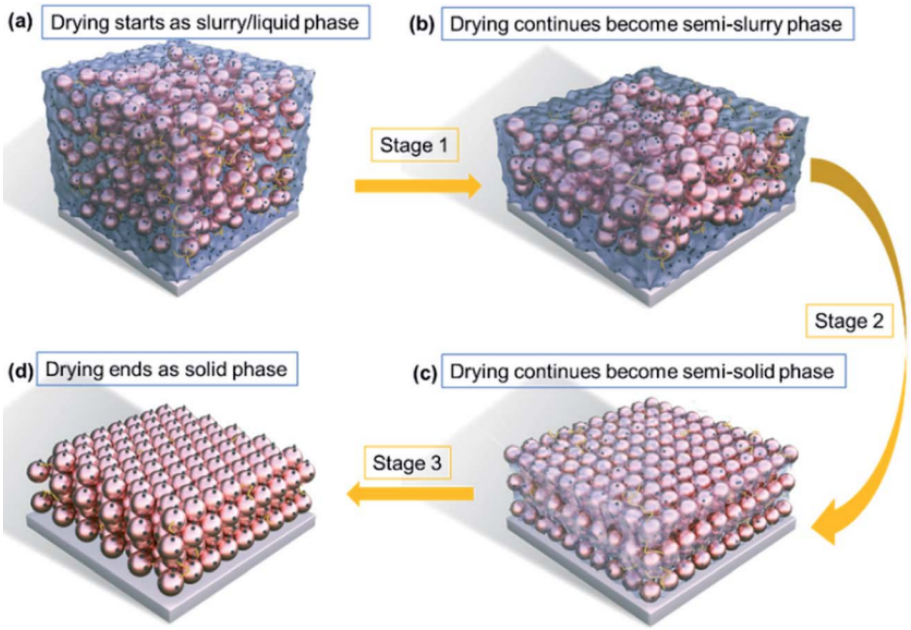

Figure 20: Schematic of electrode film drying mechanism [144].

1.13 Summary

The use of aqueous polymers as cathode binders for LIBs has been extensively studied. However, cathodes prepared with aqueous binders underperform compared to conventionally processed cathodes made with NMP/PVDF. The distribution of carbon black in the dry electrode has been shown to affect the electrochemical performance of the cathode [59]. Carbon black is well-distributed in NMP-based slurries due to interactions with NMP [70], but will agglomerate in water-based slurries due to its hydrophobicity. Therefore binder selection for aqueous systems depends on the chemical interactions between polymer and carbon black, whereby the aqueous polymer must aid the dispersion of carbon black in the slurry. As several types of aqueous binders have been previously studied, an opportunity is provided to determine the effect of the chemical affinity of polymer to carbon black on electrochemical performance. To further aid the distribution of carbon black in the electrode, amphiphilic surfactants are considered. A more comprehensive study investigating the effects of a surfactant on carbon black distribution and electrochemical performance is required.

2 Chapter 2: Experimental Methodology

2.1 Materials

Polycrystalline $LiNi_{0.6}Mn_{0.6}Co_{0.6}O_2$ (NMC; Pi-KEM Ltd, United Kingdom) was used as the cathode active material and Timcal Super C65 (carbon black: Imerys) was the carbon black. De-ionized water was the solvent and was used as is from the lab. A list of all polymers used is shown in Table 4 below.

Table 4: Suppliers and *Mw* of polymers used

Polymer	Supplier	Molecular weight (g mol^{-1})
PVDF	Sigma Aldrich	534,000
PEO	Sigma Aldrich	1,000,000
F68	Sigma Aldrich	8,400
CMC	Sigma Aldrich	250,000
PVP	Thermo Scientific	1,300,000
Na Alginate	VWR Chemicals	216,000
Chitosan	BioServ	580,000

The physical properties of the NMC 622 and carbon black powders are reported in Table 5:

Table 5: Physical properties of NMC and carbon black powders used.

Particle Species	ρ ($kg\ m^{-3}$)	Diameter	specific surface area (m^2g^{-1})
NMC 622	2500 [a]	7-19 um[a]	0.267 [a]
Carbon Black	1600 [b]	150 nm [c]	62 [b]

[a] Properties reported by the manufacturer, Targray, [147]. [b] Properties reported by the manufacturer, Imerys [148]. [c] Fused fractal diameter reported by Spahr et al. [149]; primary particles are 37-nm in diameter.

2.2 Polymer solution preparation

For each sample, the required amount of polymer was weighed into a container, and then the required amount of de-ionized water was measured and added. The polymer was dissolved using a magnetic stirrer for 24 h. DLS measurements were taken to confirm

dissolution of the polymer. Polymer solutions containing pluronic F68 solution were prepared by adding the required amount of pluronic F68 solution to either de-ionized water or the polymer solution if a blend, again using a stir plate for 24 h.

2.3 Capiliary viscometry

A capillary viscometer is a U-shaped glass tube submerged in a water bath to regulate the temperature. The measured fluid is pipetted upwards into a chamber, and the time taken to flow between two marked points on the viscometer is recorded. The dynamic viscosity is calculated by multiplying the time by a constant which is specific to the type of tube. Capillary viscometers yield reproducible data, and are cheaper to operate than rotational viscometers. Whilst this method is highly suitable for polymer solutions, it is not suited for full cathode slurries nor single-solid suspensions studied in this project, as the carbon black is opaque and causes the suspensions to stick to the glass.

2.3.1 Capiliary viscometry procedure

To determine the viscosity of aqueous polymer solutions, solutions were measured using a capillary viscometer, temperature-controlled by immersion in a water bath at 25°C. The drop-time of solution between two lines on the viscometer was recorded. Solutions were diluted until a viscosity of 52 mPa·s was attained.

2.4 Slurry preparation

Three types of slurries were prepared from each polymer solution: a dispersion of NMC, a dispersion of carbon black, and a blended NMC/carbon black dispersion. The mass fractions of each species used for a given slurry type are listed in Table 6 for Chapter 3, and Tables 7 and 8 for Chapter 5. In Chapter 4, the cathode formulation used was 95:3:2 for active material, carbon black and polymer - see Table 4, with a solids loading of 68.3 wt%. The dry powder mixture was prepared by weighing NMC and carbon black into an agate mortar and pestle and grinding them together for 15 minutes. For slurries containing only one type of solid, the grinding time was shortened to 1 min to break up any clumps. The powder was transferred into a 12-mL polypropylene container (Thinky), then the required amount of de-ionized water was measured and added. The resulting slurry was mixed using a Thinky planetary mixer at 2000 rpm for 5 minutes

followed by a degassing step for 30 seconds at 2200 rpm. Cathode slurries containing CMC contained 0.8 wt% phosphoric acid to prevent corrosion of the current collector.

Tables 6, 7, and 8 show the dry solids wt% with an associated solids loading of the slurry. The solids loadings are given as the mass of carbon black and active material divided by the mass of carbon black, active material polymer and water. In Chapter 3, the effect of the polymer on the slurry microstructure was varied. To do this, the ratio of other solid components i.e. NMC 622 and carbon black was kept constant, their mass was relative to what it would be in the full cathode slurry. The nomenclature is given as the wt% of polymer in the slurry for each sample. For example, for the sample NMC_CB_1, there is 1 wt% polymer in the cathode slurry. If 100g of slurry was made, 1g polymer/(1g polymer + 48g NMC 622 + 0.5g carbon black + 50.5g water) x 100 = 1%. But in the dried cathode, there would be 2 wt% polymer, as 1g polymer/(1g polymer + 48g NMC 622 + 0.5g carbon black) x 100 = 2%.

Table 6: Samples and compositions for Chapter 3

Sample No.	AM wt%	CB wt%	PEO wt%	Solids Loading (%)*
CB_025	0	80	20	1
CB_05	0	66.7	33.3	1
CB_1	0	50	50	1
CB_2	0	33.3	66.7	1
CB_3	0	25	75	1
CB_5	0	16.7	83.3	1
AM_025	99.6	0	0.4	59.9
AM_05	99.2	0	0.8	59.8
AM_1	98.4	0	1.6	59.5
AM_2	96.8	0	3.2	58.9
AM_3	95.2	0	4.8	58.3
AM_5	92.3	0	7.7	57.1
NMC_CB_025	98.5	1	0.5	48.5
NMC_CB_05	98	1	1	48.5
NMC_CB_1	97	1	2	48.5
NMC_CB_2	95	1	4	48.5
NMC_CB_3	93.2	1	5.8	48.5
NMC_CB_5	89.7	1	9.3	48.5

Table 7: Cathode slurry compositions for solids loading (SL) controlled samples for Chapter 5. The solids loading is kept constant at 68.3 wt%.

PEO wt%	NMC wt%	Carbon Black wt%	Polymer wt%	η (m Pas)
PEO 0	95	3	2	5
PEO 10	95	3	2	20
PEO 25	95	3	2	52
PEO 40	95	3	2	201
PEO 50	95	3	2	395
PEO 75	95	3	2	8113
PEO 100	95	3	2	64893

Table 8: Cathode slurry compositions for viscosity controlled samples for Chapter 6. Polymer solution viscosity is kept constant at 52 m Pas^{-1}.

Sample	NMC wt%	Carbon Black wt%	PEO wt%	F68 wt%	SL (%)
PEO 25	95	3	0.5	1.5	68.3
PEO 40	95	3	0.8	1.2	57.2
PEO 50	95	3	1	1	55.3
PEO 75	95	3	1.5	0.5	42.7
PEO 100	95	3	2	0	38.2

2.5 Adsorption isotherms

Adsorption isotherms were obtained, and the Freundlich model was fit to determine the chemical affinity of aqueous polymers to carbon black. This model assumes multilayer adsorption [106, 107]. The Freundlich adsorption isotherm is given by:

$$\Gamma = KC_{eq}^{\frac{1}{n}} \tag{13}$$

Where Γ is the adsorbed amount of polymer (mg m^{-2}), C_{eq} is the equilibrium concentration of the supernatant (wt%), K is the Freundlich constant, and n is an exponent.

Aqueous suspensions consisting of deionized water, 1.5 wt% carbon black, and polymer (0.01 to 0.2 wt%) were prepared. Polymer solutions were prepared at 4.26 wt% polymer and diluted to respective amounts. The diluted solutions and C65 carbon black (Imerys) were weighed into 30 ml Thinky pots. The resulting mixture was mixed in a Thinky planetary mixer at 2000 RPM for 10 min then de-gassed at 2200 RPM for

30s. Suspensions were measured into 2 ml centrifuge vials, then centrifuged at 15000 RPM for 30 min. The resulting supernatant was extracted with a syringe and filtered using 45 μm syringe filters, to remove any excess carbon black particles. The filtered supernatant was characterized using a QCM-D Quartz Crystal Microbalance (Biolin Scientific) with a sensor (5 MHz, Ti/Au). The polymer concentration of the supernatant was determined by calibration curves which were also obtained by the QCM-D method using polymer solutions of the same concentration range as the suspensions (0.01 to 0.2 wt%). The adsorbed amount of polymer was calculated by mass balance as follows:

$$m = \frac{C_i V_i - C_f V_f}{SA} \tag{14}$$

Where m is the adsorbed surfactant amount per unit area; C_i and C_f are the initial and filtrate carbon black concentrations respectively; V_i, V_f are the initial and filtrate volumes respectively; and SA is the surface area of the substrate, in this case carbon black particles.

Table 9: Adsorption samples for Chapter 4.

Polymer wt%	Mass (4.255 wt% Polymer Soln) (g)	Mass (Carbon Black) (g)	DI H_2O (g)
0.2	0.235	0.075	4.69
0.15	0.0176	0.075	4.91
0.1	0.047	0.0305	1.95
0.075	0.0353	0.0306	1.97
0.05	0.0235	0.0306	1.98
0.04	0.0188	0.0306	1.98
0.025	0.0118	0.0307	2
0.01	0.0047	0.0306	2

2.6 Zeta potential

Highly charged particles repel one another, resulting in a stable dispersion. Zeta potential characterises the surface charge of a particle [121]. The electrostatic potential changes with distance from the surface of a charged particle, dropping to an effectively zero value far into the solution. The zeta potential is not measured at the particle surface; it is the electrostatic potential at the 'slipping plane' where molecules of solution start to flow around the charges on the particle. The zeta potential is used to quantify the magnitude of the charge at the slipping plane. Values of the zeta potential below

-30 mV or above +30 mV usually indicate that the particle will remain stable and dispersed, and won't aggregate. When the potential is small, the attractive forces can be stronger than the repulsive forces, causing the dispersion to aggregate. As a result, electrically stable colloids have high absolute values of zeta potentials, whereas colloids with low absolute values of zeta potentials can flocculate or coagulate. A schematic describing zeta potential is shown in Fig. 21.

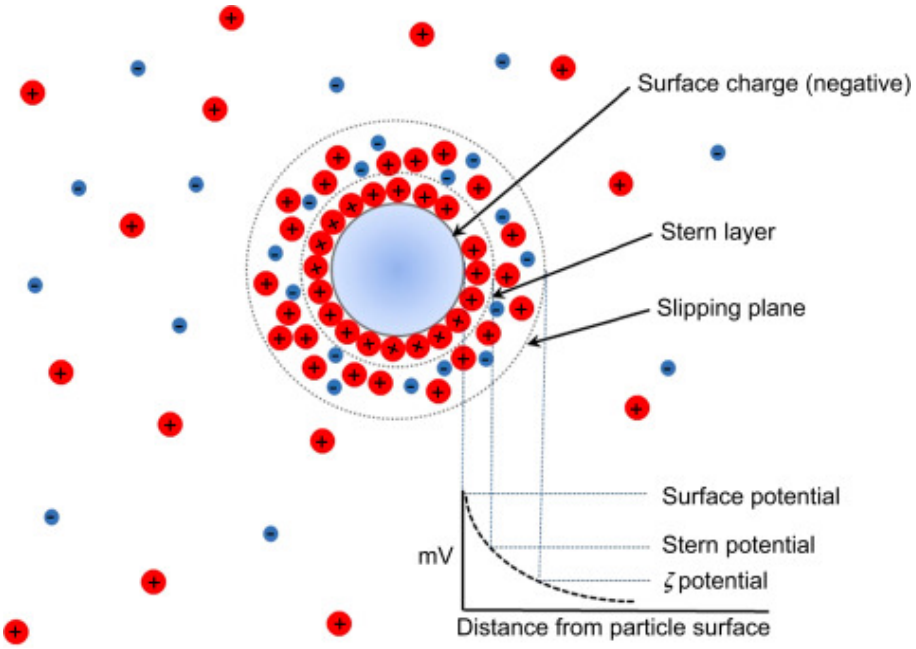

Figure 21: Schematic showing zeta potential [121].

2.6.1 Zeta Potential Procedure

Aqueous suspensions were prepared for zeta potential characterization with a 98:1:1 ratio of DI H_2O, carbon black and polymer. The mixtures were mixed in a Thinky planetary mixer at 2000 RPM for 10 min then de-gassed at 2200 RPM for 30s. Zeta potential measurements were taken with a Colloid Metrix Stabino © II. Samples were loaded into the beaker and the zeta potential was recorded via the motion of a plunger, which generates a charge separation, which is measured by electrodes on the side of the beaker. The plunger ran for three minutes per sample, recording values periodically. From this, the zeta potential was averaged. The list of compositions prepared for zeta potential measurements is shown in Table. 10.

Table 10: Slurry compositions for zeta potential measurements for Chapter 6.

PEO to Pluronic Ratio	H_2O wt%	Carbon Black	PEO wt%	PL wt%
0	98.04	0.98	0	0
10	98.04	0.98	0.1	0.9
25	98.04	0.98	0.25	0.75
40	98.04	0.98	0.4	0.6
50	98.04	0.98	0.5	0.5
75	98.04	0.98	0.75	0.25
100	98.04	0.98	1	1

2.7 Rheology

Due to the presence of carbon black, optical microscopy is not a good way to study cathode slurries. Rheology is one such method employed to study the slurry structure. Rheology is the study of the flow and deformation of matter, which explains how force applied over a material over time affects its deformation [150].

2.7.1 Steady State Rheology

Shear flow can be visualised as fluid layers sliding on top of each other, each layer moving faster than the layer below it. While the bottom layer is immobile, the topmost layer in Fig. 22 has the greatest velocity. A shear force is applied to the fluid for shear flow to occur. Shear stress (σ), which is defined as the force F acting across a unit area A, is the result of this external force. The bottom layer stays stable while the upper layer moves a predetermined distance, x, in response to this force. As a result, the sample has a gradient of displacement, known as the shear strain (γ), given by Equation 15:

$$\gamma = \frac{x}{h} \tag{15}$$

The strain is limited for an applied stress for a solid that behaves like a single block of material; flow will not occur.

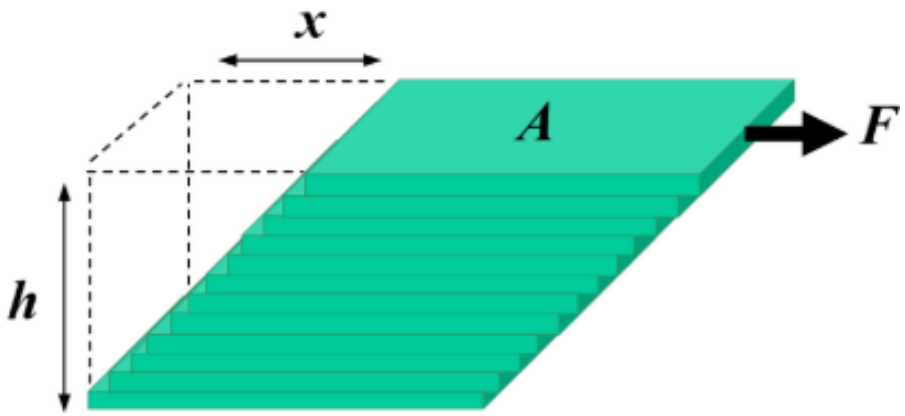

Figure 22: Depiction of shear rate and shear stress for layers of fluid sliding over each other for a section of material [150].

A single-head rotational rheometer with cone and plate geometry is used to measure the shear viscosity and stress of the cathode slurry. The sample is loaded between the plates at a known gap h as shown in Figure 23. A rotational speed is applied to the motor and the torque required to maintain that speed is measured. From this, the force F is calculated, which acts over the surface area of the plate A to give (σ). The rheometer records the shear force via the torque at each measuring point. Equation 16 is given for shear stress:

$$\sigma = \frac{F}{A} \tag{16}$$

A sample that resembles liquid, i.e. a Newtonian fluid, will flow with a shear rate based on its viscosity in response to the shear stress. The rheometer records the velocity as the rotational speed at measuring points. The size of the shear gap is also known for the measuring system used. The measurement gap h must be precisely known to calculate the shear rate from Equation 17.

$$\dot{\gamma} = \frac{V}{h} \tag{17}$$

When a shear stress is applied to a fluid momentum is transferred; the shear stress is the momentum rate transfer to the upper layer of fluid. Here, momentum is transferred through the fluid layers due to collisions and interactions with other fluid components, which slows the flow and dissipates heat. The shear viscosity or dynamic viscosity (η), which is a measurement of the internal fluid friction and relates to loss of kinetic energy

in the system, proportionality factor between the shear stress and shear rate [150]. The viscosity of a system is given by Equation 18:

$$\eta = \frac{\sigma}{\dot{\gamma}} \tag{18}$$

In Newtonian fluids, the viscosity is not affected by changes in shear rate or shear stress since the shear stress and shear rate are linearly connected in these fluids. Water, simple hydrocarbons, and diluted colloidal dispersions are examples of common Newtonian fluids. In non-Newtonian fluids, viscosity varies depending on the shear strength or rate of applied shear. Fluid viscosity depends on both pressure and temperature, typically rising with higher pressure and falling with higher temperature [150].

Shear thinning, also known as pseudoplastic flow, is where the fluid viscosity decreases with increased shear. It is the most common type of non-Newtonian behaviour observed. Shear thinning fluids exhibit a constant viscosity value, η_0, also known as the zero shear viscosity, at low enough shear rates. A significant decline in viscosity is seen at a critical shear rate or shear stress, which marks the start of the shear thinning area. Theoretically, a power law relationship appearing as a linear section when examined on a double logarithmic scale can adequately explain this area of shear thinning, which is how rheological flow curves are frequently depicted. The infinite shear viscosity plateau is a second constant viscosity plateau that is seen at very high shear rates. This is given the symbol η_∞ and can be much lower than η_0 depending on the degree of shear thinning [150].

In a typical polymer solution, there is no yield stress unless the polymer is gelled. Most polymer solutions are shear-thinning due to disentanglement in shear. The Cross model (Equation 23) is generally used to fit viscosity flow curve data of polymers (as demonstrated in the results and discussion), but many models are available.

The type of sample and its viscosity determine the kind of measurement device (geometry) that is used. For example, the cone and plate is used in this work due to the high viscosity of both polymer solutions and slurries, and practical volume constraints [150].

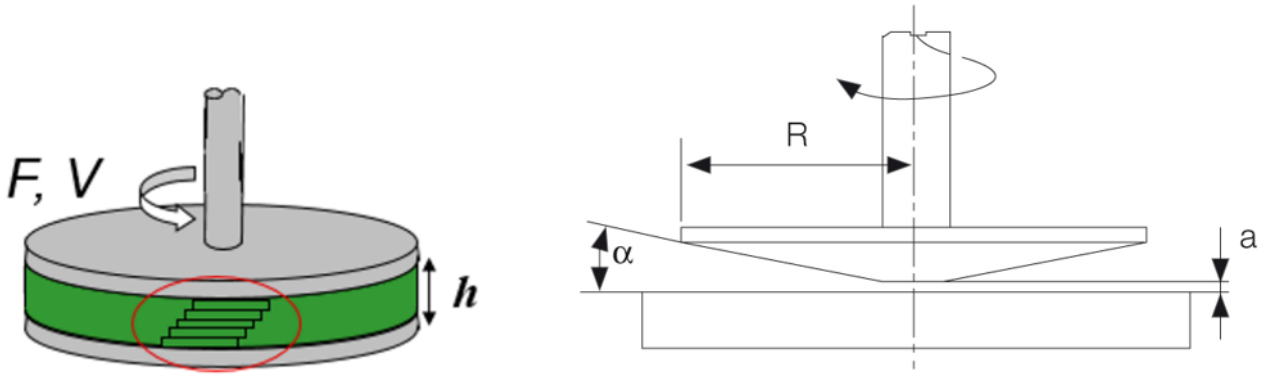

(a) (b)

Figure 23: (a) Rotational shear test using a cone and plate geometry on a sample; the cone rotates while the lower plate is stationary. Shear flow is shown by the red circle. [150]. (b) Cone-plate geometry (with radius R, cone angle α) [151].

2.7.2 Viscoelastic behaviour

Materials can exhibit both solid-like (elastic) and liquid-like (viscous) properties, known as viscoelastic behaviour. Frequency sweeps are conducted to measure these properties. To perform frequency sweeps with a plate measuring geometry, the sample is loaded between the plates and is oscillated back and forth at a given strain amplitude and frequency [150, 151]. The motion of the geometry is represented as a sinusoidal wave, with time on the x-axis and strain amplitude on the y-axis. This setup is shown in Fig. 24.

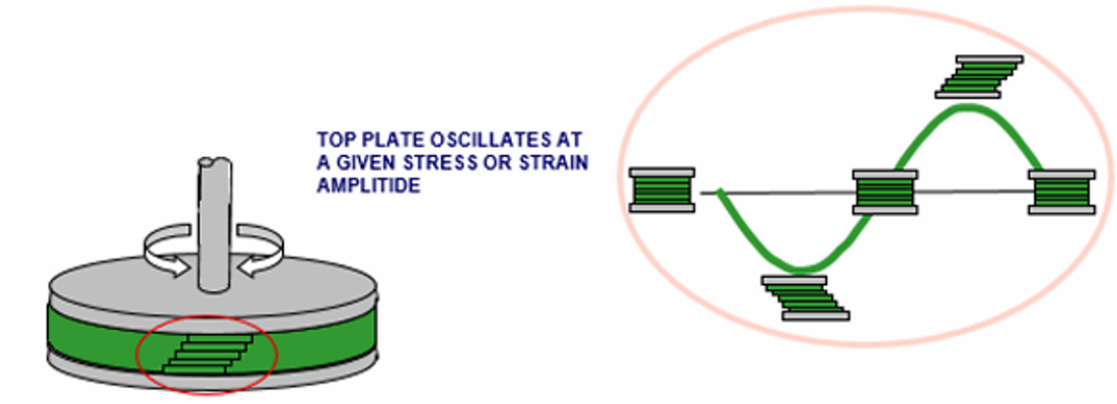

Figure 24: Schematic illustrating the principle of a frequency sweep test [150].

The ratio of the applied stress to the measured strain gives the complex modu-

lus (G*), which measures a material's resistance to deformation [150]. The complex modulus is given by Equation 19:

$$G^* = \frac{\sigma_{max}}{\gamma_{max}} \tag{19}$$

For a purely elastic material, both stress and strain are in phase. Here, stress is proportional to strain, and the maximum stress is at maximum strain. For a purely viscous material, stress and strain are out of phase by 90 deg or $\pi/2$ radians. Here, the stress is proportional to the strain rate. When the flow rate is greatest, the maximum stress is when the strain rate is maximum. A schematic for this is illustrated in Fig. 25.

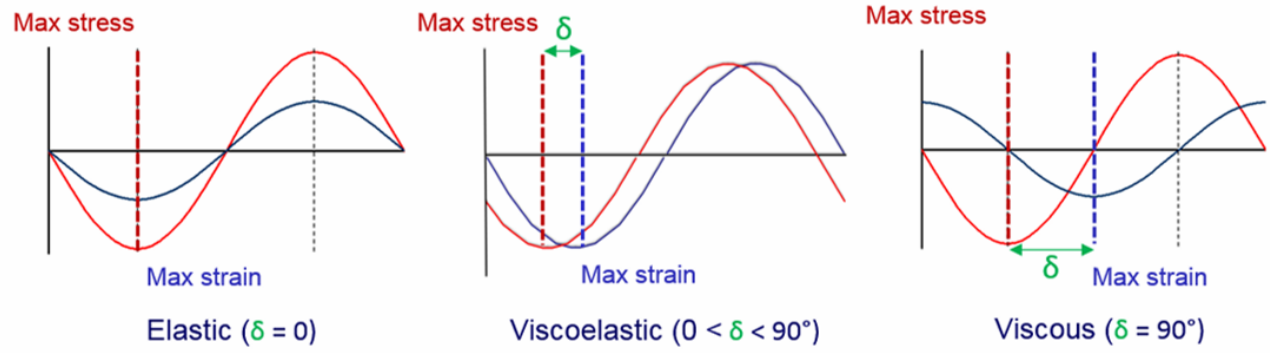

Figure 25: Stress and strain wave relationships for a purely elastic (ideal solid), purely viscous (ideal liquid) and a viscoelastic material [150].

The phase difference or phase angle (δ) determines the viscous and elastic components. The phase angle is also known as the loss tangent (tan δ). When tan δ is below 1, the material is said to be purely elastic, whereas whilst when δ is 0 °, the material is said to be purely viscous, when tan δ is 1 represents the sol-gel point, i.e. the phase transition between solid and liquid behaviour. The elastic contribution to G* is termed the storage modulus (G'), whilst the viscous contribution is called the loss modulus (G") since it represents energy loss [70, 150, 151]. Determination of G' and G" using trigonometry is shown in Fig. 26.

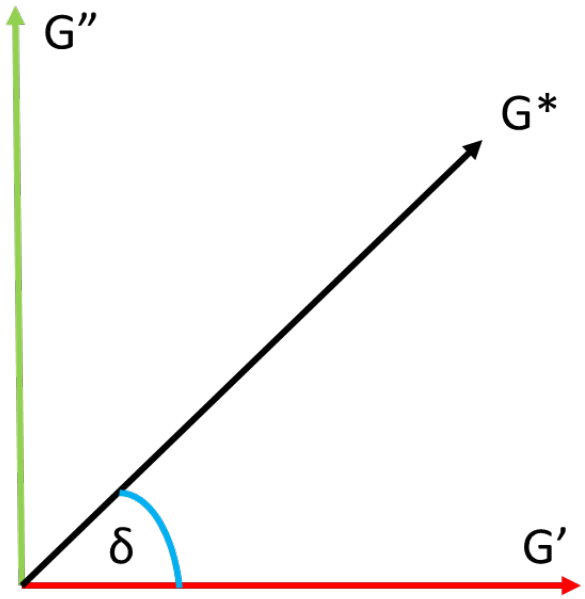

Figure 26: Trigonometric relationship between G* and its components G’ and G”.

The storage modulus is given by Equation 20

$$G' = G^* cos(\delta) \tag{20}$$

The loss modulus is given by Equation 21

$$G^{"} = G^* sin(\delta) \tag{21}$$

The tan δ is given by Equation 22

$$tan(\delta) = \frac{G^{"}}{G'} \tag{22}$$

Amplitude sweeps were performed on slurries prior to frequency sweeps, to determine the limit of the linear viscoelastic region (LVR), which is the region where an amplitude sweep is carried out without destroying the structure of the sample. Once the LVR is determined, a strain rate is chosen that is at or within the LVR for frequency sweeps. If a frequency sweep is performed at a strain rate above the LVR,the data will be inaccurate as the structure of the sample will be destroyed. Fig. 27 shows an amplitude sweep for a full cathode slurry with PEO as the binder for Chapter 5. Here, the LVE limit is determined as 0.1 %. The subsequent frequency sweeps were performed at a strain rate of 0.1 % for all slurries tested.

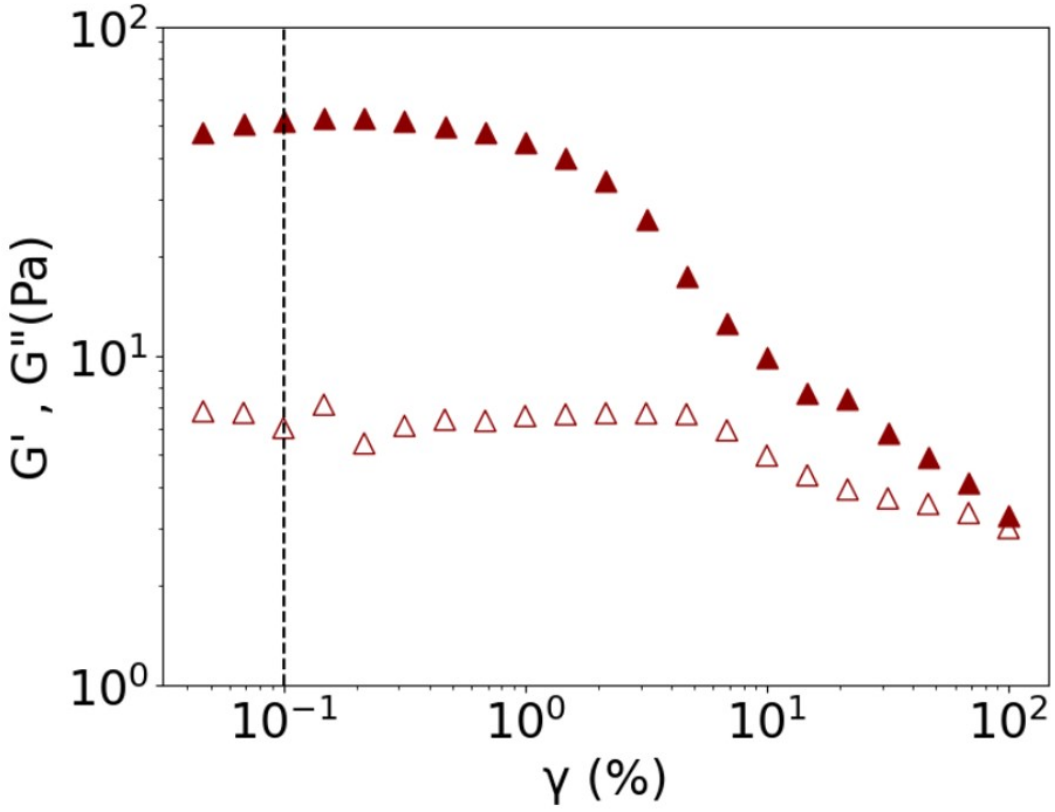

Figure 27: Amplitude sweep for a full cathode slurry using 1wt% PEO as the binder for Chapter 3, showing G' (▲) and G" (△). The limit of the linear viscoelastic region at 0.1 % is shown as a black dotted line.

2.7.3 Battery Slurry Rheology

The formulation and the interactions of each component in a mixture determine the rheology of a material or slurry, which is why rheology is a widely utilised tool in materials science. The rheological properties of the slurry (e.g. η), strongly affect the coating process, by factors such as coating speed, temperature, thickness, and slurry wetting onto the current collector. The flow rheology determines what unit operations can be used to cast a film, e.g. slot die, doctor blade etc. Viscosity affects the energy required to maintain steady-state flow. Viscoelastic behaviours, like die swell, affect ability to produce a smooth, reproducible film [70].

2.7.4 Rheological test procedures

An Anton Paar Rheometer (Modular Compact Rheometer, MCR 502) was used to carry out rheological measurements using a cone and flat plate with a cone angle of 4°, a gap of 253 µm, a diameter of 25 mm, and a temperature of 25°C. Flow curves were performed between 0.01 to 500 s^1 to determine the viscosity of each sample as a function of strain rate. The storage and loss moduli were measured using a frequency sweep at 1% strain for all slurries in Chapter 3, and 0.1% strain for slurriesfor Chapter 5, with a frequency range of 0.1 to 100 rad s^{-1} Before viscoelastic measurements, a strain sweep was performed on each sample to verify that the sample remained in the linear viscoelastic region.

2.7.5 Theoretical models and fitting

Polymer solutions may show non-Newtonian behaviour - namely a plateau at low shear followed by shear thinning due to polymer disentanglement. Therefore the Cross Model is fit to plots of η vs $\dot{\gamma}$ to extract key parameters, namely the zero shear viscosity (η_0), which is a theoretical value of the solution at zero shear, and the viscosity at infinite shear rate (η_∞). The Cross Model is given by Equation 23:

$$\eta(\dot{\gamma}) = \frac{\eta_0 - \eta_\infty}{1 + (k\gamma)^n} \tag{23}$$

where $\eta(\gamma)$ is the viscosity at shear rate $\dot{\gamma}$, k is the cross time constant, and n is a dimensionless fitting parameter. This model is fit via a difference of least squares procedure.

Like polymer solutions, battery slurries are non-Newtonian, however, they may exhibit a yield stress, which is the stress corresponding to the yield point at which the material begins to deform plastically [150–152]. Whilst the Cross Model is suitable for polymer solutions, it is not suited for suspensions that exhibit a yield stress. The presence of a yield stress in a material indicates solid-like behaviour. Multiple yielding phenomena (drops in stress-strain) may occur due to the breakup of flocs and a dynamic equilibrium between floc breakup and floc aggregation [70, 102, 120]. Slurries were fitted with the Herschel Bulkley model for viscoelastic liquids with a yield stress, The presence of a yield stress in a material indicates solid-like behavior. The yield stress is given by Equation 24:

$$\sigma = \sigma_0 + K_h \dot{\gamma}^n \tag{24}$$

Where σ_0 is the yield stress, K_h is the consistency factor and n is the flow behavior. Multiple yielding phenomena (drops in stress-strain) may occur due to the breakup of flocs and a dynamic equilibrium between floc breakup and floc aggregation [70,102,120].

The relative viscosity (η_{rel}) can be used to measure the contribution of individual components in a slurry. This is given by Equation 25:

$$\eta_{rel} = \frac{\eta_s}{\eta_{sol}} \tag{25}$$

Where η_s is the viscosity of the suspension which may contain a solid, and η_{sol} is the viscosity of the solution.

The intrinsic viscosity is used to calculate the overlap concentration, c*:

$$c* = \frac{1.45}{[\eta]} \tag{26}$$

The volume fraction, ϕ_s of each component in the slurry is given by Equation:

$$\phi_s = \frac{Vol_{NMC} + Vol_{CB}}{Vol_{NMC} + Vol_{CB} + Vol_{Polymer} + Vol_{H_2O}} \tag{27}$$

2.8 Dynamic Light Scattering (DLS)

Dynamic light scattering (DLS) is based on the Brownian motion of dispersed particles. Brownian motion is the random motion of particles that results from their collision with fast-moving solvent molecules. These collisions of particles transfer energy to one another, which causes particle movement. Energy transfer is relatively constant and therefore affects smaller particles more. Therefore, smaller particles move faster than larger particles. The Stokes-Einstein equation provides the relationship between the particle speed and size:

$$D = \frac{k_b T}{C\pi\mu R_0} \tag{28}$$

Where D is the diffusion coefficient, k_b is the Boltzmann constant, T is temperature, μ is the solvent viscosity, and R_0 is the solute radius.

The particle velocity is given by D. Furthermore, Equation 28 includes the viscosity of the dispersant and the temperature as both parameters directly influence particle movement. The particle movement must be based on Brownian motion to satisfy equation 28. If particles sediment, it prevents random motion, producing unreliable results. Smaller particles scatter less light, resulting in an inaccurate measurement signal [153]. The intensity trace generates a correlation function, which describes how long a particle is in a particular position within the sample [153]. The exponential decay in the correlation function indicates that the particle is moving. Smaller particles decay faster than larger ones. From this, the diffusion coefficient is calculated and the hydrodynamic radius of the particle is calculated from Equation 28.

In the DLS setup, a single-frequency laser is directed to the sample in a vial, where a dip probe is inserted. If particles are present, the incident laser light is scattered in all directions. Equation 28 is used to compute the diffusion coefficient and the particle size when the scattered light is detected over time at a specific angle. The scattered light intensity fluctuates over time. Smaller, faster-moving particles fluctuate faster than larger particles. The greater the amplitudes between the maximum and minimum scattering intensities, the larger the particles. The hydrodynamic diameter is the particle size of hard spheres that diffuse at the same velocity as the particles in the sample [153].

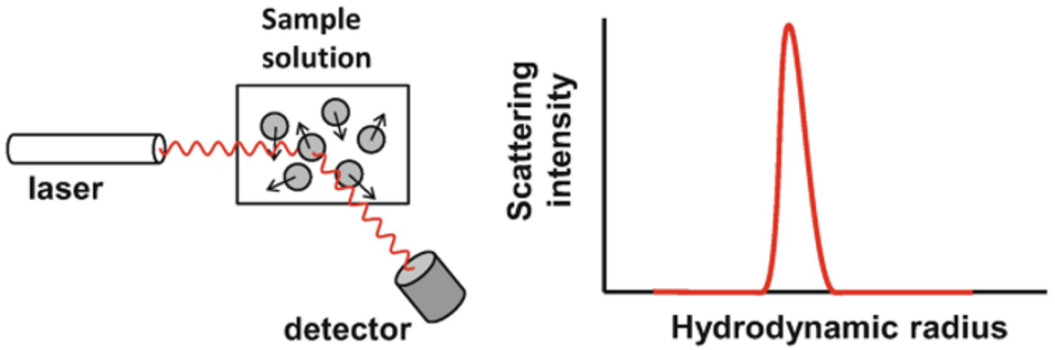

Figure 28: Schematic showing DLS set up and plot showing measurement of the hydrodynamic radius [154].

2.8.1 DLS procedure for polymer solutions

Polymer solutions were characterized using a NANO-flex® II nanoparticle measuring system. A probe was placed into each solution, enabling a measurement of particle size distribution to be taken.

2.8.2 DLS procedure for full cathode slurries

Full cathode slurries were diluted by taking approximately 1 mg of slurry on the tip of a spatula, which was added to 15 ml of de-ionized water. The dilute suspensions were left to rest for 24 hours to allow the largest particles (cathode active materials and large carbon black flocs) to settle, then were characterized using a NANO-flex® II nanoparticle measuring system. A probe was placed into each solution, enabling a measurement of particle size distribution to be taken.

2.9 Conductivity

The 2-point conductivity probe has two electrodes positioned opposite from each other. An alternating voltage is applied to the electrodes, generating a current in the sample being measured. The presence of 3D networks of carbon black in the slurry determines the magnitude of current [155–157]. Electrical conductivity and current flow increase with the amount of free anions and cations present in the sample [158].

2.9.1 Conductivity procedure

Full cathode slurries prepared in Tables 7 and 8 were characterized using the two-point method. The electrical conductivity of the slurries was measured using a Mettler Toledo FiveGo F3 conductivity meter. The tip of the probe was inserted in the slurry and a measurement was recorded. Conductivity measurements were taken for all slurries containing carbon black. Conductivity measurements were performed on slurries a day after they were made.

2.10 Scanning Electron Microscopy (SEM)

In scanning electron microscopy (SEM) an electron beam is scanned across a sample. These electrons interact with the sample surface, by being scattered by the surface or ejecting electrons from the sample. These backscattered and secondary electrons are recorded by detectors, producing an image. Electron usage produces images with high spatial resolution. This and the surface sensitivity of this technique has meant SEM is used widely in materials science [95].

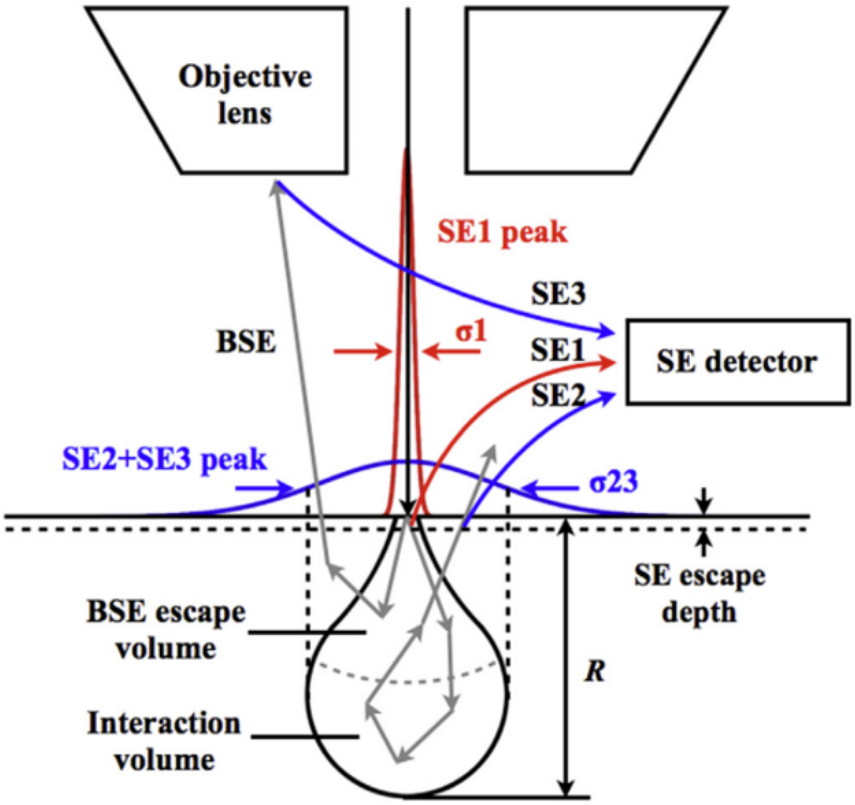

Figure 29: Schematic showing the operating principles of SEM. From below the sample surface, electrons are emitted from a range R. The different types of detected secondary electrons are SE1, SE2 and SE3. BSE refers to backscattered electrons which are from deeper within the sample than secondary electrons (SE) Image taken from [95].

2.10.1 SEM Procedure

Scanning electron microscopy was performed on cathodes using an FEI Inspect F50 SEM equipped with secondary electron (SE) and backscattering (BSE) image detectors. Samples were prepared by placing the cathodes on SEM stubs using carbon tape to reduce the effects of charging. SEM images were taken with an accelerating voltage of 20 KV.

2.11 Electrochemical characterization

Electrochemical properties of cells and batteries are characterized by cycling, whereby they are charged and discharged over 100 cycles to measure the capacity fade, and 35 cycles at seven different C rates to study their rate capability. Here, the performance

is analyzed to determine the amount of energy the cell can store and release. One cycling method is galvanostatic cycling. Here, a potential window is selected, then upon charge a constant positive current is applied to the cell until the voltage reaches the upper limit. The current is reversed to decrease the voltage to the lower limit upon discharge. Upon both charge and discharge, the change in potential is observed. The selected potential window is determined by the chemistry of the cathode material [27]. It has been discussed that the cell voltage is determined by the difference in chemical potential between the anode and the cathode, and since μ_a must be greater than μ_c to avoid lithium metal plating, the total cell voltage can only be increased by selecting a cathode material with higher chemical potential [3]. Generally, the potential window increases with the number of electrons in the d orbitals [27]. Before cycling, the cell has an open circuit voltage (OCV), which is the difference in electrical potential between the anode and the cathode without a load [26]. The objective of galvanostatic cycling is to determine the amount of energy the cell stores and releases upon charging and discharging, which is found by measuring the cell's capacity. The theoretical capacity of cathode material is determined by the number of reactive electrons and the molar weight of materials, and is given by Equation 29:

$$\bar{C} = \frac{nF}{3.6 \times M} \tag{29}$$

where n is the number of reactive electrons per formula unit, M is the molar weight of materials, and F is the Faraday constant. The number of reactive electrons corresponds to the number of electrochemically active lithium ions in the cathode material lattice [27]. The theoretical capacity of NMC 622 is 175 mAh g^{-1}, however lower capacities are obtained in practice, as less lithium ions can be inserted or extracted from the cathode material [27].

The specific capacity is the number of amp hours (Ah) per gram of lithium which is transported by the cell. Each type of cathode material has a theoretical capacity which is determined by the number of lithium ions that can be intercalated into the cathode structure. The units of specific capacity are mAh g^{-1}. The specific capacity ($\bar{C}$) of a cathode is given as:

$$\bar{C} = \frac{\int I(t)\, dt}{M_{CAM}} \tag{30}$$

The coulombic efficiency can be calculated as a measure of the amount of charge a battery can return upon discharge. The coulombic efficiency (η_{coul}) is given as:

$$\eta_{coul} = \frac{\bar{C}_{Discharge}}{\bar{C}_{Charge}} \times 100 \tag{31}$$

The C Rate is defined as the speed at which the battery is fully charged or discharged relative to its capacity. A C rate of 1C means that the cell is charged in one hour. For a 100 Ah battery, a current of 100 A is drawn for 1 hour. At a rate of 2C, the cell is (dis)charged twice in 1 hour, so a current of 50 A is needed. Cycling the battery at high C rates results in lower capacities achieved because of losses due to internal resistances, even though in theory the C rate should not affect the capacity. In an EV battery, high C rates are required. For capacity fade measurements, cells were cycled at a C rate of 1C, which was chosen as a compromise between a high C rate and obtaining reasonably high capacities. Table 11 shows the C Rates used in this thesis.

Table 11: C-rate and charging/discharging time.

C Rate	(Dis)charge Time
0.1C	10 hours
0.2C	5 hours
0.5C	2 hours
1C	1 hour
2C	30 minutes
5C	12 minutes

Cathodes were electrochemically tested as part of coin cells. These coin cells were galvanostatically cycled within a set voltage range of 3.0 to 4.3V using a Maccor cycler. The cell is encased in two aluminum cases. A spring is placed to support the battery. The spacer is to reduce compression and prevent shrinkage of the cell. Lithium metal is used as an anode to ensure an excess amount of lithium is available. The separator acts as a membrane to keep the anode and the cathode separate, to prevent short circuits while allowing diffusion of lithium ions [24]. The coin cell must be crimped at 500 psi to tightly seal the cell. The procedure of electrode preparation, assembling and testing coin cells was set out by the FutureCat consortium of The Faraday Institution and NPL [3]. The coin cells used in this investigation are half-cells, which consist of the specific fabricated cathode (NMC 622) and Li metal as the anode. This enables the

cathode material to be investigated in isolation. A full cell by contrast, consists of both a specific cathode and an anode - the purpose of studying full cells is to evaluate the overall performance of the battery system. In this investigation, only the cathode is studied; coin cells were exclusively used. A LIB coin cell schematic is shown in Fig. 30.

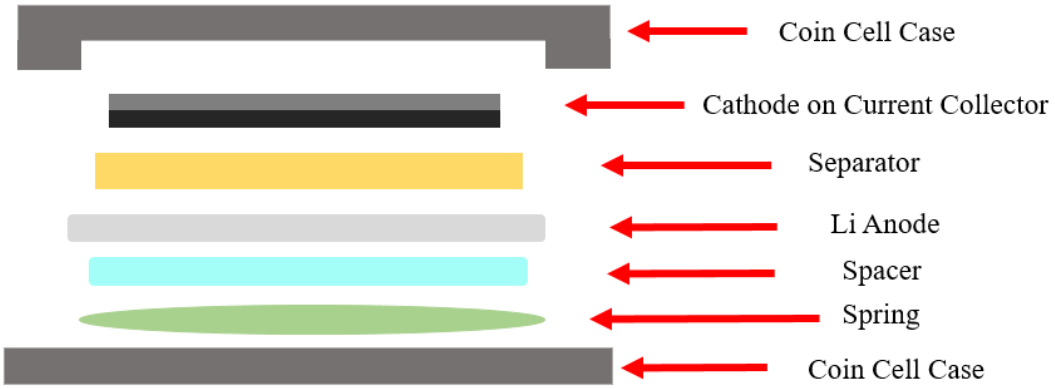

Figure 30: Schematic diagram of a coin cell.

2.12 Dry electrode preparation

Slurries prepared were coated onto 16 μm carbon-coated Al foil (MTI corporation) which was laid on top of a draw-down table using a Doctor blade, with the blade height set to a gap of 200 μm and a speed setting of 15 on the draw-down coater, which is speed of 30 mm s^{-1}. The electrodes were dried on the draw-down coater for 1 hour at 80 °C, then for 48 hours in a vacuum oven at 80 °C and advected over the film. Cathodes were cut out in a circular shape using a punch with a diameter of 12 mm and then returned to the vacuum oven for a further 24 hours to remove any water accumulated during cathode punching.

The porosity (ϵ), was calculated using the equation:

$$\epsilon = (1 - \frac{\rho_{Actual}}{\rho_{Theoretical}}) \times 100 \tag{32}$$

Where ρ_{Actual} is the measured density of the cathode, calculated by the cathode mass and volume, and $\rho_{Theoretical}$ is the theoretical density of the cathode, calculated by densities of materials. $\rho_{Theoretical}$ is given as:

$$\rho_{Theoretical} = \chi_{NMC}(\rho_{NMC}) + \chi_{CarbonBlack}(\rho_{CarbonBlack}) + \chi_{Polymer}(\rho_{Polymer}) \tag{33}$$

Where χ denotes the mass fraction of a component of the cathode.

2.13 Electrochemical testing

Half–coin cells were produced in an Ar-filled glovebox (MBraun, Germany), with H_2O and $O_2 \leq 0.1$ ppm. The coin cell type was aluminum CR 2032. Lithium chips of 11 mm (MTI Corporation) were used as the counter-electrodes Cell casings, spacers, springs, and separators were all dried in an 80 °C vacuum oven for 24 h before being taken into the glove box for battery assembly. Electrochemical testing of half coin cells was performed using a Maccor Series 4000 Automated Test System. For all cycles, cells were charged and discharged between 3.0 to 4.3 V, as this is within the voltage stability window for NMC 622 [35]. Each cell was charged and discharged at 0.05 C for 2 cycles to establish an SEI, then cycled 100 times at 1C. The slurries produced were either used to produce cathodes or for rheological or DLS measurements. The composition of cathode slurries are shown in Tables 7, and 8.

2.14 Differential capacity

During galvanostatic cycling, a cell's total charge, as well as the current and voltage, is recorded. The differential capacity of a cell is not a technique per se, but a manipulation of data. The differential capacity is given as dQ/dV, and is plotted against the cell voltage. dQ/dV plots provide information on phase transitions of the cathode active material, and where phases reach equilibria with each other. dQ/dV plots are also used to study degradation in the electrode [51].

Lists of cathodes made are shown for: Chapter 4 (Table 12), solids loading controlled cathodes in Chapter 5 (Table 13) and viscosity controlled cathodes in Chapter 5 (Table 14). The masses, thicknesses and porosities are shown.

Table 12: Mass, thickness and porosity of cathodes made for Chapter 4

Sample	Cathode Mass (mg)	Cathode Thickness (um)	ϵ (%)
PVDF	8.5	37	42
F68	10.3	50	17
CMC	11.7	92	26
PVP	8	64	54
Chitosan	4.7	36	55
Na Alginate	3.3	22	53
PEO	10.6	66	46

Table 13: Mass, thickness and porosity of solids loading controlled cathodes for Chapter 5.

Sample	Cathode Mass (mg)	Cathode Thickness (μ m)	ϵ (%)
F68	8.48	33	7
F68	4.25	37	58
F68	7.6	32	14
F68	7.6	35	21
PEO 10	16.35	96	38
PEO 10	20.5	84	12
PEO 10	21	85	11
PEO 10	18	80	19
PEO 10	11.74	80	47
PEO 25	7.96	48	40
PEO 25	6.37	42	45
PEO 25	6	44	51
PEO 25	4.39	51	69
PEO 40	5.91	111	81
PEO 40	23.5	112	24
PEO 50	7.96	113	56
PEO 50	2.57	40	86
PEO 50	7.41	41	59
PEO 75	4.07	35	78
PEO 75	4.67	42	74
PEO 100	1.3	28	93
PEO 100	3.79	28	79

Table 14: Mass, thickness and porosity of viscosity controlled cathodes for Chapter 5.

Sample	Cathode Mass (mg)	Cathode Thickness (μ m)	ϵ (%)
PEO 25	7.96	48	40
PEO 25	6.37	42	45
PEO 25	6	44	51
PEO 25	4.39	51	69
PEO 40	5.15	27	31
PEO 40	5.56	32	37
PEO 50	7.29	43	39
PEO 50	8.29	36	17
PEO 50	8.5	39	21
PEO 75	2.11	14	46
PEO 75	6.88	35	29
PEO 100	3.02	19	43
PEO 100	3.65	23	43

2.15 Electrochemical Impedance Spectroscopy

Electrochemical Impedance Spectroscopy (EIS) is a technique used to study electrochemical materials or systems. EIS is frequently employed to study batteries or half-cells. The technique is straightforward to perform, is *in situ*, and is non-destructive. However, interpreting data can be very challenging, as in the case of batteries, they consist of different components (see Fig. 30), which have different electrochemical properties, therefore making data difficult to parse.

Ohm's law is used to describe the resistance (R) of a material to the flow of electrical current. Ohm's law is given as:

$$R = \frac{V}{I} \tag{34}$$

Where V is the voltage and I is the current.

Whilst this law is well known, it only applies to one type of circuit element, an ideal resistor. Ideal resistors are limited by the following: they will obey Ohm's Law at all current and voltage levels, the R value is independent of frequency, and AC current and voltage signals through a resistor are in phase. Circuit elements are more complex than can be described by Ohm's law, so resistance is replaced with impedance, Z. Impedance is also a measure of the resistance of a material to the flow of electrical current, but is

not limited by the aforementioned factors [159] In EIS, a current or voltage is applied to a system. The voltage, (V), varies sinusoidally with time (t), and can be represented by Equation 35:

$$V = V_0 \sin(\omega t) \tag{35}$$

where V_0 is the amplitude signal and ω is the radial frequency (radians/second), which is calculated from frequency f (Hz) using Equation 36:

$$\omega = 2\pi f \tag{36}$$

In an impure resistive linear system, the current response (I) is a sinusoid at the same frequency but shifted in phase (ϕ), and has a different amplitude (I_0):

$$I = I_0(\sin \omega t - \phi) \tag{37}$$

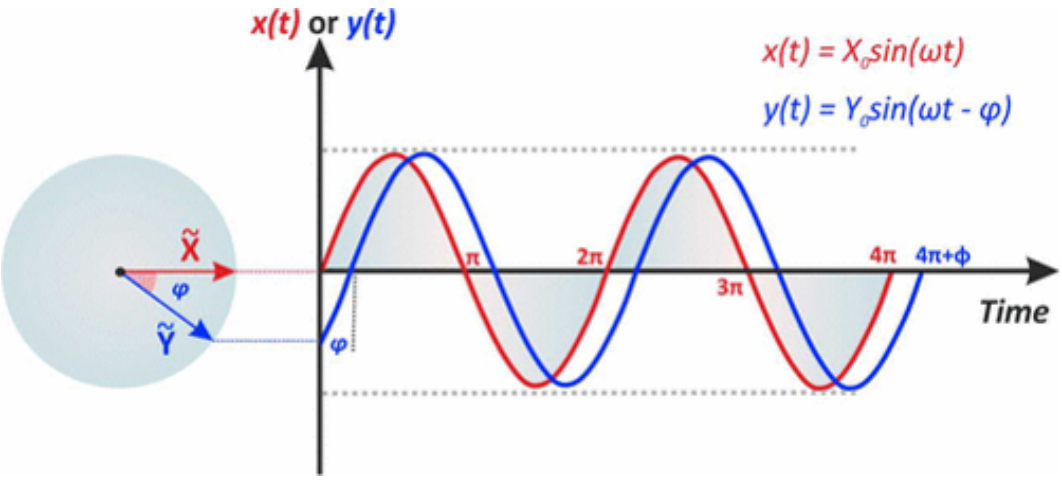

Figure 31: Relationship between the sinusoidal AC voltage signal and current response [160].

The overall impedance (Z) is therefore calculated as:

$$Z = \frac{V}{I} = \frac{V_0 sin(\omega t)}{I_0(sin\omega t - \phi)} = Z_0 \frac{sin(\omega t)}{sin(\omega t) - \phi} \tag{38}$$

With Euler's relationship, impedance can be expressed as a complex function. Euler's relationship is:

$$e^{jwt} = cos(\omega t) + jsin(\omega t) \tag{39}$$

Where j = -1

Equation 38 can be re-written as:

$$Z^* = \frac{V}{I} = \frac{V_0 sin(\omega t)}{I_0(sin\omega t - \phi)} = Z_0 \frac{sin(\omega t)}{sin(\omega t) - \phi} \tag{40}$$

The impedance is a frequency-dependent complex number characterized by the ratio of voltage to current and the phase angle shift (ϕ) between them:

$$Z = \frac{V}{I} = Z_0 e^{j\phi} = Z_0[cos(\phi) + j(sin(\phi)] = Z' + jZ" \tag{41}$$

EIS data is typically presented using complex plane plots such as Nyquist plots. Here, the imaginary reactive *Z"* component is plotted against the real resistive *Z'* component. The semicircle shown at lower impedances is for higher frequencies, representing the faster processes in the battery, i.e. metal ion diffusion in the liquid electrolyte. The spike at higher impedances and at lower frequencies is for slower processes, i.e. solid state ion diffusion in the electrode. An example of a Nyquist plot is shown below in Fig. 32.

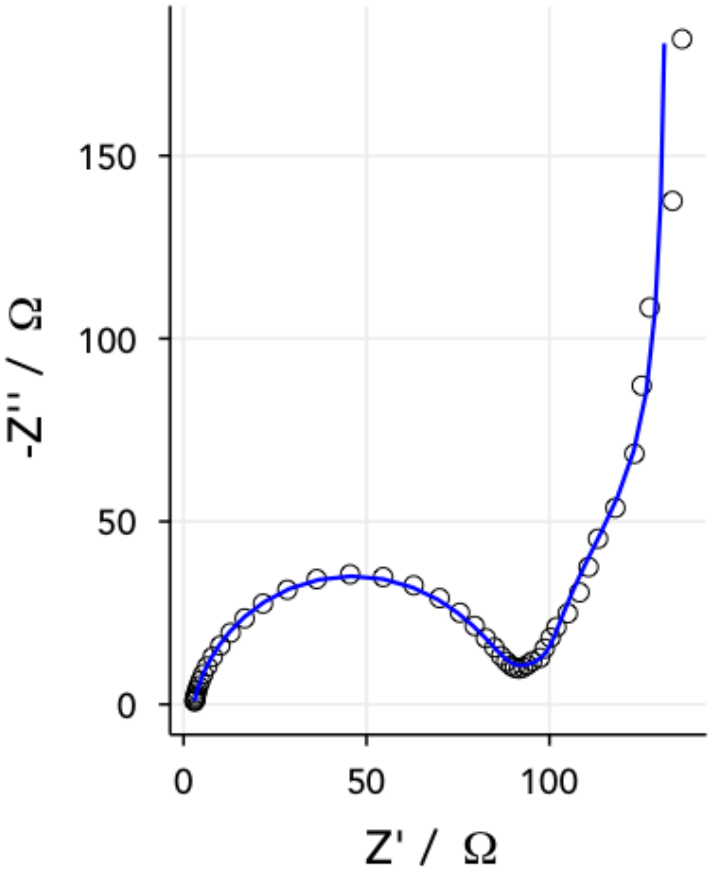

Figure 32: Example of a Nyquist plot showing EIS data [161].

2.15.1 EIS Procedures

EIS sweeps were performed on coin cells produced in the previous step, with a voltage of 10 mV and an alternating current (AC) frequency range of 0.01 to 100000 HZ. This step used the EIS channels on the Maccor Series 4000 Automated Test System.

3 Chapter 3: Effect of polymer concentration on Li-ion cathode slurry microstructure using PEO as an aqueous binder

3.1 Introduction

The manufacture of Li-ion electrodes involves mixing the cathode active material, conductive additive, and polymer binder with a solvent to form a slurry, which is coated and dried becoming a solid film. Optimizing the formulation and processing of battery electrodes is important as both affect the dispersion of the active material and conductive additive in the slurry, which in turn affect the electrochemical performance of the cathode [70, 134, 135, 143]. An ideal slurry will have a sufficiently high viscosity at low shear to prevent sedimentation of solids, yet should have a low viscosity at high shear, resulting in a slurry that can spread onto the current collector as well as achieving a uniform particle dispersion throughout the electrode [70].

Moving to aqueous processing requires water-soluble binders which have a dual role as a binder and a dispersant to hydrophobic carbon black. Whilst CMC is the most commonly studied aqueous binder for LIB cathodes in literature, it often underperforms compared to cathodes prepared conventionally using NMP and PVDF [89]. PEO has been studied extensively as a cathode binder for non-aqueous processed cathodes [10, 96,155]. PEO is soluble in water, cheap, and commercially available, and being ionically conductive it is ideal for facilitating Li-ion transport throughout the electrode [10, 99, 155]. PEO also has a strong affinity to carbon black; a study by Guy *et.al.* demonstrated the adsorption of PEO on the carbon black surface, resulting in uniform slurries [162]. Subsequent cathodes containing $Li_{1.1}V_3O_8$ were able to cycle.

In this chapter, two commercially available high molecular weights of PEO were investigated as aqueous cathode binders for high Ni NMC 622 cathodes. DLS measurements were used to verify dissolution in DI H_2O of the PEO types. Slurries consisting of all components as well as single-solid slurries carbon black/PEO/H_2O and NMC/PEO/H_2O have been prepared to determine the effect of NMC, carbon black, and polymer on slurry microstructure. Rheology has been used to characterize the microstructure of cathode slurries, namely steady-state to assess slurries under shear, and frequency sweeps to evaluate their viscoelastic behavior. Two-point probe conductivity

measurements were taken to study the slurry microstructure further. Finally, electrochemical measurements were taken using half-coin cells to evaluate the performance of aqueous processed cathodes using PEO as a binder compared to those prepared with NMP/PVDF. It was found that the concentration of polymer affects the mechanical and electronic properties of the cathode slurry, allowing the microstructure of the cathode to be tuned.

3.2 Results & Discussion

To evaluate the influence of PEO on slurry microstructure and flow properties, polymer solutions and slurries were prepared with PEO content ranging from 0.25 to 5 wt%. A list of samples and their compositions are shown in Table 6 for PEO-containing slurries. For each name of the sample given, two samples were made, one with 1000 kg mol^{-1} PEO, and one with 2000 kg mol^{-1} PEO.

3.2.1 PEO Radius of Gyration

To determine the solubility of the PEO polymers in water, DLS measurements were taken. From this, The hydrodynamic radii for PEO solutions with molecular weights of 1000 kg mol^{-1} and 2000 kg mol^{-1} were determined. The radius of gyration (R_g) was calculated from the hydrodynamic radius of each polymer using $R_g \approx R_h/0.7$. The experimentally determined values of R_g are similar to the predicted values. The DLS data of a single peak are consistent with a dissolved polymer [95]. Intensity vs particle diameter curves are shown in Fig. 33. All solutions were clear when produced. The calculated values of $[\eta]$, R_g, no of polymer coils and c* are summarised in Table 15. The viscosity of deionized water used to calculate $[\eta]$ is 1 mPas at 25 °C. The overlap concentration is determined by Equation 26 as 4.9E-3 mg/ml for 1000 kg mol^{-1} and 7E-3 mg/ml for 2000 kg mol^{-1}, meaning samples containing 0.25 and 0.5 wt% PEO for 1000 kg mol^{-1} are below c*. All samples for 2000 kg mol^{-1} are above c*, meaning that they are entangled.

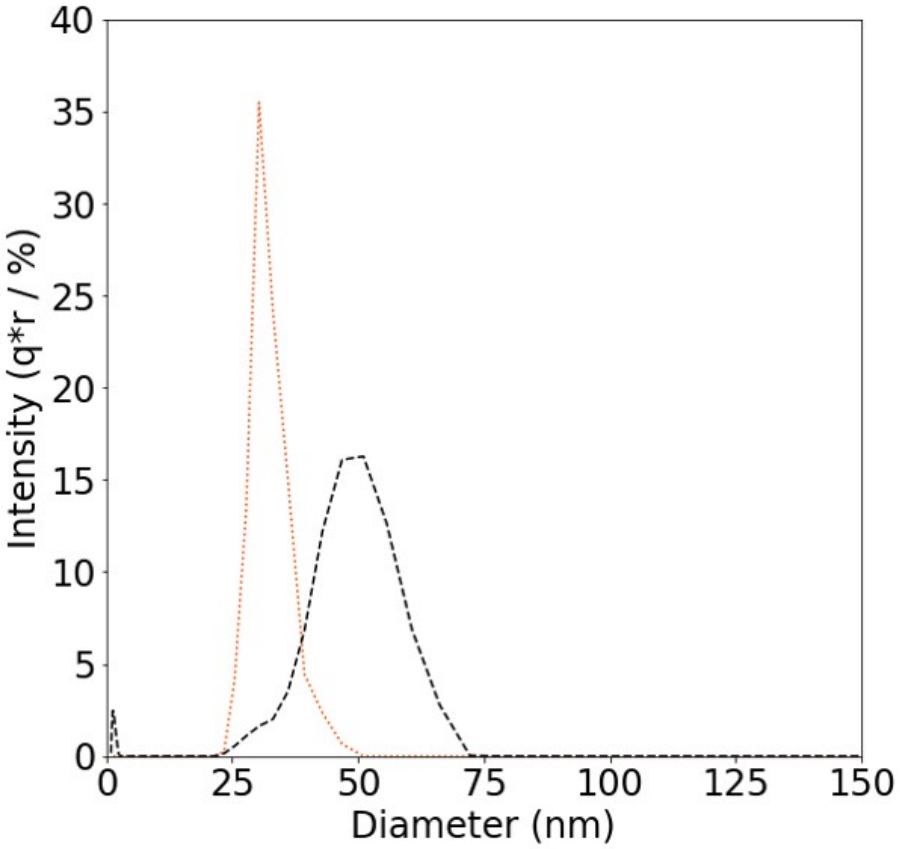

Figure 33: DLS for PEO solns 1000 kg mol^{-1} ($\cdots$), and 2000 kg mol^{-1} ($- - -$)

Quantity	1000 kg mol^{-1}	2000 kg mol^{-1}
$[\eta]$ (m Pa s)	293.4	2082.5
R_g (nm) (Theoretical)	41	52
R_g (nm) (Experimental)	37	52
c* (mg/ml)	4.94x10^{-3}	6.96x10^{-4}

Table 15: R_g and calculated number of polymer coils per PEO type

3.2.2 PEO solutions steady state rheometry

The effect of PEO concentration on the viscosity of the stock polymer solutions is characterized using rotational viscometry. Fig. 34 shows viscosity flow curves for 1000 kg mol^{-1} solutions of PEO; flow curves for 2000 kg mol^{-1} solutions are found in the appendix. Higher PEO concentrations show a low shear plateau and then exhibit shear-thinning behavior. At zero-shear, the polymer chains are entangled, whilst applying increasing shear causes polymer chain disentanglement, which decreases the viscosity. The lowest PEO concentrations show more Newtonian behavior, where viscosity does not change with shear rate, as at these concentrations, there is less entanglement between polymer chains, providing less resistance to shear.

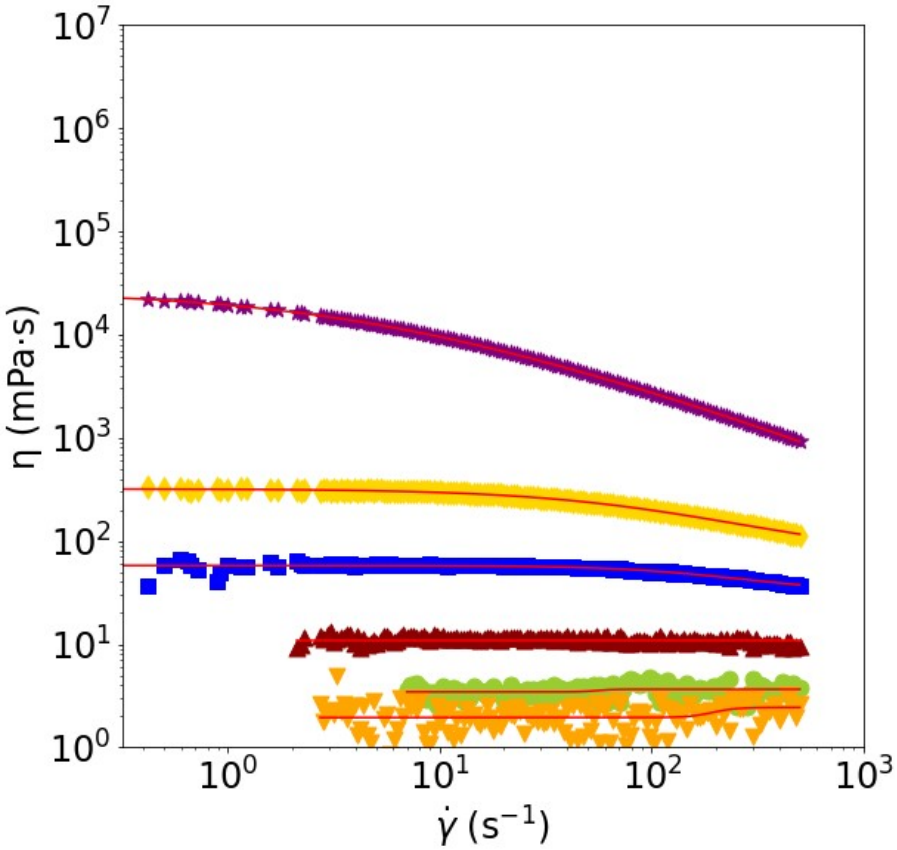

Figure 34: Flow curves for 1000 kg mol^{-1} PEO/H_2O fitted with the Cross Model, for 0.25 wt % (●), 0.5 wt % (▼), 1 wt % (▲), 2 wt % (■), 3 wt % (♦), 5 wt % (★). Red lines indicate fits with the Cross model.

The Cross equation (Equation 23) was used to fit flow curve data from a shear rate of $0.01 \leq 500\dot{\gamma}^{-1}$. There is a power law relationship between η_0 and PEO wt %, which

is expected based on literature [95]. Fig. 35 shows zero shear viscosities for PEO/H_2O solutions of 1000 kg mol^{-1} and 2000 kg mol^{-1} as a function of increasing concentration. For all concentrations, the zero shear viscosities for 2000 kg mol^{-1} samples are higher than those for the 1000 kg mol^{-1} samples. Plots of η_0 against polymer concentrations show a power law relationship; from this, the intrinsic viscosities ($[\eta]$) of the polymers are obtained.

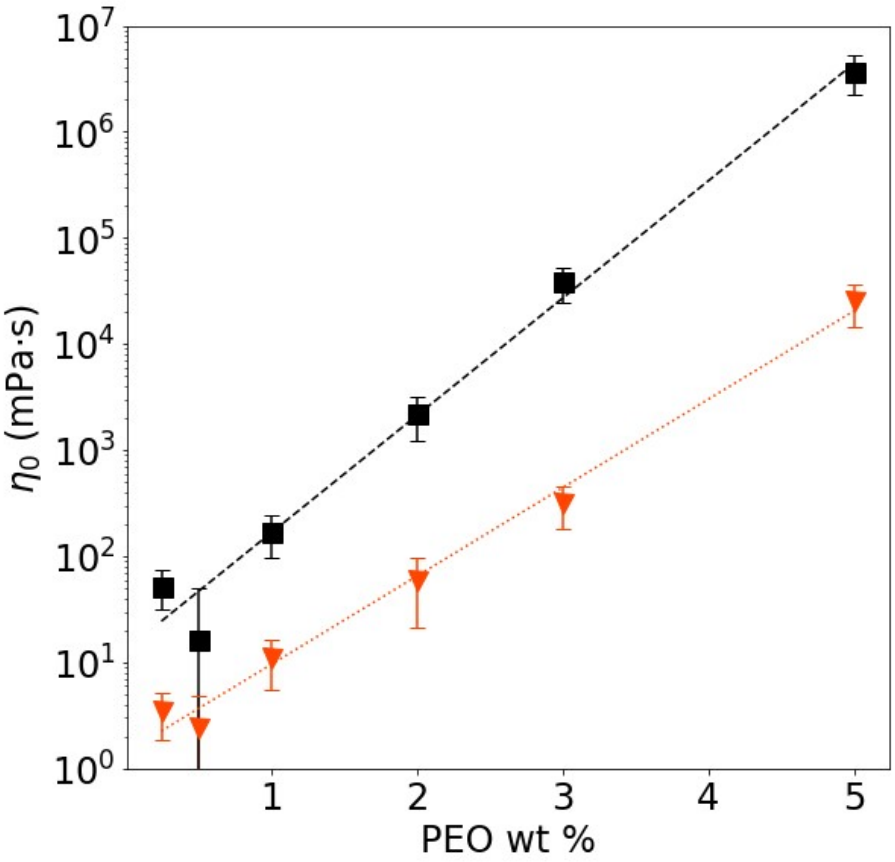

Figure 35: Power law fits of η_0 for PEO 1000 kg mol^{-1} (▼) and 2000 kg mol^{-1} (■). Error bars are the standard deviation of three repeats.

3.2.3 Full cathode slurry characterization

It was hypothesized that increasing the polymer concentration would result in stronger mechanical and electronic properties in cathodes, so steady-state rheological tests were performed on full cathode slurries. Fig. 36(a) shows the variation of viscosity with the shear rate at various concentrations of 1000 kg mol^{-1} PEO as the binder. The effect of PEO wt% was plotted against the viscosity at a shear rate of 10 s^{-1} (η_{10}),

as this shear rate corresponds to one used during slurry coating. Unlike the polymer solutions; neither the Cross model nor the Herschel-Bulkley model was used due to noisy data at low shear. Initially, slurries have a 3D network structure comprised of weakly interconnected carbon black flocs, meaning they have a yield stress. When the shear rate is low, the applied stresses are insufficient to break the 3D network structure due to strong particle interactions. Eventually, the shear rate provides enough energy to break apart the network structure into flocs. At this point, the structure of the slurry changes from more solid-like to liquid-like, where it exhibits non-Newtonian shear-thinning behavior. As the shear rate further increases, hydrodynamic forces dominate, so the particles become aligned with the direction of shear flow, which decreases the viscosity of the suspension. An increasing trend of η_{10} against polymer weight percent is seen in the full slurries (Fig. 37 (b)), which can be attributed to polymer chain entanglements [134]. Slurries made with 0.25 and 0.5 wt% PEO were not mixed well and were seen to settle. This could result from low viscosity of the polymer solution, allowing carbon black to form large agglomerates easily.

The conductivities of full slurries against polymer wt% for both molecular weights are shown in Fig. 37 (c). The 1000 kg mol^{-1} slurries show an S-shaped percolation curve against PEO wt%, with the percolation threshold between 0.5 and 1 wt% of PEO. As discussed, samples containing 0.25 and 0.5 wt% PEO for 1000 kg mol^{-1} are below c*, suggesting that polymer entanglement is necessary to enable the formation of 3D networks of carbon black in aqueous media. Literature usually reports the presence of a percolation curve arising from varying the carbon black content [51, 57, 155], however, this data shows that the polymer content can also result in carbon black percolation. The carbon black wt% is kept constant across the series at 0.5 wt%, and the volume fraction is 6%, meaning there is enough carbon black to percolate. Fig 37 (d) shows an initial increase in conductivity as a function of η_{10}, before decreasing slightly, which is likely due to an excess of polymer in the slurry, which could disrupt electron transfer [104]. Percolated network structures of carbon black are likely facilitated by PEO forming bridges between carbon black flocs, which arise in the case of polymer adsorption onto carbon black [155]. Studies have shown that PEO has a strong affinity for carbon black [155]. Even though PEO is electronically insulating, studies have suggested that the conductivity of these types of slurries is due to electron tunneling [51, 58]. This data supports the hypothesis that the percolation of carbon black in this system is controlled by the concentration of polymer.

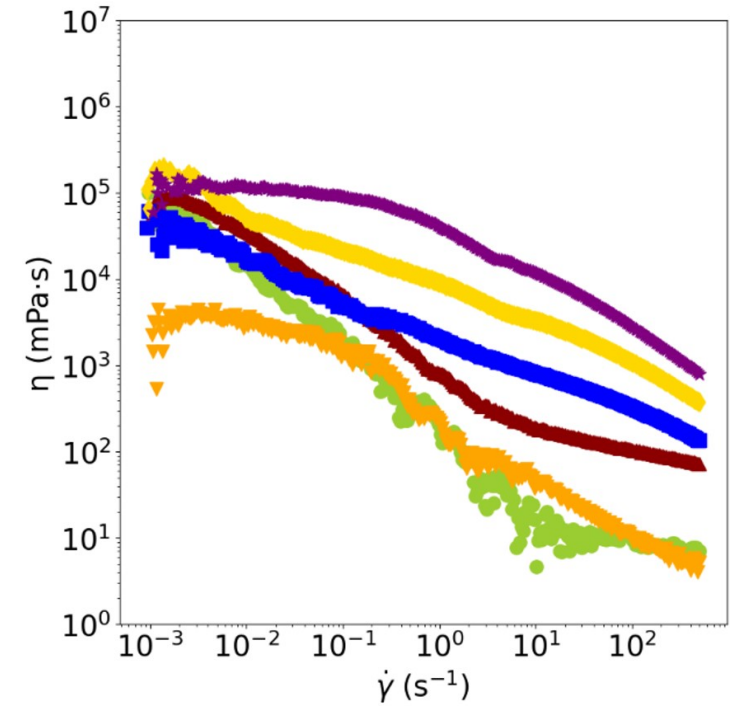

(a)

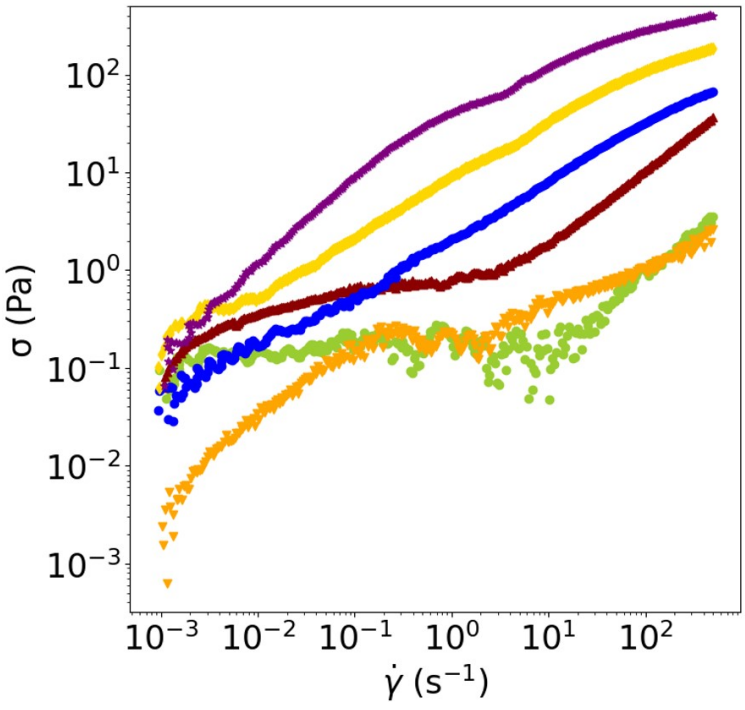

(b)

Figure 36: Flow curves for full cathode slurries (NMC/carbon black/PEO/H_2O) using 1000 kg mol^{-1} PEO as the binder, showing (a) Viscosity and (b) Shear Stress, for for 0.25 wt % (●), 0.5 wt % (▼), 1 wt % (▲), 2 wt % (■), 3 wt % (♦), 5 wt % (★).

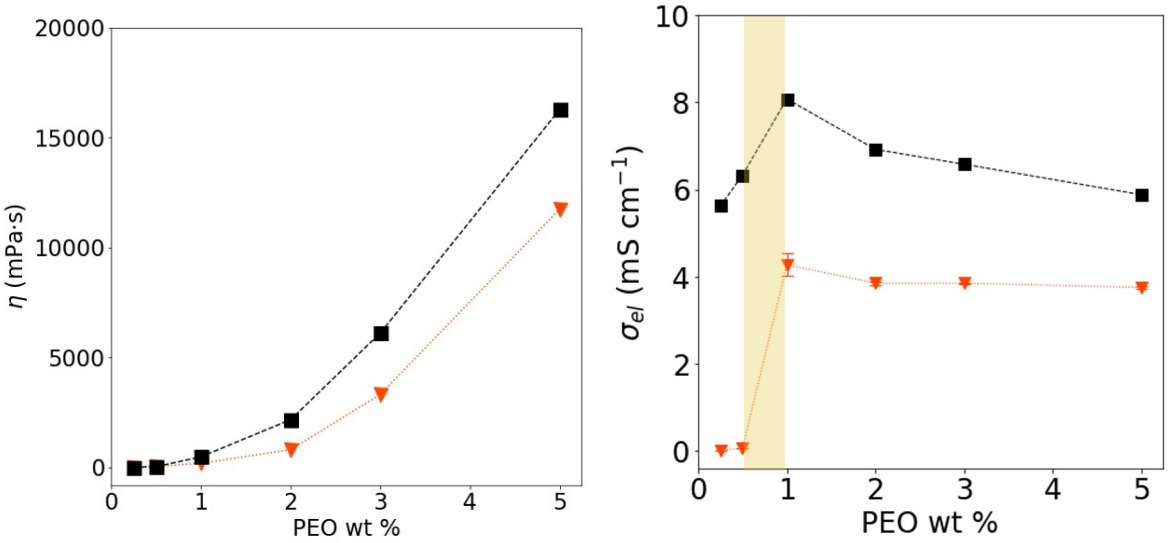

(a)

(b)

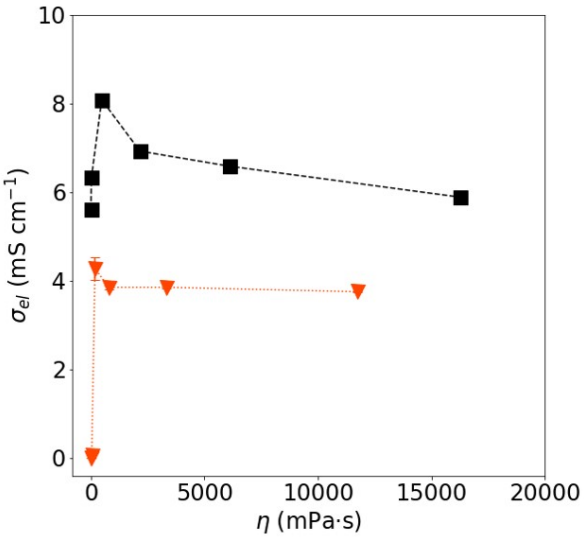

(c)

Figure 37: Full cathode slurries (NMC/carbon black/PEO/H_2O) showing (a) Viscosity at 10 s^{-1} (η_{10}) as a function of PEO wt %, (b) Conductivity (σ_{el}) as a function of PEO wt %, and (c) σ_{el} as a function of η_{10} (1000 kg mol^{-1}(▼), 2000 kg mol^{-1} (■)). Lines are a guide for the eye. The shaded yellow in (b) denotes the percolation threshold. Error bars for conductivity data are the standard deviation of three measurements.

3.2.4 Single solid slurries characterisation

The contributions of the solids present in a cathode slurry, i.e. NMC 622 and carbon black, were investigated. The solids loading was kept constant in either case (see Table 6). Flow curves showing shear stress for slurries comprised of carbon black/PEO/H_2O are shown in Fig. 38 a and b. Slurries were initially fitted with Equation 24, the Herschel-Bulkley model, yet the high shear region was found to dominate the fits for 1000 kg mol^{-1} 3 wt% and 2000 kg kg mol^{-1} 3 and 5 wt%. So these fits were weighted towards lower shear. The fitting procedure is shown in the appendix. Fig. 38 c and d show the effect of PEO concentration on the yield stress of single solid slurries. For 1000 kg mol^{-1} slurries, the addition of carbon black has a negligible effect on yield stress (σ_0) until 5 wt%, then a significant increase of σ_0 is seen. This is contrary to the expectation that yield stress would increase monotonically with polymer concentration. For 2000 kg mol^{-1} slurries, the addition of carbon black shows a non-monotonic relationship, as σ_0 increases until 3 wt% PEO, then a decrease at 5 wt%. The initial increase in yield stress can be explained by the increased concentration of PEO, which results in a higher viscosity of the polymer solution, leading to greater polymer chain entanglement. When a threshold of polymer concentration is exceeded, the excess polymer occupies more space between carbon black flocs, leading to a weaker 3D network, thus lowering the yield stress beyond 3 wt% PEO for 2000 kg mol^{-1}. The excess viscosity could prevent the weak networks of carbon black from forming. The data implies that the polymer concentration does not predict the yield stress well. Though the carbon black is said to form 3D networks within the slurry, they are also said to be weakly percolated [70, 72, 75, 130, 134, 140]. Even though networks of carbon black could be forming, they may require a low force to disrupt the structures and cause flow, hence the similar yield stresses for the 1000 kg mol^{-1} series at 3 wt% and below.

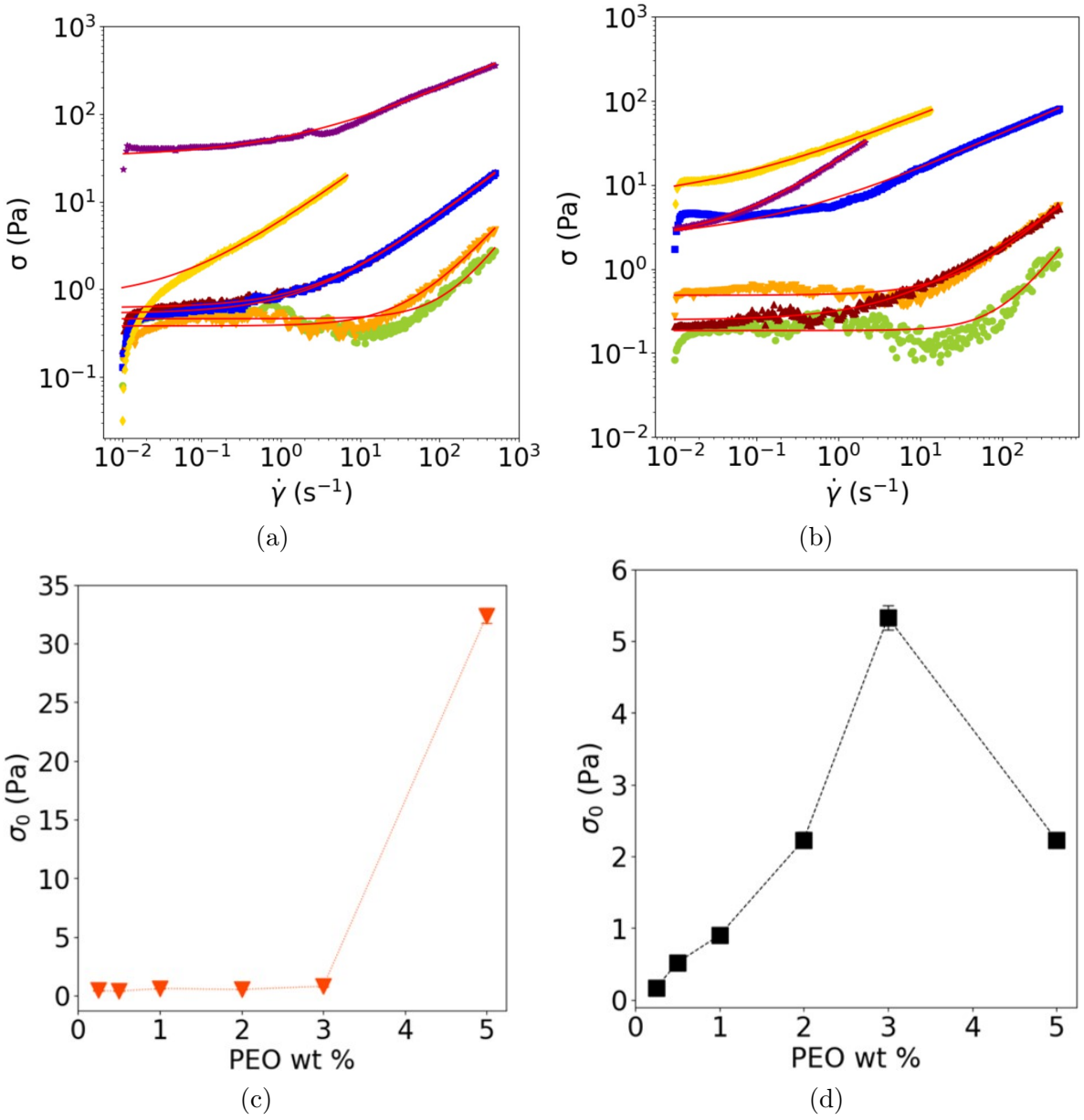

Figure 38: Flow curves of yield stress against shear rate for carbon black/PEO/H_2O using (a) 1000 kg mol^{-1} and (b) 1000 kg mol^{-1} for 0.25 wt% (●), 0.5 wt % (▼), 1 wt % (▲), 2 wt % (■), 3 wt % (♦), 5 wt % (★), and PEO wt% vs σ_0 for (c) 1000 kg mol^{-1} (▼) and (d) 2000 kg mol^{-1} (■). Herschel-Bulkley fits are shown as red lines.

Carbon black is known to flocculate into a fractal network that resists deformation until a large enough shear force is applied, breaking up the network structure into flocs. In Fig. 39a, conductivity shows a monotonic increase as a function of both polymer wt% for both molecular weights of PEO. Like the full slurries in section 3.2.3, it appears that the increased polymer entanglement aids the formation of carbon black networks. However, there is no percolation threshold in this series, likely due to the absence of large active material particles, which may prevent carbon black networks from forming at low polymer concentration. The relationship between PEO concentration and yield stress is shown in Fig. 39b and c. For 1000 kg mol^{-1} slurries, the correlation between electronic conductivity and yield stress is not strong enough to suggest a causal relationship. Whereas, for 2000 kg mol^{-1} slurries, an increase in conductivity with yield stress is seen. Yield stress does not predict the conductivity of slurries made with 1000 kg mol^{-1} PEO well, likely as the conductivity is determined by weakly connected flocs of carbon black, meaning that for most slurries, a low force is needed to break apart these networks.

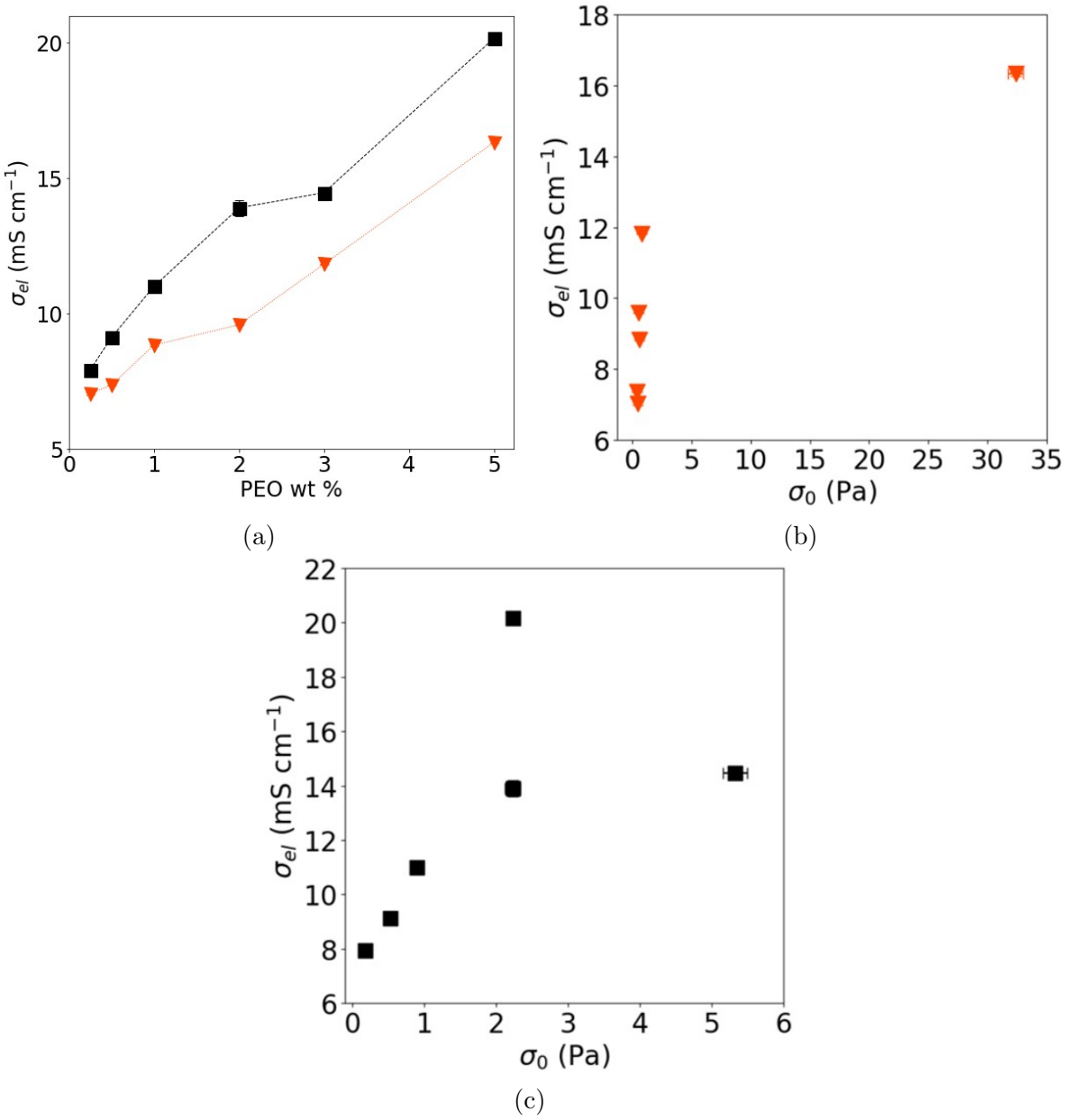

Figure 39: (a) σ_{el} vs PEO wt %, (b) σ_{el} vs PEO wt %, and (c) σ_{el} vs σ_0 for 1000 kg mol^{-1} (▼) and (d) 2000 kg mol^{-1} (■). Lines are a guide for the eye. Error bars for conductivity are the standard deviation of three measurements.

As the yield stress is not very predictable by the polymer concentration for carbon black slurries, the viscosity at a shear rate of 10 s^{-1} was used as a predictor of slurry properties, as shown in Fig. 40. Flow curves are shown in the Appendix - section 8.1.4. For both molecular weights, the viscosity increases monotonically with PEO concentration as shown in Fig. 40a. For 1000 kg mol^{-1} PEO, the viscosity is very low

and a significant increase is shown from 2 wt% PEO, whereas for 2000 kg mol^{-1} PEO, this increase occurs beyond 1 wt%. The trend of increasing viscosity with polymer concentration is expected, as this is seen with the full cathode slurries in section 3.2.3. The increased polymer concentration leads to more polymer entanglements, therefore increasing the viscosity. The viscosity at 10 s^{-1} is also shown to predict the conductivity of the slurry as shown in Fig. 40b. For both types of PEO, the conductivity increases sharply at low viscosity, before a less sharp increase at higher viscosities.

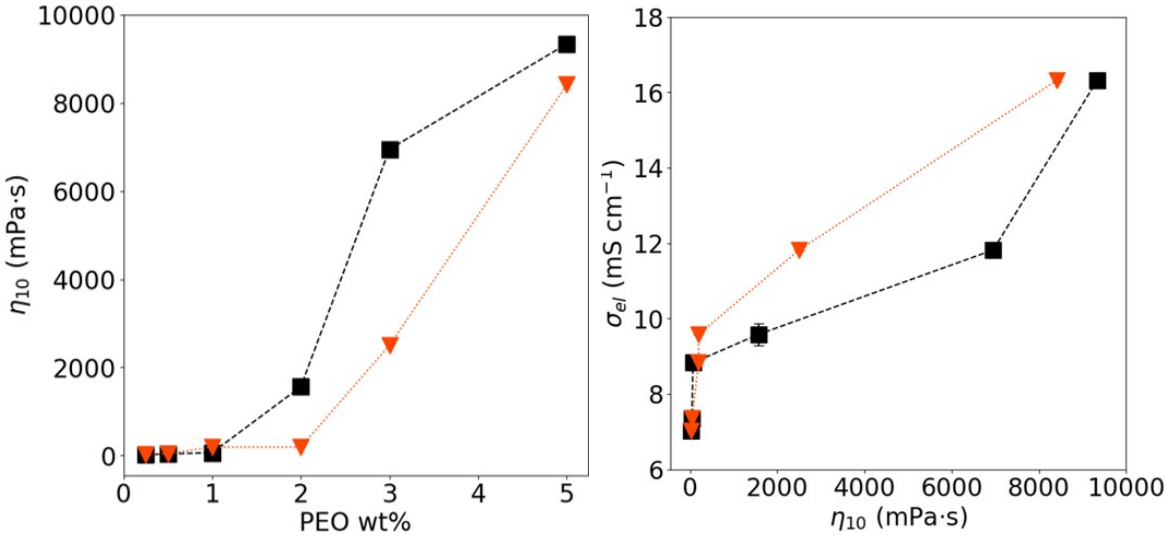

(a) (b)

Figure 40: $\eta_1 0$ vs (a) PEO wt % and (b) σ_{el}. Lines are a guide for the eye. Errors for σ_{el} are the standard deviation of three measurements.

To further visualize the effects of polymer concentration on carbon black slurry microstructure, the tangent of the phase loss angle is shown in Fig. 41. Above a tan δ value of 1, the system shows plastic "liquid-like" behavior; below this value, the system shows elastic "solid-like" behavior. The tan δ values for the 1000 kg mol^{-1} slurry at 0.5 wt% is above 1 until 10 rads s^{-1}, before dropping below 1 due to particle jamming at high frequencies. The 1000 kg mol^{-1} at 2 and 5 wt% polymer show tan δ below 1 at all frequencies, so these two slurries show more elastic properties. The 2000 kg mol^{-1} slurries at 0.25, 0.5 and 1 wt% also show tan δ below 1 at frequencies below 10 rads s^{-1} then above 1 between 0 and 100 rads s^{-1}, whereas the 2, 3 and 5 wt% samples have tan δ values below 1 at all frequencies. Overall, the data shows that increasing the polymer content increases the solid-like gel behaviour of cathode slurries.

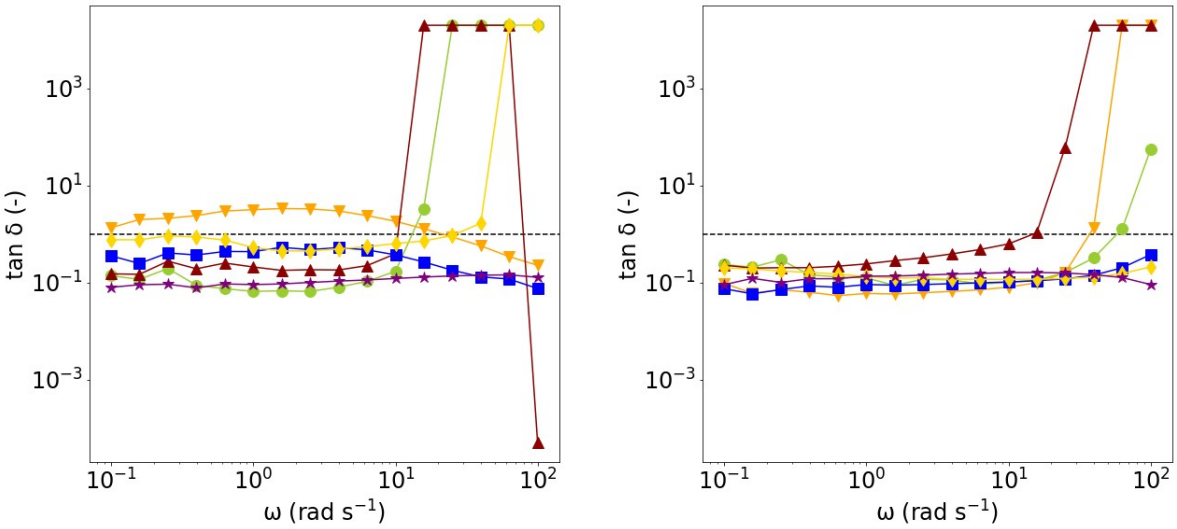

(a) (b)

Figure 41: Loss tangent for carbon black slurries made with 1000 kg mol^{-1} (a) and 2000 kg mol^{-1} (b), for 0.25 wt % (●), 0.5 wt % (▼), 1 wt % (▲), 2 wt % (■), 3 wt % (♦), 5 wt % (★).

3.2.5 Contribution of different slurry components to microstructure

To determine the contribution of each component in the cathode slurry, steady-state flow curves from a representative cathode slurry, a CB/PEO/H_2O slurry, an NMC/PEO/H_2O slurry and a polymer solution (1000 kg mol^{-1}, 5 wt%) are shown in Fig. 42. The flow curves for the full slurry and the NMC/PEO slurry show the same shape as the curve for the polymer solution yet are an order of magnitude higher, owing to large active material particles [72]. The full slurry curve is near-identical to the NMC/PEO slurry. The CB/PEO slurry differs from the other three as there is a yield stress assosciated with a percolated carbon black network - see Fig. 37a.

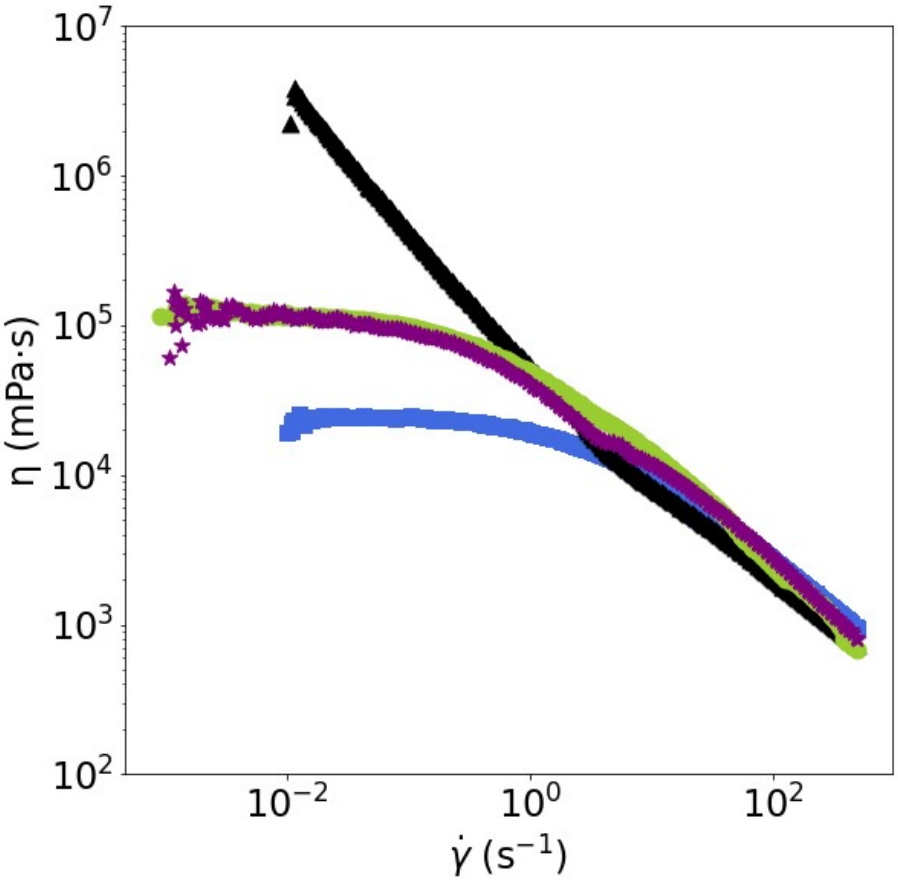

Figure 42: Flow curves for slurries made with 5 wt % solution 1000 kg mol^{-1} PEO, showing PEO solution (■), carbon black/PEO (▲), NMC/PEO (●), and NMC/carbon black/PEO (★).

The relative viscosities (η_{rel}) of carbon black were calculated using Equation. 25 for slurries containing 1000 kg mol^{-1} and 2000 kg mol^{-1} PEO as shown in Fig. 43. Relative viscosities were calculated at of 10 s^{-1}, as this shear rate corresponds to one used during slurry coating [163]. For the 1000 kg mol^{-1} slurries, there is a sharp decrease in (η_{rel}) as PEO content increases. Whereas for the 2000 kg mol^{-1} slurries, the relative viscosities drop after 1.35 wt%, then plateau. This indicates that as the viscosity of the polymer solution used in the slurry increases, the carbon black contributes less to slurry rheology, due to polymer entanglement which separates flocs of carbon black. The data indicates that the PEO contributes the most to the rheology of the cathode slurry. The greater contribution of the polymer for the rheology of aqueous slurries was also observed by Reynolds *et.al.* for anode slurries containing CMC as the binder, whereas they observed the dominant contribution of carbon black for NMP/PVDF slurries [70]. The reason for the dominant contribution of polymer in aqueous slurries over carbon black is the fact that carbon black is hydrophobic and does not disperse in water even under high-shear mixing, indicating that dispersing the carbon black requires a soluble polymer that also binds to it.

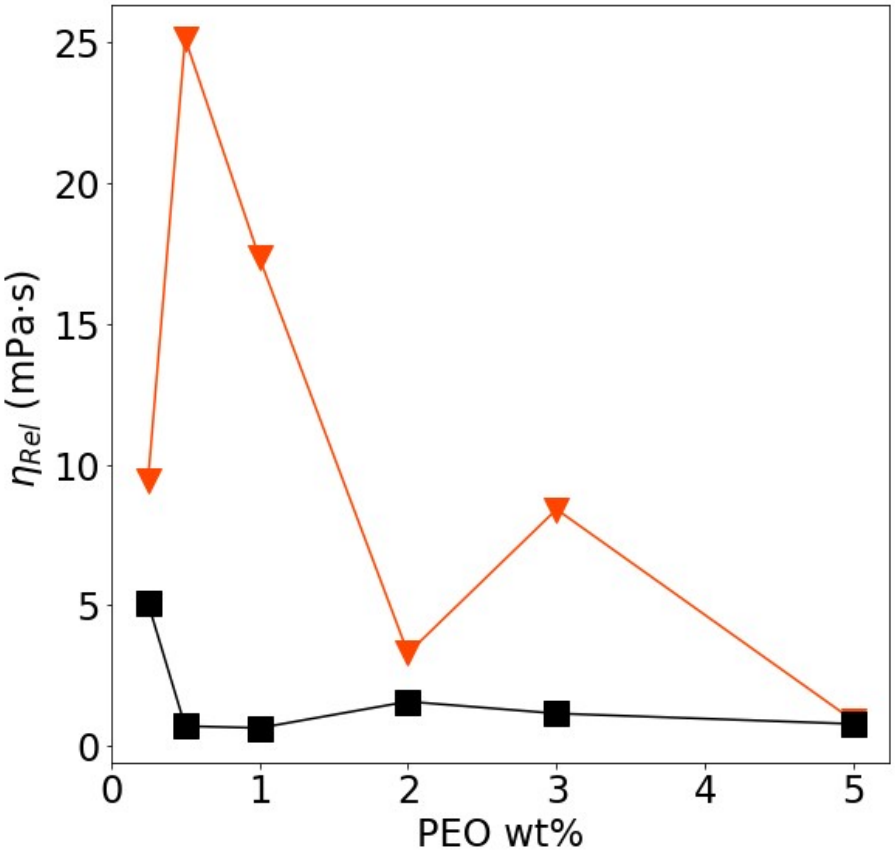

Figure 43: Relative viscosity of carbon black for slurries containing 1000 kg mol^{-1} and 2000 kg mol^{-1} PEO at a shear rate of 10 s^{-1}, for 1000 kg mol^{-1}(▼) and 2000 kg mol^{-1}(■).

The effect of polymer concentration on slurry properties, i.e., rheological and conductivity, implies that aqueous polymers drive the formation of carbon black networks. Fig. 44 illustrates the predicted cathode slurry microstructures from the addition of (i) not enough polymer to form a 3D network, i.e., below 1 wt% PEO in the slurry, and (ii) enough polymer for the formation of a 3D network, i.e., 1 wt% and above. In (i), the carbon network is non-existant, whereas in (ii), 3D networks are present. The slurry conductivity data in Fig. 37 b supports this, as all slurries made with 2000 kg mol^{-1} have conductivities of at least 7 mS cm^{-1}, whereas the two 1000 kg mol^{-1} slurries with 0.25 and 0.5 wt% PEO show little conductivity. The loss tangent data in Fig. 41 indicates solid network formation with increasing polymer content for carbon black slurries. The proposed slurry microstructures are consistent with those proposed in literature [71, 135, 143]. Increasing the concentration of polymer results in an in-

crease in yield stress and infinite shear viscosity, attributed to the polymer forming bridging interactions between carbon black flocs [135]. Whilst most studies ascribe this phenomenon to NMP-processed slurries, it is important for aqueous slurries given that carbon black does not disperse in water. Thus the polymer has an additional role as a dispersant for the conductive additive in aqueous slurries, via electrostatic repulsion forces [70, 129, 138, 164, 165].

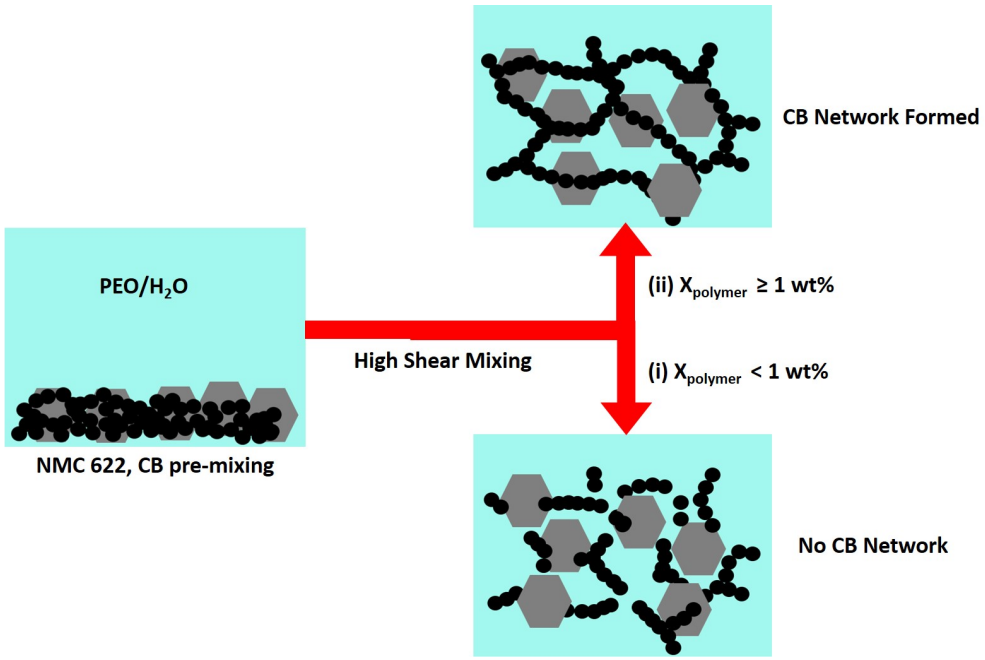

Figure 44: Structural formation of NMC/CB/PEO/H_2O slurries, with polymer concentrations which for CB/PEO/H_2O result in network formation (top) and no network formation (bottom).

3.2.6 Electrochemical Performance of PEO as a binder

To understand how PEO performs as a cathode binder, cathodes were fabricated, and half coin cells were assembled and cycled for two formation cycles at C/20, then 100 cycles at 1C. The ratio of materials for both aqueous and conventionally processed cathodes was 95% NMC 622, 3% carbon black and 2% polymer. Cathode slurries made with NMP/PVDF were prepared in the glovebox, as NMP is toxic, whereas aqueous PEO slurries were prepared outside the glovebox under a benchtop fumehood, as water should not be brought inside the glovebox to maintain a dry inert atmosphere. Only cathodes made with 1000 kg mol^{-1} PEO successfully cycled. Cycling stability data for 100 cycles at 1C for cathodes made with PEO and PVDF binders are shown in Fig. 45(a); these are from representative coin cells. For a cell to be considered "good", it had to achieve a suitable specific capacity, i.e., not higher than the theoretical specific capacity and not too low, and show little fluctuation and noise during cycling. The NMP/PVDF cathode has a 1st discharge capacity of 150 mAh g^{-1}, whereas the aqueous PEO cathode achieves only 81 mAh g^{-1}, a significant reduction in performance. The capacity retention of the PVDF cathode was 87 %, whilst the PEO cathode achieved 91.47 %. The charge/discharge curves for the 1st cycles at 1C for both PEO and PVDF are shown in Fig. 45(b). Both cells have an overpotential, which may result from insufficient crimping. The poor performance of PEO as a binder compared to PVDF has been observed by Guy *et.al.* despite PEO having strong interactions with carbon black [98]. Even though both the PEO and PVDF slurries appeared smooth, homogeneous and were of suitable coating viscosity, it is likely that the carbon black was not as well-distributed in the PEO cathode than the slurry appearance would suggest.

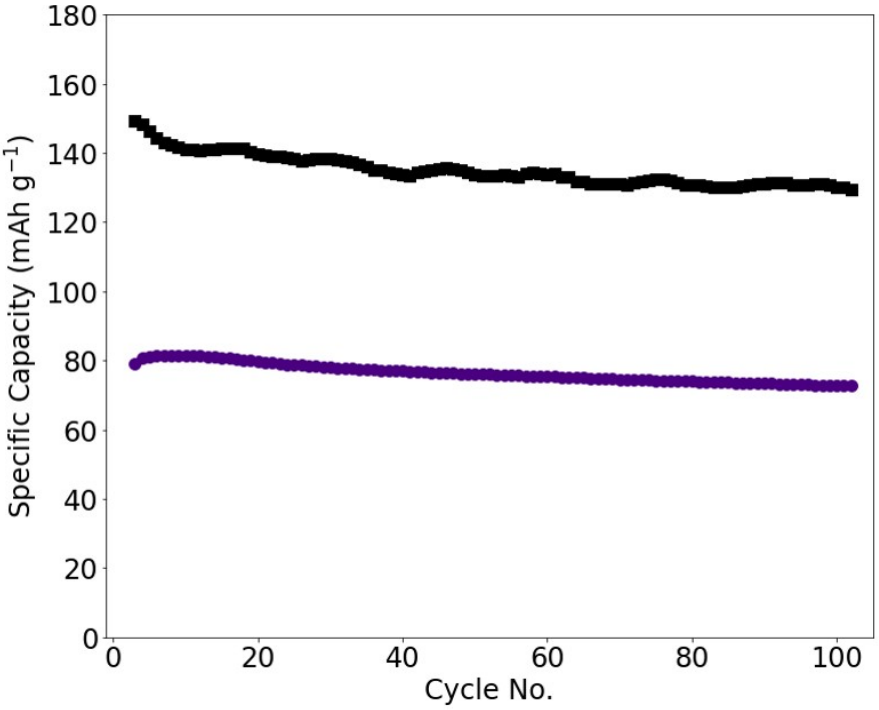

(a)

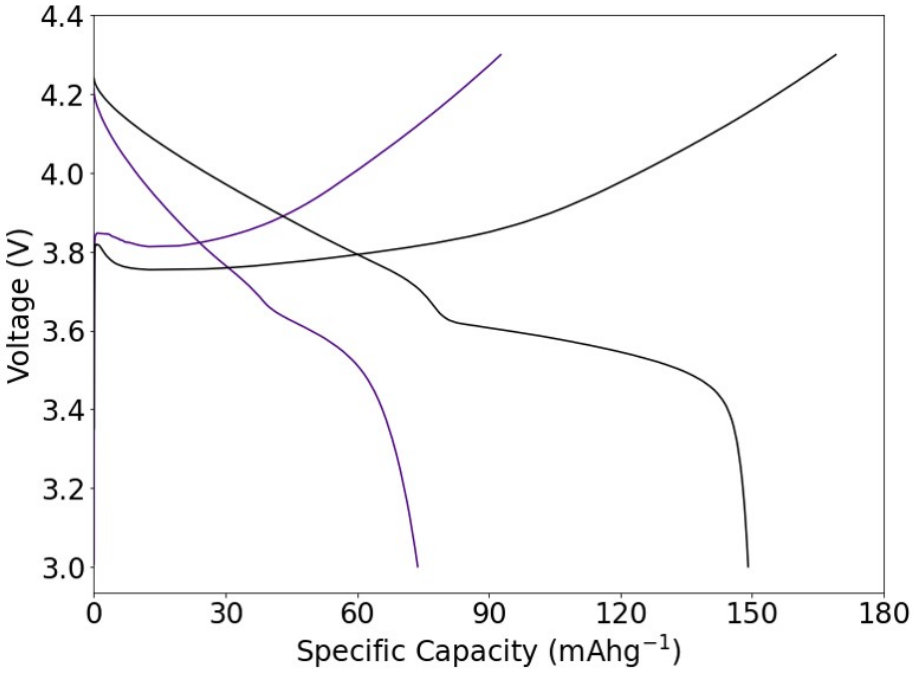

(b)

Figure 45: Cycling stability for 100 cycles at 1C for (a) PEO 1000 kg mol^{-1} (●) and PVDF (■) and (b) charge/discharge curves for the 1st cycle at 1C for PEO and PVDF. Data shown is for representative coin cells.

3.3 Conclusions

The impact of components used in aqueous cathode slurries on the slurry rheology has been assessed, and both the slurry rheology and conductivity is used to infer a microstructure within the slurry. Slurries consisting of carbon black/PEO/H_2O, NMC/PEO/H_2O and NMC/carbon black/PEO/H_2O with varying PEO M_w were produced and characterised using rheological techniques and conductivity. Half coin cells containing PEO as a binder were assembled, cycled and compared to a control containing NMP/PVDF.

- The concentration of binder drives the percolation of carbon black in aqueous slurries. The polymer content can therefore predict aspects of the slurry microstructure.
- For slurries where a yield stress is present, the yield stress does not scale with polymer concentration, nor does it predict slurry conductivity well. This could be due to the 3D networks of carbon black being weakly connected, requiring a low stress to cause flow. Slurry conductivity is therefore likely a result of the number and extent of carbon black networks, and not their strength.
- The conductivity does not change much for samples above a threshold concentration of polymer because the conduction pathway is not structurally changing. The slurry viscosity changes across these concentrations but new conductive pathways are not formed. The viscosities of slurries for different molecular weights and concentrations of PEO can now be quantitatively predicted, as long as the amount of carbon black and NMC is the same.
- The slurry behavior is a hybrid of the individual slurry behaviors, with the polymer contributing significantly to the slurry rheology. Severe agglomeration is speculated in samples with low polymer concentration. In the case of single solid slurries, carbon black forms weakly connected 3D networks, even at low polymer concentration. In the full slurries, the large active material particles may reduce the number of conductive networks, resulting in a percolation threshold. The compositions at which full cathode slurries are percolated correspond to gels in absence of active material, further alluding to the hypothesis that the polymer drives percolation.

- Half-coin cells containing PEO as the binder did not perform as well as PVDF. The 1st discharge capacities at 1C were 87 mAh g^{-1} for the cell containing PEO, and 150 mAh g^{-1} for PVDF. To pursue PEO as a cathode binder further, the introduction of surfactants into the slurry will be investigated.

4 Chapter 4: Effect of Chemical Affinity between Aqueous Polymers and Carbon Black on Electrochemical Performance of High Nickel Cathodes.

4.1 Introduction

As discussed in Chapter 1, several different aqueous polymers have been used as binders for Li-ion cathodes. The electrochemical performance of aqueous processed cathodes falls behind that of NMP/PVDF systems, therefore, selecting an ideal binder needs careful consideration. Though several different binders have been investigated, a systematic rationale for selecting a binder is lacking. It has been shown that the dispersion of carbon black in the dry electrode affects the cell conductivity and resistivity [81], in turn, the dispersion is affected by the chemical affinity of the polymer to carbon black [102]. A strong affinity leads to small, separate particles with no significant increase in viscosity whereas a weak affinity leads to space-filling fractals of carbon black [166–168]. In the slurry, carbon black is stabilized by the polymer, which prevents agglomeration [106]. Therefore it was chosen to quantify the chemical affinity between polymer and carbon black and determine the effect of this on electrochemical performance.

In the previous chapter, PEO was studied as an aqueous binder. Whilst PEO resulted in processable cathode slurries, the cathodes themselves did not perform as well compared to those conventionally made with NMP/PVDF. Other types of aqueous polymers will contain different chemistries and functional groups, which could affect their affinity to carbon black, and result in greater carbon black dispersion and improved electrochemical performance. Therefore, aqueous cathodes need to be further optimized with regards to their chemical affinity to carbon black. In this chapter, the chemical affinity of several aqueous polymer binders to carbon black will be quantified, and the effect of the chemical affinity will be studied on the electrochemical performance of cathodes made with these binders. To quantify the chemical affinity of polymer to carbon black in aqueous media, adsorption isotherms were taken for five different water-soluble polymers onto Timcal SuperC65 carbon black. Electrical conductivity measurements were performed on the cathode slurry to determine whether the chemical affinity parameter derived from the adsorption experiments affected carbon black dispersion, and

the zeta potential of dilute carbon black/polymer suspensions was measured. The electrochemical properties of cathodes were characterized using galvanostatic cycling tests, namely cycling for 100 cycles at 1C and rate capability tests, and electro-impedance spectroscopy. The data indicates that polymers that adsorb more strongly to carbon black facilitate its dispersion in the cathode slurry, leading to improved electrochemical performance.

4.2 Results & Discussion

4.2.1 Determination of Interaction Parameter

Dilute aqueous suspensions containing 1.5 wt% of carbon black and polymer concentrations between 0.01 to 0.2 wt% were prepared and centrifuged - see Table 9. Adsorption isotherms were obtained and fit the Freundlich model (Equation 13) to determine the chemical affinity of aqueous polymers to carbon black. This model assumes multilayer adsorption on heterogeneous sites on the substrate [169, 170]. The polymer concentration of the filtrate solution was determined by calibration curves shown in Fig. 85 in section 8.2 of the Appendix, which were obtained by the QCMD method as described in Chapter 2. Fig. 46 shows adsorption isotherms for all aqueous polymers in this study. The plateau region indicates a monolayer polymer coverage on carbon black [106, 107]. The calculated parameters K and n are shown in Table 16. The parameter K, is the adsorption capacity, and is used as a measure of the chemical affinity of adsorbent to adsorbate. When 1/n is between 0 and 1, adsorption is considered favourable. When 1/n is greater than 1, adsorption is considered unfavourable, and is irreversible at 1/n = 1. All values of n in Table 16 are below 1, implying that all polymers adsorb favourably onto carbon black. The highest K value was that of pluronic F68, which was calculated as 1.13. The K value for PEO is lower at 0.68, indicating that for pluronics, the hydrophobic PPO block preferentially adsorbs to the surface of carbon black. In contrast, the hydrophilic PEO chains preferentially interact with water. The high intensity of adsorption onto carbon black is expected of pluronics; Lin et.al. observed adsorption of pluronic F127 onto the surface of carbon black in aqueous media [106, 107]. Both pluronic F68 and PEO have the highest plateau values, which correspond to their K parameter values. By contrast, CMC has the third highest K value yet the lowest plateau value. Like pluronic F68, CMC is amphiphilic in nature, containing both a hydrophillic part (carboxyl groups) and a hydrophobic part - the cellulose backbone. The differences in chemical affinity may be due to the differences in polymer structure as pluronic F68 is a block copolymer, whereas CMC is not, which could make it less energetically favourable for CMC to adsorb onto the surface of carbon black than pluronic F68.

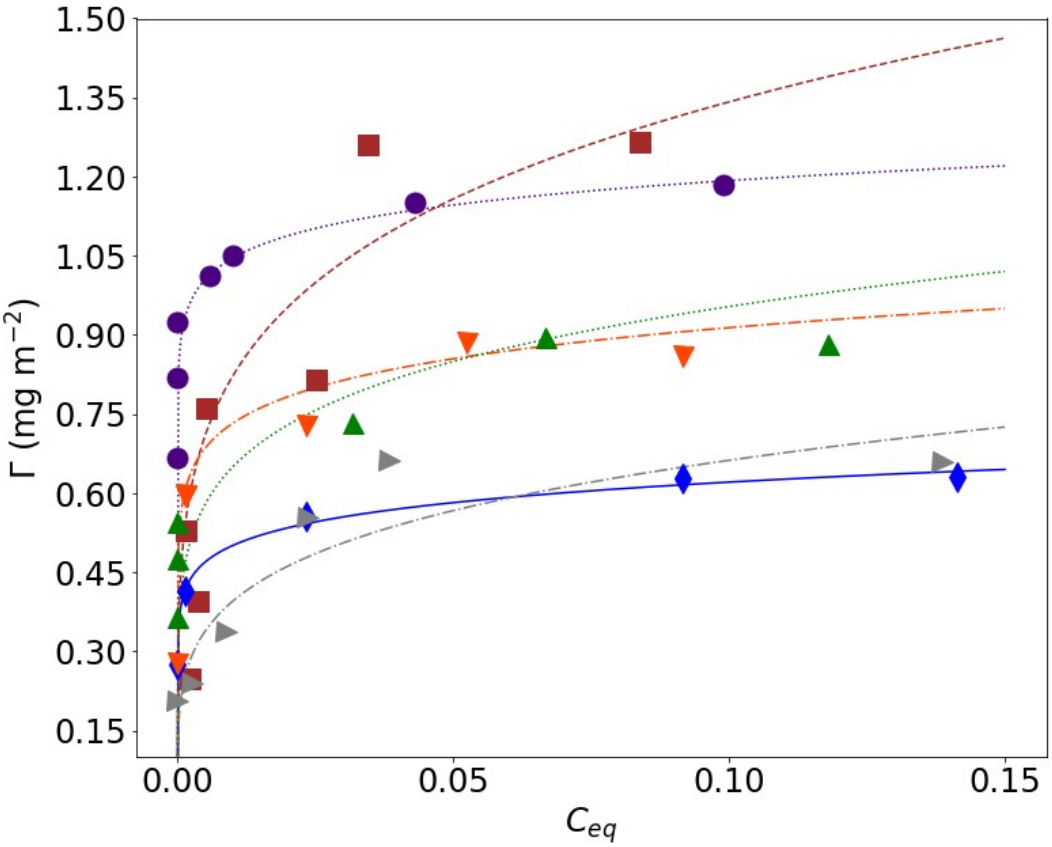

Figure 46: Freundlich adsorption isotherms for Pluronic F68 (■), PEO (●), (Na Alginate (▼), CMC (♦), PVP (▲), and Chitosan (►).

Table 16: Freundlich Isotherm Parameters for aqueous polymers adsorbed onto the surface of carbon black.

Polymer	Mw	K	n	1/n
PEO	1,000,000	1.36 ±0.03	17.53 ±2.05	0.06 ±0.01
CMC	250000	0.77 ±0.02	10.71 ±0.97	0.09±0.01
PVP	13000000	1.4 ±0.19	6 ±1.17	0.17 ±0.03
F68	8400	2.19 ±0.48	4.7 ±1.2	0.21 ±0.05
Chitosan	580000	1.14 ±0.137	4.46 ±1.92	0.22 ±0.1
Na Alginate	216000	1.11 ±0.07	10.41 ±1.62	0.1 ±0.01

4.2.2 Slurry Characterisation

The conductivity of full cathode slurries were measured to understand how the affinity of polymer to carbon black in aqueous media affects carbon black dispersion. Fig. 47 shows the conductivity of full cathode slurries against K. The slurry conductivity is

shown to decrease linearly with K. In the slurry phase, a lower conductivity implies that the carbon black flocs are well-distributed and that there is less agglomeration [101], implying that in less conductive samples, the adsorbed polymer brushes provide more steric repulsion of flocs.

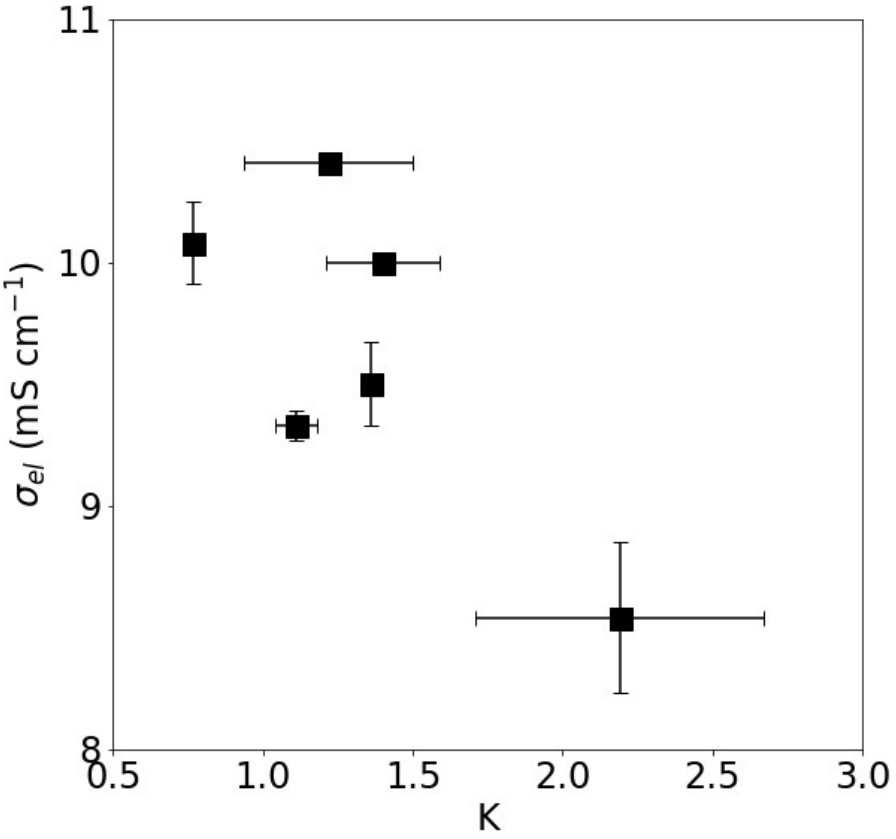

Figure 47: Chemical affinity of polymer to carbon black (K) vs full slurry conductivity. Vertical error bars represent the standard deviation, whilst horizontal error bars represent the error of fit.

To further investigate the effect of the chemical affinity of polymer to carbon black on colloidal behaviour, the zeta potential of dilute carbon black/polymer suspensions was measured. Zeta potential values for each polymer suspension are shown in Table 17. The zeta potential threshold for colloid stability is given as above +30 or below -30 mV. In Fig. 48a, zeta potential is shown to have a non-monotonic relationship with K. The suspensions containing Na Alginate, chitosan, and pluronic F68 had the highest zeta potential moduli respectively. In contrast, CMC, PEO, and PVP had the lowest zeta potentials, these values were outside the stability region. The greater

the surface charge measured by the zeta potential, the greater the repulsion forces are between colloids of carbon black and polymer. It is noted that both CMC and sodium alginate have a similar MW (250000 and 216000 Da respectively) yet different zeta potentials and K values. Before the investigation, it was hypothesized that increased polymer adsorption to carbon black would increase colloidal stability [171]. Though there was little correlation between zeta potential and K, a clearer trend is seen when plotting zeta potential against n, the maximum adsorbed amount of polymer per unit surface area. It is also worth noting that the chitosan swells in water, resulting from electrostatic repulsion from ionized amino groups. Though chitosan is shown to weakly interact with carbon black, the high zeta potential of suspensions is likely due to its swelling behaviour, preventing carbon black flocs from re-agglomerating. Figs 48c and d were plotted to investigate whether the molecular weight of the polymer affected the zeta potential or surface coverage. Both plots show no correlation between either factor. With no clear trend shown by this data, the colloidal stability of carbon black suspensions containing aqueous polymers is likely the result of several parameters as opposed to one.

Table 17: Zeta potential values for aqueous suspensions of polymer and carbon black.

Polymer	ZP (mV)
PEO	-18.27 ±0.49
PVP	-14.2 ±0.28
CMC	-22 ±0.24
F68	+59 ±1.17
Chitosan	+244.67 ±0.4
Na Alginate	-329 ±18.82

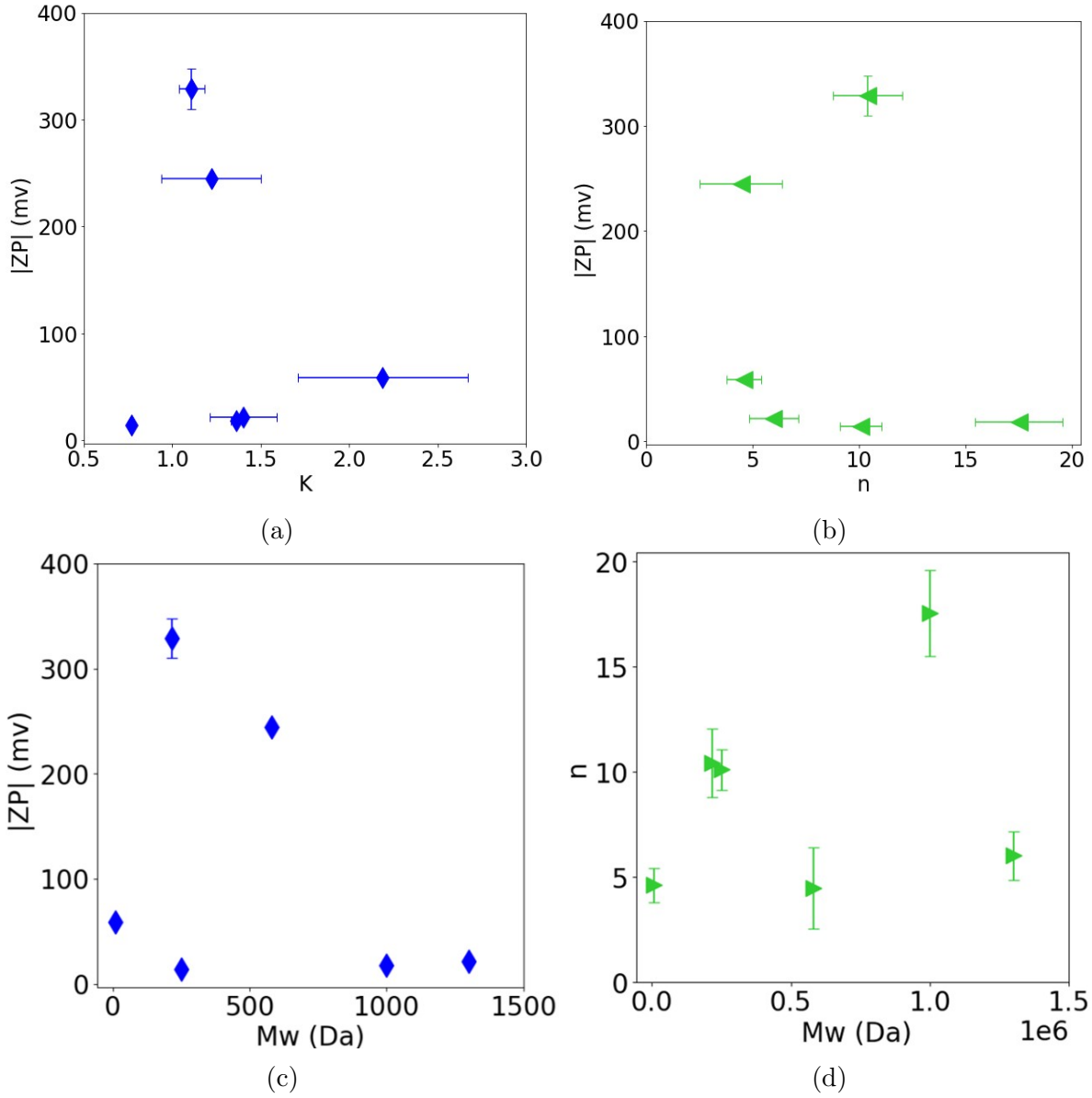

Figure 48: Zeta potential of carbon black/polymer suspensions containing 0.1 wt% polymer against (a) Chemical affinity of polymer to carbon black (K), (b) Surface coverage (n) of polymer on carbon black, (c) Zeta potential vs Mw, and (d) n vs Mw. Vertical error bars represent the standard deviation, whilst horizontal error bars represent the error of fit.

To illustrate the potential behaviour of these systems, a schematic is shown in Fig. 49. The surface coverage does not always correspond to the chemical affinity of the polymer to carbon black, as determined by the Langmuir fits in Table. 16, In the case of stable suspensions, i.e. PEO, CMC, and pluronic F68, the adsorbed polymer

chains sterically repulse one another, keeping the carbon black flocs dispersed, therefore preventing their agglomeration. In the case of unstable suspensions, i.e. chitosan, polymer adsorption upon carbon black is reversible despite high surface coverage, so polymer chains easily desorb to allow carbon black to agglomerate.

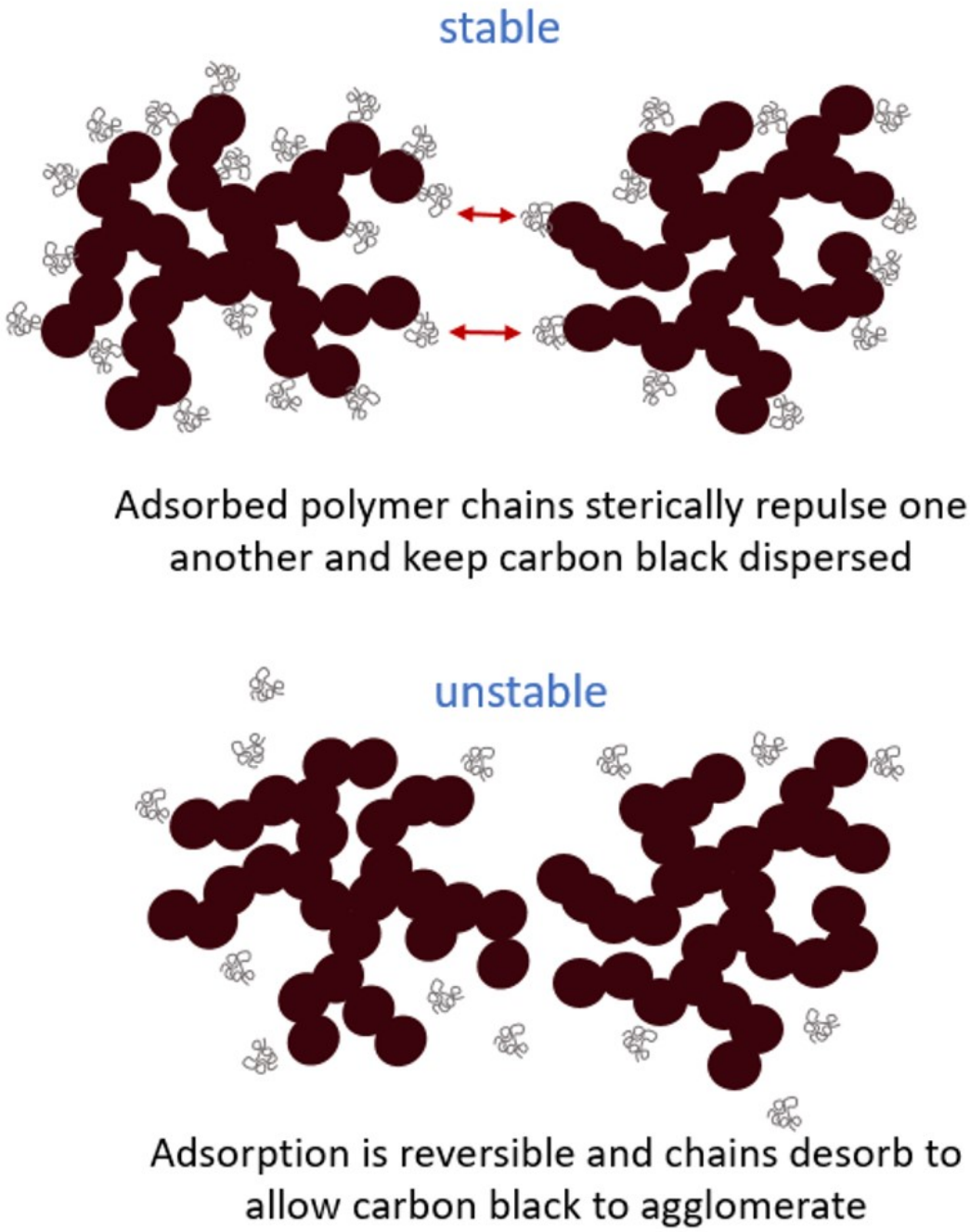

Figure 49: Schematic showing polymer adsorption onto carbon black

4.2.3 Electrochemical Performance

The effect of chemical affinity of polymer to binder was investigated by fabricating half coin-cells and cycling them between 3.0 and 4.3 V. The rate capability and capacity fade were both studied. It was expected that the chemical affinity of polymer to binder would affect the electrochemical performance of resulting coin cells. The rate capability data for aqueous cathodes are shown in Fig. 51 (discharge capcacity against cycle number) and Fig. 52 (discharge cycles), whilst Fig. 53 shows the rate capability data for PVDF. The first cycles at 0.1C were performed to establish the formation of a stable solid electrolyte interface (SEI) on the lithium anodes. At low C rates, the coin cell made with pluronic F68 achieves the highest specific capacities achieving 161 mAh g^{-1}, followed by CMC, achieving 150 mAh g^{-1} at 0.1C. The discharge curves for each polymer at every C-rate are shown in Fig. 52. At 0.1C, (Fig. 52b.), the F68, CMC, and PVP curves show smooth discharge curves, whilst those for PEO, chitosan, and sodium alginate show bumps. The PVDF curve also shows some noise at high voltage in the Li-poor phase, but the curve becomes smooth at 3.8 V. The curves at 0.2C and 0.5C are smooth, though from 1C onwards the curve is noisy at higher voltage, likely due to internal resistances at higher C rates. For cathodes made with chitosan and PVP, no capacity was produced at C rates of 1C or above. As the C rate increases, the performance of the CMC cell drops to become comparable with PEO and sodium alginate. At 5C, the performance of PEO and Pluronic F68 are comparable with PVDF, possibly due to PEO being ionically conductive, enhancing Li-ion transport in the cathode by creating more pathways for Li-ions to diffuse.

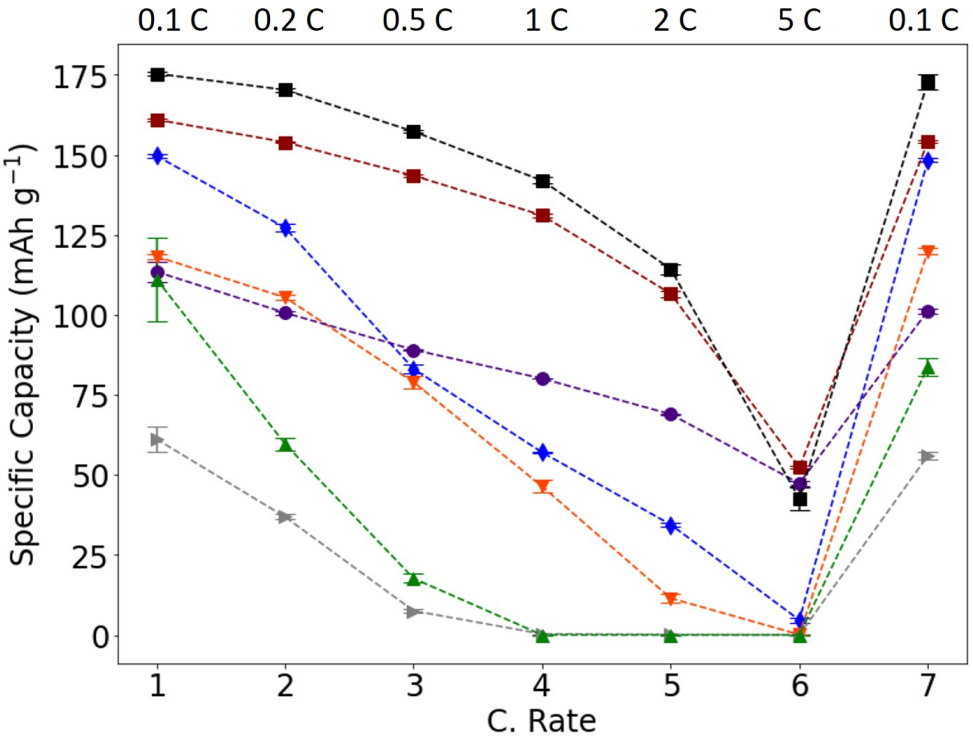

Figure 50

Figure 51: Rate Capability for cathodes made using: PVDF (■), Pluronic F68 (■), (Na Alginate (▼), CMC (♦),PEO (●), PVP (▲), and Chitosan (►).

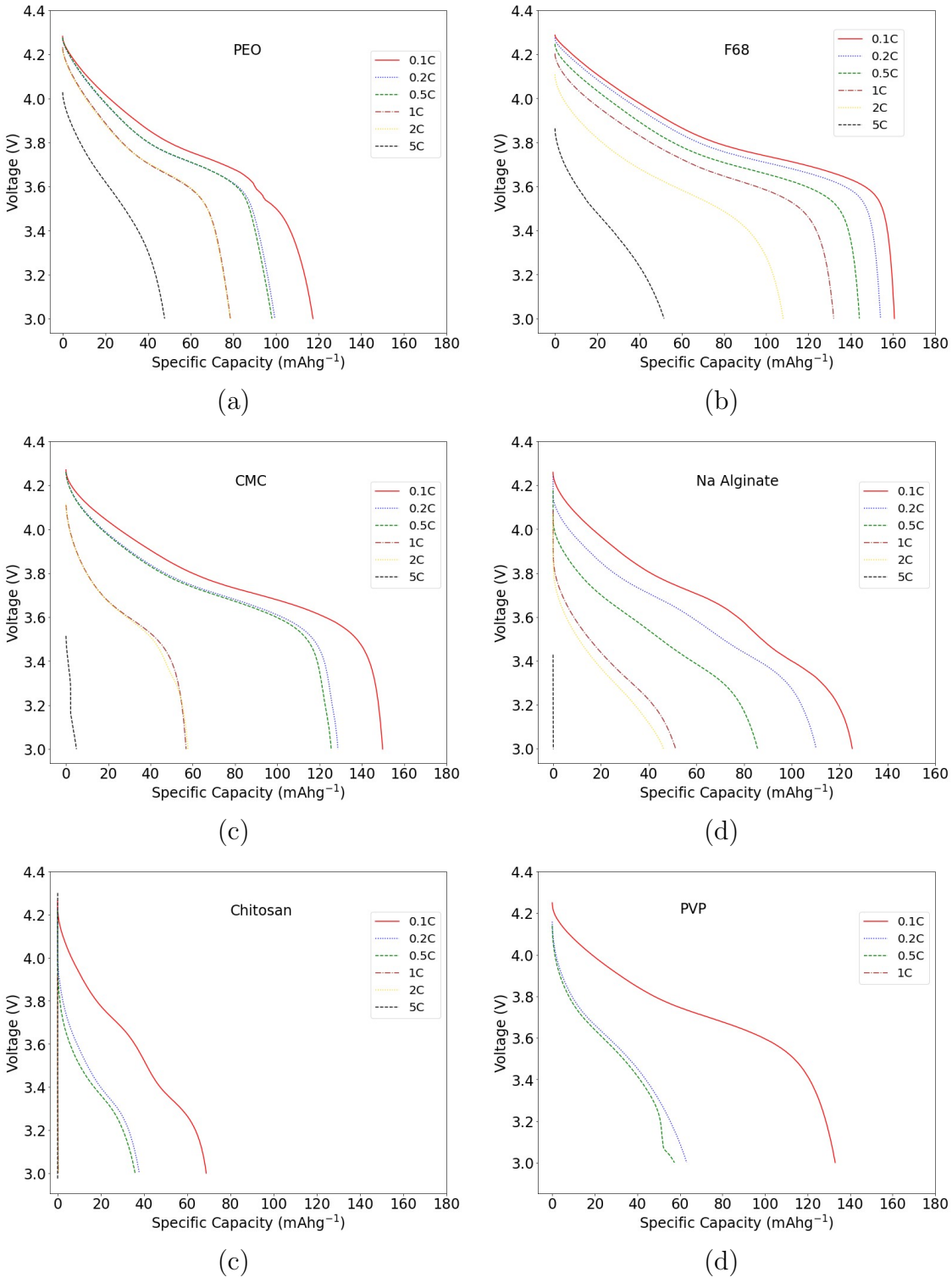

Figure 52: Rate capability discharge cycles for cathodes made using the following polymers: a) PEO, b) Pluronic F68, c) CMC, d) Chitosan, e) Na Alginate, and f) PVP. Cycles shown are the first cycle in each series.

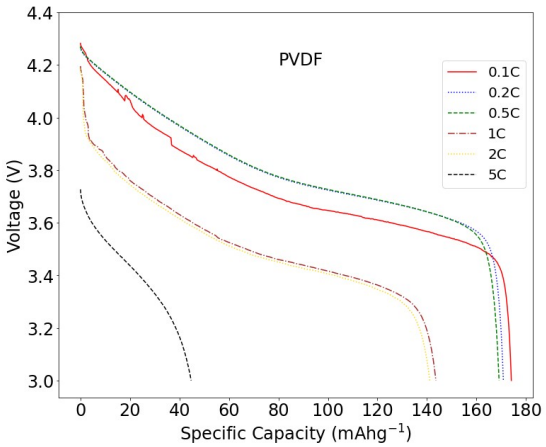

Figure 53: Rate capability discharge cycles for cathodes made using PVDF. Cycles shown are the first cycle in each series.

To further investigate the differences in rate capability between aqueous polymers, i.e. how the electron transfer network impacts the charge and discharge properties of the different electrodes, the differential capacity (dQ/dV) profiles were plotted in Fig. 54. The cycles shown are the first of 0.5 to 5C; the first cycles for 0.1 and 0.2C are not shown due to noisy data. For all cathodes, there is one charging peak at circa. 3.7 V at 0.5C, indicative of the hexagonal (H1) to monoclinic (M) phase transition that occurs during cycling [172–174]. As the C rate increases, the oxidation peak (charging) shifts to higher potentials, whilst the reduction peak (discharging) shifts to lower potentials. For cathodes made with CMC and sodium alginate, the shift in potential with increasing C rates is significant, particularly from 0.5 to 1C, whereas these shifts are less pronounced for the PEO and pluronic F68 cathodes. The PVP and chitosan cathodes show no performance from 1C onwards in Fig. 51, in Fig. 54 the curves show a low area, commensurate with their low specific capacity. These observations suggest that cathodes made with PEO and pluronic F68 display greater cycling stability and reversibility during the H1-M transition whilst cycling [172–174], implying that these cathodes have a more robust mechanical structure with a greater electronic conductivity network. By contrast, cathodes made with chitosan and PVP are therefore implied to have a less homogeneous structure, making it more difficult for Li ions to be (de)inserted. These morphologies likely result from the poorer distribution of carbon black in the dry electrode. The cathodes that show inhomogeneity from dQdV results are also the ones that exhibit poorer distribution of carbon black in the slurry from conductivity measurements, namely chitosan and PVP. It is also likely that poor

adhesion of the cathode to the current collector contributes to their performance.

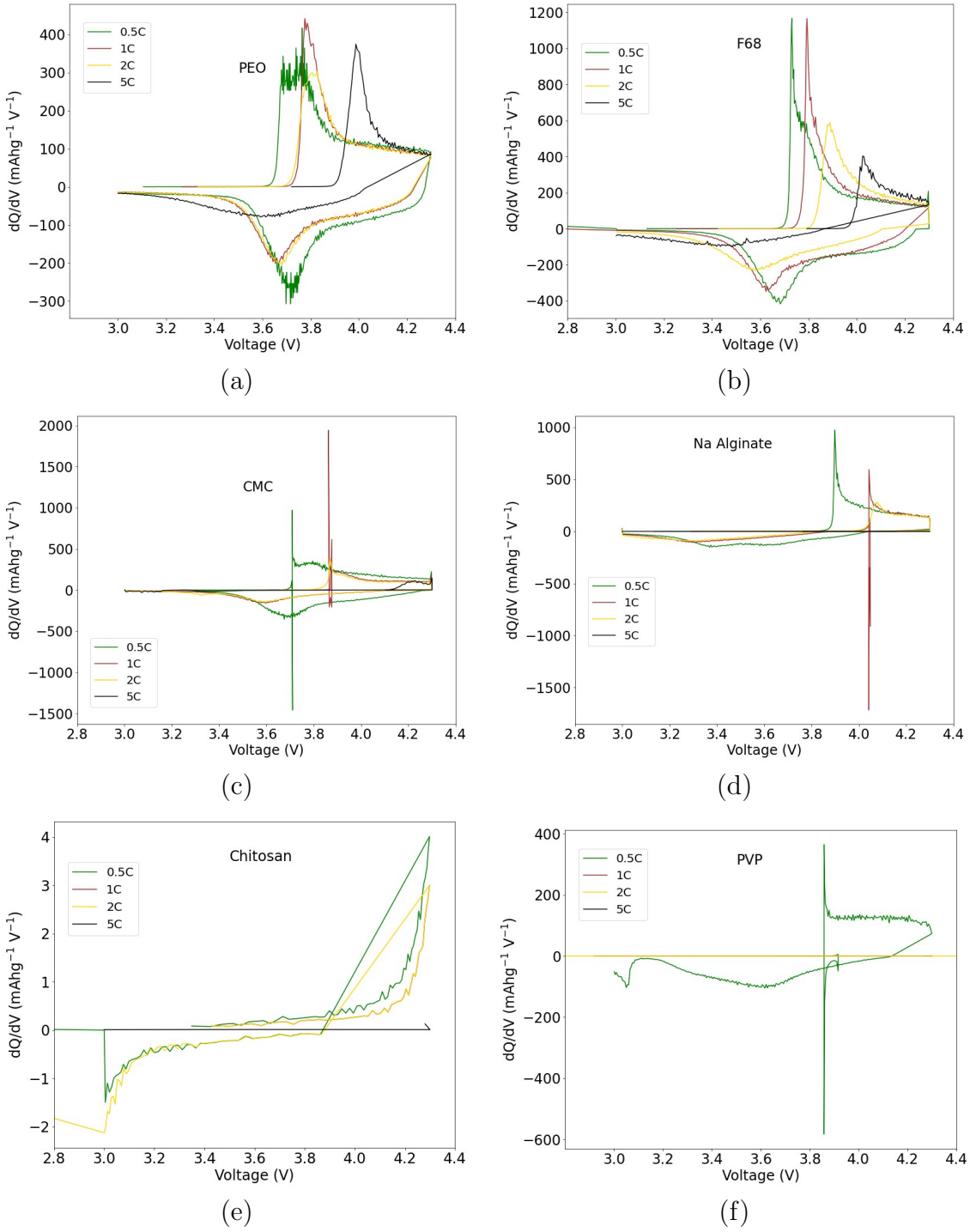

Figure 54: Differential capacity (dQ/dV) for cathodes made using the following polymers: a) PEO, b) Pluronic F68, c) CMC, d) Chitosan, e) Na Alginate, and f) PVP. Cycles shown are the first cycle in each series.

The effect of the K parameter on rate capability is shown in Fig. 55 for 0.1C, 1C, and 5C. For all C rates, the general trend is that specific capacity increases against K, though CMC performs higher than its K value would predict at 0.1C. At 5C, the four cathodes with the lowest K values of polymer produced little to no capacity, whereas those made with PEO and pluronic F68 were still performing. The K parameter has been shown to positively affect the dispersion of carbon black in the cathode slurry as shown in Fig. 47. Strong polymer adsorption onto the carbon black surface produces electrostatic repulsion between the coated carbon black particles, resulting in better dispersion [70]. It is known that a well-distributed network of conductive additives improves cathode electrochemical performance [81, 103], so the network present in the slurry is likely retained upon film-drying. The high performance of the cathode made with pluronic F68 even at high C rates is likely because pluronics are amphiphilic surfactants, which could aid dispersion of carbon black.

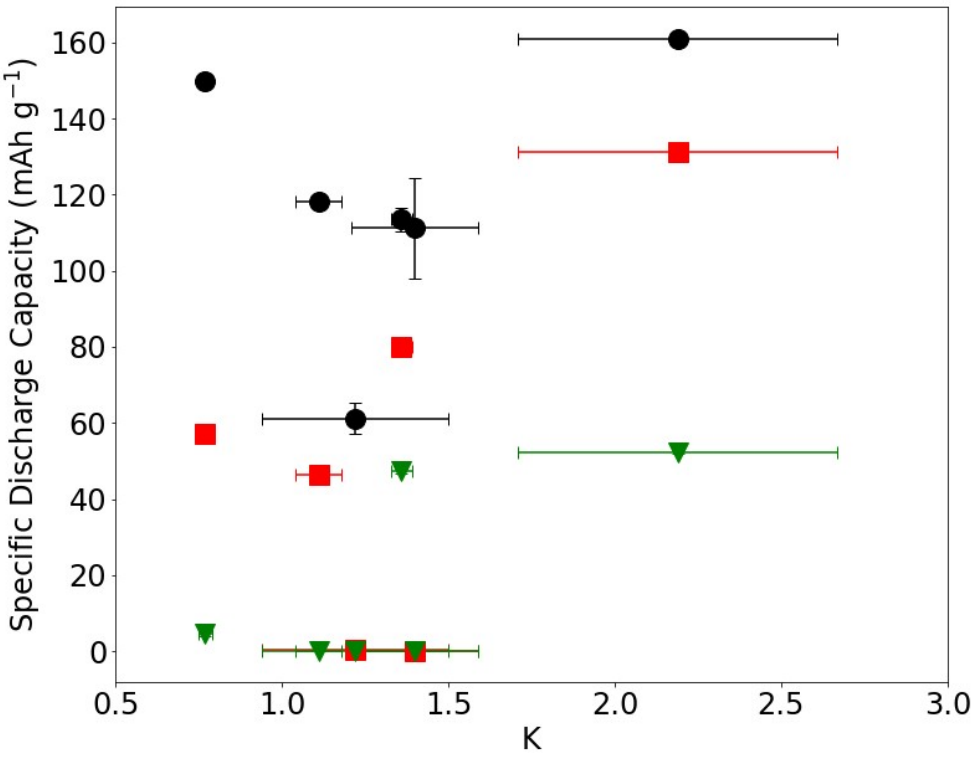

Figure 55: K vs against rate capability for 0.1C (●), 1C (■), and 5C (▼). Linear fits are shown as dotted lines.

To determine the effect of slurry microstructure on electrochemical performance, the rate capability data from Fig. 51. was plotted against slurry conductivity as shown in

Fig. 56. For all C rates shown, there is a decreasing trend of specific capacity against slurry conductivity. At 0.1C, the trend is relatively strong, with CMC as an outlier, showing a specific discharge capacity of 149.1 mAh g^{-1} and a high slurry conductivity of 10.08 mAh g^{-1}. The trend is less definitive at 5C, with PVP and chitosan coin cells producing no capacity at 5C. This contradicts the initial hypothesis of high slurry conductivity resulting in high electrochemical performance.

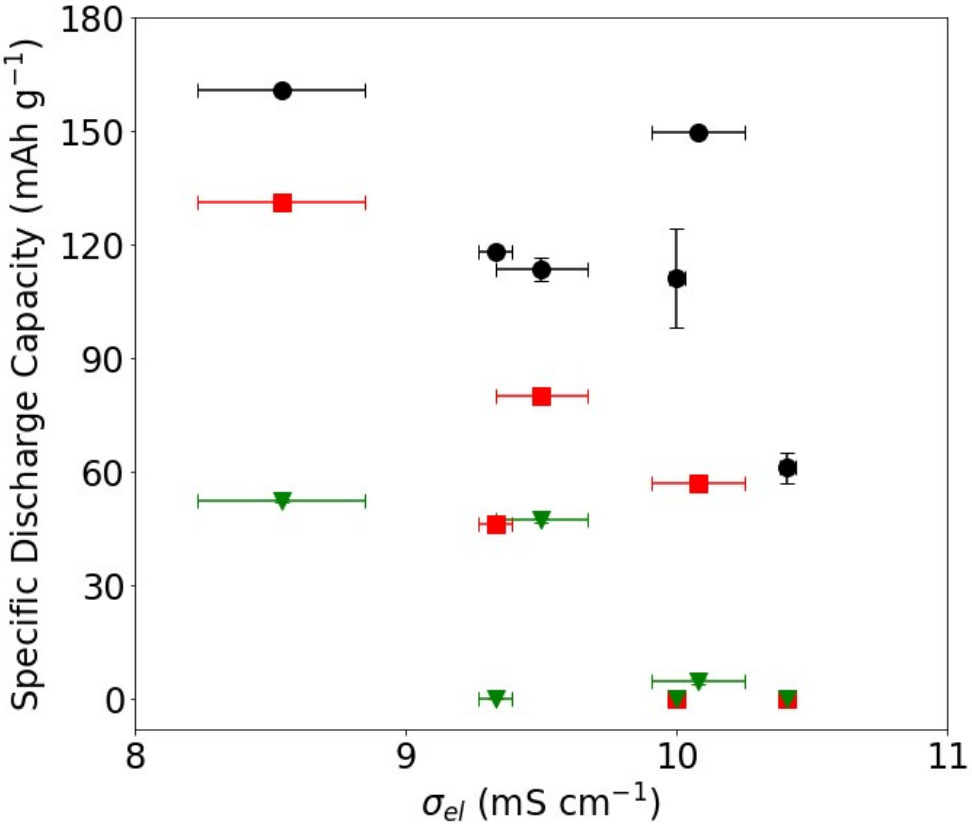

Figure 56: Slurry conductivity vs rate capability for 0.1C (●), 1C (■), and 5C (▼). Error bars are the standard deviation of three measurements

To further investigate why specific capacity decreases with slurry conductivity, the cathode porosity (ϵ) was considered. The cathode porosity was calculated using Equation 33. The relationship between cathode porosity and specific discharge capacity at 1C is shown in Fig. 57a, where for both 0.1C and 1C, a decrease in capacity with increasing porosity is seen. Studies disagree on the effect of NMC 622 cathode porosity on performance; some such as Parikh et.al. observe that low porosity is linked to reduced resistances and improved performance [175], whereas others, such as Haider et.al. and Heubner et.al., observe that higher porosities result in increased performance at low C rates and reduced performance at high C rates, [176, 177]. The data presented here contradicts those findings, as electrochemical performance at both 0.1 and 1C show the same trend of decreasing specific capacity with porosity. Reasons for decreasing electrochemical performance with porosity are fewer particle contacts, i.e. between the active material and the conductive carbon network. Whereas for studies where improved performance is observed with increased porosity, enhanced Li-ion diffusion is given [176,177]. To investigate the origins of the effect of porosity on performance, cathode porosity was plotted against slurry conductivity as shown in 57b. Here, the slurry conductivity increases with porosity. Comparing this with Fig. 47, where conductivity decreases with carbon interaction, Fig. 56 where conductivity decreases with specific capacity and Fig. 57a, the higher slurry conductivities result in lesser dispersion of the CBD in the dried cathode, leading to greater porosities in the dry cathode films. This in turn, leads to reduced electrochemical performance. The values for cathode mass, thickness and porosity are shown in Table 12 in Chapter 2.

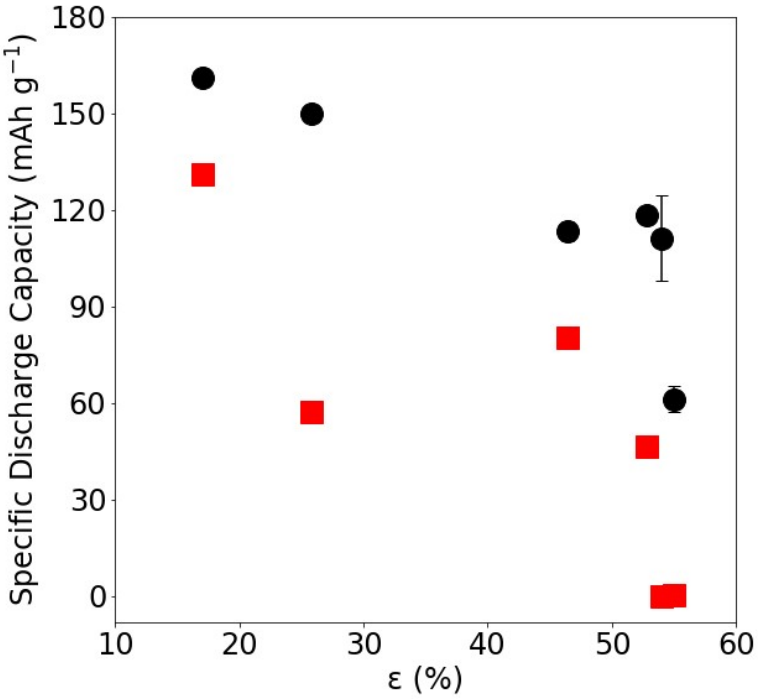

(a)

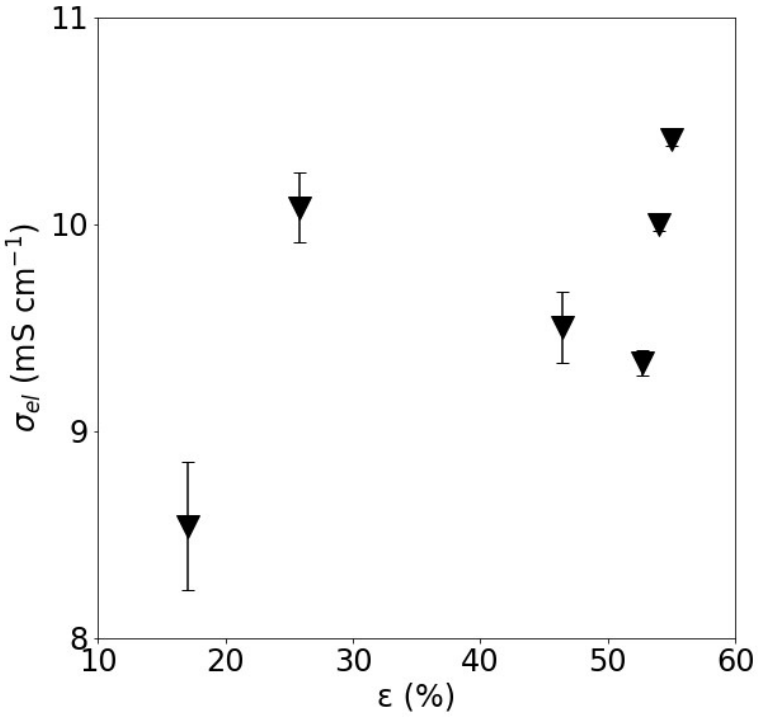

(b)

Figure 57: Cathode porosity vs (a) rate capability specific capacity at 0.1C (●), and 1C (■), and (b) slurry conductivity. Error bars are the standard deviation of three measurements.

Cycling stability tests were performed at 100 cycles at 1C for aqueous polymers, with one made with NMP/PVDF as a control. Cathodes made with PVP and chitosan cycled poorly and were irreproducible, so data is not included here. In the case of PVP, cathodes produced easily peeled off the current collector; the low adhesion strength may have been a factor for its low performance. Cathodes with low adhesion to the current collector are more likely to delaminate. When delamination occurs, contact is lost between the cathode and current collector, which reduces the electrochemically active surface area. This reduces the number of conductive pathways for electrons and Li ions, increasing the cell resistance, and reducing electrochemical performance [178, 179]. As discussed above, the dQdV data for PVP indicate an inhomogeneous electrode; the poor adhesion strength of the cathodes also suggests a network of CBD that is neither mechanically robust nor well-dispersed [172]. Unlike the rate capability data, the first specific discharge capacities do not scale with the obtained chemical affinity parameters, contrary to the hypothesis. Out of the successfully cycled aqueous processed coin cells, CMC yielded the highest 1st specific discharge capacity of 136 mAh g^{-1}. The CMC cathode cycled in these tests achieved a higher first specific capacity than the cathode cycled in the rate capability experiment at 1C, which could be due to resistances caused by structural degradation of the cathode during cycling [22, 38]. The effect of chemical affinity on electrochemical performance is therefore more visible at low C rates. Although lower than the NMP/PVDF control at 150 mAh g^{-1}, the performance is comparable after 30 cycles. By contrast, the performance of PVDF does not overlap with cells made with pluronic F68, PEO, and sodium alginate. The specific capacity of the sodium alginate cell sharply decreases for the first six cycles, then steadily increases until the 100th cycle. This could be due to the structural changes of the Li anode as opposed to the cathode; Li anodes with a non-uniform surface may release more Li ions during cycling, leading to an increase of capacity over time [180, 181].

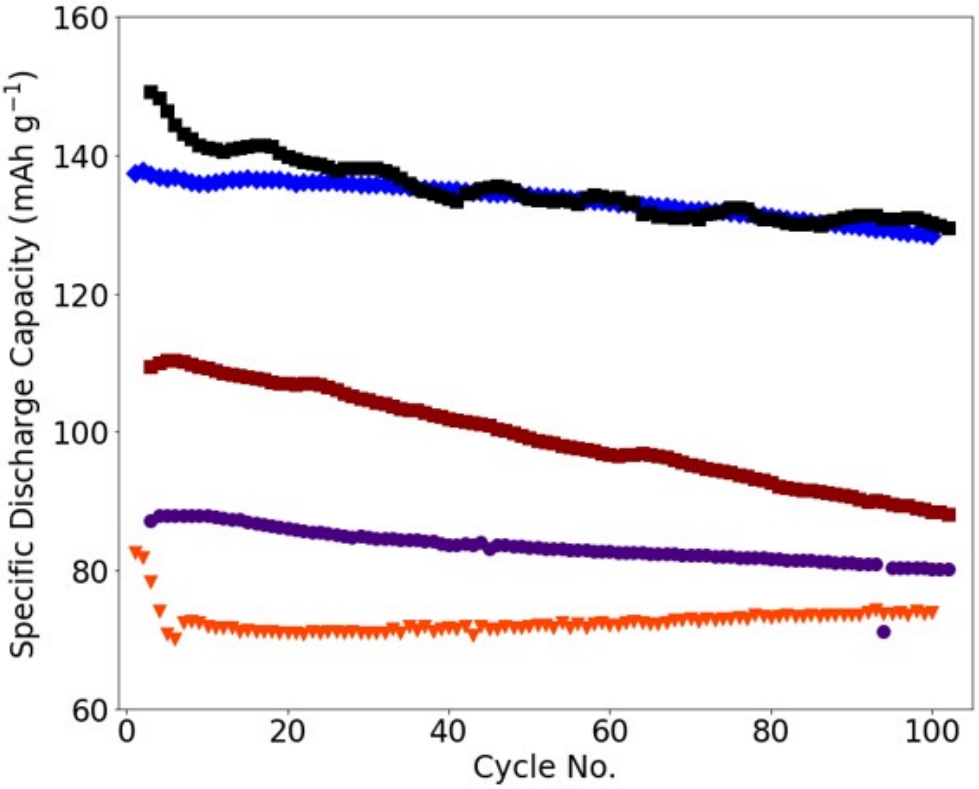

Figure 58: First discharge capacity vs voltage plots showing representative coin cells from each sample: PVDF (■), Pluronic F68 (■), (Na Alginate (▼), CMC (♦), and PEO (●).

4.2.4 Cell Impedance

To further investigate the differences between each cell for capacity fade, EIS measurements were performed on each coin cell. To determine how these electrochemical processes evolve with cycling, measurements were taken after two formation cycles at C/20, shown in Fig. 59a., then again after 100 cycles at 1C, shown in Fig. 59b. Data for chitosan and PVP are not shown in Fig. 59b as cells made with these binders did not cycle at 1C. The electrolyte resistance, R_e, is where the semicircle intercepts the x-axis. The charge-transfer resistance, R_{ct}, is the resistance arising from the Li^+ intercalation reaction in the active materials of the electrode [182]. Both before and after cycling, R_e is similar for all samples, meaning R_e provides a small contribution to the overall cell resistance. R_e is calculated from the lowest intercept of the Nyquist plot on the x-axis, whilst the charge-transfer resistance, is calcuated by subtracting the second intercept of the Nyquist plot away from R_e. The R_{ct} values for all coin cells increase

after cycling, indicating structural degradation of the cathode. CMC has the lowest R_{ct} before cycling, followed by PEO, sodium alginate and Pluronic F68 respectively. Values for R_e and R_{ct} are shown in Table 18.

Table 18: Parameters R_e and R_{ct} for aqueous processed cathodes made with different polymer binders.

Polymer	R_e Post Formation	R_{ct} Post Formation
CMC	4	84
PVP	2	165
Chitosan	3	48
Na Alginate	4	83
PEO	3	75
F68	4	150

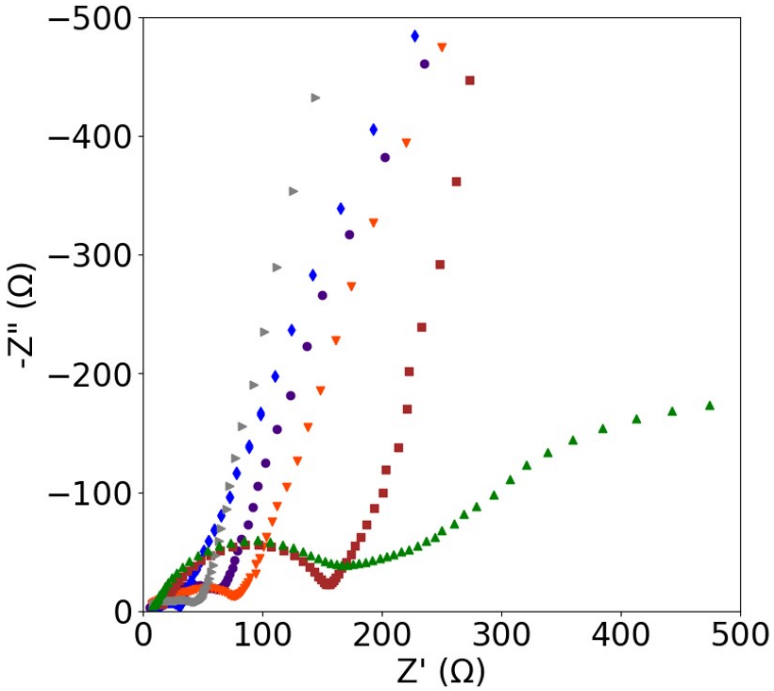

(a)

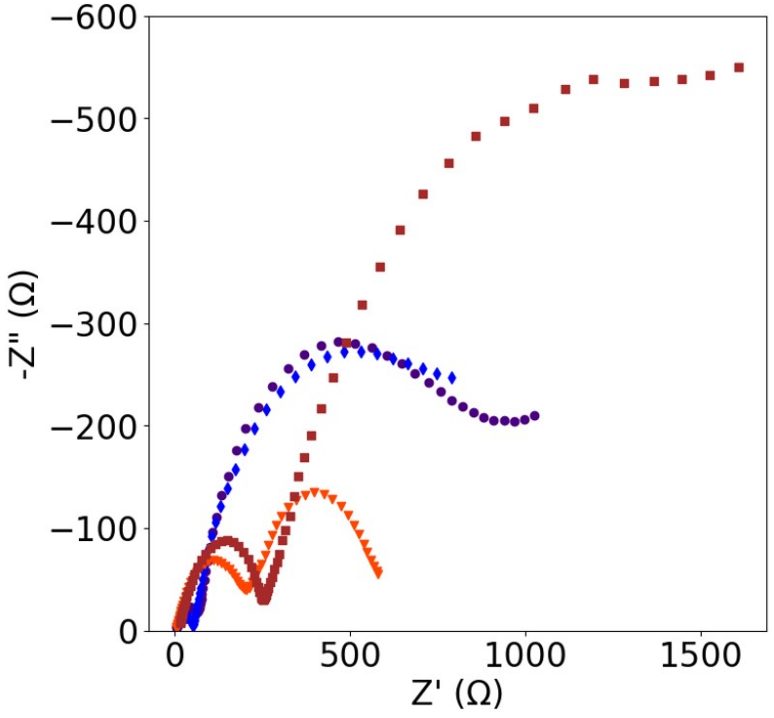

(b)

Figure 59: Nyquist plots for coin cells taken before 100 cycles at 1C:(Pluronic F68 (■), (Na Alginate (▼), CMC (♦), PVP (▲), and Chitosan (▶), and PEO (●) for (a) post formation for 2 cycles at C/20 and (b) taken after 100 cycles at 1C, as shown in Fig.58.

To understand whether the chemical affinity of polymer to carbon black or the microstructure of the slurry affects the electrochemical properties of the dried cathode, slurry conductivity was plotted against the R_{ct} of the dry electrode, as shown in Fig. 60. In Fig. 60, the R_{ct} is shown to increase with K. The cell resistance is affected by the presence of conductive networks of carbon black in the electrode, [51], supporting the hypothesis that a strong chemical affinity of the poplymer to carbon black aids dispersion, therefore forming more conductive networks. To investigate this further, R_{ct} was plotted against slurry conductivity in Fig. 60b. The R_{ct} of the dried electrode in the coin cell after two formation cycles at C/20 decreases with increasing slurry conductivity. The exception is PVP, which had a slurry conductivity of 10 $mScm^{-1}$ yet had a high R_{ct} of 165 Ω. It is worth noting that PVP cathodes easily peeled off the current collector - this low adhesion may have accounted for the high R_{ct} as well as the inability of the cell to cycle. In the slurry, conductive properties arise from weakly interconnected flocs of carbon black forming a 3D network [51]. This data indicates that the conductive networks of carbon black in the cathode slurry are retained upon drying. These results enable the prediction of electrochemical properties of cathodes based on aspects of the slurry microstructure.

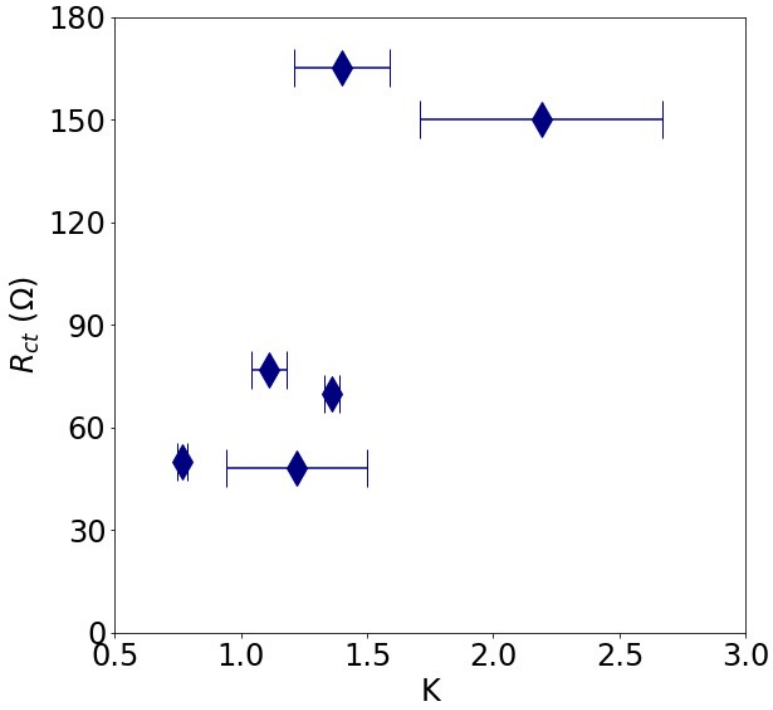

(a)

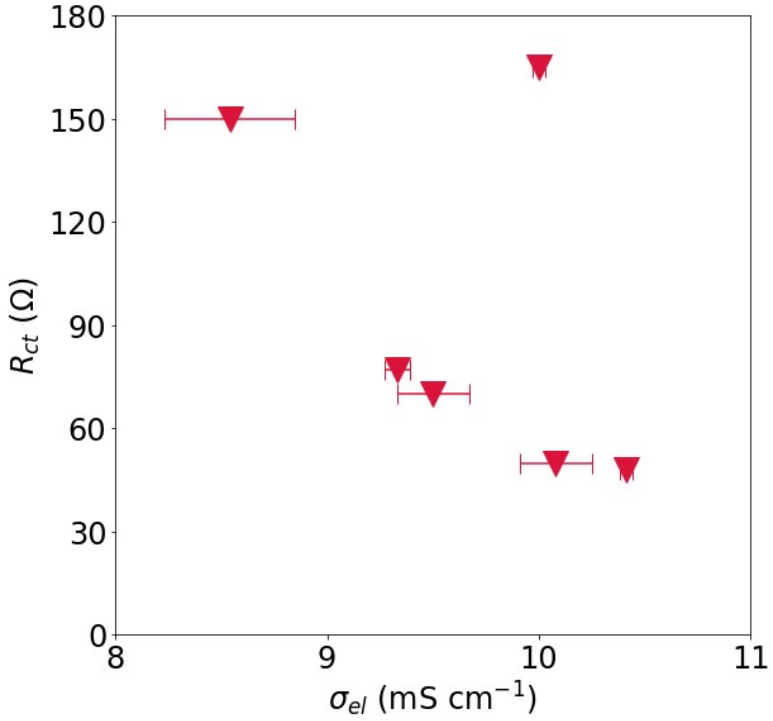

(b)

Figure 60: Slurry conductivity vs R_{ct} of cathodes after two formation cycles at C/20.

4.3 Conclusions

- Strong polymer adsorption was shown to affect the dispersion of carbon black particles in aqueous suspension. Pluronic F68 and PEO adsorb strongly onto carbon black relative to chitosan, sodium alginate, PVP and CMC; but neither binder on its own yields highly performing battery half-cells.

- Cathodes containing more dispersed carbon black particles had lower resistances and better electrochemical performance. As the polymer adsorption was shown to affect carbon black dispersion, it can be concluded that the chemical affinity of the polymer to carbon black affects the cathode's electrochemical performance.

- Slurry conductivity decreases with impedance in the dry electrode, likely as slurries with a greater dispersion of carbon black are less conductive, yet having a greater dispersion in the slurry translates to weakly connected networks in the dry phase. By contrast, slurries that are more conductive may result in films that have thicker CBDs, leading to agglomerated carbon black and fewer conductive networks, thus decreasing the electrochemical performance.

- Electrochemical performance decreases with increasing cathode porosity, which itself increases with slurry conductivity. This relationship is likely due to higher slurry conductivities resulting in lesser dispersion of the CBD in the dried cathode, leading to greater porosities in the dry cathode films. This in turn, could lead to reduced electrochemical performance.

- Rate capability performance decreases with slurry conductivity. Several studies use slurry conductivity to optimise electrode manufacturing methods [138, 156, 157], however, these results indicate that maximising slurry conductivity is not the best approach to achieve this.

The chemical affinity of aqueous polymers to carbon black affects the distribution of carbon black in both the slurry and film phases, and is therefore a useful predictor of electrochemical performance.

5 Chapter 5: Optimizing the Performance of NMC622 Battery Half-Coin Cells by Using Amphiphilic Aqueous Binders to Modulate the Percolation of Carbon Black

5.1 Introduction

N-methyl-2-pyrrolidone (NMP) is the conventional solvent for processing high-nickel cathodes as it dissolves the polymer binder polyvinylidene fluoride (PVDF) and does not leach nickel from the cathode material. NMP is restricted under REACH regulations as a 'substance of very high concern' [183]. Aqueous processing with hydrophilic polymer binders is an emerging alternative to the NMP/PVDF solvent/binder system. Aqueous processed cathodes offer advantages over conventional processing with NMP, namely nontoxic, unrestricted use and cost-effectiveness being 100 times less expensive than NMP/PVDF. However, carbon black is hydrophobic so it does not disperse in water. One way around this problem is to substitute the binder for one that is water-soluble so it can bind to and disperse the carbon black.

Aqueous binders have generally yielded unimpressive battery performance, therefore a novel binder system has been studied. In the previous chapter, the chemical affinity of aqueous polymers to carbon black was shown to affect the electrochemcial performance of cells via the distribution of carbon black. An amphiphilic polymer (pluronic F68) and a high Mw PEO were shown to have the greatest chemical affinity to carbon black, yet neither binder on its own could outperform conventionally processed cathodes. Here, blends of these polymers were prepared; pluronic F68 was used to control the dispersion of carbon black in the slurry, and PEO was used as a viscosity modifier.

Two sets of experiments were conducted using blends of PEO and pluronics. In both, the ratio of PEO to pluronics was varied. In one set of experiments, the slurries' solids loading (SL) was kept constant, meaning that the viscosity of the polymer blends was varied, decreasing with increasing PEO content. In the other set, the viscosity of the polymer blends was kept constant, so the solids loadings varied, decreasing with increasing PEO content. It was impossible to keep either variable constant without varying the other, which is why both experiments were conducted.

Slurries are optically opaque and difficult to characterize, so zeta potential measurements were taken to assess the degree of carbon-black dispersion in the slurry. Measuring steady-state viscosity flow curves and oscillatory strain measurements, a narrow viscosity range in which carbon black percolates in the cathode slurry was identified, and validated by conductivity data. Working within this range of viscosities, a series of formulations were developed that maximize the mass fraction of active material whilst ensuring enough binder is present to disperse the carbon black in water. Ultimately, the formulations presented have a constant viscosity, attained by controlling the solids loading. Half-coin cells were cycled at charge and discharge rates of 1C, using a voltage range of 3.0 to 4.3 V.

An optimal ratio of 25% PEO to 75% pluronic-F68 was identified; half-coin cells achieved a mean 1st specific discharge capacity of 147 mAh g^{-1} with a mean capacity retention of 86%. Through adsorption measurements, it was found that the affinity between the binder and carbon black seems to correlate with the size of carbon black flocs that form, enabling the tuning of the percolation of carbon black in the slurry. By carefully controlling the viscosity, it was shown that electrochemical cell performance correlates very strongly with both the PEO to pluronic ratio and the slurry conductivity for this system. The results indicate that the affinity of the polymer binder(s) to carbon black can determine the electrochemical performance of the cell.

5.2 Results & Discussion

5.2.1 PVDF Coin Cell Reproducibility

Coin cells using conventionally processed cathodes using NMP as the solvent and PVDF as the binder were produced as control experiments. Three cells were successfully cycled, with a further two cells failing to cycle. The 1st specific discharge capacities were 154, 112, and 149.39 mAh g^{-1} Fig. 61a., resulting in a mean of 138.46 mAh g^{-1} and a standard deviation of 21. The 100th specific discharge capacities were 134.02, 54.57, and 135.71 mAh g^{-1} respectively as shown in Fig. 61b, resulting in a mean of 108.1 mAh g^{-1} and a standard deviation of 37.86. The capacity retention of the cells similarly showed much variation as seen in Fig. 62, with cell 1 achieving 87%, cell 2 45%, and cell 3 90.84%, resulting in a mean of 56.67% and a standard deviation of 19.22. Whilst cells 1 and 3 achieved similar performances which is expected of this type of cell, cell 2 performed much worse. There are several possible reasons why this is the case. Cell 2 had a mass loading of 17.61 mg, compared to 10.63 and 11 mg for cells 1 and 3 respectively. The extra mass of cell 2 may have contributed to mass transport limitations, making it more difficult for Li ions to diffuse through the cathode microstructure [86]. Other considerations include possible contamination of the cathode film whilst being transferred from the vacuum oven to the glovebox, or misalignment of coin cell components during cell assembly. It is worth noting that cells 1 and 2 were produced from the same cathode film, whereas cell 3 was from a different film produced on a different day, suggesting that the data could be reproducible. Whilst two cells perform similarly, the outlier that is cell 2 demonstrates the difficulty in obtaining reproducible coin cell data.

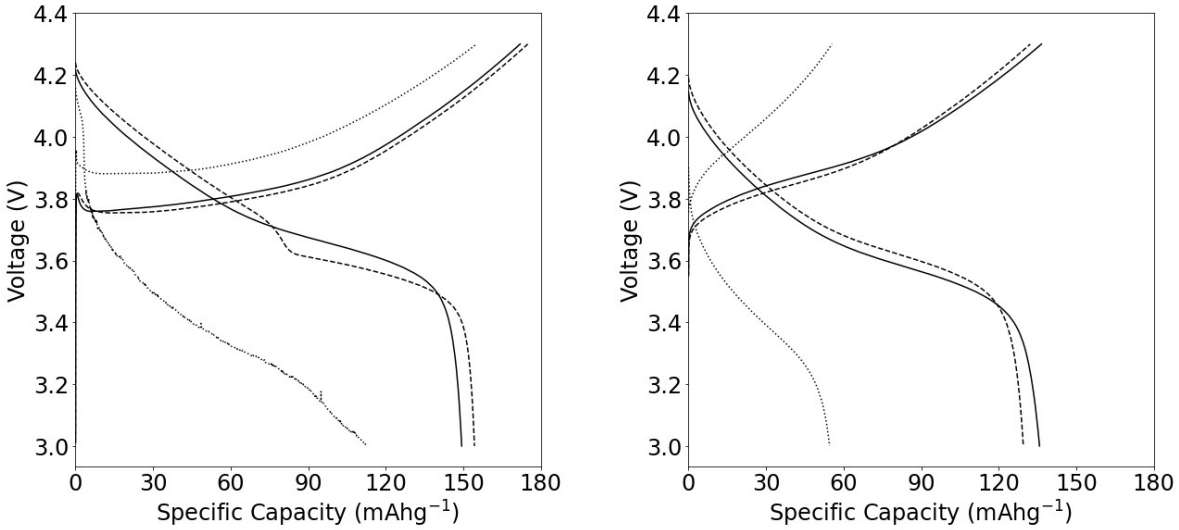

Figure 61: Charge/Discharge curves at 1C for coin half-cells processed with NMP/PVDF, for (a) the 1st cycle, and (b) the 100th cycle.

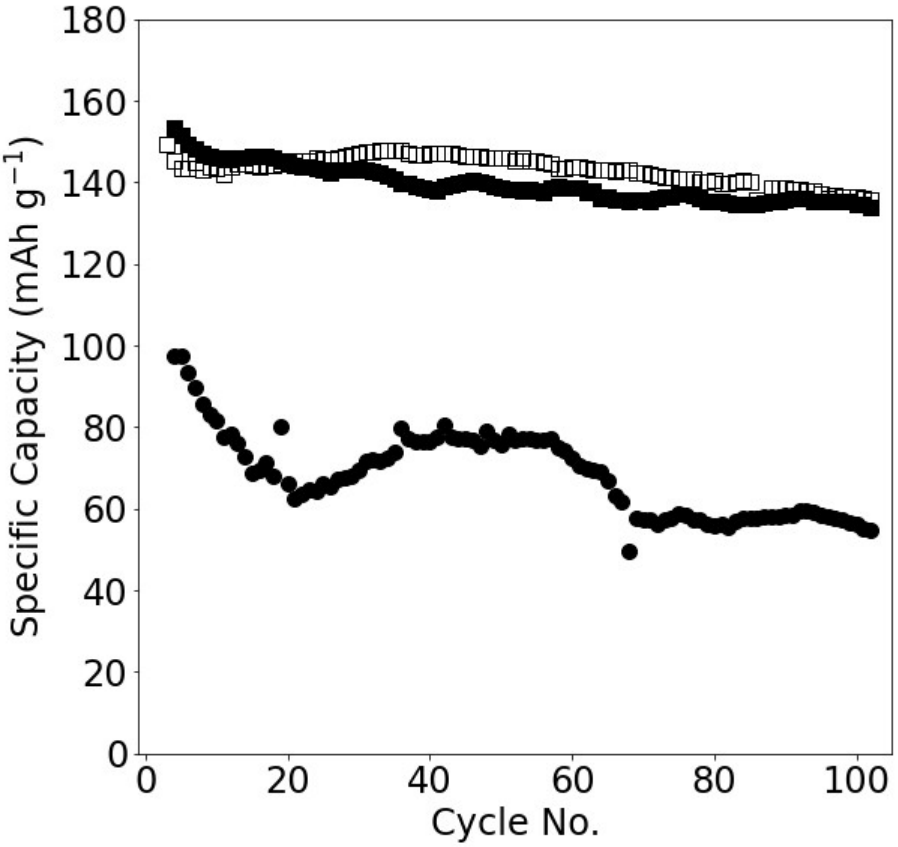

Figure 62: Cycling at 1C for 100 cycles showing representative coin cells from each sample.

5.2.2 Solids Loading Optimization

When working with a new battery system, the formulation needs to be optimized. Pluronics were expected to better stabilize the carbon black flocs in solution due to their amphiphilic nature [109]. Initially, a low solids loading (SL) of 50% was chosen, as this is what was used to produce cathodes with 1000 kg mol^{-1} in Chapter 3. However, the resulting slurry did not coat well and was uneven as shown in Fig. 64a, rendering this formulation unsuitable for cycling. Pluronics have much lower molecular weights than both PVDF and the PEO used in these studies, resulting in lower viscosities of the resulting slurries. A study by Airoldi *et.al.* used a 68% solids loading for a cathode formulation using only pluronic P123 as the binder [109], so the same solids loading was chosen. Increasing the solids loading also increases the percolation of carbon black in both the slurry and solid phases [72], as shown in Fig. 63, where the slurry made with 68% solids loading has a conductivity of 8 ms cm^{-1}, which is around twice as high as the slurry made with 50 wt$ solids loading. Fig. 64b shows a pluronic F127 slurry produced with this solid loading - it is much more homogeneous and more suitable for cycling. Fig. 64c shows a slurry produced with pluronic F68 at 68% solids loading. This cathode shows even more uniformity than the cathode produced with pluronic F127, rendering it more suitable for cycling.

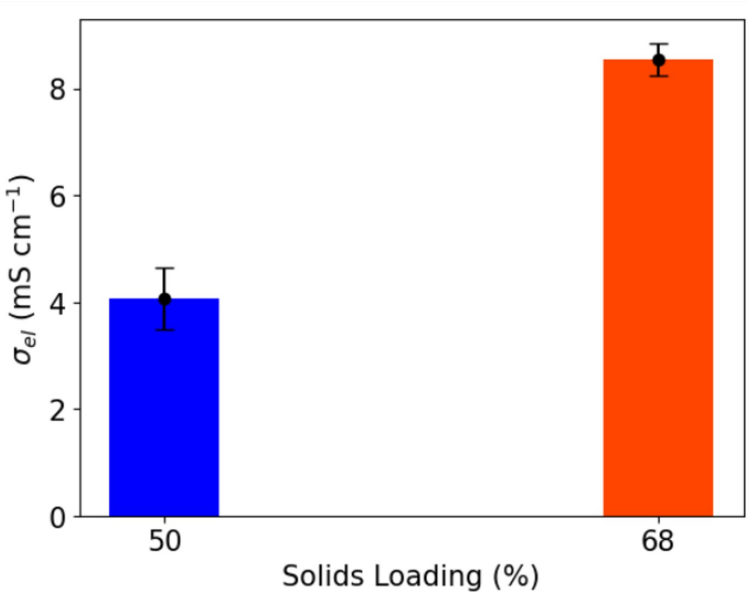

Figure 63: Conductivity of full cathode slurries made with pluronic F68 at low and high solids loadings. Error bars are the standard deviation of three repeats.

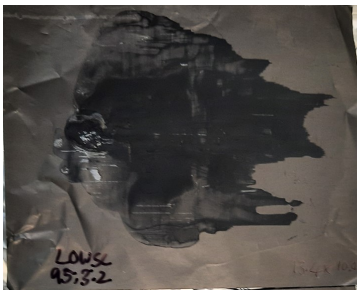

(a)

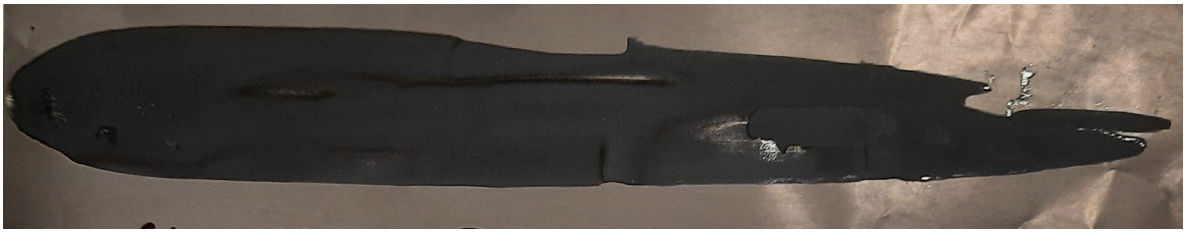

(b)

(c)

Figure 64: Photos of dried cathode films for (a) Pluronic F127 low SL, (b) Pluronic F127 high SL, and (c) Pluronic F68 high SL.

5.2.3 Choice of Pluronics

A selection of pluronics was chosen as shown in Table 19, to investigate the effect of the hydrophobic block size on the electrochemical performance of cathodes. It was proposed that the size of the hydrophobic PO block might affect the distribution of carbon black flocs in the cathode film, which would, in turn, affect the electrochemical performance of the cathode. Coin cell cycling data was obtained for the selected pluronics. The 1st and 100th discharge capacities obtained by cycling coin cells for 100 cycles at 1C is shown in Fig. 65. The mean 1st discharge capacities of F68, F77, F127 and P123 were 120.53, 134.07, 120.90 and 138.29 mAh g^{-1} respectively. All pluronics resulted in good capacity retention, in the 80 to 90% range. Whilst this data is reproducible for all pluronics in this study, the cathodes exhibit little difference in performance. The 1st specific discharge capacity is plotted against the hydrophobic block (PO) Mw (Fig

65c) and number of units in the polymer block (Fig 65d), where it is seen that the hydrophobic block size does not influence the electrochemical performance. Differences in these pluronics as cathode binders may be negligible due to the low Mw, *circa.* 10000 Mw, one to two orders of magnitude lower than the Mws of PVDF and PEO. For further investigation, the pluronic F68 was chosen despite not resulting in the highest 1st discharge capacities, as it offered more facile processing than the others in the series. Cathode films using this pluronic were more uniform, and film cracking was not observed, unlike P123 and F77.

Table 19: Types of pluronics investigated in this chapter

Pluronic Type	PO Block Size (Units)	EO Block Size (Units)	EO wt %	Mw
P123	62	18	30	5800
P217 (F77)	38	53	70	6600
P188 (F68)	30	80	80	8400
P407 (F127)	64	100	70	12500

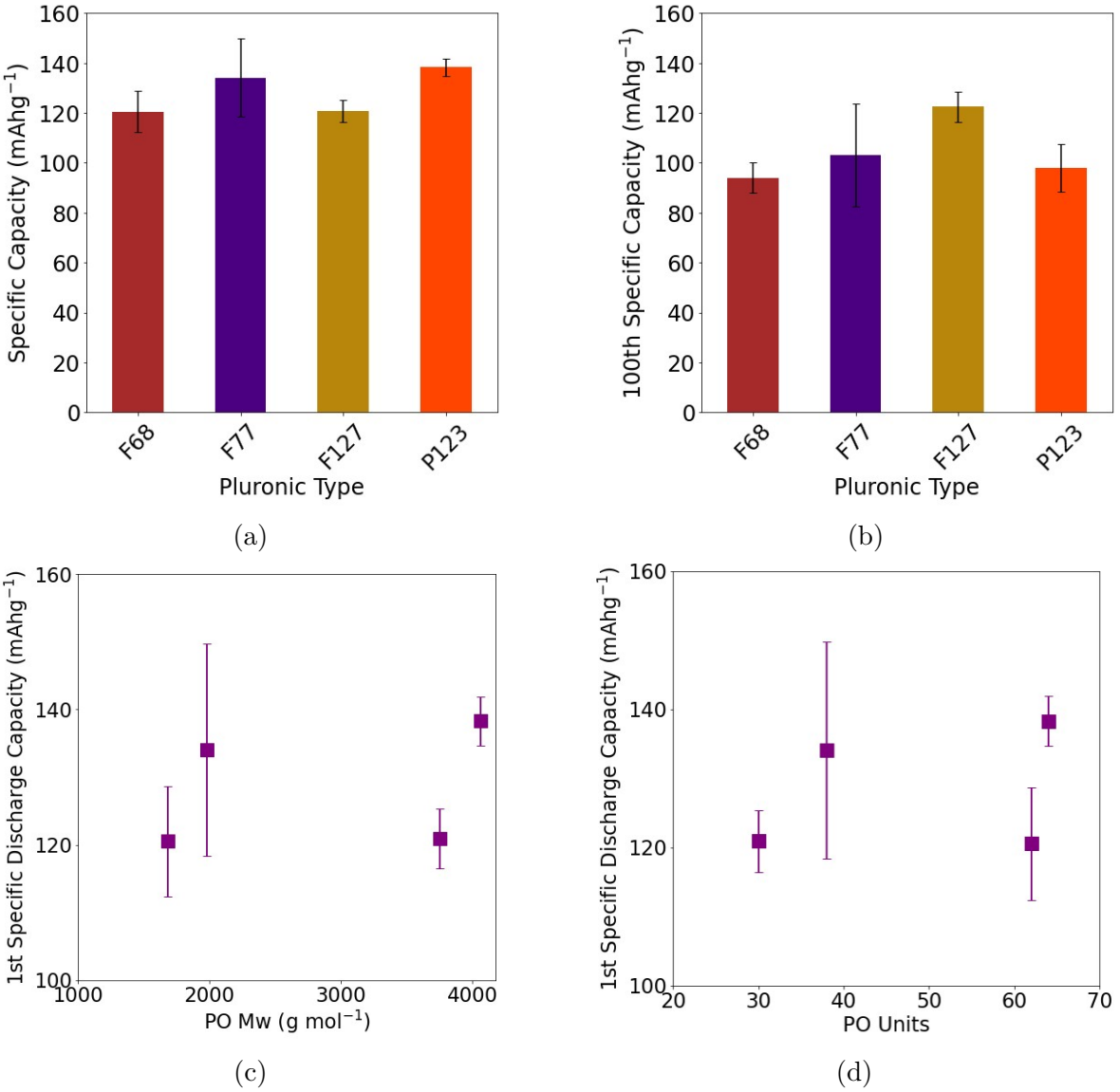

Figure 65: Specific discharge capacities for (a) 1st and (b) 100th cycles for pluronics F68, F77, F127, and P123, and (c) specific capacities plotted against the *Mw* of the hydrophobic PO block, and (d) the number of PO units.

5.2.4 Constant solids loading experiment

As the pluronics series tested in the previous section utilized solutions of 4.255 wt % in DI H_2O, blends using this concentration were produced using PEO and pluronic F68. The viscosity of these blends is shown in Fig. 66a to increase logarithmically with PEO wt %. Experiments were conducted by controlling the cathode slurry solids loading (SL). Polymer solutions were prepared using the same wt % of polymer in water, so the same solution mass was used for each sample. As the viscosity increases with increasing PEO concentration, the viscosity varies across the sample range. Fig. 66 b. shows the 1st specific discharge capacities for all coin cells for these experiments. The electrochemical performance varies non-monotonically with PEO wt% / polymer solution viscosity - there is a peak at 25 wt % PEO in solution. The 100th specific discharge capacities are shown in Fig. 66c, and conversely do not show a trend. This indicates that capacity fade does not correlate with the sample's viscosity. However, this data set is noisy. It has been shown that the de-agglomeration of solids under high shear mixing is non-monotonic with viscosity in colloidal systems [138]. The non-monotonic trend suggests that at low PEO concentrations, the slurry viscosity is not high enough to prevent particle sedimentation, leading to inhomogeneous cathodes. As the PEO concentration increases to 25 wt%, a heterogeneous slurry is achieved by both dispersion of the carbon black via pluronics and the viscosity provided by PEO, resulting in improved electrochemical performance. At high concentrations of PEO and lower concentrations of pluronics, carbon black forms more agglomerates due to fewer pluronics to disperse it, as well as the higher polymer solution viscosity reducing the size of a 3D network of carbon, leading to reduced electrochemical performance.

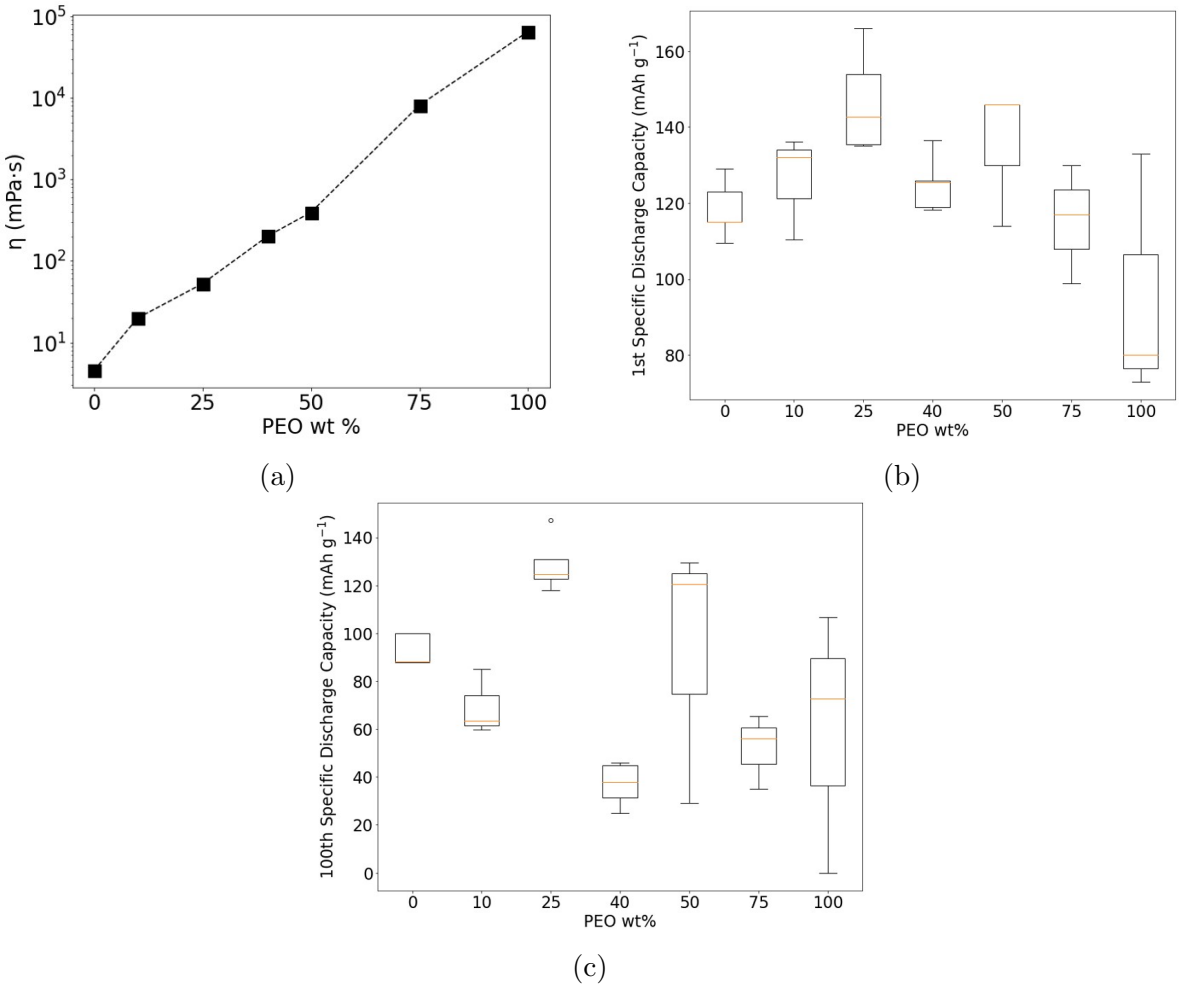

Figure 66: (a) Viscosities of PEO/Pluronic blends in DI water, (b) 1st specific discharge capacities, and (c) 100th discharge capacities of coin half-cells made with these blends.

5.2.5 Viscosity controlled experiments - electrochemical performance

As the cathode microstructure is affected by viscosity of the polymer, experiments to keep the viscosity of polymer blends constant were conducted. A list of these samples are shown in Table 8. Fig. 67c shows data for 100 cycles at 1C for representative samples of PEO:PL F68 blends and conventional NMP/PVDF cathodes. Fig. 67a and b show 1st and 100th discharge capacities of half-coin cells made with PEO/Pluronic F68 blends. The blend with the highest PL F68 ratio is 25% PEO, the maximum achievable pluronics ratio due to sphere packing constraints - above this, cathodes could not be formed because the volumetric concentration of cathode particles in the slurry was greater than 66% - the hard sphere packing limit [184] - see Equation 27 for the

calculation. This blend produced the highest average 1st discharge capacity of 147 mAh g^{-1} (range of 135 - 166 mAh g^{-1}), and an average capacity retention of 86 %. This is comparable to the performance of conventional NMP/PVDF processed cathodes, with a 1st discharge capacity range of 147 - 154 mAh g^{-1}. Cathodes with PL F68 ratios higher than this could not be made due to sphere packing at low SL – see Table 1. This highest-performing blend was obtained from experiments controlling the solids loading (see section 5.2.4). The same trend of decreasing electrochemical performance with decreasing F68 content and increasing PEO content is observed for both solids loading and viscosity-controlled experiments, beyond 25 wt% PEO. By increasing the ratio of surfactant F68 in the blends, the 1st discharge capacity increases. From this data, it is hypothesized CBD is more evenly distributed in cathodes with higher electrochemical performance – leading to the formation of more short-range and long-range electronic contacts of carbon black upon mixing, where short-range contacts are defined as contact between the active material and carbon black, and long-range contacts are percolated carbon black networks in the dried cathode [51]. In this way, the greater distribution of carbon black is likely due to pluronic adsorption, facilitating dispersion in the slurry.

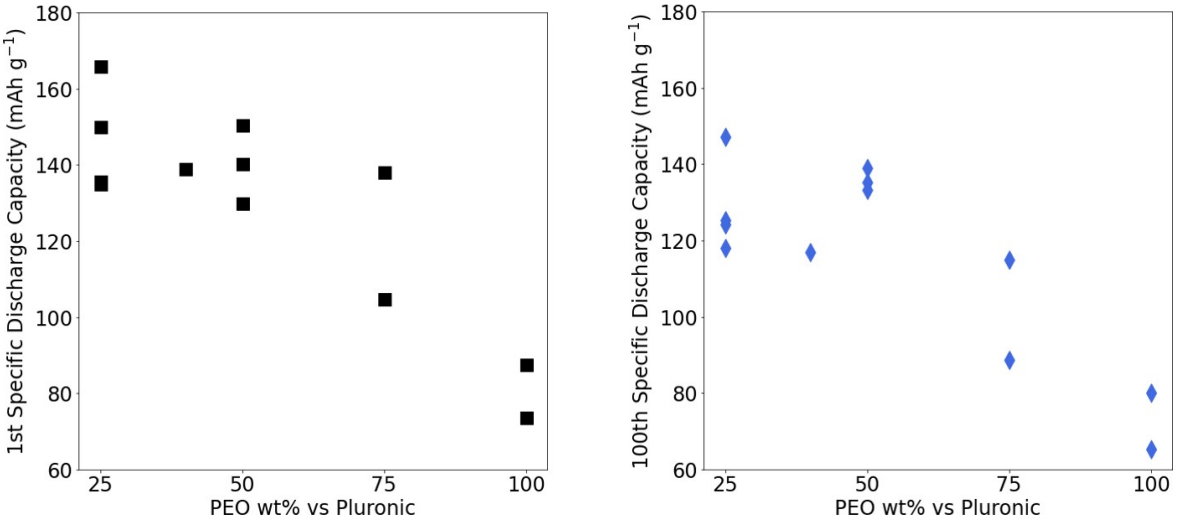

(a) (b)

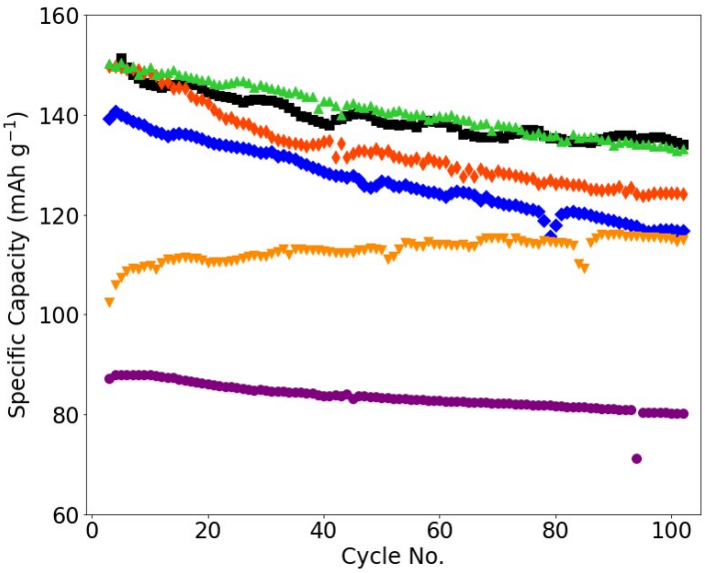

(c)

Figure 67: PEO wt % vs PL for (a) 1st discharge capacity (■), (b) 100th discharge capacity (♦), and (c) capacity fade data for 100 cycles at 1C made with polymer solutions expressed as a ratio of PEO to PL F68: 25% (♦), 40% (◆), 50% (▲), 75% (▼), and 100% (●), and PVDF (■) Each data point in figures 2 (a) and (b) represents a different coin cell.

5.2.6 Cathode cycling performance

The 1st discharge curves are shown in Fig. 68a. Some of these curves show a sudden drop before resuming a normal shape. This feature is not present by the 100th cycle as shown in Fig. 68b. To understand the impact of the binder on the charging and discharging properties of the cathodes, dQdV was calculated. Figs. 68c and d show the dQdV plots respectively for the 1st cycle and 100th cycle at 1C. Here, the dQ/dV data is divided by the mass of active material. For the 100th cycle, the PVDF peak is shifted to a slightly higher oxidation potential, and to a lower reduction potential than the PEO and PEO/PL F68 cathodes. The PVDF has a sharper, more defined peak, so Li is extracted/inserted over a more defined range. Hence, it's a more homogeneous electrode. The broader peaks of the PEO cathode can mean that the electrode differs at different points – is more heterogeneous This means a smoother transition when Li is extracted or inserted. Therefore the PEO only cathode has less reversible capacity.

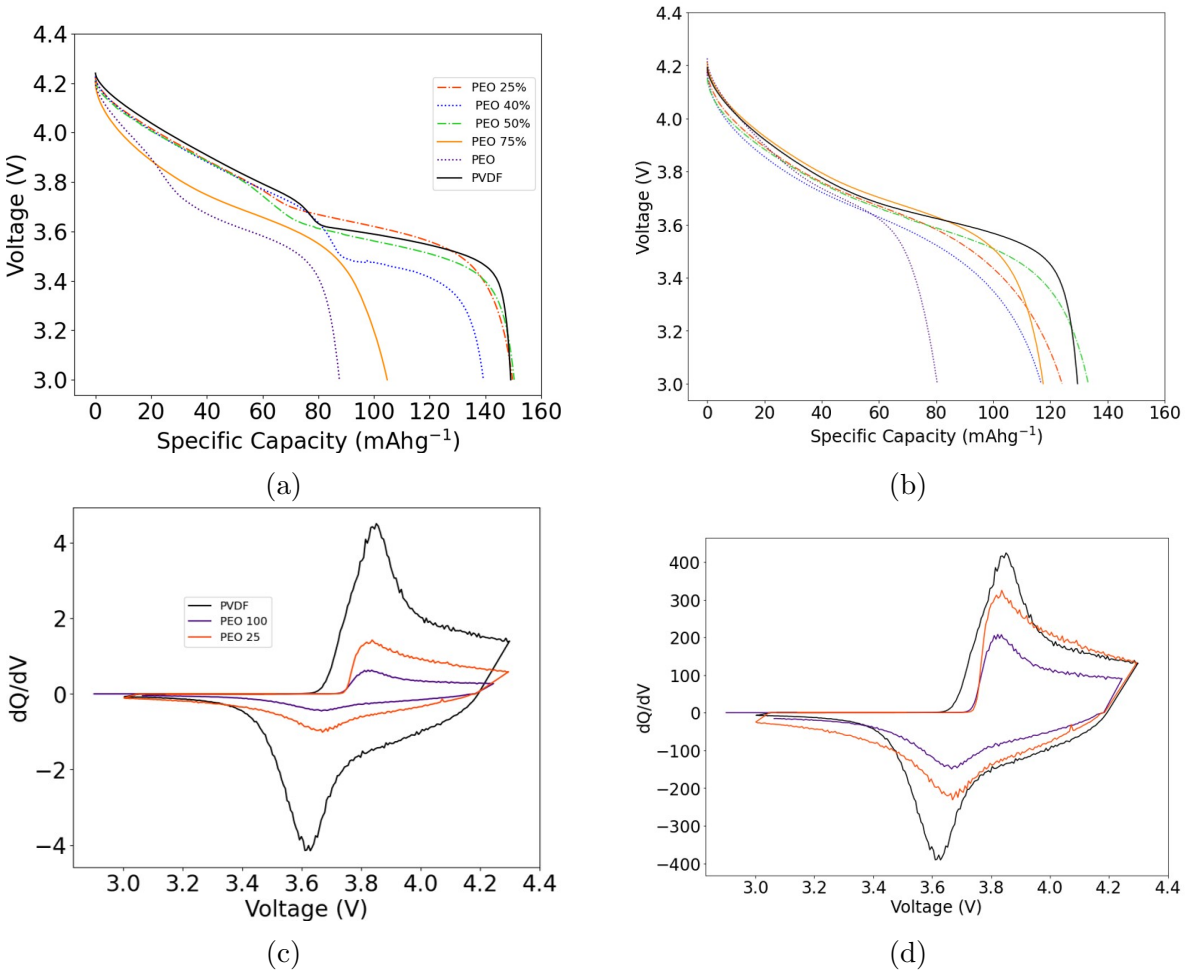

Figure 68: Discharge curves 100 cycles at 1C for all cathodes for (a) cycle 1 and (b) cycle 100, and dQdV curves for (c) cycle 1 and (d) cycle 100, for PEO 100 wt%, PEO 25 wt% and PVDF.

Fig. 69a shows the rate capability data for all cathodes. At low C rates, PVDF has the highest specific capacities. The PEO to Pl F68 ratio is a good indicator of performance at low C rates, as seen in Fig. 69b, and follows the same decreasing trend with PEO ratio as long-term cycling at 1C (Fig. 69c). However at 5C, the sample with 25 wt% PEO and 100 wt% PEO are comparable with PVDF, with capacities of 38.47, 47.69 and 42.54 mAh g^{-1} respectively. It is worth noting that the performance of the PEO 75 wt% dropped to zero from 0.5C to 5C, though the capacity retention at 0.1C was 102%. The PEO/pluronics blends can facilitate good transfer kinetics, which may be a result of PEO being an ionic conductor [95]. This data indicates that high Mw polymer and surfactant blends can be competitive with PVDF.

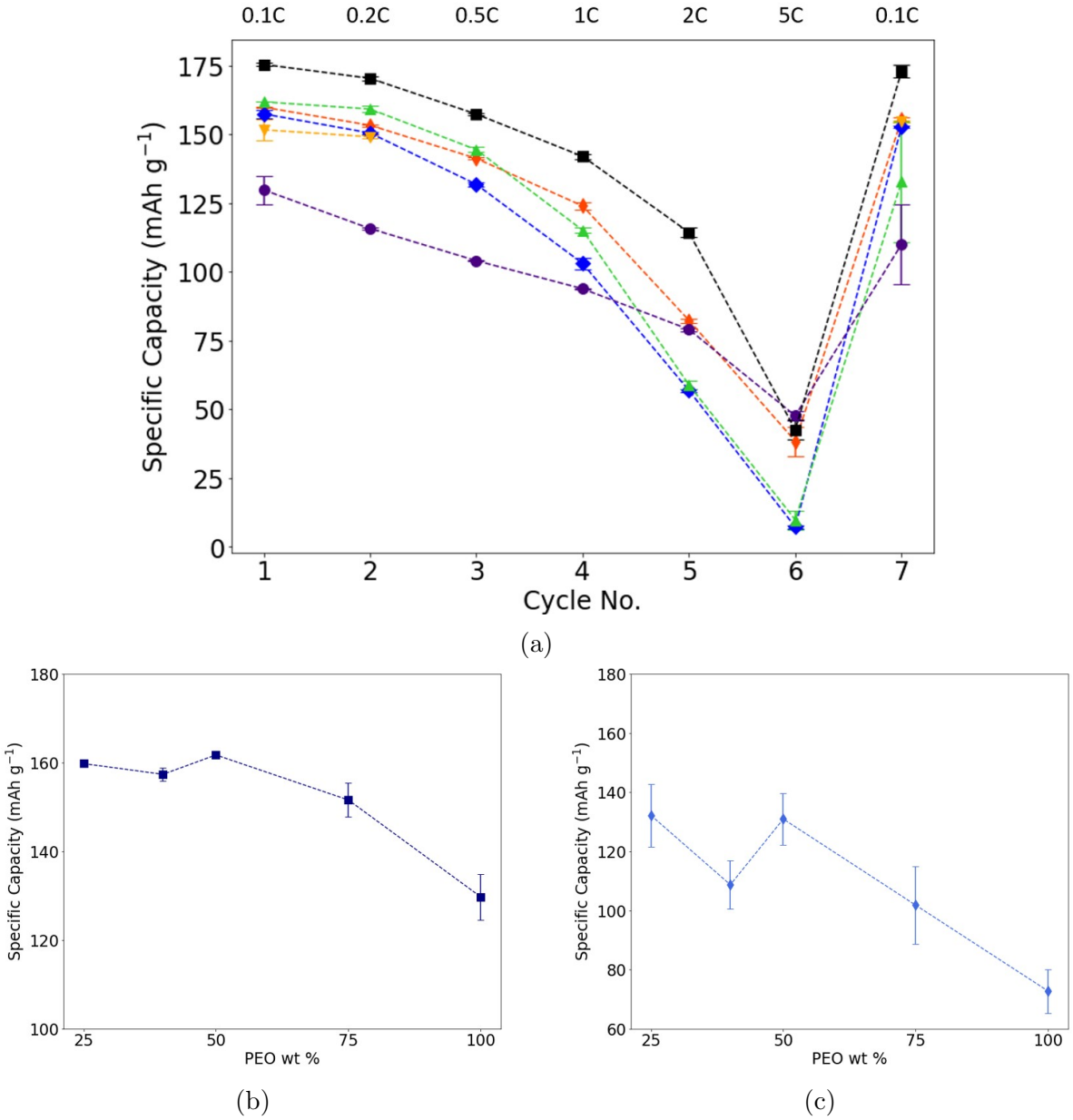

Figure 69: (a) Rate capability performance with five cycles at 0.5C, 1C, 2C, 5C and 0.1C, made with polymer solutions expressed as a ratio of PEO to PL F68: 25% (♦), 40% (◆), 50% (▲), 75% (▼), and 100% (●), and (b) Average discharge capacity for aqueous polymers at 0.1C (1st cycles), and (c) 100th discharge capacities after 100 cycles at 1C. Lines are a guide for the eye.

5.2.7 Viscosity controlled experiments - electrode morphology

SEM images shown in Fig. 70 were taken to show the distribution of CBD around the micron-sized NMC 622 particles for pristine electrodes, i.e. un-cycled. It was hypothesized that increasing the concentration of pluronics would result in a greater distribution of carbon black in both the slurry and the dry electrode. These images show little difference in terms of CBD distribution within the electrode. These images however, show a discrepancy between the size of active material as presented vs the size range of 7 - 19 $u\text{m}^a$ as given by the manufacturer [147]. It is possible that active material particles were broken up upon mixing with carbon black in the mortar and pestle.

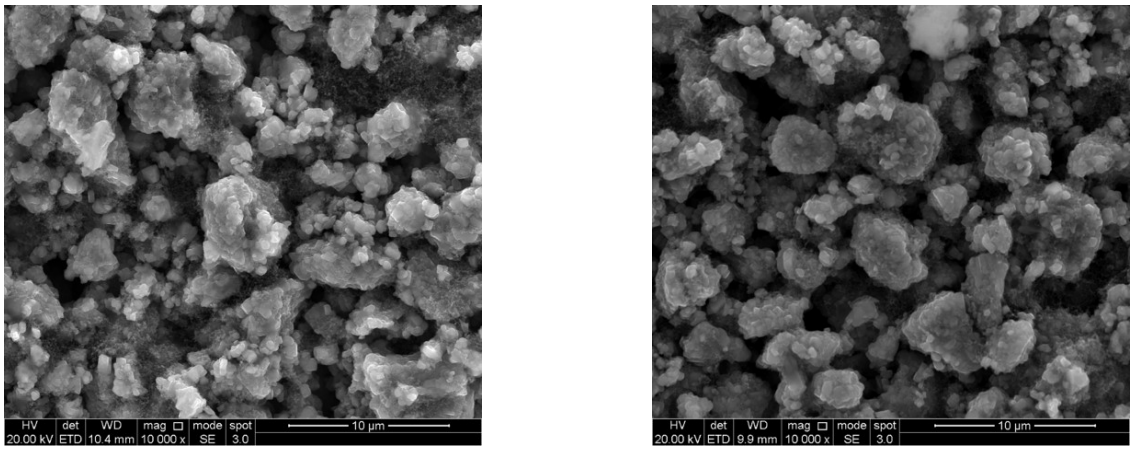

(a)

(b)

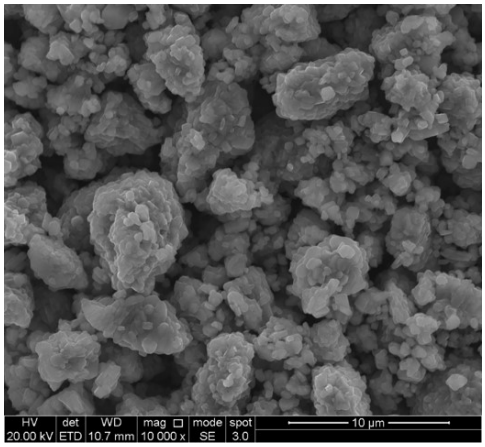

(c)

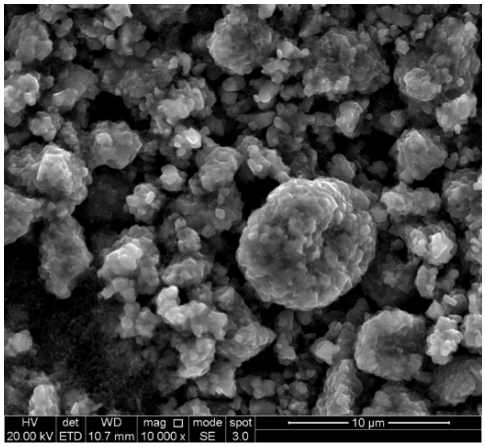

(d)

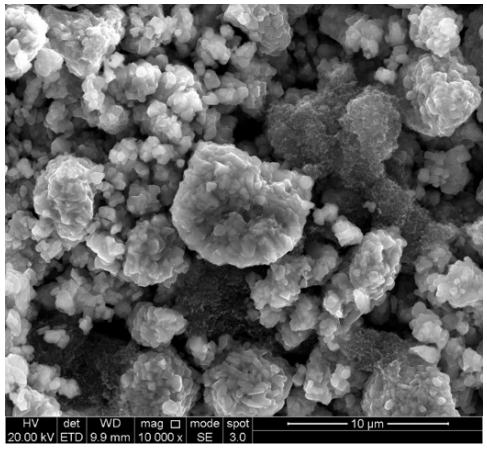

(e)

Figure 70: SEM Images at 10 μm for cathodes containing PEO blends of (a) 25 %, (b) 40 %, (c) 50 %, (d) 75 %, and (e) 100 %.

5.2.8 Cell impedance

EIS measurements were taken between 0.01 HZ and 100000 HZ to further investigate the electrochemical performance of the coin half cells. Impedance measurements were taken before charging at the OCV, and after 100 cycles at 1C at a discharge state. Fig. 71 a. shows the EIS Nyquist plots for coin cells of all formulations before cycling. The semicircle at higher frequencies represents a time constant - indicating the resistance of electrodes, and the 45° line at lower frequencies is the Warburg impedance, which accounts for slow diffusion of ions between electrodes. The electrolyte resistance, R_e, is where the semicircle intercepts the x-axis. The bulk resistance R1, is the value of the plot at the point between the semicircle and the Warburg impedance minus the R_e. The charge-transfer resistance, R_{ct}, is the resistance arising from the Li^+ intercalation reaction in the active materials of the electrode [182]. The pre- cycling R_{ct} values of the 25 and 40 wt% cathodes are 157 and 126 Ω respectively, yet drops to 84 Ω at 50 wt%, then increases to 206 and 189 Ω for 75 and 100 wt% respectively. All cathodes show an increase of R_{ct} after cycling. The PEO 50 wt% sample shows the lowest difference in R_{ct} before and after cycling, and indeed the lowest R_{ct} in the series, which could account for its high capacity retention, suggesting that this cathode exhibited fast lithiation and de-lithiation kinetics [182]. By contrast, R_{ct} for the sample containing only PEO as the binder increased by several orders of magnitude after cycling. In this dataset, the R_{ct} does not correlate to the electrochemical performance of cells produced as this technique is overly sensitive to cell resistances that do not affect the number of ions that diffuse through the electrode. These resistances can be caused by additional contact resistances originating from components i.e. springs and spacers [185]. Further investigation is needed.

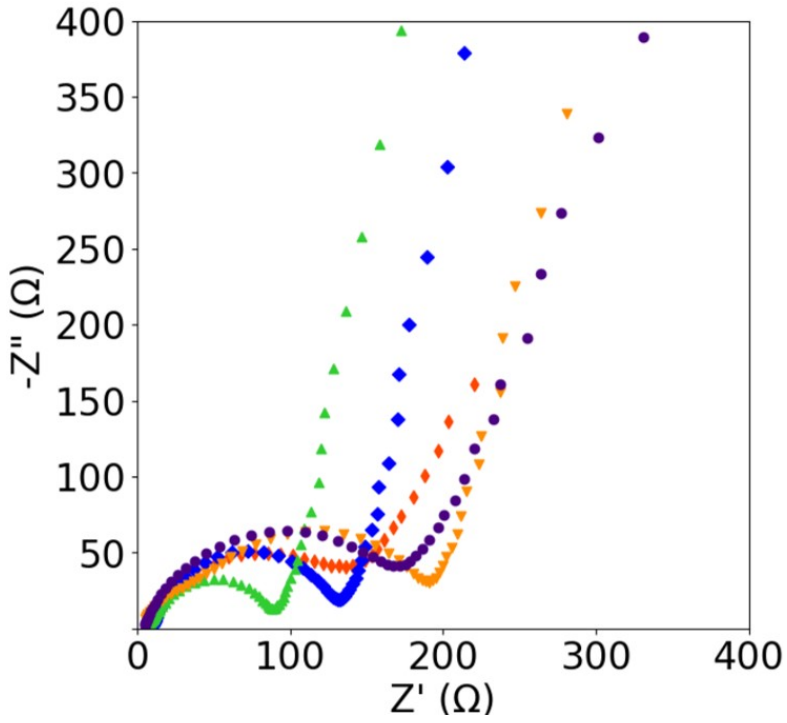

(a)

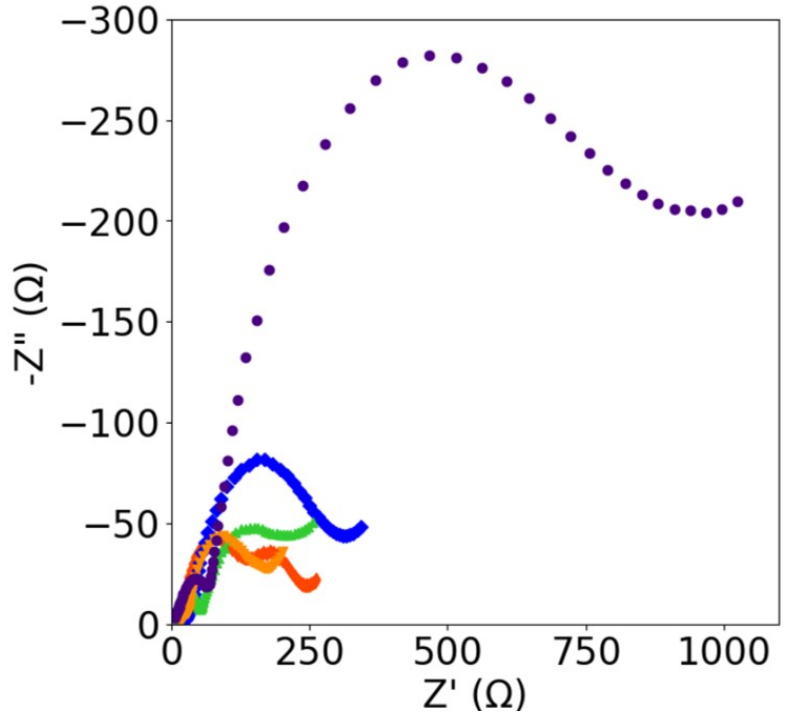

(b)

Figure 71: PEO wt % vs PL EIS, made with polymer solutions expressed as a ratio of PEO to PL F68: 25% (♦), 40% (◆), 50% (▲), 75% (▼), and 100% (●). The data shown is for coin cells cycled in Fig. 67.

5.2.9 Slurry Conductivity

Carbon black is very hydrophobic and does not disperse in water, even under high shear mixing it quickly forms large agglomerates [103], as it is energetically favourable due to strong attractive forces between carbon black primary particles [56]. Upon the addition of an amphiphilic surfactant i.e. pluronics via high shear mixing, it is more energetically favourable for the surfactant to bind to the carbon black particles and prevent re-agglomeration. It is expected that pluronics will stabilize floc sizes of carbon black in aqueous suspension, resulting in more percolated networks of carbon black, as shown in Fig. 76. This will lead to increased connectivity of carbon black flocs, resulting in increased conductivity of slurries and dry cathode films. Thus the conductivity of full cathode slurries was measured. Fig. 72a shows the conductivity of slurries with viscosity controlled. As PEO content increases and PL F68 content decreases, the conductivity of slurries decreases. The conductivity of both slurries and dry cathodes is due to the presence of carbon black, with classical percolation theory used to describe this phenomenon [56]. So samples exhibiting higher conductivity will have more percolated carbon black networks. The presence of such networks in the suspension phase can be attributed to a greater degree of dispersity of carbon black particles. As the conductivity of suspensions increases with increasing PL F68 content, the pluronics likely are facilitating carbon black dispersion to a greater extent than PEO. By contrast, the conductivity of slurries in which the solids loading is controlled is presented in Fig. 72b, where the opposite trend is observed, whereby the conductivity of slurries increases then plateaus with increasing PEO content. As in this case, the wt % of DI H_2O is constant, the trend can be attributed to high Mw PEO facilitating more bridging interactions in which carbon black flocs are connected via adsorbed PEO coils on the surface. The same effect is observed in Chapter 1.

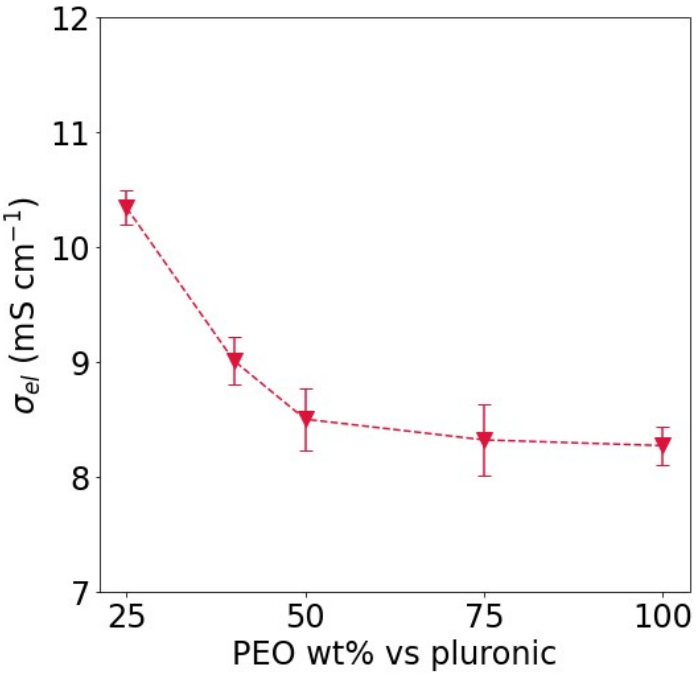

(a)

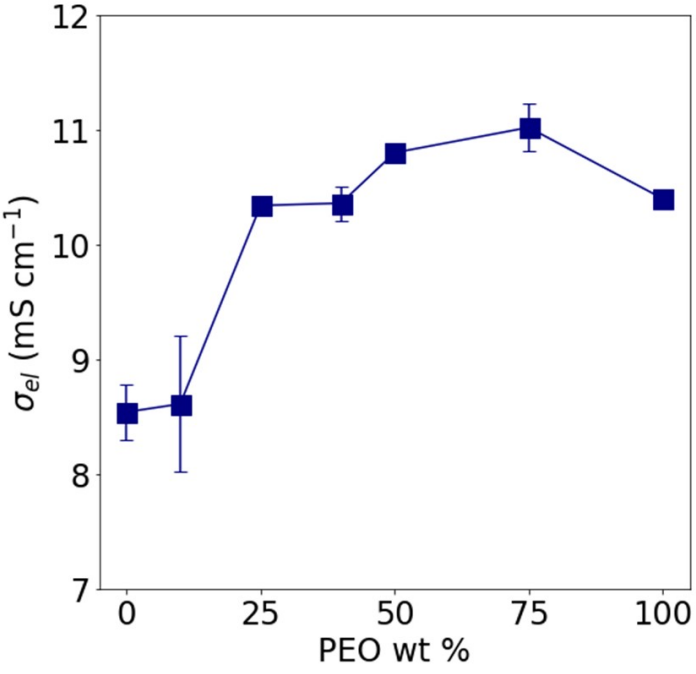

(b)

Figure 72: Conductivity of full cathode slurries made with polymer solutions expressed as a ratio of PEO to PL F68 for (a) viscosity - controlled slurries and (b) solids loading - controlled slurries. Error bars are the standard deviation for three measurements. Lines are a guide for the eye.

5.2.10 Film drying and network formation

Networks of carbon black in the dry film are formed upon film drying. As the solvent evaporates, the film shrinks, leading to the formation of contacts between the active material and conductive additive [103, 145]. A more detailed description of the drying process is given in Chapter 1. In the case of slurries with reasonably well-dispersed carbon black, drying will lead to a 3D interconnected network in the film, which could result in lower resistances and high performance. However, if there is too much percolation of carbon black in the slurry caused by high viscosity of the polymer solution, drying could lead to thick layers or clumps of CBD, which could result in high resistances and therefore low electrochemical performance. This effect is likely the case for solids-controlled slurries; as Fig. 72b shows an increase in conductivity with PEO content, whilst Fig. 66 shows a decrease in electrochemical performance. For electrode formulations, this data indicates that a slurry should be neither too dispersed nor too percolated, in order to form a well-dispersed CBD network in the dry film.

5.2.11 Zeta Potential

A dilute series of slurries comprising only carbon black and the binder blend were prepared to evaluate the effect of polymer adsorption on the stability of carbon black agglomerates. It was hypothesised that pluronics would stabilise flocs of carbon black, so zeta potential measurements were taken. A lower concentration of binder (1 wt%) was used to reduce the effects of different initial viscosities on the size of carbon black particles deagglomerated by shear mixing. Fig. 73 shows the dependence of zeta potential on the PEO to PL F68 ratio. The sample containing no PEO has a zeta potential value of + 59 mV, whilst the sample containing no pluronics has a value of - 20 mV. The different signs indicate that pluronic adsorption on carbon black results in a positive surface charge on the resulting colloids, and the reverse for the PEO-only containing samples. Increasing the PEO fraction of PEO in the binder blend led to a relatively monotonic decrease in zeta potential. The composition of binder adsorbed to the carbon black changes nearly linearly with the composition of binder in the solution. The first 5 samples are in the stable region, yet when the PEO to PL F68 ratio reaches 75%, the zeta potential is below +30 mV. The fact that the surface potential of carbon black varies systematically with the composition of binder indicates that both polymers have a roughly commensurate affinity for carbon black, otherwise one polymer would preferentially adsorb.

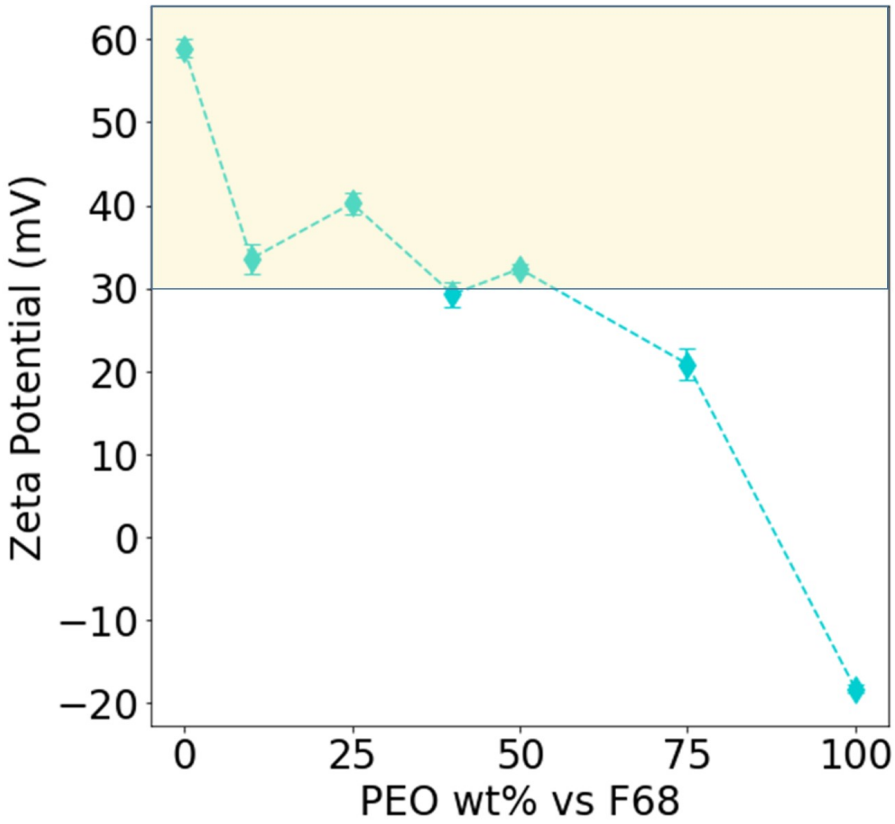

Figure 73: Zeta potential of carbon black/polymer slurries. The dashed line is a guide for the eye. The shaded yellow area represents the stability region.

5.2.12 Particle Size

Following the zeta potential measurements, it was hypothesized that stable suspensions containing pluronics contained smaller flocs of carbon black. DLS measurements were taken to determine the effect of pluronic content on carbon black particle size in the cathode slurry. Slurries were prepared without polymer, PL F68 only, and PEO/pluronic blends. Fig. 74 shows the mean carbon black particle diameters of these slurries. The mean diameter of carbon black particles is high, then increases upon adding PEO. The mean diameter of carbon black flocs from the sample prepared without polymer was 331 nm, with great uncertainty in this data point. This value is greater than all the samples containing PL F68. The effect of surfactant concentration on reducing carbon black floc size is documented in the literature, as the adsorbed surfactant results in steric stabilization between particles [80]. The increase in mean carbon black particle diameter implies that PL F68 reduces the size of carbon black

flocs upon mixing. During the mixing process, carbon black flocs are broken up, and the pluronics are likely adsorbing onto the carbon black surfaces, causing steric repulsion between the resulting carbon black/PL F68 colloids. The plateau implies that PEO does not preferentially adsorb onto the carbon black surface in place of PL F68.

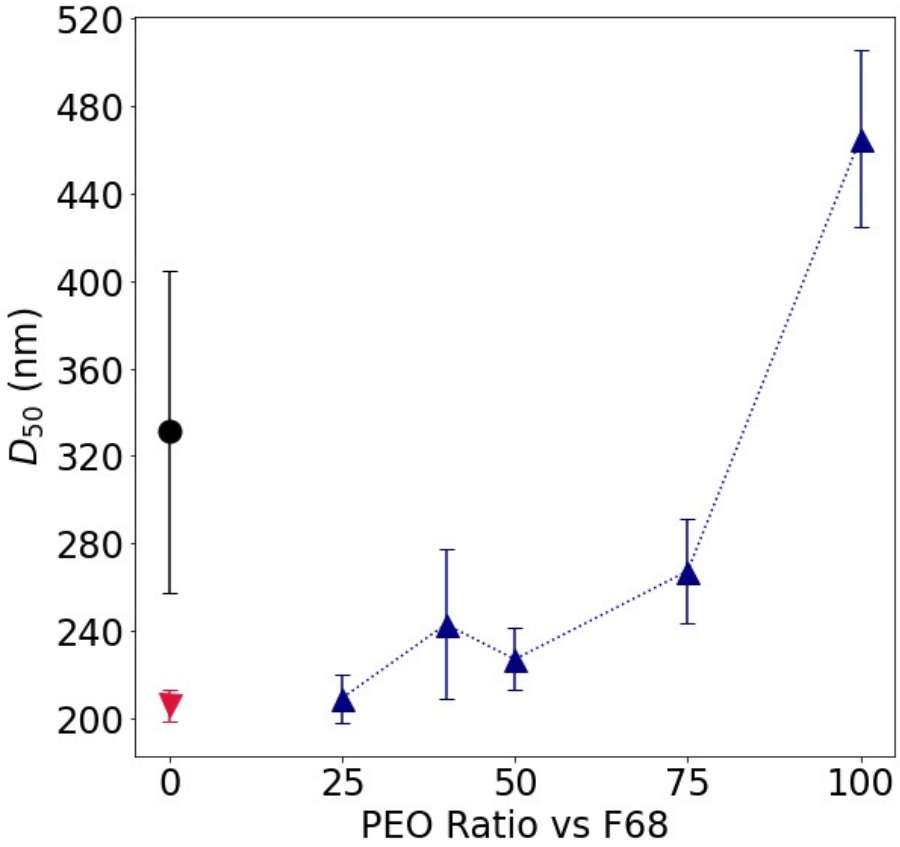

Figure 74: Particle size of carbon black flocs as determined by DLS measurements, showing data from slurries with no polymer (●), PL F68 (▼), and blends of PEO and PL F68 (▲). Error bars are ther standard deviation of three measurements.

5.2.13 Polymer and carbon black interactions

Studies have shown that the work of adhesion of carbon black-PVDF is lower than that of carbon black-NMP, indicating carbon black interacts weakly with PVDF in NMP [102]. This is illustrated in Fig. 75, which shows large loops of PVDF and small trains of polymer adsorbed onto the carbon black surface, and a smaller excluded radius of the polymer coil. Carbon black interacts weakly with water in aqueous systems as it is very hydrophobic. Using pluronics as a surfactant, it is hypothesized that the

hydrophobic PPO block would interact strongly with carbon black, and the hydrophilic PEO chains would aid dispersion of carbon black flocs in water. This is illustrated on the left of Fig. 76, which shows the adsorption of a pluronic molecule onto the carbon black surface. The PPO chain is shown to adsorb onto the carbon black surface leading to long trains, and the PEO side chains forming spiky 'brushes' and stretching into the solvent. These long 'brushes' of PEO would result in smaller flocs of carbon black in suspension due to more steric repulsion between polymer chains, as shown on the right of Fig. 76.

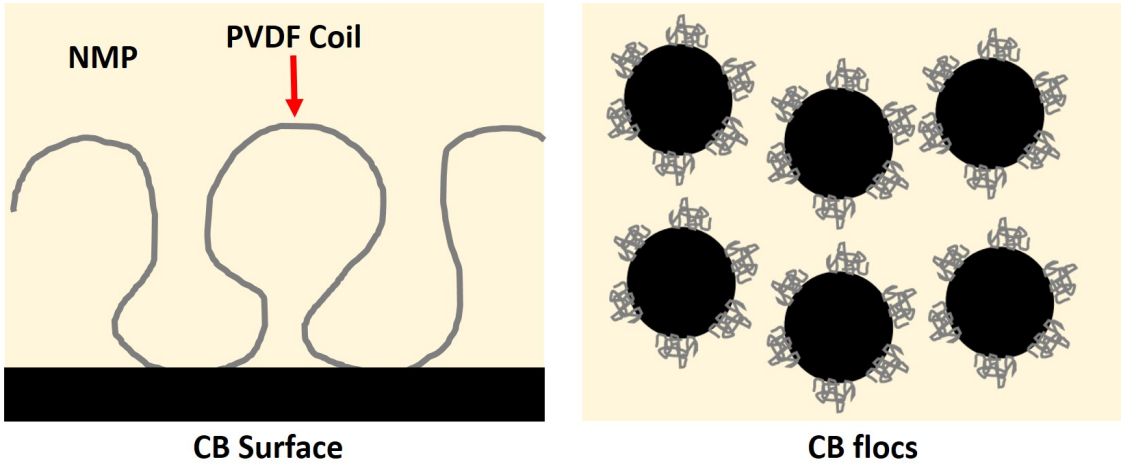

Figure 75: Schematic showing adsorption of PVDF on carbon black in NMP (left) and carbon black flocs (right).

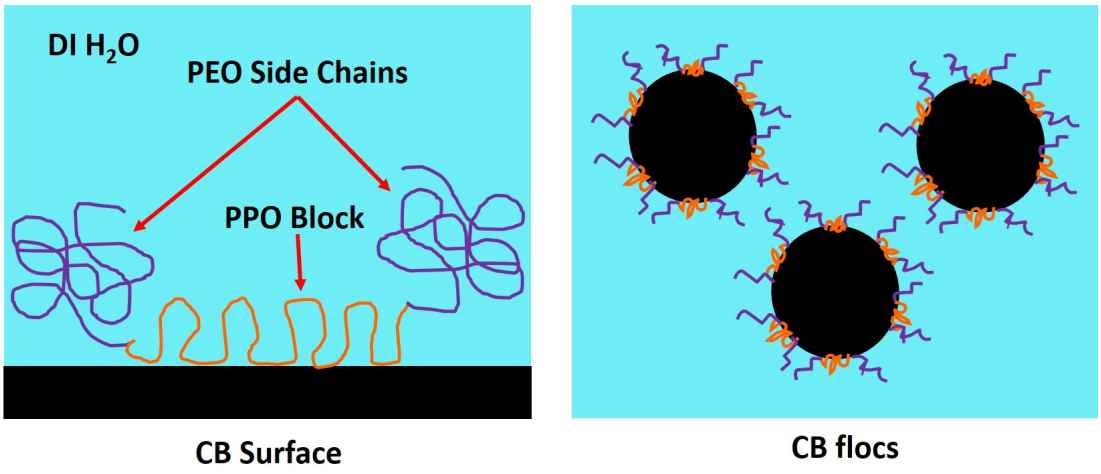

Figure 76: Schematic showing adsorption of Pluronics on carbon black in DI H_2O (left) and carbon black flocs (right).

5.2.14 Frequency Sweeps

The rheological properties of electrode slurries directly affect the coating process and microstructure [70]. It has been shown that slurries consisting of NMC and polymer do not form a stable gel, suspensions consisting of carbon black and polymer do so via forming a percolated network. So in full cathode slurries, percolated carbon black networks stabilize the heavier cathode particles from sedimentation [51]. The viscosity of cathode slurries is known to affect the dispersion of carbon black; viscous polymer solutions dissipate more of the mechanical energy applied by shear mixing than less viscous solutions, resulting in less de-agglomeration of the carbon black. To control for this effect, the viscosity of the precursor polymer solutions was controlled across the range of binder compositions. The viscoelastic properties of the resulting cathode slurries are measured using low-amplitude oscillatory shear, as shown in Fig 77(a). With increasing PL F68 content, the storage modulus (G') overall shows an increase and a reduced dependency on frequency, indicating a higher solids content. All slurries exhibit a crossover of storage and loss moduli, likely caused by particle-particle collisions at high frequencies.

The loss factor, or tan δ, is a measure of how plastic or liquid-like (tan $\delta \leq 1$) or elastic or solid-like (tan $\delta \geq 1$) a material is. The loss factor is calculated by dividing the averaged values as such - tan δ = [G"/G']. Fig 77(b) shows the tan δ plots for all aqueous slurries. All slurries exhibit similar behaviour: liquid-like flow at low frequencies with an increasingly elastic response at high frequencies. The loss tangents for all samples overlap strongly, indicating no significant mechanical difference between the samples. This means that chemical effects of blending can be studied independently of the rheological effects.

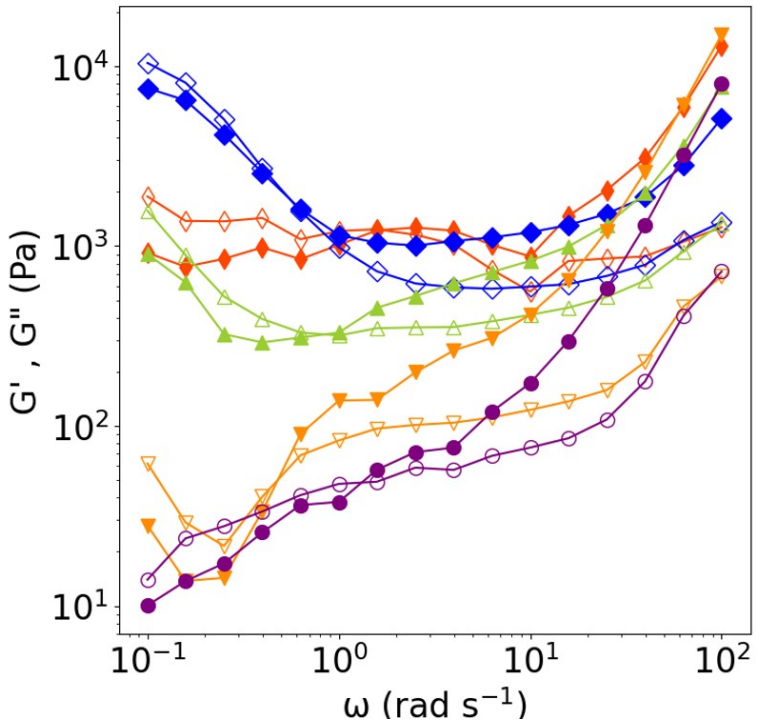

(a)

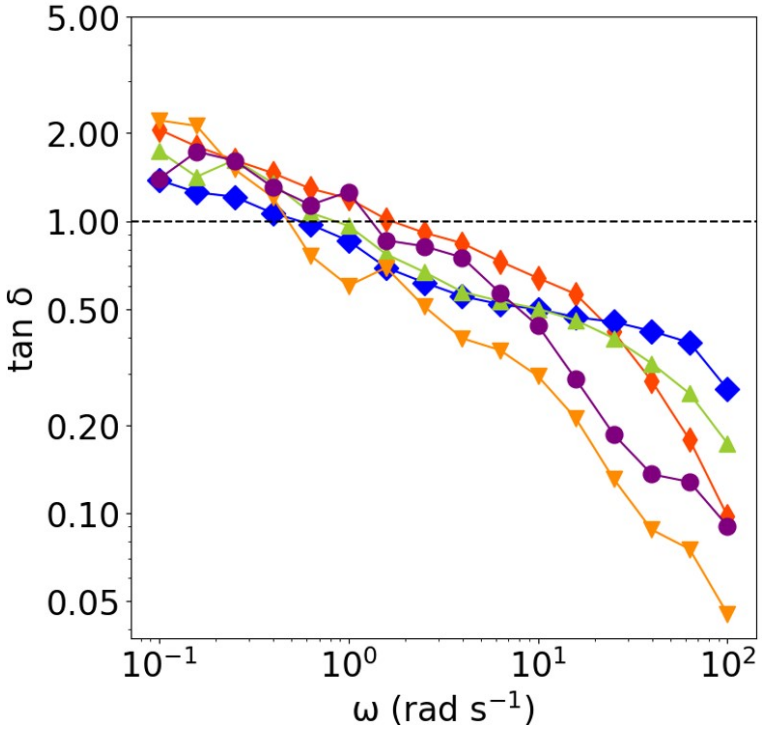

(b)

Figure 77: Frequency sweeps of viscosity-controlled slurries, showing (a) the storage and loss moduli, and (b) the tan δ data, for PEO 25% (♦), 40% (◆), 50% (▲), 75% (▼), and 100% (●). In Fig. 77 (a), filled symbols represent G', and open symbols represent G".

5.3 Conclusions

The effect of the ratio of a high molecular weight polymer with a low molecular weight surfactant on the electrochemical performance of NMC 622 cathodes was investigated. Electrochemical testing was performed by cycling half coin cells at 1C and rate capability tests. The electrical properties of cells were analyzed using EIS, whilst the electrical properties of cathode slurries were measured using a two-point probe. The particle sizes of carbon black were analyzed using DLS measurements. The morphology of the slurries were characterized via rheological frequency sweeps, and SEM was used for the morphology of particles in the dry films.

Pluronics were investigated as binders for aqueous processed cathodes due to their amphiphilic nature. A series of pluronics were selected to determine whether the size of the hydrophobic PO block would affect the carbon black distribution in the electrode, and subsequently the electrochemical performance of half-cells. No correlation was found between electrochemical performance and the PO block size. A limitation in this study was that the pluronics studied were all of low molecular weight; so the viscosity provided by the pluronics was insufficient to form homogeneous cathode slurries and dry films. Therefore, PEO was chosen to act as a viscosity modifier. Blending the miscible binders enables a high degree of control over the viscosity of the cathode slurry, enabling formulations with a high solid loading and consequently lower energy requirements for drying.

Pluronics and PEO adsorb strongly onto the surface of carbon black, though neither binder alone results in a strong electrochemical performance. Blending at least 75 wt% Pluronic into a combined Pluronic/PEO binder phase stabilizes carbon black particles as small as 200 nm in the cathode slurry. Controlling the solids loading, the electric conductivity of the cathode slurries decreases with the size of carbon black particles, suggesting that the adsorption of Pluronic creates an electrically insulating layer. Once dried, there is no correlation between the impedance of cathodes and their composition, nor any microscopic evidence of differences between the samples; however, there is a clear optimum in the discharge capacity of battery half cells when the composition of the binder is 75:25 pluronic:PEO. These optimized cells exhibit capacity-fade profiles that overlap with that of a conventional PVDF/NMP cell at 1C, and outperform the PVDF/NMP cell at 5C.

Controlling either the solids loading or the polymer solution viscosity results in the same trend of decreasing electrochemical performance with increasing PEO to pluronics ratio beyond an optimum ratio. With the solids loading-controlled series, the 25 wt% PEO sample with optimal performance is a peak, with performance increasing from 0% PEO. With the viscosity-controlled series, slurries made with below 25 wt% PEO could not be coated due to the limitation around the hard sphere packing limit of 66 vol%; higher loadings cannot be coated and formed into working cells.

This chapter demonstrates that aqueous-processed battery half-cells containing high nickel NMCs can achieve the same performance as those processed with conventional organic solvents when the formulation is adapted to compensate for the hydrophobicity of carbon black.

6 Conclusions & Future Work

6.1 Conclusions

The overarching aim of this thesis was to understand and control the formulation and processing of aqueous cathode slurries to optimize Li-ion battery performance. This was achieved by systematically varying the binder-to-carbon black ratio to control the cathode slurry microstructure, quantifying the chemical affinity of different aqueous polymers to carbon black and studying the effect of this affinity on electrochemical performance, and studying the effect of a chosen surfactant on carbon black dispersion and electrochemical performance.

In Chapter 3, the microstructure of aqueous cathode slurries was investigated using rheology and conductivity measurements. Two high molecular weights of PEO were selected, and the concentrations were systematically varied to match the viscosity of polymer solutions with different molecular weights. It was found that the polymer concentration in the slurry could control the percolation of carbon black, as shown by conductivity measurements and amplitude sweeps, which revealed that percolated slurries without active material formed gels. For slurries exhibiting a yield stress, it was found that the yield stress was not a predictor of other slurry properties, namely, conductivity and high shear viscosity. This could be due to the 3D networks of carbon black being weakly connected, requiring a low stress to induce flow. Slurry conductivity is therefore likely a result of the number and extent of carbon black networks, and not their strength. In an aqueous system, the polymer was shown to have the most effect on the rheological properties of the slurry, agreeing with the literature [70]. The presence of large active material particles was shown to impede the formation of 3D conductive networks, determined by measuring both the slurry conductivity, and the amplitude sweep data of the single solid slurries. Whilst percolated PEO slurries appeared homogeneous, the electrochemical performance of half-coin cells made with PEO did not perform as well as half-coin cells conventionally made with NMP/PVDF.

The aims of Chapter 4 were to determine whether the chemical affinity of aqueous polymers to carbon black affected its distribution in the slurry and the dry film, and to determine whether the chemical affinity could predict electrochemical performance. Using a selection of binders studied frequently in literature, the chemical affinity of polymer to carbon black was quantified via adsorption measurements and Langmuir

fits. The determined chemical affinity was shown to affect the dispersion of carbon black particles in aqueous suspension, via conductivity measurements. The chemical affinity was also indirectly shown to positively affect electrochemical performance, possibly due to greater distribution of carbon black in the dried film. The distribution of carbon black in the slurry is likely to affect the distribution in the dry film. This is implied by the increase in cathode porosity with slurry conductivity. Highly conductive slurries may have less carbon black distribution, which could cause poorly distributed CBD in the dry cathode. This hypothesis is supported by the inverse relationship between slurry conductivity and porosity on electrochemical performance, which itself is attributed to high porosities resulting from inhomogeneously distributed CBD throughout the electrode. The homogeneity of the electrode was investigated by dQdV plots, which revealed that the inhomogeneous cathodes were those made with slurries with poor distribution of carbon black. The chemical affinity parameter was also shown to indirectly affect the resulting cell resistance, as shown by EIS measurements. The polymers Pluronic F68 and PEO adsorbed the strongest onto carbon black relative to chitosan, sodium alginate, PVP, and CMC; but neither binder on its own yielded highly performing battery half-cells.

In Chapter 5, it was chosen to systematically investigate blends of the surfactant pluronic F68 with a high molecular weight PEO, following the findings from Chapter 4. In one set of experiments, the solids loading was controlled, and in another set, the viscosity of the polymer blends was controlled. For both experiments, the highest electrochemical performance was seen using a blend consisting of 25 wt% PEO and 75 wt% pluronic F68. This blend resulted in electrochemical performances comparable to cells made with NMP/PVDF. From the solids loading controlled series, the electrochemical performance varies non-monotonically with the PEO ratio. At low PEO content, the slurry viscosity is not high enough to prevent particle sedimentation, leading to inhomogeneous cathodes. As the PEO concentration increases to 25 wt%, a heterogeneous slurry is achieved by both dispersion of the carbon black via pluronics and the viscosity provided by PEO, resulting in improved electrochemical performance. At high concentrations of PEO and lower concentrations of pluronics, carbon black likely forms more agglomerates due to fewer pluronics to disperse it, as well as the higher polymer solution viscosity reducing the size of a 3D network of carbon, leading to reduced electrochemical performance. The trend of increasing pluronics content with improved electrochemical performance was also observed in the viscosity-controlled series from 25

wt% PEO, though working half-cells could not be made with PEO content below this due to sphere packing constraints at 66 vol%. These trends indicate that the effects of the surface chemistry between polymer and carbon additive contribute more to electrochemical performance than viscosity and solids-loading. The dispersion of carbon black was investigated via slurry conductivity measurements, zeta potential of dilute carbon black/ polymer suspensions, and particle sizing via DLS, all techniques showing that a greater proportion of pluronics leads to smaller flocs of carbon black and greater distribution in the slurry. The overall conclusion was that increasing the amount of pluronic adsorbs strongly to carbon black, prevents large agglomerates from forming, therefore allowing greater distribution in the cathode, which by creating more electronic conductive pathways, improves the electrochemical performance of the cathode.

6.2 Future Work

The following suggestions are outlined to further optimize the processing of aqueous cathodes based on the conclusions of this thesis:

Investigate the effect of the size of the hydrophobic block on carbon black distribution and electrochemical performance. Whilst this was attempted in Chapter 5, no discernable difference was seen between different pluronics. However, based on results from the same chapter where a high molecular weight PEO was used as a viscosity thickener, it is recommended that this study is repeated using blends of PEO and pluronics.

Move to higher Ni NMC cathode active materials, i.e. compositions of NMC 811. As discussed in Chapter 1, increasing the Ni content results in higher theoretical capacities of active materials, though NMC 811 has been studied less for aqueous processing due to transition metal leaching. To mitigate this, coatings on NMC 811 should be used. The aim would be to determine whether cathodes made with PEO/pluronic blends are competitive with PVDF using higher Ni NMCs.

Investigate amphiphilic polymers with different chemistries as the hydrophobic block. Examples could include polylactic acid or polycaprolactam.

7 Bibliography

References

[1] HM Government. Taking charge: the electric vehicle infrastructure strategy. Unpublished Manuscript, 2022.

[2] Richard Schmuch, Ralf Wagner, Gerhard Hörpel, Tobias Placke, and Martin Winter. Performance and cost of materials for lithium-based rechargeable automotive batteries. *Nature Energy*, 3(4):267–278, 2018.

[3] Samuel G Booth, Alisyn J Nedoma, Nirmalesh N Anthonisamy, Peter J Baker, Rebecca Boston, Hugo Bronstein, Simon J Clarke, Edmund J Cussen, Venkateswarlu Daramalla, Michael De Volder, et al. Perspectives for next generation lithium-ion battery cathode materials. *Apl Materials*, 9(10):109201, 2021.

[4] M.Dowson. From research and manufacturing to application and end of life – enabling electrification across sectors. Unpublished Manuscript, 2020.

[5] Brent C Melot and J-M Tarascon. Design and preparation of materials for advanced electrochemical storage. *Accounts of chemical research*, 46(5):1226–1238, 2013.

[6] Weikang Li, Yoon-Gyo Cho, Weiliang Yao, Yixuan Li, Ashley Cronk, Ryosuke Shimizu, Marshall A Schroeder, Yanbao Fu, Feng Zou, Vince Battaglia, et al. Enabling high areal capacity for co-free high voltage spinel materials in next-generation li-ion batteries. *Journal of Power Sources*, 473:228579, 2020.

[7] Chaofeng Liu, Zachary G Neale, and Guozhong Cao. Understanding electrochemical potentials of cathode materials in rechargeable batteries. *Materials Today*, 19(2):109–123, 2016.

[8] Da Deng. Li-ion batteries: basics, progress, and challenges. *Energy Science & Engineering*, 3(5):385–418, 2015.

[9] CL Tsai, Q Ma, C Dellen, S Lobe, F Vondahlen, A Windmuller, D Gruner, H Zheng, S Uhlenbruck, M Finsterbusch, et al. Building better batteries m. armand and j.-m. tarascon researchers. *Sustainable Energy Fuels*, 3:280–291, 2019.

[10] Bernard Lestriez. Functions of polymers in composite electrodes of lithium ion batteries. *Comptes Rendus Chimie*, 13(11):1341–1350, 2010.

[11] Jianlin Li, Beth L Armstrong, Jim Kiggans, Claus Daniel, and David L Wood III. Optimization of lifepo4 nanoparticle suspensions with polyethyleneimine for aqueous processing. *Langmuir*, 28(8):3783–3790, 2012.

[12] Ki Yeon Cho, Young Il Kwon, Jae Ryoun Youn, and Young Seok Song. Interaction analysis between binder and particles in multiphase slurries. *Analyst*, 138(7):2044–2050, 2013.

[13] Graham Swift. Directions for environmentally biodegradable polymer research. *Accounts of Chemical research*, 26(3):105–110, 1993.

[14] RUSTGI Chandra and Renu Rustgi. Biodegradable polymers. *Progress in polymer science*, 23(7):1273–1335, 1998.

[15] Flash Battery. Electric vehicle batteries global market report 2023.

[16] National Grid. How much of the uk's energy is renewable?

[17] Wangda Li, Evan M Erickson, and Arumugam Manthiram. High-nickel layered oxide cathodes for lithium-based automotive batteries. *Nature Energy*, 5(1):26–34, 2020.

[18] CC Change. Net zero the uk's contribution to stopping global warming. 2019.

[19] The Faraday Institution. Faraday battery challenge projects, Sep 2023.

[20] John B Goodenough. Changing outlook for rechargeable batteries, 2017.

[21] Wen Qi, Joseph G Shapter, Qian Wu, Ting Yin, Guo Gao, and Daxiang Cui. Nanostructured anode materials for lithium-ion batteries: principle, recent progress and future perspectives. *Journal of Materials Chemistry A*, 5(37):19521–19540, 2017.

[22] Joe C Stallard, Laura Wheatcroft, Samuel G Booth, Rebecca Boston, Serena A Corr, Michaël FL De Volder, Beverley J Inkson, and Norman A Fleck. Mechanical properties of cathode materials for lithium-ion batteries. *Joule*, 2022.

[23] Dean J Miller, Christian Proff, JG Wen, Daniel P Abraham, and Javier Bareño. Observation of microstructural evolution in li battery cathode oxide particles by in situ electron microscopy. *Advanced Energy Materials*, 3(8):1098–1103, 2013.

[24] Christopher J Orendorff. The role of separators in lithium-ion cell safety. *The Electrochemical society interface*, 21(2):61, 2012.

[25] Lithium-ion batteries: Modelling and state of charge estimation.

[26] John B Goodenough and Youngsik Kim. Challenges for rechargeable li batteries. *Chemistry of materials*, 22(3):587–603, 2010.

[27] Chaofeng Liu, Zachary G Neale, and Guozhong Cao. Understanding electrochemical potentials of cathode materials in rechargeable batteries. *Materials Today*, 19(2):109–123, 2016.

[28] Tianyu Li, Xiao-Zi Yuan, Lei Zhang, Datong Song, Kaiyuan Shi, and Christina Bock. Degradation mechanisms and mitigation strategies of nickel-rich nmc-based lithium-ion batteries. *Electrochemical Energy Reviews*, 3:43–80, 2020.

[29] Weikang Li, Yoon-Gyo Cho, Weiliang Yao, Yixuan Li, Ashley Cronk, Ryosuke Shimizu, Marshall A Schroeder, Yanbao Fu, Feng Zou, Vince Battaglia, et al. Enabling high areal capacity for co-free high voltage spinel materials in next-generation li-ion batteries. *Journal of Power Sources*, 473:228579, 2020.

[30] Akhilash Mohanan Pillai, Patteth S Salini, Bibin John, and Mercy Thelakkattu Devassy. Aqueous binders for cathodes: a lodestar for greener lithium ion cells. *Energy & Fuels*, 36(10):5063–5087, 2022.

[31] Dhrubajyoti Das, Sanchita Manna, and Sreeraj Puravankara. Electrolytes, additives and binders for nmc cathodes in li-ion batteries—a review. *Batteries*, 9(4):193, 2023.

[32] Ana Clara Rolandi, Iratxe de Meatza, Nerea Casado, Maria Forsyth, David Mecerreyes, and Cristina Pozo-Gonzalo. Unlocking sustainable power: advances in aqueous processing and water-soluble binders for nmc cathodes in high-voltage li-ion batteries. *RSC Sustainability*, 2(8):2125–2149, 2024.

[33] Iratxe De Meatza, Idoia Urdampilleta, Iker Boyano, Iker Castrillo, Imanol Landa-Medrano, Susan Sananes-Israel, Aitor Eguia-Barrio, and Verónica Palomares. From lab to manufacturing line: Guidelines for the development and upscaling of aqueous processed nmc622 electrodes. *Journal of The Electrochemical Society*, 170(1):010527, 2023.

[34] Marissa Wood, Yangping Sheng, Tamara J Keever, Jianlin Li, and David L Wood III. Stability of ni-rich nmc cathode materials in water and electrolyte solutions during aqueous electrode processing. In *Electrochemical Society Meeting Abstracts 231*, number 5, pages 376–376. The Electrochemical Society, Inc., 2017.

[35] Hyung-Joo Noh, Sungjune Youn, Chong Seung Yoon, and Yang-Kook Sun. Comparison of the structural and electrochemical properties of layered li [nixcoymnz] o2 (x= 1/3, 0.5, 0.6, 0.7, 0.8 and 0.85) cathode material for lithium-ion batteries. *Journal of power sources*, 233:121–130, 2013.

[36] Steven Lee, Wangda Li, Andrei Dolocan, Hugo Celio, Hyoju Park, Jamie H Warner, and Arumugam Manthiram. In-depth analysis of the degradation mechanisms of high-nickel, low/no-cobalt layered oxide cathodes for lithium-ion batteries. *Advanced Energy Materials*, 11(31):2100858, 2021.

[37] Arumugam Manthiram. An outlook on lithium ion battery technology. *ACS central science*, 3(10):1063–1069, 2017.

[38] Laura Wheatcroft, Arron Bird, Joe C Stallard, Ria L Mitchell, Samuel G Booth, Alisyn J Nedoma, Michael FL De Volder, Serena A Cussen, Norman A Fleck, and Beverley J Inkson. Fracture testing of lithium-ion battery cathode secondary particles in-situ inside the scanning electron microscope. *Batteries & Supercaps*, 6(5):e202300032, 2023.

[39] Laura Wheatcroft, Arron Bird, Naresh Gollapally, Samuel G Booth, Serena A Cussen, and Beverley J Inkson. In situ fracture behavior of single crystal lini0. 8mn0. 1co0. 1o2 (nmc811). *Batteries & Supercaps*, 7(6):e202400077, 2024.

[40] Marcus Müller, Lukas Pfaffmann, Stefan Jaiser, Michael Baunach, Vanessa Trouillet, Frieder Scheiba, Philip Scharfer, Wilhelm Schabel, and Werner Bauer.

Investigation of binder distribution in graphite anodes for lithium-ion batteries. *Journal of Power Sources*, 340:1–5, 2017.

[41] Ritu Sahore, David L Wood III, Alexander Kukay, Kelsey M Grady, Jianlin Li, and Ilias Belharouak. Towards understanding of cracking during drying of thick aqueous-processed lini0. 8mn0. 1co0. 1o2 cathodes. *ACS Sustainable Chemistry & Engineering*, 8(8):3162–3169, 2020.

[42] The business research company, 2020. Accessed on 02, 2022.

[43] Jiangong Zhu, Mariyam Susana Dewi Darma, Michael Knapp, Daniel R Sørensen, Michael Heere, Qiaohua Fang, Xueyuan Wang, Haifeng Dai, Liuda Mereacre, Anatoliy Senyshyn, et al. Investigation of lithium-ion battery degradation mechanisms by combining differential voltage analysis and alternating current impedance. *Journal of Power Sources*, 448:227575, 2020.

[44] Aleksander Cholewinski, Pengxiang Si, Marianna Uceda, Michael Pope, and Boxin Zhao. Polymer binders: Characterization and development toward aqueous electrode fabrication for sustainability. *Polymers*, 13(4):631, 2021.

[45] Rui Wang, Lili Feng, Wenrong Yang, Yinyin Zhang, Yanli Zhang, Wei Bai, Bo Liu, Wei Zhang, Yongming Chuan, Ziguang Zheng, et al. Effect of different binders on the electrochemical performance of metal oxide anode for lithium-ion batteries. *Nanoscale research letters*, 12:1–11, 2017.

[46] John Wang, Justin Purewal, Ping Liu, Jocelyn Hicks-Garner, Souren Soukazian, Elena Sherman, Adam Sorenson, Luan Vu, Harshad Tataria, and Mark W Verbrugge. Degradation of lithium-ion batteries employing graphite negatives and nickel–cobalt–manganese oxide+ spinel manganese oxide positives: Part 1, aging mechanisms and life estimation. *Journal of Power Sources*, 269:937–948, 2014.

[47] Jake Entwistle, Ruihuan Ge, Kunal Pardikar, Rachel Smith, and Denis Cumming. Carbon binder domain networks and electrical conductivity in lithium-ion battery electrodes: A critical review. *Renewable and Sustainable Energy Reviews*, 166:112624, 2022.

[48] Xin Qi, Berislav Blizanac, Aurelien DuPasquier, Archit Lal, Philip Niehoff, Tobias Placke, Miodrag Oljaca, Jie Li, and Martin Winter. Influence of thermal

treated carbon black conductive additive on the performance of high voltage spinel cr-doped lini0. 5mn1. 5o4 composite cathode electrode. *Journal of The Electrochemical Society*, 162(3):A339, 2014.

[49] Jingwei Hu, Shengwen Zhong, and Tingting Yan. Using carbon black to facilitate fast charging in lithium-ion batteries. *Journal of Power Sources*, 508:230342, 2021.

[50] Reza Younesi, Ane Sælland Christiansen, Roberto Scipioni, Søren Bredmose Simonsen, Kristina Edström, Johan Hjelm, Poul Norby, et al. Analysis of the interphase on carbon black formed in high voltage batteries. *Journal of The Electrochemical Society*, 162(7):A1289, 2015.

[51] Jake Entwistle, Ruihuan Ge, Kunal Pardikar, Rachel Smith, and Denis Cumming. Carbon binder domain networks and electrical conductivity in lithium-ion battery electrodes: A critical review. *Renewable and Sustainable Energy Reviews*, 166:112624, 2022.

[52] Fabian Coupette, Long Zhang, Björn Kuttich, Andrei Chumakov, Stephan V Roth, Lola González-García, Tobias Kraus, and Tanja Schilling. Percolation of rigid fractal carbon black aggregates. *The Journal of Chemical Physics*, 155(12):124902, 2021.

[53] Christopher G Robertson and Ned J Hardman. Nature of carbon black reinforcement of rubber: perspective on the original polymer nanocomposite. *Polymers*, 13(4):538, 2021.

[54] Hiroki Kondo, Hiroshi Sawada, Chikaaki Okuda, and Tsuyoshi Sasaki. Influence of the active material on the electronic conductivity of the positive electrode in lithium-ion batteries. *Journal of The Electrochemical Society*, 166(8):A1285, 2019.

[55] Lionel Flandin, A Chang, S Nazarenko, A Hiltner, and E Baer. Effect of strain on the properties of an ethylene–octene elastomer with conductive carbon fillers. *Journal of Applied Polymer Science*, 76(6):894–905, 2000.

[56] Jan-Chan Huang. Carbon black filled conducting polymers and polymer blends. *Advances in Polymer Technology: Journal of the Polymer Processing Institute*, 21(4):299–313, 2002.

[57] Ali Awarke, Sven Lauer, Stefan Pischinger, and Michael Wittler. Percolation–tunneling modeling for the study of the electric conductivity in lifepo4 based li-ion battery cathodes. *Journal of Power Sources*, 196(1):405–411, 2011.

[58] Tim Mike de Rijk and Walter Lang. Low-cost and highly sensitive pressure sensor with mold-printed multi-walled carbon nanotubes dispersed in polydimethylsiloxane. *Sensors*, 21(15):5069, 2021.

[59] Robert Dominko, Miran Gaberšček, Jernej Drofenik, Marjan Bele, and Janez Jamnik. Influence of carbon black distribution on performance of oxide cathodes for li-ion batteries. *Electrochimica Acta*, 48(24):3709–3716, 2003.

[60] Hao Chen, Min Ling, Luke Hencz, Han Yeu Ling, Gaoran Li, Zhan Lin, Gao Liu, and Shanqing Zhang. Exploring chemical, mechanical, and electrical functionalities of binders for advanced energy-storage devices. *Chemical reviews*, 118(18):8936–8982, 2018.

[61] Dominic Bresser, Daniel Buchholz, Arianna Moretti, Alberto Varzi, and Stefano Passerini. Alternative binders for sustainable electrochemical energy storage–the transition to aqueous electrode processing and bio-derived polymers. *Energy & Environmental Science*, 11(11):3096–3127, 2018.

[62] Fabian Jeschull, Matthew J Lacey, and Daniel Brandell. Functional binders as graphite exfoliation suppressants in aggressive electrolytes for lithium-ion batteries. *Electrochimica Acta*, 175:141–150, 2015.

[63] Amanda Rensmo, Eleni K Savvidou, Ian T Cousins, Xianfeng Hu, Steffen Schellenberger, and Jonathan P Benskin. Lithium-ion battery recycling: a source of per-and polyfluoroalkyl substances (pfas) to the environment? *Environmental Science: Processes & Impacts*, 25(6):1015–1030, 2023.

[64] Patteth S Salini, Sumol V Gopinadh, Athira Kalpakasseri, Bibin John, and Mercy Thelakkattu Devassy. Toward greener and sustainable li-ion cells: an overview of aqueous-based binder systems. *ACS Sustainable Chemistry & Engineering*, 8(10):4003–4025, 2020.

[65] Pratyusha Das and Barry C Thompson. Development of design strategies for conjugated polymer binders in lithium-ion batteries. *Polymer Journal*, 55(4):317–341, 2023.

[66] Pratyusha Das, Billal Zayat, Qiulong Wei, Charlene Z Salamat, Ioan-Bogdan Magdau, Rodrigo Elizalde-Segovia, Dakota Rawlings, Dongwook Lee, Gordon Pace, Ahamed Irshad, et al. Dihexyl-substituted poly (3, 4-propylenedioxythiophene) as a dual ionic and electronic conductive cathode binder for lithium-ion batteries. *Chemistry of Materials*, 32(21):9176–9189, 2020.

[67] Shuai Ma, Modi Jiang, Peng Tao, Chengyi Song, Jianbo Wu, Jun Wang, Tao Deng, and Wen Shang. Temperature effect and thermal impact in lithium-ion batteries: A review. *Progress in Natural Science: Materials International*, 28(6):653–666, 2018.

[68] Yan-Bo Wang, Qi Yang, Xun Guo, Shuo Yang, Ao Chen, Guo-Jin Liang, and Chun-Yi Zhi. Strategies of binder design for high-performance lithium-ion batteries: a mini review. *Rare Metals*, pages 1–17, 2022.

[69] Jianchao Chen, Jianyong Liu, Yue Qi, Tao Sun, and Xiaodong Li. Unveiling the roles of binder in the mechanical integrity of electrodes for lithium-ion batteries. *Journal of The Electrochemical Society*, 160(9):A1502, 2013.

[70] Carl D Reynolds, Sam D Hare, Peter R Slater, Mark JH Simmons, and Emma Kendrick. Rheology and structure of lithium-ion battery electrode slurries. *Energy Technology*, 10(10):2200545, 2022.

[71] Carl D Reynolds, Helen Walker, Ameir Mahgoub, Ebenezer Adebayo, and Emma Kendrick. Battery electrode slurry rheology and its impact on manufacturing. *Energy Advances*, 4(1):84–93, 2025.

[72] Lixia Ouyang, Zhaohui Wu, Jun Wang, Xiaopeng Qi, Qiang Li, Jiantao Wang, and Shigang Lu. The effect of solid content on the rheological properties and microstructures of a li-ion battery cathode slurry. *RSC advances*, 10(33):19360–19370, 2020.

[73] E Ligneel, B Lestriez, A Hudhomme, and Dominique Guyomard. Effects of the solvent concentration (solid loading) on the processing and properties of the composite electrode. *Journal of The Electrochemical Society*, 154(3):A235, 2007.

[74] Z Fu, HL Feng, XD Xiang, MM Rao, W Wu, JC Luo, TT Chen, QP Hu, AB Feng, and WS Li. A novel polymer composite as cathode binder of lithium-ion batteries

with improved rate capability and cyclic stability. *Journal of Power Sources*, 261:170–174, 2014.

[75] Hye-Kyoung Park, Byung-Seon Kong, and Eun-Suok Oh. Effect of high adhesive polyvinyl alcohol binder on the anodes of lithium ion batteries. *Electrochemistry Communications*, 13(10):1051–1053, 2011.

[76] R Sahore, DL Wood, A Kukay, KM Grady, J Li, and I Belharouak. Acs sustainable chem. *Eng*, 8:3162–3169, 2020.

[77] Italo Doberdò, Nicholas Löffler, Nina Laszczynski, Dario Cericola, Nerino Penazzi, Silvia Bodoardo, Guk-Tae Kim, and Stefano Passerini. Enabling aqueous binders for lithium battery cathodes–carbon coating of aluminum current collector. *Journal of power sources*, 248:1000–1006, 2014.

[78] Marie Bichon, Dane Sotta, Eric De Vito, Willy Porcher, and Bernard Lestriez. Performance and ageing behavior of water-processed lini0. 5mn0. 3co0. 2o2/graphite lithium-ion cells. *Journal of Power Sources*, 483:229097, 2021.

[79] Marissa Wood, Jianlin Li, Rose E Ruther, Zhijia Du, Ethan C Self, Harry M Meyer III, Claus Daniel, Ilias Belharouak, and David L Wood III. Chemical stability and long-term cell performance of low-cobalt, ni-rich cathodes prepared by aqueous processing for high-energy li-ion batteries. *Energy Storage Materials*, 24:188–197, 2020.

[80] Franca Tiarks, Katharina Landfester, and Markus Antonietti. Encapsulation of carbon black by miniemulsion polymerization. *Macromolecular chemistry and physics*, 202(1):51–60, 2001.

[81] W Porcher, B Lestriez, S Jouanneau, and Dominique Guyomard. Optimizing the surfactant for the aqueous processing of lifepo4 composite electrodes. *Journal of Power Sources*, 195(9):2835–2843, 2010.

[82] Thomas Heinze and Andreas Koschella. Carboxymethyl ethers of cellulose and starch–a review. In *Macromolecular Symposia*, volume 223, pages 13–40. Wiley Online Library, 2005.

[83] Mamdouh T Ghannam and M Nabil Esmail. Rheological properties of carboxymethyl cellulose. *Journal of applied polymer science*, 64(2):289–301, 1997.

[84] Babak Ghanbarzadeh, Hadi Almasi, and Ali A Entezami. Physical properties of edible modified starch/carboxymethyl cellulose films. *Innovative food science & emerging technologies*, 11(4):697–702, 2010.

[85] Niranjanmurthi Lingappan, Lingxi Kong, and Michael Pecht. The significance of aqueous binders in lithium-ion batteries. *Renewable and Sustainable Energy Reviews*, 147:111227, 2021.

[86] Alexander Kukay, Ritu Sahore, Anand Parejiya, W Blake Hawley, Jianlin Li, and David L Wood III. Aqueous ni-rich-cathode dispersions processed with phosphoric acid for lithium-ion batteries with ultra-thick electrodes. *Journal of Colloid and Interface Science*, 581:635–643, 2021.

[87] Zhongli Wang, Nicolas Dupré, Anne-Claire Gaillot, Bernard Lestriez, Jean-Frédéric Martin, Lise Daniel, Sébastien Patoux, and Dominique Guyomard. Cmc as a binder in lini0. 4mn1. 6o4 5 v cathodes and their electrochemical performance for li-ion batteries. *Electrochimica acta*, 62:77–83, 2012.

[88] Lei Qiu, Ziqiang Shao, Daxiong Wang, Feijun Wang, Wenjun Wang, and Jianquan Wang. Carboxymethyl cellulose lithium (cmc-li) as a novel binder and its electrochemical performance in lithium-ion batteries. *Cellulose*, 21:2789–2796, 2014.

[89] M Wood, J Li, RE Ruther, Z Du, EC Self, HM Meyer, C Daniel, I Belharouak, and DL Wood. Chemical stability and long-term cell performance of low-cobalt, ni-rich cathodes prepared by aqueous processing for high-energy li-ion batteries, energy storage mater. 24 (2020) 188–197.

[90] Ana Clara Rolandi, Aitor Barquero, Cristina Pozo-Gonzalo, Iratxe De Meatza, Nerea Casado, Maria Forsyth, Jose R Leiza, and David Mecerreyes. Biobased acrylic latexes/sodium carboxymethyl cellulose aqueous binders for lithium-ion nmc 811 cathodes. *ACS Applied Polymer Materials*, 6(2):1236–1244, 2024.

[91] Jiantie Xu, Shu-Lei Chou, Qin-fen Gu, Hua-Kun Liu, and Shi-Xue Dou. The effect of different binders on electrochemical properties of lini1/3mn1/3co1/3o2 cathode material in lithium ion batteries. *Journal of Power Sources*, 225:172–178, 2013.

[92] Francesca Bigoni, Francesca De Giorgio, Francesca Soavi, and Catia Arbizzani. Sodium alginate: a water-processable binder in high-voltage cathode formulations. *Journal of The Electrochemical Society*, 164(1):A6171, 2016.

[93] Minghao Sun, Haoxiang Zhong, Shuren Jiao, Hanqi Shao, and Lingzhi Zhang. Investigation on carboxymethyl chitosan as new water soluble binder for lifepo4 cathode in li-ion batteries. *Electrochimica acta*, 127:239–244, 2014.

[94] K Prasanna, T Subburaj, Yong Nam Jo, Won Jong Lee, and Chang Woo Lee. Environment-friendly cathodes using biopolymer chitosan with enhanced electrochemical behavior for use in lithium ion batteries. *ACS applied materials & interfaces*, 7(15):7884–7890, 2015.

[95] Koblan Wilfried Ebagninin, Adel Benchabane, and Karim Bekkour. Rheological characterization of poly (ethylene oxide) solutions of different molecular weights. *Journal of colloid and interface science*, 336(1):360–367, 2009.

[96] Jinshan Mo, Dongmei Zhang, Mingzhe Sun, Lehao Liu, Weihao Hu, Bing Jiang, Lihua Chu, and Meicheng Li. Polyethylene oxide as a multifunctional binder for high-performance ternary layered cathodes. *Polymers*, 13(22):3992, 2021.

[97] RWA Franco, José Pedro Donoso, Cláudio José Magon, Cristiane Barbieri Rodella, Ariovaldo de Oliveira Florentino, Margarida Juri Saeki, JM Pernaut, and AL De Oliveira. Electric and magnetic properties of polymer electrolyte/carbon black composites. *Solid State Ionics*, 113:149–160, 1998.

[98] Delphine Guy, Bernard Lestriez, and Dominique Guyomard. New composite electrode architecture and improved battery performance from the smart use of polymers and their properties. *Advanced Materials*, 16(6):553–557, 2004.

[99] D Guy, B Lestriez, R Bouchet, V Gaudefroy, and D Guyomard. Improvement of lithium battery performance through composite electrode microstructure optimization. *Ionics*, 10:443–449, 2004.

[100] Mahadevappa Y Kariduraganavar, Arjumand A Kittur, and Ravindra R Kamble. Polymer synthesis and processing. In *Natural and synthetic biomedical polymers*, pages 1–31. Elsevier, 2014.

[101] Yi-Hung Liu, Chung-Hsuan Hsueh, and Yen-Shen Kuo. In situ formation of partially carbonized polyvinylpyrrolidone as a green binder for high-voltage li-ion battery cathode with improved electrochemical performance. *Journal of Energy Storage*, 72:108746, 2023.

[102] Sang Hoon Sung, Sunhyung Kim, Jeong Hoon Park, Jun Dong Park, and Kyung Hyun Ahn. Role of pvdf in rheology and microstructure of ncm cathode slurries for lithium-ion battery. *Materials*, 13(20):4544, 2020.

[103] Zhian Zhang, Changming Qu, Tao Zheng, Yanqing Lai, and Jie Li. Effect of triton x-100 as dispersant on carbon black for lifepo4 cathode. *International Journal of Electrochemical Science*, 8(5):6722–6733, 2013.

[104] Chia-Chen Li, Xing-Wei Peng, Jyh-Tsung Lee, and Fu-Ming Wang. Using poly (4-styrene sulfonic acid) to improve the dispersion homogeneity of aqueous-processed lifepo4 cathodes. *Journal of the Electrochemical Society*, 157(4):A517, 2010.

[105] R.A. Shirwaiker, M.F. Purser, and R.A. Wysk. 6 - scaffolding hydrogels for rapid prototyping based tissue engineering. In Roger Narayan, editor, *Rapid Prototyping of Biomaterials*, pages 176–200. Woodhead Publishing, 2014.

[106] Yining Lin and Paschalis Alexandridis. Temperature-dependent adsorption of pluronic f127 block copolymers onto carbon black particles dispersed in aqueous media. *The Journal of Physical Chemistry B*, 106(42):10834–10844, 2002.

[107] Yining Lin, Thomas W Smith, and Paschalis Alexandridis. Adsorption of a rake-type siloxane surfactant onto carbon black nanoparticles dispersed in aqueous media. *Langmuir*, 18(16):6147–6158, 2002.

[108] Cristina Di Donato, Rosa Iacovino, Carla Isernia, Gaetano Malgieri, Angela Varela-Garcia, Angel Concheiro, and Carmen Alvarez-Lorenzo. Polypseudorotaxanes of pluronic® f127 with combinations of α-and β-cyclodextrins for topical formulation of acyclovir. *Nanomaterials*, 10(4):613, 2020.

[109] Lorenzo Airoldi, Umberto Anselmi-Tamburini, Barbara Vigani, Silvia Rossi, Piercarlo Mustarelli, and Eliana Quartarone. Additive manufacturing of aqueous-processed limn2o4 thick electrodes for high-energy-density lithium-ion batteries. *Batteries & Supercaps*, 3(10):1040–1050, 2020.

[110] Yaqing Zhang, Hongyan Xie, Huixin Jin, Qiang Zhang, Yezhu Li, Xiaohui Li, Kaifeng Li, and Chongjun Bao. Research status of spinel limn2o4 cathode materials for lithium ion batteries. In *IOP Conference Series: Earth and Environmental Science*, volume 603, page 012051. IOP Publishing, 2020.

[111] Shuwen Kang, Haiming Xie, Wei Zhai, Zi-feng Ma, Rongshun Wang, and Weimin Zhang. Enhancing performance of a lithium ion battery by optimizing the surface properties of the current collector. *Int. J. Electrochem. Sci*, 10:2324–2335, 2015.

[112] PG De Gennes. Scaling theory of polymer adsorption. *Journal de physique*, 37(12):1445–1452, 1976.

[113] Florian Schmidt, Sebastian Ehrling, Kay Schönherr, Susanne Dörfler, Thomas Abendroth, Holger Althues, and Stefan Kaskel. The importance of swelling effects on cathode density and electrochemical performance of lithium- sulfur battery cathodes produced via dry processing. *Energy Technology*, 10(2):2100721, 2022.

[114] Qingsong Liu, Willa Brenneis, Gergely Nagy, Mathieu Doucet, Jeffrey Lopez, and Jeffrey J Richards. Structure–performance relationships of lithium-ion battery cathodes revealed by contrast-variation small-angle neutron scattering. *Journal of Materials Chemistry A*, 12(47):33114–33124, 2024.

[115] Wei-Ren Liu, Mo-Hua Yang, Hung-Chun Wu, SM Chiao, and Nae-Lih Wu. Enhanced cycle life of si anode for li-ion batteries by using modified elastomeric binder. *Electrochemical and Solid-State Letters*, 8(2):A100, 2004.

[116] Mehdi Chouchane, Alexis Rucci, Teo Lombardo, Alain C Ngandjong, and Alejandro A Franco. Lithium ion battery electrodes predicted from manufacturing simulations: Assessing the impact of the carbon-binder spatial location on the electrochemical performance. *Journal of Power Sources*, 444:227285, 2019.

[117] Lukas Zielke, Tobias Hutzenlaub, Dean R Wheeler, Chien-Wei Chao, Ingo Manke, André Hilger, Nils Paust, Roland Zengerle, and Simon Thiele. Three-phase multiscale modeling of a licoo2 cathode: combining the advantages of fib–sem imaging and x-ray tomography. *Advanced Energy Materials*, 5(5):1401612, 2015.

[118] Zhian Zhang, Tao Zeng, Changming Qu, Hai Lu, Ming Jia, Yanqing Lai, and Jie Li. Cycle performance improvement of lifepo4 cathode with polyacrylic acid as binder. *Electrochimica acta*, 80:440–444, 2012.

[119] Waleed M Abed, Richard D Whalley, David JC Dennis, and Robert J Poole. Experimental investigation of the impact of elastic turbulence on heat transfer in a serpentine channel. *Journal of Non-Newtonian Fluid Mechanics*, 231:68–78, 2016.

[120] Fuduo Ma, Yanbao Fu, Vince Battaglia, and Ravi Prasher. Microrheological modeling of lithium-ion battery anode slurry. *Journal of Power Sources*, 438:226994, 2019.

[121] Suryadevara Babu. *Advances in chemical mechanical planarization (CMP)*. Woodhead Publishing, 2016.

[122] Yoko Hanada, Shoichi Masuda, Motoyuki Iijima, and Hidehiro Kamiya. Analysis of dispersion and aggregation behavior of carbon black particles in aqueous suspension by colloid probe afm method. *Advanced Powder Technology*, 24(5):844–851, 2013.

[123] Jeffrey J Richards, Julie B Hipp, John K Riley, Norman J Wagner, and Paul D Butler. Clustering and percolation in suspensions of carbon black. *Langmuir*, 33(43):12260–12266, 2017.

[124] Paul J Flory. Thermodynamics of high polymer solutions. *The Journal of chemical physics*, 10(1):51–61, 1942.

[125] MA Stuart. Adsorbed polymers in colloidal systems: from statics to dynamics. *Polymer Journal*, 23(5):669–682, 1991.

[126] Yan He, Lei Jing, Yuan Ji, Zhiwei Zhu, Lanxiang Feng, Xuewei Fu, and Yu Wang. Revisiting the electrode manufacturing: A look into electrode rheology and active material microenvironment. *Journal of Energy Chemistry*, 2022.

[127] Dominika Gastol, Matthew Capener, Carl Reynolds, Christopher Constable, and Emma Kendrick. Microstructural design of printed graphite electrodes for lithium-ion batteries. *Materials & Design*, 205:109720, 2021.

[128] Ye Shui Zhang, Josh J Bailey, Yige Sun, Adam M Boyce, Will Dawson, Carl D Reynolds, Zhenyu Zhang, Xuekun Lu, Patrick Grant, Emma Kendrick, et al. Applications of advanced metrology for understanding the effects of drying temperature in the lithium-ion battery electrode manufacturing process. *Journal of Materials Chemistry A*, 10(19):10593–10603, 2022.

[129] Carl D Reynolds, Peter R Slater, Sam D Hare, Mark JH Simmons, and Emma Kendrick. A review of metrology in lithium-ion electrode coating processes. *Materials & Design*, 209:109971, 2021.

[130] Valentin Wenzel, Hermann Nirschl, and Dorit Nötzel. Challenges in lithium-ion-battery slurry preparation and potential of modifying electrode structures by different mixing processes. *Energy Technology*, 3(7):692–698, 2015.

[131] Jeong Hoon Park, Sun Hyung Kim, and Kyung Hyun Ahn. Role of carboxymethyl cellulose binder and its effect on the preparation process of anode slurries for li-ion batteries. *Colloids and Surfaces A: Physicochemical and Engineering Aspects*, 664:131130, 2023.

[132] Ernest Jun Jie Tang, Rodney Chua, Yi Cai, Yuqi Guo, Wei How Chong, Suminto Winardi, Tanto Soh, Richa Chaudhary, and Madhavi Srinivasan. Rheological studies of lini0. 6mn0. 2co0. 2o2-based slurry for the development of energy dense li-ion applications. *Journal of The Electrochemical Society*, 171(2):020518, 2024.

[133] Peipei Su, Haitao Zhang, Lipeng Yang, Chunxian Xing, Shanshan Pan, Wei Lu, and Suojiang Zhang. Effects of conductive additives on the percolation networks and rheological properties of limn0.7fe0.3po4 suspensions for lithium slurry battery. *Chemical Engineering Journal*, 433:133203, 2022.

[134] Werner Bauer and Dorit Nötzel. Rheological properties and stability of nmp based cathode slurries for lithium ion batteries. *Ceramics International*, 40(3):4591–4598, 2014.

[135] Bin Zhao, Deshun Yin, Yunfei Gao, and Jiangtao Ren. Concentration dependence of yield stress, thixotropy, and viscoelasticity rheological behavior of lithium-ion battery slurry. *Ceramics International*, 48(13):19073–19080, 2022.

[136] Bin Zhao, Deshun Yin, Yunfei Gao, and Jiangtao Ren. Effect of various components on time-dependent rheological behavior of cathode slurries for lithium-ion batteries. *Journal of Electronic Materials*, 51(7):3885–3895, 2022.

[137] Ritu Sahore, Marissa Wood, Alexander Kukay, Zhijia Du, Kelsey M Livingston, David L Wood, and Jianlin Li. Performance of different water-based binder formulations for ni-rich cathodes evaluated in lini0. 8mn0. 1co0. 1o2//graphite pouch cells. *Journal of The Electrochemical Society*, 169(4):040567, 2022.

[138] Ronald Gordon, Meriem Kassar, and Norbert Willenbacher. Effect of polymeric binders on dispersion of active particles in aqueous lifepo4-based cathode slurries as well as on mechanical and electrical properties of corresponding dry layers. *ACS omega*, 5(20):11455–11465, 2020.

[139] Kwang Man Kim, Woo Sung Jeon, In Jae Chung, and Soon Ho Chang. Effect of mixing sequences on the electrode characteristics of lithium-ion rechargeable batteries. *Journal of power sources*, 83(1-2):108–113, 1999.

[140] Xuesong Lu, Guo J Lian, Ruihuan Ge, James Parker, Milan K Sadan, Rachel Smith, and Denis Cumming. Microstructure of conductive binder domain for electrical conduction in next-generation lithium-ion batteries. *Energy Technology*, 11(10):2300446, 2023.

[141] Zhilong Wang, Jialong Tu, Xinhao Yu, Feixiang Li, Zhenzhen Zhao, Yahui Cui, and Tong Zhao. Optimization of mixing speed and time to disperse the composite conductive agent composed of carbon black and graphene in lithium-ion battery slurry. *Particuology*, 92:1–12, 2024.

[142] Alice Hoffmann, Emanuel A Heider, Christian Dreer, Claudia Pfeifer, and Margret Wohlfahrt-Mehrens. Influence of the mixing and dispersing process on the slurry properties and the microstructure and performance of ultrathick cathodes for lithium-ion batteries. *Energy Technology*, 11(5):2200484, 2023.

[143] Yoshiyuki Komoda, Kaoru Ishibashi, Kentaro Kuratani, Ruri Hidema, Hiroshi Suzuki, and Hironori Kobayashi. Rheological interpretation of the structural change of lib cathode slurry during the preparation process. *JCIS Open*, 5:100038, 2022.

[144] Ye Shui Zhang, Anand Narayanan Pallipurath Radhakrishnan, James B Robinson, Rhodri E Owen, Thomas G Tranter, Emma Kendrick, Paul R Shearing, and Dan JL Brett. In situ ultrasound acoustic measurement of the lithium-ion battery electrode drying process. *ACS Applied Materials & Interfaces*, 13(30):36605–36620, 2021.

[145] Stefan Jaiser, Jana Kumberg, Jop Klaver, Janos L Urai, Wilhelm Schabel, Joyce Schmatz, and Philip Scharfer. Microstructure formation of lithium-ion battery

electrodes during drying–an ex-situ study using cryogenic broad ion beam slope-cutting and scanning electron microscopy (cryo-bib-sem). *Journal of Power Sources*, 345:97–107, 2017.

[146] Stefan Jaiser, Marcus Müller, Michael Baunach, Werner Bauer, Philip Scharfer, and Wilhelm Schabel. Investigation of film solidification and binder migration during drying of li-ion battery anodes. *Journal of Power Sources*, 318:210–219, 2016.

[147] Targray. Targray nmc powder for battery manufacturers.

[148] Imerys. Cenergy.

[149] Michael E Spahr, Dietrich Goers, Antonio Leone, Salvatore Stallone, and Eusebiu Grivei. 'development of carbon conductive additives for advanced lithium-ion batteries'. *Journal of Power Sources*, 196(7):3404–3413, 2011.

[150] Malvern Instruments Ltd. A Basic Intro to Rheology. Technical report, Malvern Instruments Ltd, 01 2016.

[151] Anton Paar Ltd. Basics of rheology.

[152] Kumari Konda, Sahana B Moodakare, P Logesh Kumar, Manjusha Battabyal, Jyoti R Seth, Vinay A Juvekar, and Raghavan Gopalan. Comprehensive effort on electrode slurry preparation for better electrochemical performance of lifepo4 battery. *Journal of Power Sources*, 480:228837, 2020.

[153] Anton Paar Ltd. The principles of dynamic light scattering.

[154] Masahiko Abe. *Measurement techniques and practices of colloid and interface phenomena*. Springer, 2019.

[155] D Guy, B Lestriez, R Bouchet, and Dominique Guyomard. Critical role of polymeric binders on the electronic transport properties of composites electrode. *Journal of The Electrochemical Society*, 153(4):A679, 2006.

[156] Mitsuhiro Takeno, Seiji Katakura, Kohei Miyazaki, Takeshi Abe, and Tomokazu Fukutsuka. Analysis of intermediate states of electrode-slurry by electronic conductivity measurements. *Carbon Reports*, page 020201, 2023.

[157] Mitsuhiro Takeno, Tomokazu Fukutsuka, Kohei Miyazaki, and Takeshi Abe. Influence of carbonaceous materials on electronic conduction in electrode-slurry. *Carbon*, 122:202–206, 2017.

[158] Endress. Conductivity sensors and transmitters.

[159] Gamry. Basics of eis.

[160] Alexandros Ch Lazanas and Mamas I Prodromidis. Electrochemical impedance spectroscopy a tutorial. *ACS Measurement Science Au*, 3(3):162–193, 2023.

[161] Matthew Lacey. Principles of eis.

[162] D Guy, B Lestriez, R Bouchet, V Gaudefroy, and D Guyomard. Tailoring the binder of composite electrode for battery performance optimization. *Electrochemical and solid-state letters*, 8(1):A17, 2004.

[163] Tainstruments. Rheological evaluation of battery slurries with different graphite particle size and shape.

[164] Chia-Chen Li, Jyh-Tsung Lee, and Xing-Wei Peng. Improvements of dispersion homogeneity and cell performance of aqueous-processed licoo2 cathodes by using dispersant of paa–nh4. *Journal of the Electrochemical Society*, 153(5):A809, 2006.

[165] Fatih A Cetinel and Werner Bauer. Processing of water-based lini 1/3 mn 1/3 co 1/3 o 2 pastes for manufacturing lithium ion battery cathodes. *Bulletin of Materials Science*, 37:1685–1690, 2014.

[166] CL Barrie, PC Griffiths, RJ Abbott, I Grillo, E Kudryashov, and C Smyth. Rheology of aqueous carbon black dispersions. *Journal of colloid and interface science*, 272(1):210–217, 2004.

[167] H Yamada, I Manas-Zloczower, and DL Feke. The influence of matrix viscosity and interfacial properties on the dispersion kinetics of carbon black agglomerates. *Rubber chemistry and technology*, 71(1):1–16, 1998.

[168] S-P Rwei, F-H Ku, and K-C Cheng. Dispersion of carbon black in a continuous phase: Electrical, rheological, and morphological studies. *Colloid and Polymer Science*, 280:1110–1115, 2002.

[169] Keng Yuen Foo and Bassim H Hameed. Insights into the modeling of adsorption isotherm systems. *Chemical engineering journal*, 156(1):2–10, 2010.

[170] Shams Kalam, Sidqi A Abu-Khamsin, Muhammad Shahzad Kamal, and Shirish Patil. Surfactant adsorption isotherms: A review. *ACS omega*, 6(48):32342–32348, 2021.

[171] Sanghyuk Lim, Sunhyung Kim, Kyung Hyun Ahn, and Seung Jong Lee. The effect of binders on the rheological properties and the microstructure formation of lithium-ion battery anode slurries. *Journal of Power Sources*, 299:221–230, 2015.

[172] S.Huotari M.Colalongo S.Mousavihashemi S.Hamed, F.Obrezkov and T.Kallio. Optimized nmc622 electrodes with a high content of the active material: A comprehensive study. *Journal of Power Sources*, 608:234549, 2024.

[173] Atif Javed, Ardavan Makvandi, Feleke Demelash, Egy Adhitama, Bastian Heidrich, Martin Peterlechner, Gerhard Wilde, Martin Winter, and Markus Borner. Interphase design of lini0. 6mn0. 2co0. 2o2 as positive active material for lithium ion batteries via al2o3 coatings using magnetron sputtering for improved performance and stability. *Batteries & supercaps*, 7(6):e202300580, 2024.

[174] Wenzao Li, Lisa M Housel, Garrett P Wheeler, David C Bock, Kenneth J Takeuchi, Esther S Takeuchi, and Amy C Marschilok. Thermodynamic analysis of lini0. 6mn0. 2co0. 2o2 (nmc622) voltage hysteresis induced through high voltage charge. *ACS Applied Energy Materials*, 4(11):12067–12073, 2021.

[175] Dhrupad Parikh, Tommiejean Christensen, and Jianlin Li. Correlating the influence of porosity, tortuosity, and mass loading on the energy density of lini0. 6mn0. 2co0. 2o2 cathodes under extreme fast charging (xfc) conditions. *Journal of power sources*, 474:228601, 2020.

[176] Christian Heubner, Alexander Nickol, Jann Seeba, Sebastian Reuber, Nils Junker, Mareike Wolter, Michael Schneider, and Alexander Michaelis. Understanding thickness and porosity effects on the electrochemical performance of lini0. 6co0. 2mn0. 2o2-based cathodes for high energy li-ion batteries. *Journal of Power Sources*, 419:119–126, 2019.

[177] Haidar Y Alolaywi, Kubra Uzun, and Yang-Tse Cheng. "zero" porosity high loading nmc622 positive electrodes for li-ion batteries. *Journal of The Electrochemical Society*, 171(1):010514, 2024.

[178] Kwangjin Park, Sungoh Yu, Joongmyeon Bae, Hyungsop Kim, and Yoonki Ko. Fast performance degradation of sofc caused by cathode delamination in long-term testing. *International Journal of Hydrogen Energy*, 35(16):8670–8677, 2010.

[179] Pallab Barai, Tomas Rojas, Badri Narayanan, Anh T Ngo, Larry A Curtiss, and Venkat Srinivasan. Investigation of delamination-induced performance decay at the cathode/llzo interface. *Chemistry of Materials*, 33(14):5527–5541, 2021.

[180] Jia Guo, Yaqi Li, Jinhao Meng, Kjeld Pedersen, Leonid Gurevich, and Daniel-Ioan Stroe. Understanding the mechanism of capacity increase during early cycling of commercial nmc/graphite lithium-ion batteries. *Journal of Energy Chemistry*, 74:34–44, 2022.

[181] Balazs Gyenes, DA Stevens, VL Chevrier, and JR Dahn. Understanding anomalous behavior in coulombic efficiency measurements on li-ion batteries. *Journal of The Electrochemical Society*, 162(3):A278, 2014.

[182] S Radloff, R-G Scurtu, M Hölzle, and M Wohlfahrt-Mehrens. Water-based lini0. 83co0. 12mn0. 05o2 electrodes with excellent cycling stability fabricated using unconventional binders. *Journal of The Electrochemical Society*, 169(4):040514, 2022.

[183] European Agency for Health and Safety at Work. Regulation (ec) no 1907/2006 of the european parliament and of the council of 18 december 2006 concerning the registration.

[184] CR Wildemuth and MC Williams. Viscosity of suspensions modeled with a shear-dependent maximum packing fraction. *Rheologica acta*, 23:627–635, 1984.

[185] Yeonguk Son, Hyungyeon Cha, Taeyong Lee, Yujin Kim, Adam Boies, Jaephil Cho, and Michael De Volder. Analysis of differences in electrochemical performance between coin and pouch cells for lithium-ion battery applications. *Energy & Environmental Materials*, 7(3):e12615, 2024.

8 Appendix

8.1 Chapter 3

8.1.1 Polymer solution flow curves

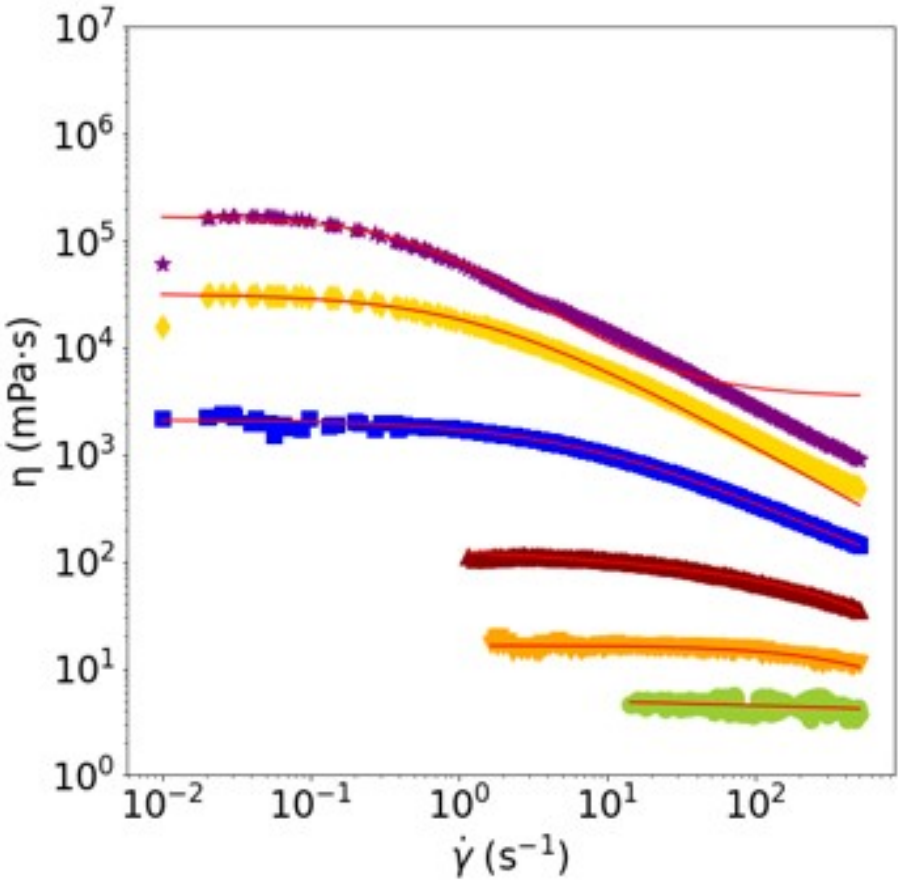

Figure 78: Flow curves for 2000 kg mol^{-1} PEO/H_2O fitted with the Cross Model, for 0.25 wt % (●), 0.5 wt % (▼), 1 wt % (▲), 2 wt % (■), 3 wt % (♦), 5 wt % (★). Red lines indicate fits with the Cross model.

8.1.2 Full slurry flow curves

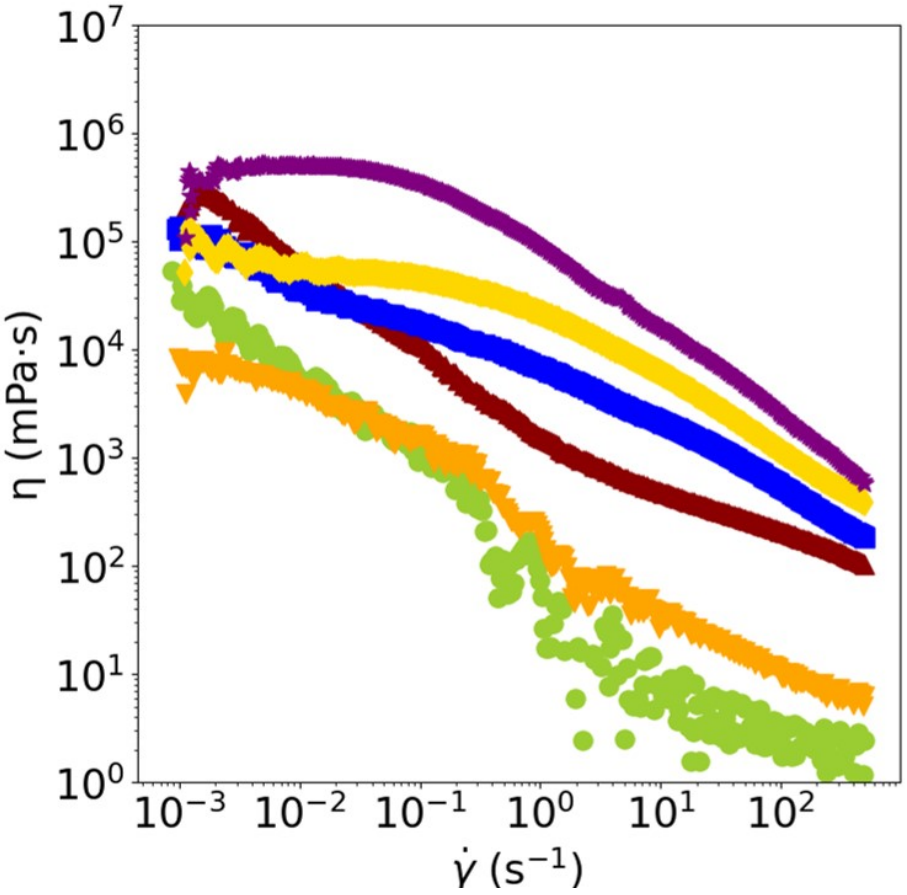

Figure 79: Flow curves of viscosity for 2000 kg mol^{-1} for 0.25 wt % (●), 0.5 wt% (▼), 1 wt% (▲), 2 wt% (■), 3 wt% (♦), and 5 wt% (★).)

8.1.3 Oscillatory sweeps

Oscillatory sweep measurements were taken on full cathode slurries and shown in Fig. 80. For both Mws, the storage modulus, G', monotonically increases with polymer concentration. All slurries have a crossover point for G' and G", likely due to inter-particle collisions at high frequencies. This and the fact that G' shows frequency dependency indicates that none of these samples are gelled.

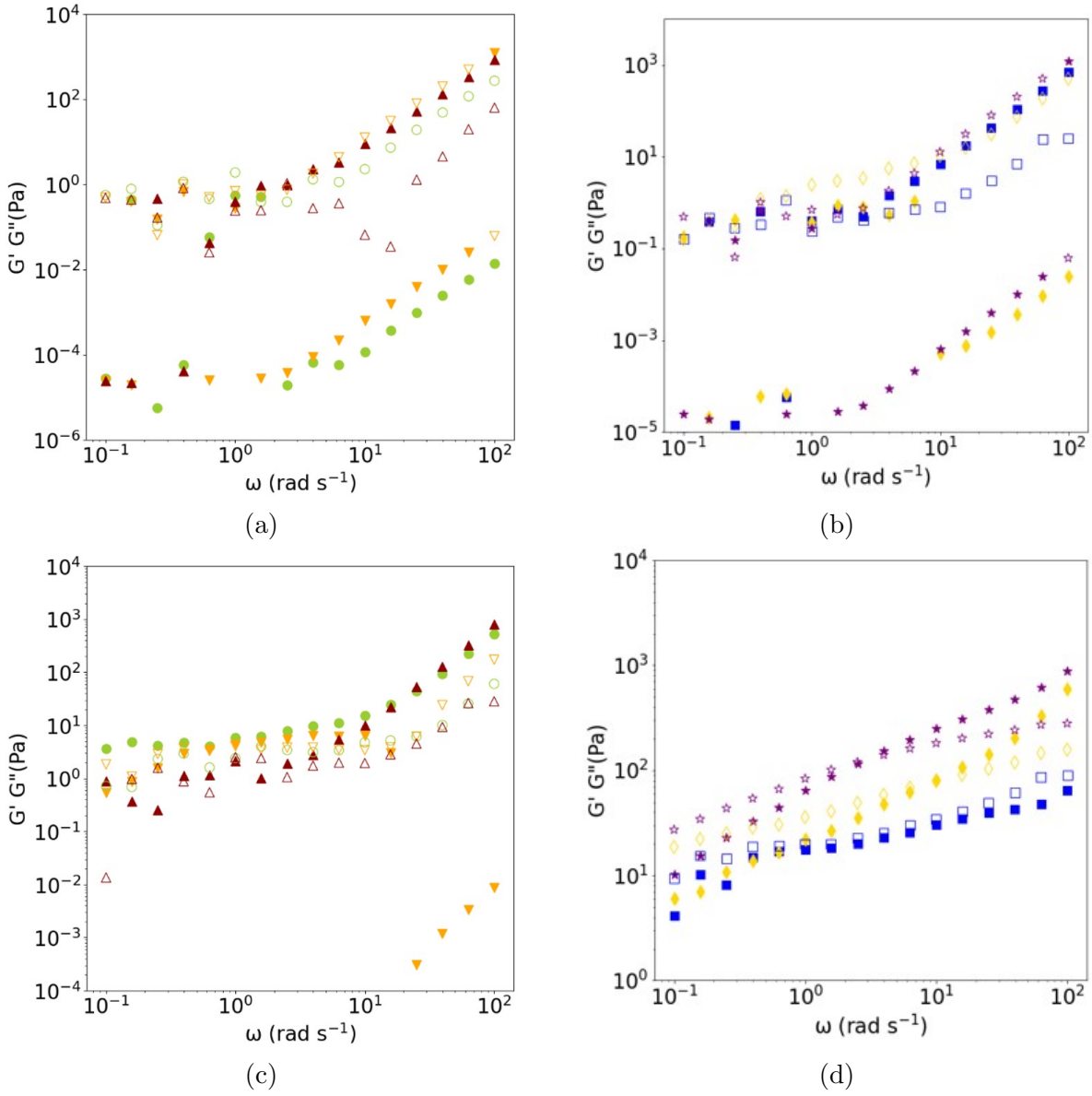

Figure 80: Storage and loss moduli curves for full cathode slurries containing 1000 kg mol^{-1} PEO (a) and (c), and 2000 kg mol^{-1} for (b) and (d), for 0.25 wt% (●), 0.5 wt% (▼), 1 wt% (▲), 2 wt% (■), 3 wt% (♦), 5 wt% (★). Filled symbols are for storage moduli whilst open symbols are for loss moduli.

8.1.4 Single Solid Slurries

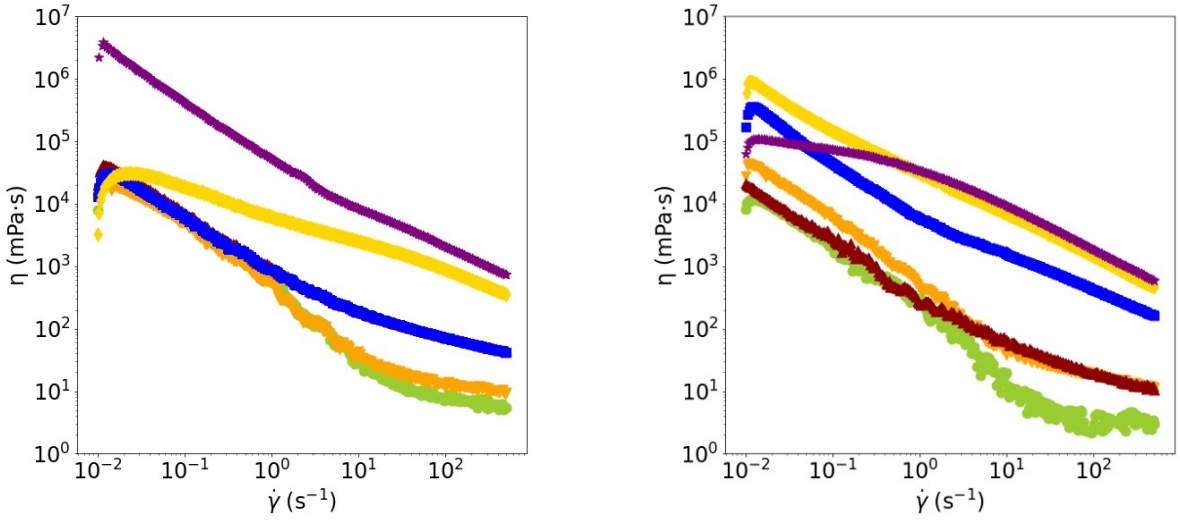

(a) (b)

Figure 81: Flow curves of viscosity for 1000 kg mol^{-1} carbon black/PEO/H_2O (a) and 2000 kg mol^{-1} carbon black/PEO/H_2O (b) fitted with the Cross Model, for 0.25 wt % (●), 0.5 wt % (▼), 1 wt % (▲), 2 wt % (■), 3 wt % (♦), 5 wt % (★))

8.1.5 Herschel-Bulkley Python Fitting Procedure

For slurries consisting of carbon black, PEO and water, the Herschel-Bulkley model was fit to determine a yield stress. Samples $1M_3$, $2M_3$ and $2M_5$ required a weighted fit to reduce the influence of noisy or less reliable data at high shear. The fitting procedure is shown below in Fig. 82, with weights added to the ascribed samples starting with "weights" in line 8.

```python
import numpy as np
import matplotlib.pyplot as plt
from scipy.optimize import curve_fit

# Herschel-Bulkley model function
def herschel_bulkley_model(gamma, tau_0, K, n):
    """
    Herschel-Bulkley model: τ = τ₀ + K * γ^n

    Parameters:
        gamma (array): Shear rate (independent variable).
        tau_0 (float): Yield stress (τ₀).
        K (float): Consistency index (K).
        n (float): Flow behavior index (n).

    Returns:
        tau (array): Shear stress (dependent variable).
    """
    return tau_0 + K * gamma**n

# Example data (replace with your actual data)
gamma =  x2M_5_2 = df_PEO_EXPT_140223_Int_1 .loc[(df_PEO_EXPT_140223_Int_1.index > 150 ,"2M_5_wt%_Shear Rate")]
tau = y2M_5_2 = df_PEO_EXPT_140223_Int_1 .loc[(df_PEO_EXPT_140223_Int_1.index > 150 ,"2M_5_wt%_Shear Stress")]
weights = 1 / (gamma + 1e1)  # Adding a small constant to avoid division by zero

# Perform weighted curve fitting
popt, pcov = curve_fit(herschel_bulkley_model, gamma, tau, sigma=weights, p0=[0.1, 1, 0.8])

# Extract the optimal parameters
tau_0_opt, K_opt, n_opt = popt

# Calculate the fitted values
tau_fit = herschel_bulkley_model(gamma, *popt)
tau_0_std, K_std, n_std = np.sqrt(np.diag(pcov))

#Get R Squared Value
residuals = y2M_5_2 - herschel_bulkley_model(x2M_5_2, *popt)
ss_res = np.sum(residuals**2)
ss_tot = np.sum((y2M_5_2-np.mean(y2M_5_2))**2)
r_squared = 1 - (ss_res / ss_tot)

# Print the optimal parameters
print(f"Optimal parameters:")
print(f"Yield stress (τ₀) = {tau_0_opt:.4f}", tau_0_std)
print(f"Consistency index (K) = {K_opt:.4f}", K_std,)
print(f"Flow behavior index (n) = {n_opt:.4f}", n_std)
print(r_squared)

# Plot the data and the fitted curve
plt.scatter(gamma, tau, label="Data", color='red')
plt.plot(gamma, tau_fit, label=f"Fitted Herschel-Bulkley model\nτ₀={tau_0_opt:.4f}, K={K_opt:.4f}, n={n_opt:.4f}", color='blue')
plt.xlabel('Shear rate (γ)')
plt.ylabel('Shear stress (τ)')
plt.xscale('log')
plt.yscale('log')
plt.legend()
plt.title('Herschel-Bulkley Model Fit')
plt.show()
```

Figure 82: Python code for Herschel-Bulkley model fitting

Fig. 83(a - d) shows frequency sweeps for carbon black/PEO/H_2O slurries. Samples for both Mws show solid-like behavior between 2 - 5 wt% polymer; here G' is higher than G" without a crossover point, and shows less dependency on frequency. This is indicative of a gel. The exception is the 1000 kg mol^{-1} at 3 wt%, which does have a crossover between G' and G" - the reason is unclear. Interestingly, the polymer concentrations at 1000 kg mol^{-1} which do not show evidence of gelling correspond to samples of low conductivity in the full cathode slurry, whereas the samples that do show gelling correspond to samples of high conductivity (see Fig. 37 (c)).

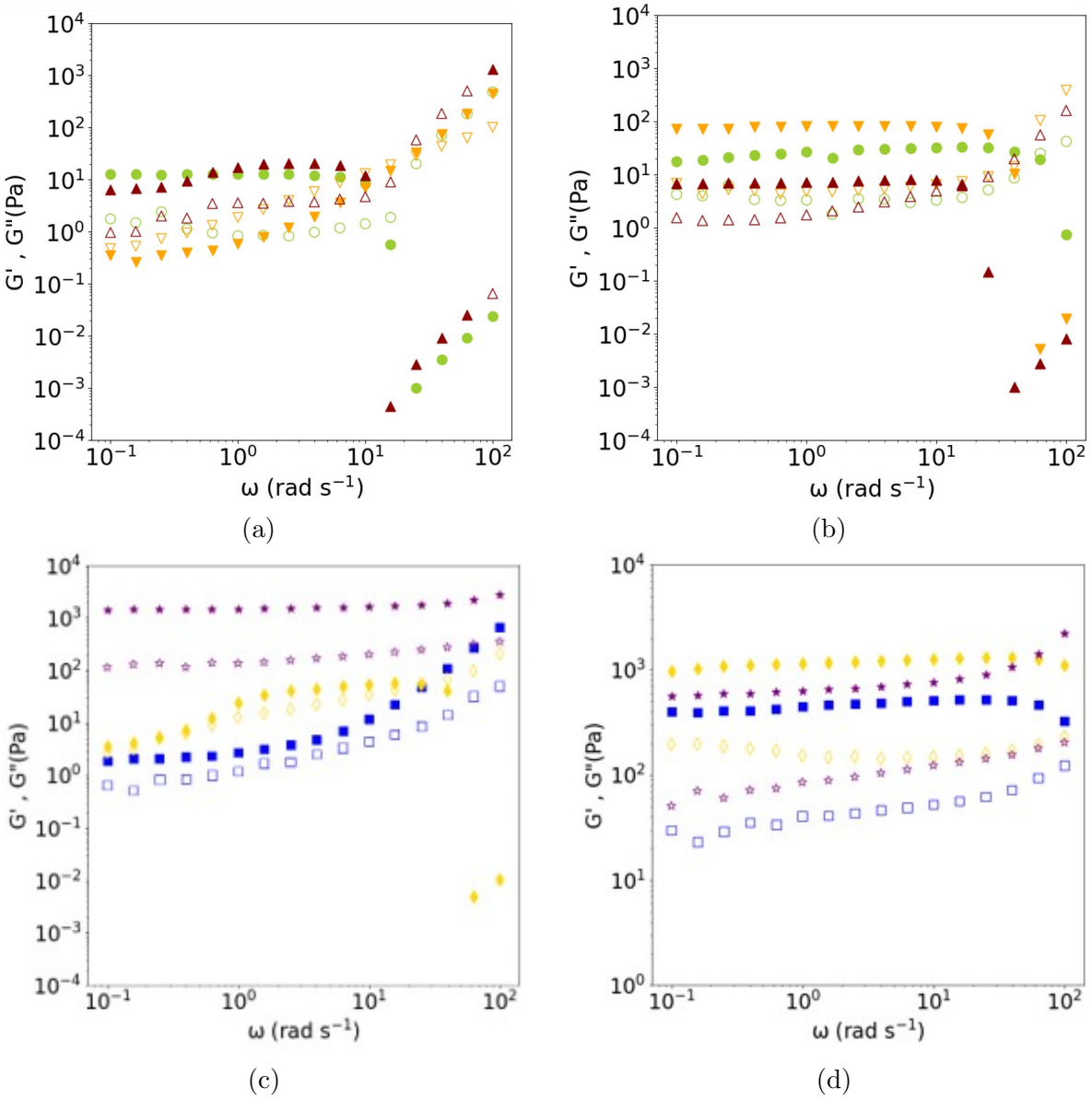

Figure 83: Storage and loss moduli curves for carbon black slurries containing 1000 kg mol^{-1} PEO (a) and (c), and 2000 kg mol^{-1} for (b) and (d), for 0.25 wt % (●), 0.5 wt % (▼), 1 wt % (▲), 2 wt % (■), 3 wt % (♦), 5 wt % (★). Filled symbols are for storage moduli whilst open symbols are for loss moduli.

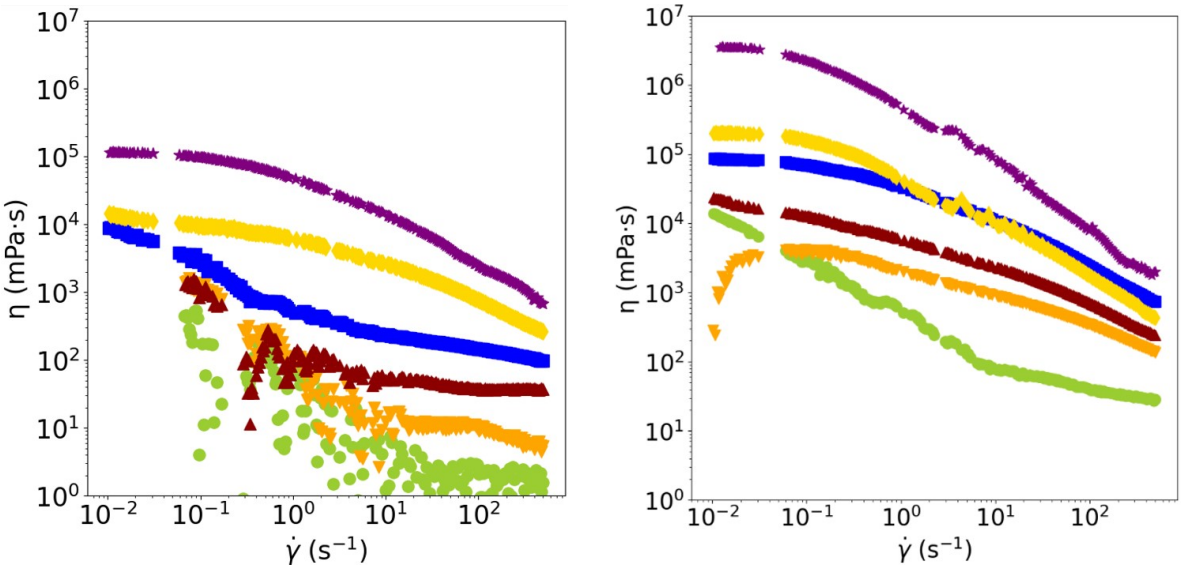

(a) (b)

Figure 84: Flow curves of viscosity for 1000 kg mol^{-1} NMC 622/PEO/H_2O (a) and 2000 kg mol^{-1} NMC 622/PEO/H_2O (b) fitted with the Cross Model, for 0.25 wt% (●), 0.5 wt% (▼), 1 wt % (▲), 2 wt% (■), 3 wt% (♦), 5 wt % (★))

8.2 Chapter 5 QCMD Calibration

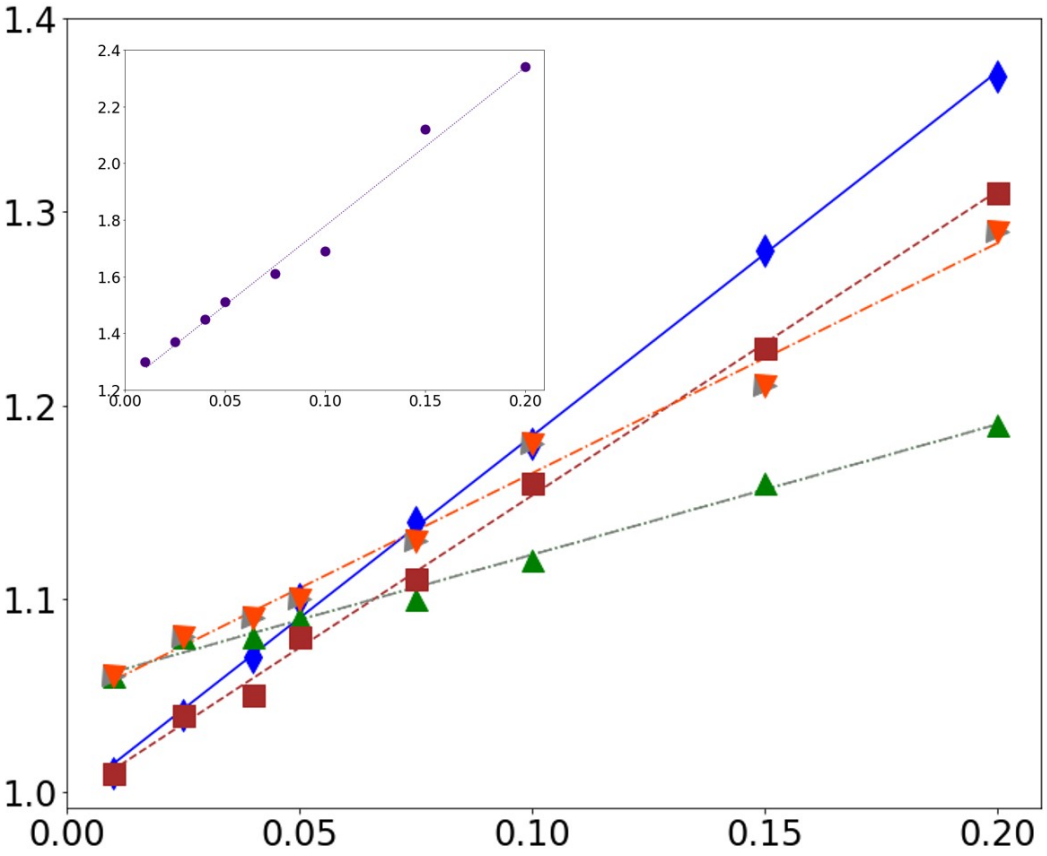

Figure 85: Calibration for the QCMD determination of the concentration of Pluronic F68 (■), (Na Alginate (▼), CMC (♦), PVP (▲), Chitosan (►) and PEO (●) in the inset, in the concentration range 0.01 to 0.2 %.